Department of Civil and Environmental Engineering
University of Strathclyde

Novel Methods for Monitoring Grout Penetration in Hard Rock

A Thesis presented for the Degree of Doctor of Philosophy

by

Claire Pearl Howell

2017

This thesis is the result of the author's original research. It has been composed by the author and has not been previously submitted for examination which has led to the award of a degree.

Signed:

Date:

Abstract

Grouting has been used in ground engineering since the early 19th century. Grouts are injected into the ground both for the creation of hydraulic barriers and for ensuring ground stability. Example applications are dam sealing, underground isolation of waste disposal sites, stabilisation of mine workings and prevention of water ingress during tunnelling. A key problem facing the grouting industry is that once the grout has been injected into the ground, it is impossible to detect where the grout material has gone. As a consequence, the integrity of the hydraulic barrier, or in the case of ground improvement the filling of all significant voids, cannot be guaranteed. This leads to huge conservatism in the industry, with large numbers of unnecessary injection boreholes being drilled. This Ph.D. thesis aims to create a detectable grout by the addition of magnetic materials to traditional cementitious grouts. Laboratory experiments have been undertaken to determine both the magnetic susceptibility and engineering properties of the detectable grout. These experiments have shown that, with the addition of magnetite, a viable detectable cementitious grout mixture can be produced. Samples of the detectable grout were then produced for use in two field trials. The first field trial provided the proof of concept that the grout could be detected both outside of the laboratory environment and at depth. The second field trial established how the magnetic field of the detectable grout changed with distance. The rate of decay of the magnetic field in all directions was established, with the grout being detected at a maximum distance of 3 m. This thesis has provided the first proof of concept that a magnetically susceptible cementitious grout, once injected into the subsurface, can be detected with a magnetometer. The data could then be used to determine the location and shape of the grouted rock volume. This detectable grouting system has the potential to reduce the inefficiencies and uncertainties currently present in the grouting industry.

Acknowledgements

Firstly, I would like to thank both of my supervisors, Professor Rebecca Lunn and Dr Gráinne El Mountassir for all their support and advice throughout my Ph.D.

Thanks also to Chris Wong and Chris Reid for their help during my field trials, especially for driving the van, carrying equipment, and lifting the large grout discs. I would also like to thank Dr Stella Pytharouli for organising the loan of the surveying equipment for the second field trial.

Also, thanks to all the technical staff within the geotechnical labs, especially John and Chris, who enabled the smooth running of my laboratory experiments, and the preparation and casting of my grout discs.

Finally, I would like to thank my family for their continued support throughout my Ph.D. journey.

Contents

List of Figures

List of Tables

Chapter 1

Introduction

1.1 Background

Grouting was first successfully used in ground engineering in the early 19th century to improve the properties of foundations (Widmann, 1996). Since this time, grouting has been applied to a wide range of engineering and geological contexts, with differing methods and materials being utilised (Emmelin *et al.*, 2007). Grouting is mainly used to fill cavities and pore spaces in soils and rocks and to fill rock fractures, with the objective of improving strength and hence the stability of the subsurface and/or to reduce permeability (Nicholson, 2015). Historically, grouting has been primarily used in remedial works, but it is included as part of the design in many engineering applications including tunnels, shafts, dams, and nuclear waste repositories (Donaldson Associates, 2012; Tolppanen and Syrjänen, 2003; Nicholson, 2015). For these applications it is crucial to reduce the amount of ground water inflow during construction work and subsequent operations.

The main factor that determines the success of a grouting operation is how well fractures, cavities, or pore spaces are filled with grout. However, successful grouting remains a matter of trial and error, as it is difficult to determine how well a volume below ground has been filled with grout. Therefore, it is difficult to determine the extent of grout penetration in the subsurface (Emmelin *et al.*, 2007; Tolppanen and Syrjänen, 2003). Due to the inability to ascertain the location of the grout, the integrity of grout barriers cannot be verified, and any gaps present may permit fluid flow. In the case of tunnels and shafts, the inflow of fluid can cause disruption during the construction phase and also after excavations have been completed. Ground stabilisation works may intersect pre-existing natural or man-made features (e.g. old mine workings) and permit a large volume of grout to be injected but the distribution of the grout may not be as planned. In this instance compensation grouting may not

reduce subsidence sufficiently under effected buildings. The result of this uncertainly leads to grouting campaigns being over-designed to compensate for the inability to determine the grout location, and include post grouting validation to ensure that the emplaced grout will contribute to the overall desired outcome, either ground improvement, a reduction in groundwater ingress, or both.

Several different methods have been developed to attempt to determine the location of grout once it has been injected, including: fluorescent imaging (Chen *et al.*, 2000), seismic monitoring (Majer, 1989), ground penetrating radar (Zhang *et al.*, 2010), and down-hole monitoring (Henderson *et al.*, 2008). However, each method has its limitations and none is currently able to definitively determine the location of grout once injected into the ground.

This thesis presents the development of a new grout material that enables the detection of cement grouts through the addition of magnetic minerals. This research is the first step towards developing a detectable cement grout material and a method of detection, which could ultimately be deployed in practice. This technology could revolutionise current grouting practice by reducing some of the uncertainty present in grouting campaigns, therefore reducing costs, wastage of materials, and also the carbon footprint of the grouting operation.

1.2 Research Aim and Questions

The main aim of this thesis was to investigate the potential use of magnetic minerals in cementitious grouts to enable the detection of grouts in the subsurface. This study addresses the following research questions:

1. Does the addition of magnetic minerals into a cementitious grout mixture sufficiently change its magnetic properties to enable it to become detectable? How are magnetic properties influenced by type and concentration of magnetic minerals in the grout mix?

2. Can a workable grout, in terms of cement grout properties, be achieved using magnetic additives?

3. Can the location of magnetic grouts be detected in the environment? What survey methods can be used to detect grouts present at depth? Over what distance are magnetite-based magnetic grouts detectable?

The following paragraphs will describe how the research questions above have been addressed in this thesis.

The first research question of determining whether the addition of a magnetic mineral into a cementitious grout would enable the mixture to become detectable, was addressed firstly by undertaking laboratory magnetic susceptibility measurements. A range of detectable grouts were produced containing differing amounts of magnetic minerals, and cement additives. A magnetic grout mixture was then chosen to be taken outside of the laboratory environment and scaled up so that detectability field trials could be undertaken.

The second research question of establishing if the addition of magnetic minerals to the cementitious grout results in a detrimental change occurring to the cement properties was addressed using a number of different laboratory experiments. Testing of the pure cement, cement with the magnetic mineral added, and the magnetic cement with additional additives was undertaken.

The third research question ascertaining the location of the detectable grout, and whether it could be detected at depth was addressed by undertaking two field trials. The first field trial initially focused on determining whether the magnetic grout materials were still able to be detected outside of the laboratory environment. When the detectability of the magnetic grout was established on the surface, depth trials were then undertaken. The second field trial built upon the results of the first, with the trial simulating a magnetic survey method that could be deployed at depth, via the use of boreholes. This was simulated by taking magnetic measurements in all orientations

around the magnetic grout and at different vertical heights, and from these results it has been possible to establish how the magnetic field of the magnetic grout changes with distance and with height.

1.3 Outline of Thesis

This thesis has been organised into the following chapters:

Chapter 2 Review of Grout Materials, Properties, and Detection Methods: presents an overview of grouting, including what a grout is and the process of grouting. Common grouts (cementitious and chemical), the key properties of grout, and the applications of where grouts are used are described. A review of previous attempts at grout detection is presented at the end of this chapter.

Chapter 3 Magnetic Materials: presents an introduction to magnetism, and basic magnetic theory. It discusses different magnetic materials, their properties, and the various types of equipment which can be used to detect magnetic fields.

Chapter 4 Developing a Magnetic Grout: presents the experimental laboratory work that has been undertaken to develop a magnetic grout. It outlines the materials, methods, and results for the flow, bleed, setting time, temperature, and magnetic susceptibility testing that has been undertaken. This chapter also presents the Scanning Electron Microscope (SEM) and thin section images of the different magnetic grout mixtures produced.

Chapter 5 Detecting the Magnetic Grout: focuses on the two field trials undertaken as part of the PhD research. It details the rationale behind each field trial layout, the survey methods used and the production of the magnetic test specimens. The methods used to analyse the magnetic field data and the results from each field trial are presented.

Chapter 6 Application to Industry: discusses the potential engineering uses of the magnetic grout which has been developed in this research.

***Chapter 7 Conclusions and Future Work*:** outlines the main conclusions of this thesis and gives recommendations in the areas of further work.

Chapter 2

Review of Grout Materials, Properties, and Detection Methods

2.1 Introduction

This chapter presents an overview of the process and materials used for grouting, the environments in which grouting is used, and also the key properties of grout that control its workability. In industry the primary challenge surrounding the use of grout is the inability to know the location of the grout after it has been injected into the subsurface. As a result there have been a number of attempts made (both by the research community and by industry) using different techniques to detect grout location. A review of these techniques is also presented in this chapter.

2.2 Grouting and Applications

Grouting is a process where a material (grout) is injected through boreholes at pressure into fractures or voids that are found in rock, soil or any other man-made cavities (Emmelin *et al.*, 2007; Hollmén, 2008). Grout can be injected into the ground to: (a) reduce the mass permeability of the ground forming a barrier to groundwater or contaminant flow, (b) stiffen soils to improve foundation response and to improve excavation stability, (c) to increase the density of soils to prevent liquefaction, (d) stabilise the ground to facilitate tunnelling or shaft excavation, and (e) fill natural cavities and voids adjacent to structures (Rawlings *et al.*, 2000; Healy and Head, 1984). The purpose of grouting generally falls under one of two categories, to alter the hydraulic properties of the ground (a and e), or mechanical behaviour of the ground (b, c, d, and e), or both. The term ‘grout’ does not refer to any particular material type (Nicholson, 2015).

The use of grouting has become more widespread and varied with the development of new techniques. Rock grouting is used in many different engineering scenarios, such as in nuclear waste repositories, dams, tunnels, and shafts (Donaldson Associates, 2012; Tolppanen and Syrjänen, 2003). For these engineered structures, a reduction in the rock mass permeability is crucial, primarily to reduce ground water inflow during construction works and also to ensure that contaminants are unable to migrate from the site. In the following a brief summary of how grouting campaigns can achieve permeability reduction in different engineering applications is presented.

2.2.1 Grout Curtains

Dam grouting is often carried out during construction in order to prevent underseepage occurring below a dam. This is often achieved by creating a grout curtain (Knappett and Craig, 2012). The size and shape of the grout curtain is dependent on the size of the dam and also on the underlying geology. Ideally, the grout curtain should extend to a depth where there is a naturally occurring low permeability layer, or where the permeability is of an acceptable limit (Figure 2.1) (Rawlings *et al.*, 2000).

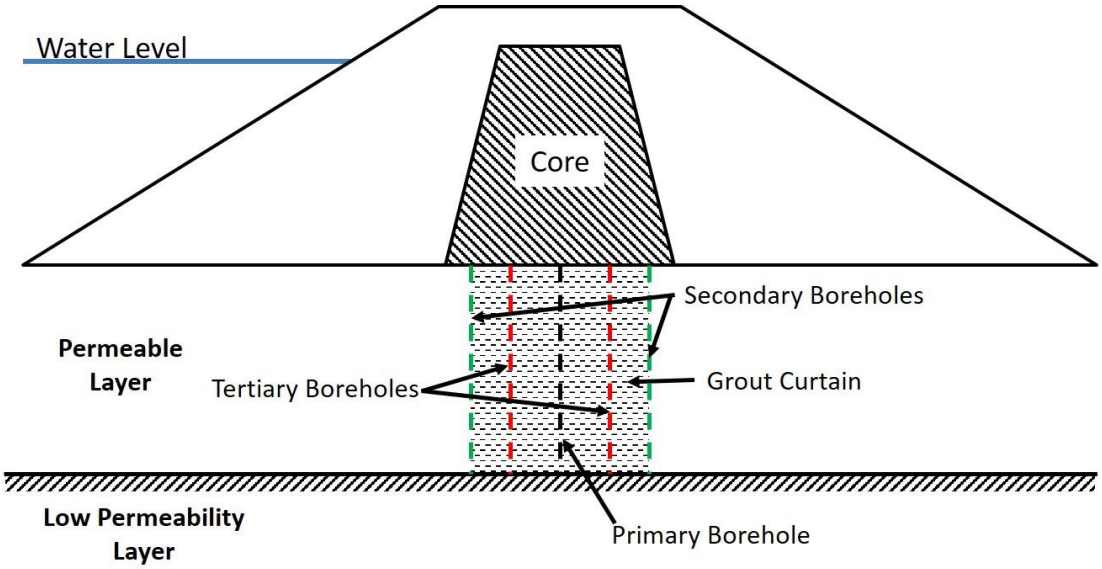

Figure 2.1: *Schematic diagram of a dam grout curtain (After Knappett and Craig, 2012).*

In rock grouting, to ensure that there is a uniform background coverage of grout, a split spacing method of grouting is used (Rawlings *et al.*, 2000). This method entails firstly drilling and grouting primary boreholes before secondary and tertiary boreholes are drilled and then grouted (Figure 2.1 and Figure 2.2). The spacing of these boreholes should be decided based on grouting tests that have been completed previously or on experience (Rawlings *et al.*, 2000). Further boreholes that are more closely spaced can then be used where necessary to ensure that an even coverage of grout has been achieved. These boreholes are also used to ensure that all of the water flowing features have been sealed and none are left ungrouted (Rawlings *et al.*, 2000).

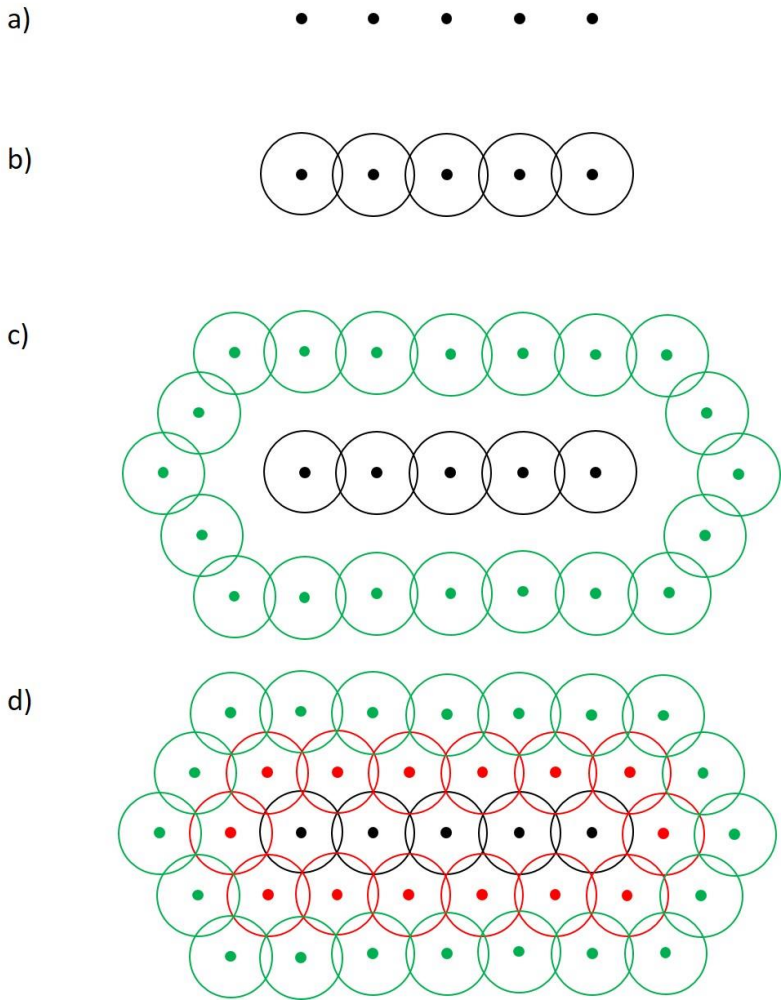

Figure 2.2: *The formation of a grout curtain, a) Primary boreholes, b) Primary boreholes showing the extent of the first grouting stage, c) Second phase of grouting showing secondary boreholes (in green), and d) Third phase of grouting showing tertiary boreholes (in red) with the three grouting stages overlapping.*

2.2.2 Tunnels

In tunnels, grout curtains are often created radially around the whole of the structure (Henn, 1996). The grouting can be carried out either before blasting work is completed (pre-grouting) or after excavation has taken place (post-grouting) (Figure 2.3a). Pre-grouting is mainly carried out to tighten the rock mass around the tunnel periphery to reduce the hydraulic conductivity (Tolppanen and Syrjänen, 2003). In pre-grouting a 'hedgehog' array of boreholes is drilled in front of the excavation face and usually one borehole is grouted at a time (Gustafson, 2012). There are several advantages to pre-grouting. It provides some protection against a high-water inflow during the excavation work and can limit lowering of the water table. It also strengthens the rock around the tunnel, which also leads to an increase in the safety of the working environment (Tolppanen and Syrjänen, 2003). However, there are some disadvantages to pre-grouting. Pre-grouting can cause a disruption to excavation work by increasing the amount of time required for the work to take place. Also, the orientation of the grouting holes may not be in an optimal position to intersect water flowing features, as the source of water leaks cannot be directly seen. Furthermore, blasting and deformations around the excavation once work has recommenced might potentially re-open joints and fractures (Tolppanen and Syrjänen, 2003).

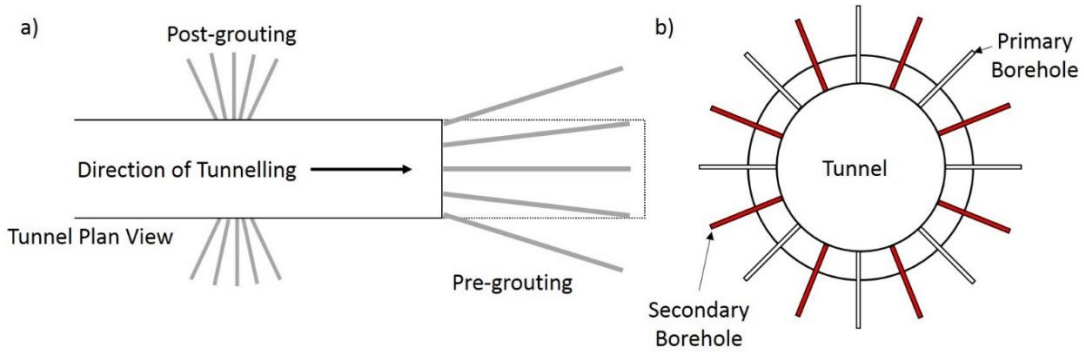

Figure 2.3: *a) A schematic diagram of pre- and post-grouting (After Hollmén, 2008), and b) a section of a tunnel grout curtain (After Henn, 1996).*

Post-grouting is a method that is used to grout in an area that has already been excavated. The need for post-grouting depends on the apparent leakage amount in the excavation and on the stipulated requirements (Tolppanen and Syrjänen, 2003). The requirements on the ingress of water into excavations varies between different projects, for example, the Løren road tunnel in Oslo, Norway had groundwater ingress requirements after grouting of between 7 to 10 l/min/100m (Høien and Nilsen, 2014). For the Dounreay Shaft, located on the North coast of Scotland, inflow into the shaft was set at no more than 15 m^3 per day (Whitfield and Henderson, 2008). In post-grouting the lengths of the grouting holes are typically shorter and the hole spacing is denser than in pre-grouting as the targets are more local. It is typically easier to plan a post-grouting campaign by focussing on fracture zones, areas of bad rock quality or areas that have been disturbed or damaged due to blasting. However, post-grouting is much more expensive than pre-grouting due to the larger number of boreholes required to grout small localised areas (Tolppanen and Syrjänen, 2003).

The formation of a grout curtain around a tunnel is undertaken in stages with primary boreholes grouted first, followed by secondary boreholes (Figure 2.3b). This grouting method continues until the entire perimeter of the tunnel is grouted. Ensuring that the excavation has limited groundwater inflow is especially important in the case of railway tunnels, as water ingress from the surrounding rock mass can prevent excavations from being operational. Additionally, water on the rails can cause erosion, which in extreme cases can result in derailments occurring. An example of this can be seen in the Uebonmechi-Nipponbashi Tunnel in Japan, where inflow of acidic groundwater into the tunnel since construction has led to severe corrosion of the rails occurring (ITA Working Group, 1991). Also, if electrical systems are present in the tunnels, water needs to be prevented from reaching them.

2.2.3 Shafts

Shaft grout curtains, like tunnel grout curtains are created radially around the whole of the structure (Henn, 1996). They are used to reduce and control the inflow of groundwater into the shaft. As shafts may often cut though several different geological formations, the groundwater flow into the shaft will vary with depth depending on the permeability of the surrounding rock. The groundwater inflow accumulates at the base of the shaft, leading to pumping being required to produce a safe working environment (Henn, 1996). Therefore, by forming a grout curtain around the shaft the groundwater inflow can be significantly reduced in accordance with the requirements of the project. Shaft grouting can be performed both from the surface, prior to excavation work commencing, and from within the shaft itself. A combination of both of these techniques may be used depending on the project specific requirements (Henn, 1996).

An example of a shaft grouting project can be seen in the Dounreay Shaft, located on the North coast of Caithness, in the Scottish Highlands. In this project a grout curtain was installed to reduce groundwater inflow into the shaft containing nuclear waste to < 15 m^3/day to enable dry retrieval of the waste (Whitfield and Henderson, 2008). The shaft grout curtain was produced using several grouting stages as has been seen previously in the formation of dam and tunnel grout curtains. Figure 2.4 shows a 3D schematic representation of the grout curtain surrounding the Dounreay shaft.

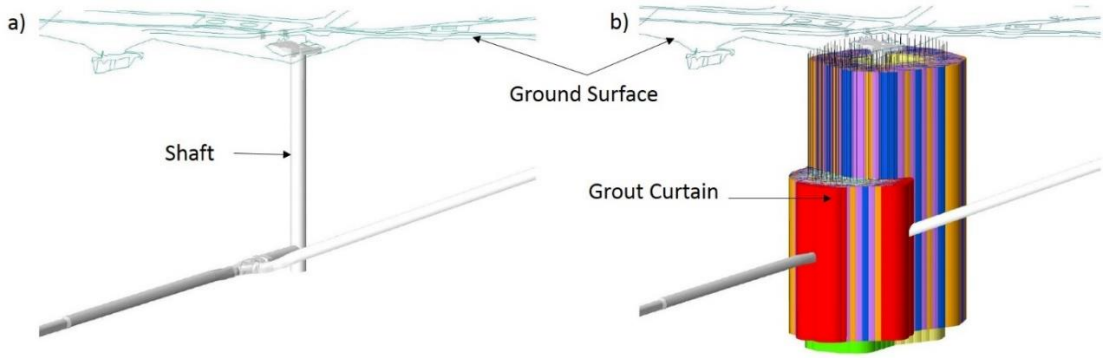

Figure 2.4: *a) Dounreay shaft before the grout curtain was installed, and b) the shaft showing the different grouting stages (represented by different colours) forming the grout curtain (After Whitfield and Henderson, 2008).*

2.3 Grout Materials

The type of grout material that is used for a project will depend on several different variables, such as the specific project requirements, the environmental requirements, and the geological and hydraulic properties of the rock or soil mass (Tolppanen and Syrjänen, 2003). Grout material types can be separated into particulate (e.g. cementitious) grouts, where solid particles are suspended in a fluid, and chemical grouts (Nicholson, 2015). This section will discuss both types of grout material below.

2.3.1 Cementitious Grouts

The most common particulate grouts are composed of cement, which often contain a range of additives (Nicholson, 2015). Cements can be divided into different classes depending on their grain size, as follows: Ordinary Portland Cement (OPC) (d_{95} < 128 µm, where d_{95} is the particle diameter at which 95% of the cement mass is comprised of particles with a diameter less than this), Microcements (d_{95} < 20 µm), and Ultrafine cements (generally accepted d_{95} < 12 µm) (Donaldson Associates, 2012). The penetrability of each cement grout varies due to their differing grain sizes. Penetration of a cementitious grout into small fractures is especially limited by its grain size (Draganović and Stille, 2011).

OPC is the most common type of cement in general use. It was first developed in 1824 and its name originates from Portland limestone in Dorset due to its close resemblance to the rock after hydration has taken place (Dhir and Jackson, 1980). The basic raw materials used in the manufacture of OPC are calcium carbonate, silica, alumina, and iron oxide (Dhir and Jackson, 1980). A mixture of these raw materials is then heated in a kiln to a temperature of around 1450°C to produce a clinker. The clinker is then ground with gypsum to its required fineness (Neville, 1973; Dhir and Jackson, 1980; Taylor, 1997). The clinker typically has a composition of around 67% CaO, 22% SiO_2, 5% Al_2O_3, 3% Fe_2O_3, and 3% other components (Taylor, 1997). The components are usually contained in four major mineral phases called, alite, belite, aluminate, and

ferrite (Taylor, 1997). The chemical compositions of these mineral phases can be found in Table 2.1.

Table 2.1: *A table showing the composition of the major mineral phases found in OPC (After Gani, 1997).*

Mineral Phase	Idealised Chemical Composition	Abbreviation
Alite	Ca_3SiO_5	C_3S
Belite	Ca_2SiO_4	C_2S
Aluminate	$Ca_3Al_2O_6$	C_3A
Ferrite	Ca_2AlFeO_5	C_4AF

Alite is the most important constituent of OPC, as it makes up around 50-70% of the cement clinker. It is tricalcium silicate (Ca_3SiO_5 (C_3S)), which is modified in composition and crystal structure by ionic substitutions (Taylor, 1997). It reacts relatively quickly with water to form mainly calcium silicate hydrate ($CaO.SiO_2H_2O$ (CSH)), and calcium hydroxide ($Ca(OH)_2$ (CH)) (Gani, 1997). The chemical equation of this reaction is as follows using cement chemist notation (abbreviations):

$$2C_3S + 7H \rightarrow C_3S_2H_4 + 3CH \qquad \textit{(Gani, 1997)}$$

This reaction generates a considerable amount of heat and it makes a significant contribution to the development of early strength particularly during the first 14 days (Dhir and Jackson, 1980; Taylor, 1997).

Belite constitutes around 15-30% of the cement clinker. It is dicalcium silicate (Ca_2SiO_4 (C_2S)) modified by ionic substitutions and is normally present wholly or largely as the β polymorph (Taylor, 1997). Belite has five different polymorphs (crystal structures), but the β polymorph structure is the one that is most commonly found in cement. Belite reacts slowly with water and forms calcium silicate hydrate

and calcium hydroxide, the same products produced in the reaction with alite. The chemical equation of this reaction is as follows (in cement chemist notation):

$$2C_2S + 5H \rightarrow C_3S_2H_4 + CH \qquad \text{(Gani, 1997)}$$

Due to the slow reaction with water, belite contributes little to the strength of the cement during the first few days; however, it is mainly responsible for the development of strength after 7 days. Over a year, the strengths that are attainable from pure alite and belite are about the same under comparable conditions (Dhir and Jackson, 1980; Taylor, 1997).

Calcium aluminate consists of around 5-10% of the OPC clinker. It is tricalcium aluminate ($Ca_3Al_2O_6$ (C_3A)) which can be substantially modified in composition and sometimes also in structure by ionic substitutions. It reacts rapidly with water and initially forms hexagonal hydrates, C_2AH_8 and C_4AH_{13}. These are then converted over time into C_3AH_6 (hydrogarnet) which is more stable. The chemical equation for these reactions are as follows:

$$2C_3A + 21H \rightarrow C_4AH_{13} + C_2AH_8 \qquad \text{Hexagonal hydrates (Gani, 1997)}$$

$$C_4AH_{13} + C_2AH_8 \rightarrow 9H + 2C_3AH_6 \qquad \text{Hydrogarnet (Gani, 1997)}$$

To control the rate of the hydration, a set controlling agent, normally gypsum ($CaSO_4.2H_2O$ ($C\bar{S}H_2$)) is used (Gani, 1997; Taylor, 1997). The addition of gypsum helps to control the hydration rate by reacting with the C_3A by firstly forming a hydrated calcium aluminosulphate (ettringite), which is only stable in the presence of a plentiful supply of gypsum (Gani, 1997). As the gypsum gets consumed by the reaction, the gypsum concentration lowers. This results in the ettringite becoming unstable and converts into a monosuplhoaluminate hydrate ($3C_4A\bar{S}H_{12}$) (Gani, 1997). The chemical equations for these reactions are as follows:

$$C_3A + 3C\bar{S}H_2 + 26H \rightarrow C_6A\bar{S}_3H_{32}$$ Ettringite (Gani, 1997)

$$C_6A\bar{S}H_{32} + 2C_3A + 4H \rightarrow 3C_4A\bar{S}H_{12}$$ Monosulphoaluminate hydrate (Gani, 1997)

Ferrite makes up around 5-15% of normal OPC clinkers. It is tetracalcium aluminoferrite (Ca_2AlFeO_5), which is substantially modified in composition by the variation in the Al/Fe ratio and ionic substitutions. The rate at which it reacts with water appears to be somewhat variable, which is possibly due to differences in composition or other characteristics, but in general the reaction rate is high initially and low to very low at later stages (Taylor, 1997).

2.3.2 Chemical Grouts

Grout materials that are in solution, as opposed to being composed of suspended solids, are termed chemical grouts (Nicholson, 2015). Chemical grouts typically have a low viscosity and high penetrability, and as a result of this they were developed as an alternative to cement-based grouts in response to a need to control water flow and increase strength in geological units where the pore sizes / fracture apertures were too small for conventional cementitious grouts to penetrate (US Army Corps of Engineers, 1995).

There are several different types of chemical grouts such as, sodium silicates, acrylates, lignin, urethane, resin and colloidal silica (Nicholson, 2015; US Army Corps of Engineers, 1995). Silicate Resin grouts are a solution of organics within water or a solvent. This tends to make resins the most expensive chemical grout, and is only used when a very low viscosity, a rapid gain in strength, and a high chemical resistance is required. Colloidal silica is a colloidal hydrosol (a colloidal solution in water) which consist of amorphous silica particles. This chemical grout can penetrate into micro-fractures as the silica particles present are only tens of nanometres in diameter (Funehag and Gustafson, 2008).

Chemical grouts often contain different reagents that will chemically react with their surroundings (or different components) causing them to harden over time. The types of reagents used within the chemical grouts can be used to control the viscosity, strength, and durability of the grout (Nicholson, 2015). An advantage of chemical grouts, over cementitious grouts, is that the setting times can be precisely controlled from seconds to hours or even days depending on the application (Nicholson, 2015).

The main advantages of using chemical grouts is that due to their effective penetration, chemical grouting is usually faster than using a cementitious grout (Tolppanen and Syrjänen, 2003). Also, due to their early setting the chemical grout does not get flushed away easily. However, the disadvantages are that chemical grouts are more expensive than cementitious grouts, and some products may present a health and safety risk due to toxic components. Also, the longevity and stability properties of the chemical grouts are not well known for all of the materials, and special equipment may be required (Tolppanen and Syrjänen, 2003).

This thesis will focus on cementitious grouts as these are the most widely used in grouting practice.

2.4 Grout Properties

There are several important properties of a grout that need to be taken into consideration. The rheological properties govern the ability of the grout to flow and penetrate into the subsurface, which include the flowability, bleed, and penetrability of the grout, and depend primarily on the water to cement ratio. The water to cement ratio (wcr) is the mass of water (M_w) divided by the dry mass of cement (M_c).

$$wcr = \frac{M_w}{M_c} \tag{2.1}$$

However, the rheological properties are also influenced by the specific surface of the cement, cement type, cement hydration, mixing time and mixing intensity, and also temperature (Emmelin *et al.*, 2007; Håkansson *et al.*, 1992).

The rheology of a particulate cementitious grout can be very complex due to the interaction between the physical and chemical processes that take place between the solid and fluid phases (Håkansson *et al.*, 1992). The interparticle forces between the solids result in a yield stress that must be exceeded in order for the cement grout to flow (Håkansson *et al.*, 1992; Fransson, 2008). Therefore, the yield stress represents the transition between the solid-like and fluid-like behaviour of the cementitious grout (Håkansson *et al.*, 1992). A rheological model that describes the flow properties of a cementitious grout is the Bingham model. This model consists of two parameters, plastic viscosity and yield stress (Figure 2.5). The Bingham model can be expressed as:

$$\tau = \tau_0 + \mu_B \gamma \tag{2.2}$$

Where: τ is the shear stress, μ_B the plastic viscosity, τ_0 the yield stress, and γ is the shear rate (Håkansson *et al.*, 1992; Emmelin *et al.*, 2007).

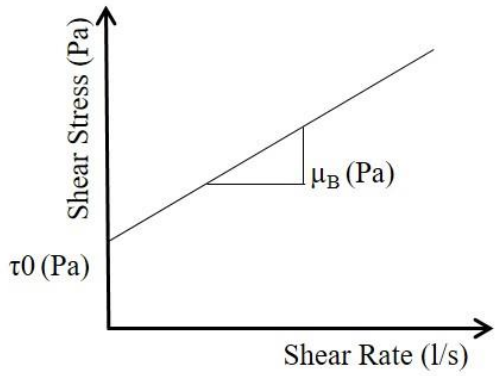

Figure 2.5: *Bingham rheological model (After Emmelin et al., 2007).*

The flow of the grout is dependent on the temperature, the viscosity of the grout, and the amount of time that has elapsed after mixing (Widmann, 1996). The viscosity of the grout controls the ability of the grout mixture to flow and penetrate into fractures. The viscosity can be partly controlled by the water to cement ratio, with higher amounts of water (higher water to cement ratio) resulting in a lower viscosity grout which has the ability to penetrate greater distances (Nicholson, 2015). However, this can result in a less stable grout mixture that has a greater tendency to separate. Figure 2.6 gives an example of the changing viscosity of three different cement over time. As

the cement begins to set, the viscosity changes which dictates the penetration distance achieved. The flowability of cement grout is tested using a flow cone (ASTM C939) and this method is described in Chapter 4.

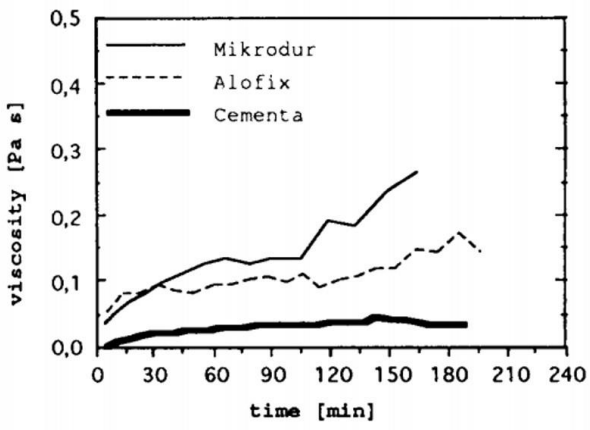

Figure 2.6: *A graph showing an example of the viscosity of three different cements over time (From: Håkansson et al., 1992).*

Grout bleed refers to the separation of the water from the solid particles, which causes a layer of water to form on the top of the grout, which is known as bleeding (Tan *et al., 2005;* Emmelin *et al.*, 2007). The bleed of the grout can have an influence on the grout's ability to fill and seal fractures as the layer of bleed water can create a potential flow path. There are four main processes which cause bleeding to occur. They are sedimentation, consolidation, hydration, and flocculation of the grout (Draganović, 2009). The sedimentation process is caused by cement particles sinking due to gravity, and the process is complete when all of the particles have already settled and / or the hydration reaction has already begun. This results in a water layer forming on the top of the grout (Dragonović, 2009). The consolidation of the grout is caused by the settled particles being compressed by the weight of the particles on top. This causes pore water in the grout to be pushed to the surface of the grout (Dragonović, 2009). The hydration of the grout can also affect the amount of bleed produced due to the amount of water that is utilised during the hydration reaction. When the cement particles react with water the cement particles become covered in a layer of reaction products. These reaction products form layers around the outside of the cement particles and may prevent water penetrating through this layer to the unreacted cement below. This therefore results in excess water being present in the cement grout, leading to

bleed occurring (Dragonović, 2009). Flocculation can also result in bleed, as single cement particles can clump together due to their attractive forces being larger than any repulsive forces present. This can result in water getting trapped within the clumps of particles, which can lead to bleed occurring when the grout becomes consolidated (Dragonović, 2009). Bleed tests are conducted by observing a volume of water separating from the cementitious grout over time. A description of this method (ASTM C232) is presented in Chapter 4.

The penetrability of a cement based grout is influenced by many different factors including, the grain size of the cement, flocculation and hydration of the cement, the water to cement ratio, and the grouting injection pressure (Dragonović and Stille, 2011). The penetration of the grout is important in that it determines the distance to which the grout permeates into the fractures (Dragonović and Stille, 2011).

Another important property of cement based grouts is the initial and final setting times. These setting times can be influenced by the type of cement used, the water content, and the properties of any additives in the grout mixture (Tan and Zaimoglu, 2004). The initial setting time details the time at which the grout mixture can no longer be injected and the final setting time details the point at which the grout mixture begins to harden and strength develops. These are important properties to determine as it provides a timescale for when the grout mixture can be used for injection (Tan and Zaimoglu, 2004). Figure 2.7 gives an example of initial and final setting times of an OPC CEM I cement at a range of water to cement ratios. From the results it can be seen that both the initial and final setting time increase with increasing water to cement ratio.

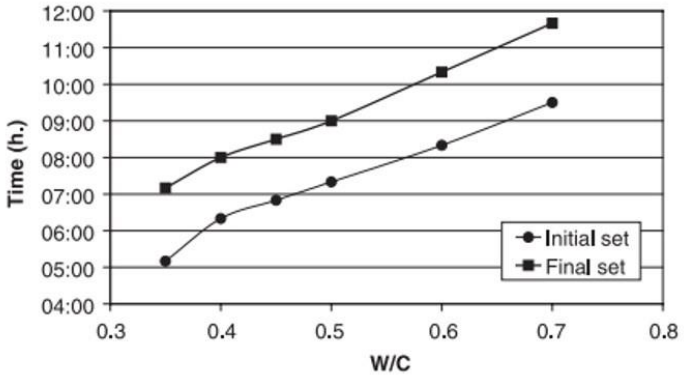

Figure 2.7: *An example of initial and final set times determined by the Vicat needle for different water to cement ratios (From: Rosquoët et al., 2003).*

The mechanical properties of the grout also need to be taken into consideration if the purpose of the grouting is for mechanical improvement, hydraulic improvement or both. To ensure the continued longevity of the grout within a rock mass, a high strength, in particular adhesive strength and shear strength is important (Widmann, 1996). It is common for grouting campaigns to have desired compressive strength targets for early (2 days) and late (28 days) strength. A comparison of three classes of strength taken over periods of 2 days, 7 days, and 28 days are given in Table 2.2. The three classes of strength within Table 2.2 are a class with ordinary early strength (N), a class with a high early strength (R), and a class with a low early strength (L), which is only applicable for CEM III cements (British Standards Institution, 2011). The mechanical properties of the grout are not investigated in this thesis.

Table 2.2: *The compressive strength of a range of classes of cement (After: British Standards Institution, 2011).*

Strength Class	Compressive Strength (MPa)			
	Early Strength		Standard Strength	
	2 Days	7 Days	28 Days	
32,5 L	-	≥ 12,0	≥ 32,5	≤ 52,5
32,5 N	-	≥ 16,0		
32,5 R	≥ 10,0	-		
42,5 L	-	≥ 16,0	≥ 42,5	≤ 62,5
42,5 N	≥ 10,0	-		
42,5 R	≥ 20,0	-		
52,5 L	≥ 10,0	-	≥ 52,5	-
52,5 N	≥ 20,0	-		
52,5 R	≥ 30,0	-		

2.4.1 Cementitious Grout Additives

To improve the behaviour of cementitious grout mixtures, additives can be used to enhance the properties of the grout. There are several different types of additives that can be used such as superplasticisers to reduce the water to cement ratio, accelerators that prevent the grout leaking into the surrounding rock or ground surface, additives that reduce the amount of bleed and shrinkage of the grout, expanding additives, and retarders that slow the hydration of the grout, however retarders are not commonly used in grouting (Bye, 1999; Tolppanen and Syrjänen, 2003).

Superplasticisers are used to increase the fluidity of the grout without having to increase the water content which would result in a loss of strength and an increased segregation of the grout (Gani, 1997). The increase in the fluidity is achieved by the superplasticiser being adsorbed onto the surface of the hydrating cement particle. This adsorption causes the cement particles to become repulsive to each other normally by opposing the attractive forces of the cement particles with steric and electrostatic

forces, which then leads to the cement particles becoming dispersed (Gani, 1997; Nkinamubanzi *et al.*, 2016; Sakai *et al.*, 2006). Using superplasticizers within the grout can help the grout penetrate and reach greater distances before it begins to harden (Tolppanen and Syrjänen, 2003). Figure 2.8 shows how the flow time of the cement with a water to cement ratio of 0.4 can vary with different dosages of superplasticiser. In increasing the percentage of superplasticiser, the flow time is reduced which gives an indication that the grout mixture is becoming more fluid (i.e. it takes a shorter time for a given volume to flow through a cone of particular geometry and opening size). In testing the same cement mixture at 5 minutes and 60 minutes after mixing, the flow time is significantly different with lower percentages of superplasticiser, however as the percentage of superplasticiser increases this difference decreases.

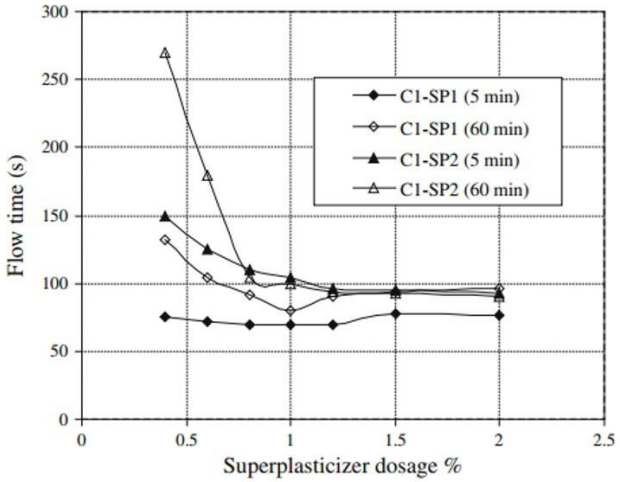

Figure 2.8: *A graph showing the variation in the flow time for differing dosages of superplasticisers (From Hallal et al., 2010).*

Accelerators are used to reduce the setting time of the grout mixture, and therefore increase the early strength of the grout. There are many inorganic and organic compounds that can be used as accelerators; however, the most common are calcium chloride and sodium chloride (Gani, 1997). Calcium chloride affects both the setting and early strength development of the grout. Generally, around 1 to 6% of calcium chloride is added to the grout by weight of cement, however in extreme cases up to 15% of calcium chloride can be used (Henn, 1996; Tolppanen and Syrjänen, 2003). Sodium chloride is used in concentrations of around 1.5 to 5% by weight of the cement, however it is less effective than calcium chloride (Henn, 1996).

Additives such as bentonite or silica based products like GroutAid, can reduce the bleed and shrinkage of the grout, and these are referred to as stabilising agents (Tolppanen and Syrjänen, 2003). Bentonite is a volcanic clay which can absorb large amounts of water and is normally added to grout to stabilise the mixture against separation (Tolppanen and Syrjänen, 2003). GroutAid is a silica fume (microsilica) additive that has been developed by Elkem Materials. The particles within this additive are very fine, with more than 90% of the particles being less than 1 μm (Galíndez and Molinero, 2010). The small particle size and the reactivity of the microsilica cause a reduction in the bleeding and segregation of the grout mix. This leads to the development of a stronger and more permeable grout (Galíndez and Molinero, 2010).

This thesis will investigate the behaviour of cementitious grouts with the presence of superplasticiser and stabilising agent within the grout mixture.

2.5 Grout Injection

Before grouting can commence, criteria controlling when to cease injecting grout are set. These criteria define the measurements of typically, the injection pressure and injected volume of grout which are continually recorded during grouting (Donaldson Associates, 2012). There are several different stop criteria that have been developed, two of these methods are described below.

Traditionally, the limits for grouting are defined by the maximum grouting pressure and/or the maximum grout volume. In the case of pressure, a maximum pressure value is set which is set to ensure that deformation of the rock mass does not occur (Stille *et al.*, 2012). The maximum grout volume can also result in the stopping of the grouting process, and this can take place without the maximum grouting pressure being reached. The minimum flow can also be used as a stop criterion in conjunction with the maximum grouting pressure. This occurs when there has been no flow of the grout over a set time period, and as a result the grouting is stopped (Emmelin *et al.*, 2007; Hollmén, 2008).

Another method for controlling grout injections is the GIN-method (Grouting Intensity Number). Lombardi (1996) defines the grouting intensity 'as the product of the final grouting pressure times the grout take per metre of borehole at the end of the grouting process in a single borehole interval injection, such that the grouting intensity number is given by the equation

$$GIN = P_f.V_f \quad (2.3)$$

Where:

P_f = final injection pressure (bars)

V_f = final injected grout volume per metre (l/m)

The GIN-method was initially developed to control the grouting operations of dam construction (Hollmén, 2008). It is intended for use with cementitious grout mixtures that exhibit cohesion or a yield point (Lombardi, 1996). Throughout the whole grouting process using the GIN-method, only one stable and thick grout is injected. The main aim of the GIN-method is to obtain the best grouting results, (i.e. damage to the rock mass is avoided, and the grouting is achieved at the lowest cost and in the simplest way) (Lombardi, 1996).

Figure 2.9 below illustrates the limiting grouting curve (1) that has been chosen for a project or for a given area of a project (Lombardi and Deere, 1993). This curve includes the limiting pressure (P_{max}) and the limiting grout volume (V_{max}). The actual grouting path (2) is plotting the instantaneous grouting pressure versus the cumulative grout volume. This path intersects the GIN curve at a final pressure P_f and a total grout take (V_f) (Lombardi and Deere, 1993).

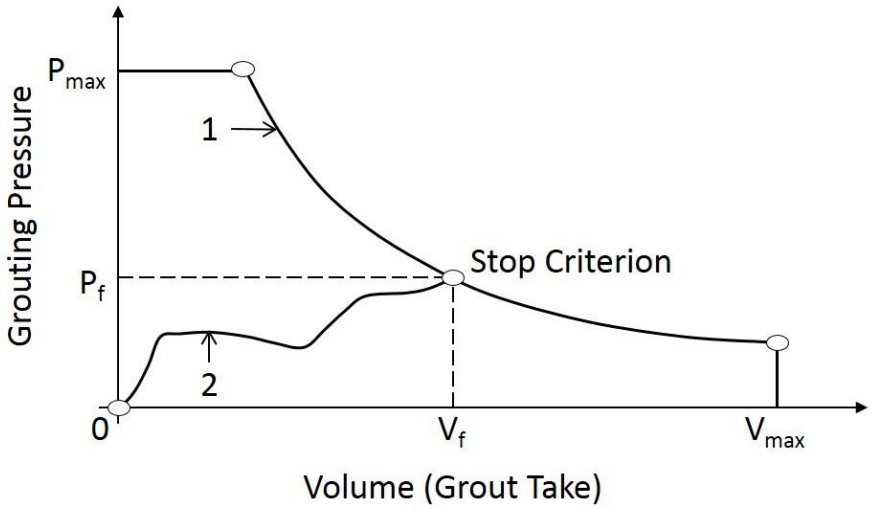

Figure 2.9: *The typical grouting process of a single borehole. (1) A GIN curve, and (2) the grouting path (After Lombardi and Deere, 1993).*

In the GIN method a constant value of GIN is maintained (Lombardi and Deere, 1993). This means that for easily grouted (large aperture) fractures, they will have a high volume take at low injection pressures, whereas finer aperture fractures will have a low volume take at higher injection pressures (Lombardi and Deere, 1993).

The advantages of keeping a constant GIN value throughout all the stages of the grouting process is that in theory a constant spread of the grout can be achieved, whilst the pressure and volume of the grout injection can be changed to adapt to each grouting phase (Figure 2.10) (Lombardi and Deere, 1993). Figure 2.10 illustrates the sequence in which different sets of boreholes are grouted. The primary boreholes are grouted first, with a high grout take at low injection pressures. The aim of these boreholes is to fill the more open fractures. The secondary boreholes are then grouted, with a smaller grout take at higher injection pressures. The pressure again increases with the tertiary boreholes and the grout take is also reduced. For both the secondary and tertiary boreholes the fractures to be filled become increasingly smaller, hence the need for higher pressures to push the grout into these fractures. The additional boreholes are then grouted at a higher pressure to target the smallest fractures (or openings) present. In using the GIN-method it automatically limits the volume of grout used in wide, open fractures, but also allows a higher pressure to be used in areas where there

are smaller fractures. It also eliminates the possibility of having a high pressure and high volume scenario, which could possibly cause damage to the rock mass (Lombardi and Deere, 1993).

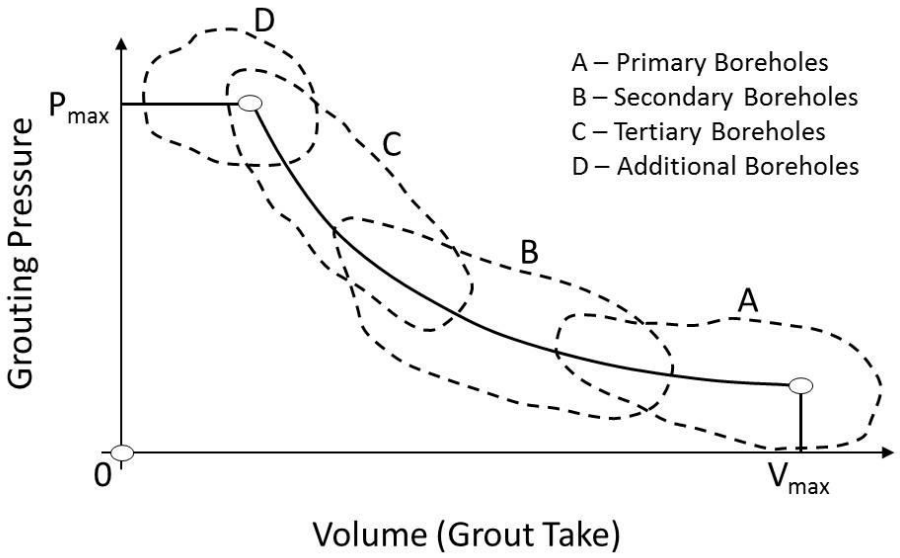

Figure 2.10: *Changing grouting pressure and volume in relation to the stage in the grouting process (After Lombardi and Deere, 1993).*

2.6 The Challenge of Verifying the Grout Location

In large-scale projects, there is a large amount of uncertainty present in the grouting process. The use of GIN curves are an attempt to control the energy applied to the subsurface during grouting. However, it still remains impossible to determine how far the grout has penetrated into the subsurface. This results in a large amount of wastage of materials and therefore cost. An example of a large grouting project is the mine stabilisation works that took place before the construction of the Emirates Arena and the Sir Chris Hoy Velodrome in Glasgow. This project injected 41,430 tonnes of grout into the ground at a cost of £5 million (Barton, 2013). Figure 2.11a shows a schematic diagram of the ideal spread of grout from an injection borehole into a planar fracture. However, if grout take (volume) measurements increased suddenly, it may be due to the intersection of the fracture with a much larger void or cavity (Figure 2.11b) in the subsurface. With only measurements of pressure and volume it is not possible to know the location, orientation, or geometry of such a cavity. Furthermore, if a stop criteria

related to maximum volume has been set, it may result in incomplete sealing, or gaps being created in grout curtains. Due to the inability to image grout penetration there is a significant amount of conservatism employed in grouting campaigns. It is also very difficult to verify the geometry of a grout curtain/barrier and its integrity, and these are of upmost importance in campaigns where hydraulic containment is the priority (e.g. in nuclear projects).

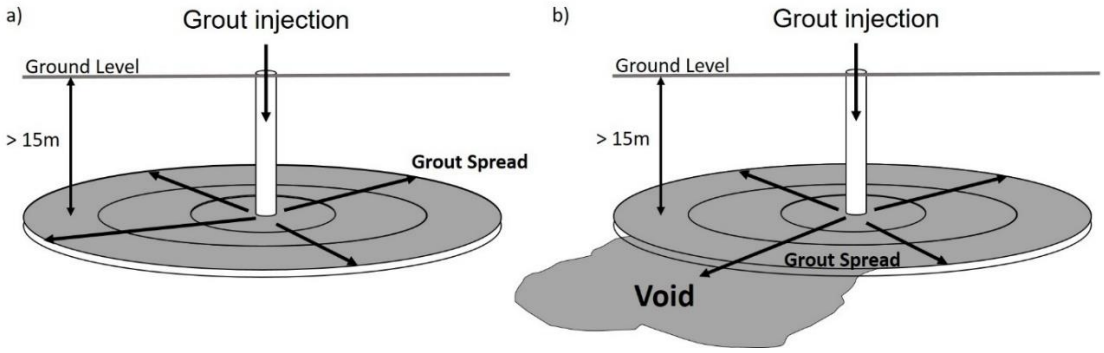

Figure 2.11: *A schematic diagram showing, a) the ideal radial spread of the grout, and b) the grout spreading into an unknown void.*

2.7 Previous Work on Detecting Grout Location In-situ

Several methods have previously been researched or used to attempt to identify the location of grout once it has been injected. These methods have been utilised in order to try to reduce the amount of uncertainty that surrounds the grouting process. This section will detail the methods of fluorescent imaging, seismic monitoring, ground penetrating radar, and down-hole monitoring.

2.7.1 Fluorescent Imaging

Chen *et al.* (2000) developed a fluorescent approach to visualise grout. As a clear distinction between the grout and rock mass is difficult to achieve due to similarities in the colouring of both substances, a fluorescent substance was added to the grout mixture (Chen *et al.*, 2000) (Figure 2.12). The fluorescent grout could then be identified after injection into the ground using a borehole television system using

ultraviolet light and microscopic observation of cored samples. The fluorescent material was composed of a fine resin (Melamine paratoluenesulfonamide formaldehyde polycondensation), the fluorescent substance (Eosine, Rhodamine B, and others), and additives (2-Hydroxyethyl ether, Polyethylene polypropyleneoxide block copolymer, and Glycerol). The fluorescent particles that were added to the grout mixture were less than 1µm, which is less than the particle size of the cement used, and did not readily react with the other components of the grout mixture (Chen *et al.*, 2000). The fluorescent particles were added to the grout mixture in a range of 1 to 10% and this addition did not adversely affect the workability or strength of the grout materials, with the values obtained being virtually the same as for a grout without the added fluorescent particles (Chen *et al.*, 2000).

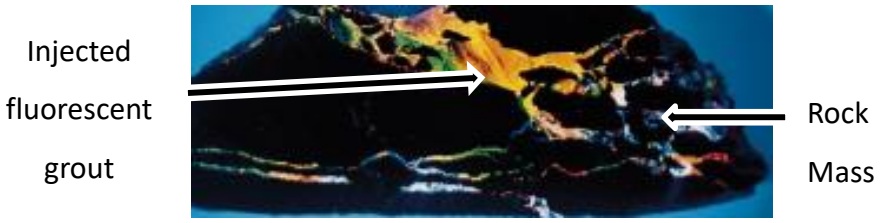

Figure 2.12: *A cored sample showing injected grout containing a fluorescent substance (After Chen et al., 2000).*

The grouting process was split into three different stages and for each stage a different coloured fluorescent substance was mixed with the grout. This allowed the different grouting phases to be easily identified by the borehole television system (Chen *et al.*, 2000). After the grouting had been completed additional boreholes were drilled at sites 0.2 – 2 metres away from the boreholes used for the grout injection. These additional boreholes were required to use a conventional borehole television system and to obtain core samples (Chen *et al.*, 2000). The conventional borehole television system was used under ultraviolet light instead of the natural light lamp which is normally used. This allowed the cracks and pore spaces that had been filled with the fluorescent grout mixture to be identified in-situ (Chen *et al.*, 2000). Polished sections were taken from the core samples from the boreholes. These sections were then examined using conventional light microscopy methods using ultraviolet light. By using this method, microcracks that had been filled with the fluorescent grout, could not be detected using natural light but could be easily seen under ultraviolet light (Chen

et al., 2000). Even though the fluorescent grout could be easily visualised in the core samples taken, there is the limitation to this technique that it is highly intrusive as additional boreholes are required to be drilled through the rock mass in which the fluorescent grout has been injected to identify its location. This is counterproductive as in order to identify its presence you need to drill through the grouted rock volume you may be trying to seal up, requiring further grouting.

2.7.2 High Frequency Seismic Monitoring

High frequency seismic monitoring has also been used to attempt to detect the location of grout in the subsurface (Majer, 1989). This work was undertaken by the Lawrence Berkeley Laboratory to map the location of grout injections in real time, with the main aim being to evaluate passive seismological methods for locating the injection of grout in tight rock (Majer, 1989). It is already known that seismic signals are generated during and after hydrofracturing. It is these signals which were monitored during the process of grouting. The main mechanism which produces these seismic signals is shear events. Due to the high frequency of these seismic signals they were considered to offer a potential real time monitoring method (Majer, 1989). The field experiments were undertaken at two different sites. The first field location was at a U.S. Army Corps of Engineers site close to the McNary Dam in Oregon on the Columbia River. The second field location was at an Underground Research Laboratory near Pinowa, Manitoba, Canada (Majer, 1989). At the first field location a 3D array of seismic sensors were located in ten boreholes surrounding the injection well. A series of grouting experiments were undertaken using a synthetic drilling mud, Poly-Sal, which breaks down in the viscosity of water. By using this gel, the viscosity could be varied within the same fracture system. For the last injection a cementitious grout was used (Majer, 1989).

At the second field location, the Underground Research Laboratory in Canada, the experiments were undertaken around an access shaft to a mine at a depth of 240 metres below the ground surface (Majer, 1989). The main target for the grouting was a fracture zone within granite that was located between 30 to 35 metres below the floor

of the mine. An array of sensors were used around the grout zone located within three boreholes (Majer, 1989). Two of the boreholes were inclined, with the third one in a vertical orientation. Three sensors were placed in each borehole, and were spaced at 5 metre intervals. The central sensor of the three was placed so that it was as close as possible to the middle of the fracture zone (Majer, 1989). During the experiment, data was recorded before, during, and after the injection of the grout.

From both of these field experiments, acoustic emission (AE) activity was present at the pressure and injection rates used. The pressures used were below (1-2 MPa above hydrostatic) the pressure required to cause hydraulic fracturing, and the injection rates were generally low with rates of several litres per minute (Majer, 1989). The viscosity of the grout had a significant effect on the AE activity, however a linear correlation between the two was not observed. The amplitude of the continuous activity increased as the viscosity of the grout increased (Majer, 1989). All of the operational sensors detected AE activity, however it was very localised. The largest events however, occurred after the pumping had ceased, and these were the only locatable seismic events (Majer, 1989).

From the results of the study by Majer (1989) it is clear that the potential use of seismic monitoring to detect the location of grout injections is very limited. It is difficult to correlate the AE activity with the grout location, due to the fact that the activity could not be directly attributed to the grout itself and was likely caused by changes to the pore pressures, which may be affected by grout injection over a much larger volume than is taken up by the grout itself. Also the largest detectable seismic events occurred after grout injection had ceased, and were likely due to the relaxation of the rock mass, again an indirect effect of the grout injection.

2.7.3 Ground Penetrating Radar

A further method which has been used to attempt to detect grout after it has been injected is ground penetrating radar (GPR). GPR is a geophysical method that sends short bursts of electromagnetic energy into the ground and detects the reflected signals

(Milsom, 2003). GPR has been previously used for detection in tunnels, where it has been used to infer the structure of the tunnel by detecting changes in material properties, and to image geological profiles. It has also widely been used to study areas of archaeological interest, construction sites, and the shallow subsurface of landfill sites (Milsom, 2003; Zhang *et al.*¸ 2010). Zhang *et al.* (2010) used GPR as a non-destructive testing method to determine the thickness and detect the distribution of grout behind concrete lining segments of metro lines in Shanghai, China. The type of grout that was used was formed from two separate slurries (slurry A and slurry B). Slurry A was a cementitious grout that contained a stabiliser and bentonite, while slurry B was sodium silicate. Both slurry A and slurry B were mixed together in situ before being injected into the gap between the concrete lining segments and the soil (Zhang *et al.*, 2010). The grout was injected to strengthen and stabilise the tunnel structure and to make it waterproof, therefore the distribution and uniformity of the grout were of great importance. GPR was considered for use in this scenario as the concrete segments, grout, and soil were all located at a distance of less than 1 m from the tunnel, and the dielectric constants of the grout, soil, and the concrete segments, predetermined in laboratory experiments indicated a sufficiently large contrast (Zhang *et al.*, 2010). The dielectric constant is a measure of the ability of a substance to store electrical energy in an electric field.

In undertaking the field tests, GPR's with three different frequencies of 250 MHz, 500 MHz, and 1 GHz were used. In the results gained, the effectiveness of the GPR detection mainly depended on the transmitting frequency (Zhang *et al.*, 2010). Grout detection using a GPR frequency of 250 MHz was undertaken on a 10 m section, one month after the grout had been injected. From 0 to 5 m, no obvious reflection of the grout was detected, however grout was recorded to be leaking from this area when the injection took place (Zhang *et al.*, 2010). Between 5 and 10 m a strong reflection was recorded suggesting an even layer of grout was present (Zhang *et al.*, 2010). GPR grout detection using a frequency of 500 MHz was undertaken 20 days after the grout had been injected. At this frequency two areas were tested for comparison: (i) an un grouted location (where air was present behind the concrete segments), and (ii) a grouted location.

In comparing the two data sets a clear distinct boundary between the concrete segments and the air, and also between the segments and the grout was detected (Zhang *et al.*, 2010). The test undertaken using a GPR frequency of 1 GHz did not penetrate deep enough to be able to detect the boundary between the concrete segments and the injected grout.

The tests undertaken with the higher frequencies produced results with a higher resolution. However, the higher frequency waves attenuate and are absorbed faster, which results in them penetrating a shorter distance than the lower frequency waves (Zhang *et al.*, 2010). The degree to which the waves attenuate and are absorbed depends on the electrical conductivity of the ground. This means that a balance between the resolution of the data and the detecting depth needs to be met when choosing the GPR frequency to be used in this method (Zhang *et al.*, 2010).

Even though Zhang *et* al. (2010) managed to detect the grout behind the concrete segment using GPR, there are also limitations to this technique. The main limitation is the distance over which the GPR can penetrate, as this study only detects up to 1 m due to the attenuation of the electro-magnetic waves by the ground. Additionally, the presence of utilities in the tunnel resulted in a large amount of noise being present in the results. The speed of data collection also needed to be relatively fast for real time detection of the grout, however slower speeds were desirable for a better data resolution (Zhang *et al.*, 2010).

2.7.4 Down-hole Sensor Monitoring

A non-geophysical technique to detect the location of grout after injection, was trialled by Henderson *et al.* (2008) at the D1225 Shaft at Dounreay Nuclear Establishment on the North coast of Scotland. This shaft was an authorised disposal facility for Intermediate Level Waste (ILW) from 1959 until 1971 (Henderson *et al.*, 2008). It was constructed entirely within rock and had a diameter of 4.8 m, and a depth of 65 m, however only the top 8 m was lined. Within the shaft there is 620 m^3 of recorded ILM deposits which is entirely flooded with groundwater (Henderson *et al.*, 2008). As part

of the on-going decommissioning programme at Dounreay Nuclear Establishment, the contents of this shaft are to be retrieved and sent to alternative storage sites, and the contaminated groundwater is to be treated (Henderson *et al.*, 2008). To enable the contents of the shaft to be retrieved using a dry retrieval method, the groundwater level in the shaft needed to be reduced. To ensure that the reduction in the groundwater level was successful, the groundwater ingress rate was required to be limited to a rate of < 10 m^3 per day (Henderson *et al.*, 2008). To achieve this reduction in groundwater inflow an engineered barrier was constructed around the shaft using controlled injection of stable ultrafine cementitious grouts into the rock surrounding the shaft (Henderson *et al.*, 2008). To create the engineered barrier around the shaft, grout was injected into the rock via boreholes, using a split spacing technique. The design of the barrier relied on the grout spread from each injection treating a specific volume of the rock mass, and overlapping with grout spread from other boreholes (Henderson *et al.*, 2008).

In order to characterise the anticipated grout spread during injection (and hence design the borehole spacings) a pre-works trial was undertaken prior to grouting work commencing on the D1225 Shaft. This trial was undertaken 65 m to the North East of the shaft. The experiment was arranged around a 75 m deep central injection borehole (P1), with three 75 m observation boreholes (PO11 – PO13) situated on a 4 m radius from the central borehole. There were a further three observation boreholes (PO14 – PO16) located on a 6 m radius from the central borehole (Henderson *et al.*, 2008). Figure 2.13 shows a plan view of the experiment with the location of the boreholes marked with crosses. Geophysical logging was undertaken of the central injection borehole and the inner observation boreholes. This allowed the rock strata to be split into 3 m sections that could be accurately referenced to their stratigraphical position within the sequence. These sections were also hydraulically tested to determine the hydraulic conductivity of the ground prior to the grout injections (Henderson *et al.*, 2008).

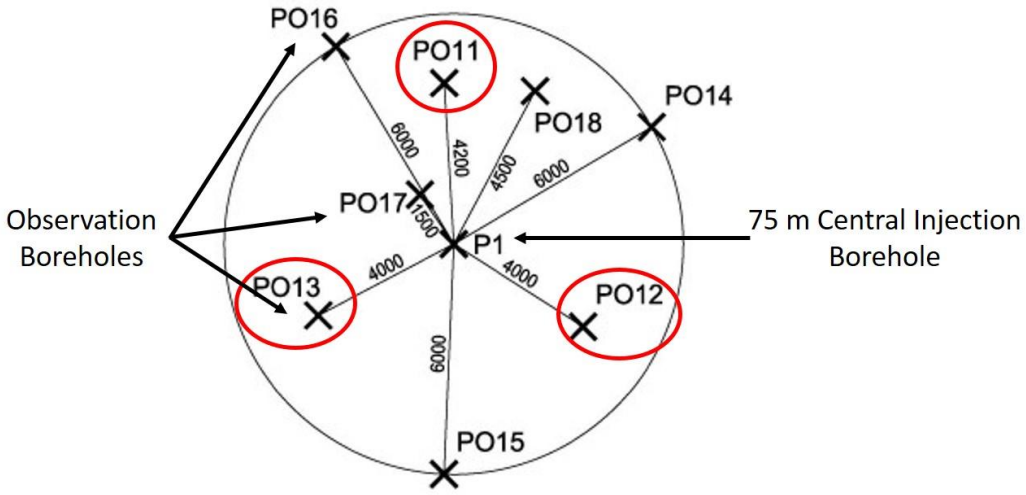

Figure 2.13: *Plan view of the experiment showing the central borehole surrounded by the additional observation boreholes (After Henderson et al., 2008).*

Down each of the observation boreholes (PO11 – PO16), a packer was fitted which contained pH and pressure/temperature transducers, to detect grout arrival in real-time. Datalogging was commenced in advance of the grout injection to establish a pre-injection baseline (Henderson *et al.*, 2008). The packer also included water flushing lines which were used to reduce the pH level in between injections. This allowed the arrival of the fresh grout to be detected (Henderson *et al.*, 2008).

Throughout the experiment 25 grout injections were undertaken. The temperature probes located within observational boreholes PO11, PO12, and PO13 (circled in Figure 2.13), did not show a large response during the grout injection. Within two of the observation boreholes the temperature did not change. This can be seen within (Figure 2.14). Due to the clean water flushing of the system to reduce the pH after each grout injection, it is possible that any temperature response was masked by the water / ground temperature gradient (Henderson *et al.*, 2008). The pressure probes did record responses at both the start of the grout injection and at the arrival of the grout. However, these responses were variable and therefore could not be classed as a credible indicator of grout arrival (Henderson *et al.*, 2008). Finally, the pH probes showed a distinct response as the grout approached and arrived at each observation borehole as shown in Figure 2.14 for observation boreholes PO11, PO12 and PO13.

The pH results display a very distinct increase towards alkaline values inferred to correspond with grout arrival at the observation boreholes. The pH values recorded during the perceived grout approach match with values measured in laboratory experiments for different grout dilutions. Additionally, the peak pH values recorded for the perceived grout arrival matched with laboratory values gained for undiluted grout mixtures (pH ~ 13) (Henderson *et al.*, 2008). In many cases the physical arrival of the grout at the observation boreholes could be confirmed by the presence of the grout on the instruments when they were removed for cleaning (Henderson *et al.*, 2008).

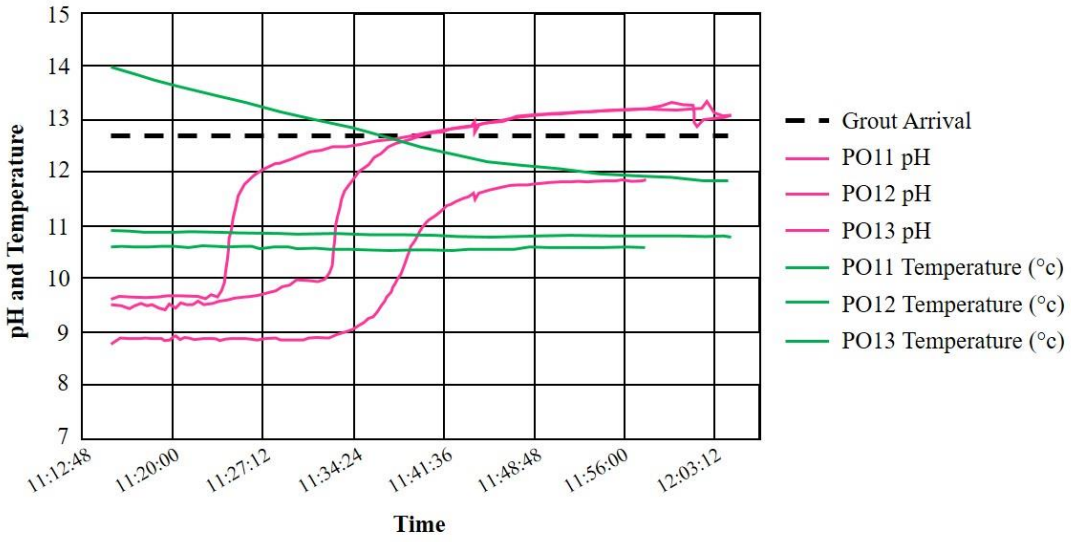

Figure 2.14: *Results from the temperature and pH probes in the observation boreholes located 4 m away from the injection borehole (After Whitfield and Henderson, 2008).*

From this trial it appears that pH monitoring is a feasible method to detect grout arrival. However, this is an invasive method which requires additional observation boreholes to be drilled into the rock volume to be grouted. This would therefore lead to further grouting having to be undertaken in the observation boreholes, to ensure that the whole rock mass is sufficiently sealed to the project requirements, or to conduct a trial carried out by Henderson *et al.*, (2008) in a near-by geologically similar location. However, at the Dounreay shaft this was possible given the remote location of the site and the strict water ingress requirements. In most common grouting campaigns the additional space (and funding) to conduct such a trial is unlikely to be available. It also relies on

the geology being similar, and individual features (geological or man-made) could result in significant differences in grout spread achieved between a pre-works trial and the main grouting works.

From analysing the four different methods of fluorescent imaging, seismic monitoring, GPR, and down-hole monitoring to attempt to detect grout in-situ, no satisfactory methods have been realised. Table 2.3 below summarises the limitations discovered in each of the methods described

Table 2.3: *A summary table of limitations of the previous work on detecting grouts in-situ.*

Method	Reference	Limitations
Fluorescent Imaging	Chen *et al.* (2000)	• An intrusive process as additional boreholes need to be drilled through the fluorescent grout to determine its location.
Seismic Monitoring	Majer (1989)	• Unable to correlate the location of the grout to seismic activity recorded.
GPR	Zhang *et al.* (2010)	• Attenuation of the waves in the ground which limit penetration. • Presence of utilities effects the data collected. • Need to compromise resolution for speed of data collection.
Down-hole Sensor Monitoring	Henderson *et al.* (2008)	• An intrusive technique as additional observation boreholes need to be drilled to accommodate the pH and temperature/pressure probes.

2.8 Conclusions

Overall, the previous methods used to attempt to detect grout injections have either not produced satisfactory results due to both interference and inability to correlate the results with the grout location, or use intrusive methods by drilling additional boreholes directly into the rock volume to be grouted. This thesis focuses on the development of a new method to detect grout injections by adding magnetic additives to the grout, thereby enabling the remote detection of the grout injections. Chapter 3 presents an overview of magnetism, magnetic materials and methods for detecting magnetic materials.

Chapter 3

Magnetic Materials

3.1 Introduction

This chapter gives an introduction to magnetism, and basic magnetic theory. It presents a brief overview of the different types of magnetic materials, their properties, and equipment used to detect magnetic fields. A section of this chapter will also present techniques used for the detection of magnetic objects in mineral prospecting and archaeology.

3.2 Background Magnetic Theory

The first magnetic material that was known to mankind was magnetite. Magnetite is a mineral that has the chemical formula Fe_3O_4. It can be found in various locations around the world, however it gets its name from the district of Magnesia, now in modern Turkey (Cullity and Graham, 2009). Large amounts of magnetite are naturally magnetised, often due to lightning strikes, and this enables the magnetite to attract iron (Blundell, 2012). Magnetite occurs as a primary or secondary mineral in continental and oceanic igneous, sedimentary, and metamorphic rocks (Dunlop, 1990). For many centuries magnetised rocks were referred to as loadstones and were used for navigational purposes (Blundell, 2012). The first scientific study of magnetism was made by William Gilbert who published the book *De Magnete* in 1600, in which he inferred that the Earth was a magnet (Coey, 2010). Even though magnetism has been known about for thousands of years, it is only relatively recently that the underlying mechanism and principals have begun to be understood. Magnetism and magnetic minerals have a wide range of uses and many current technological devices rely on them to function, such as radio, television, computers, electrical power generators, and electric motors (Callister, 2007).

3.2.1 The Earth's Magnetic Field

The geomagnetic field that is located at or near to the surface of the Earth originates largely from within and around the Earth's core (Reynolds, 1997). The main component of the geomagnetic field is called the dipolar field, as it behaves like the field of a magnetic dipole situated at the centre of the Earth. However, this field deviates by 11.5° to the rotational axis. This therefore means that neither the magnetic equator, nor the magnetic poles coincide with their geographical equivalents (Figure 3.1) (Reynolds, 1997; Milsom, 2003; Mussett and Khan, 2007). There are significant deviations between the observed Earth's total magnetic field and the inclined centred geomagnetic dipole field, due to non-dipole components in the magnetic field. This produces large scale anomalies, up to 20,000 nT (nanotesla), which is around one third of the Earth's total field (Reynolds, 1997; Lowrie, 2007). The Earth's total magnetic field varies with latitude, with the minimum being seen at the magnetic equator (~30,000 nT) to a maximum at the magnetic poles (~60,000 nT) (Reynolds, 1997).

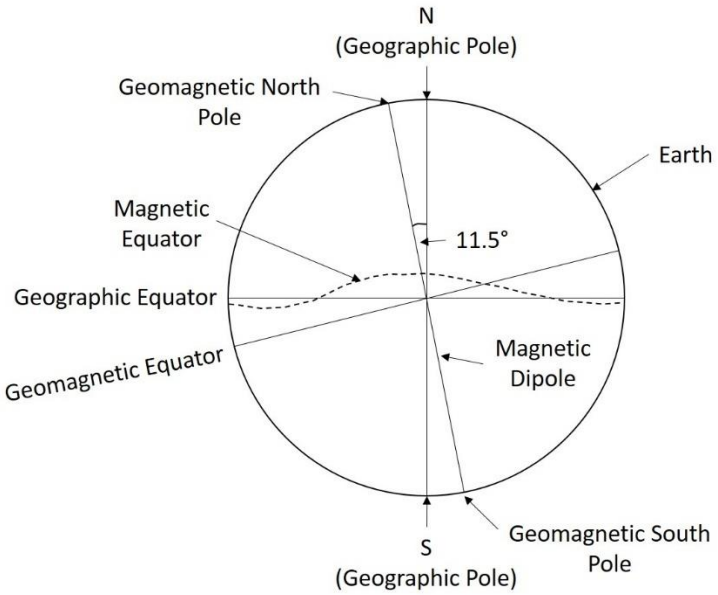

Figure 3.1: *A schematic diagram of the Earth showing the locations of the geomagnetic poles, geomagnetic equator, and the magnetic equator (After Reynolds, 1997).*

The geomagnetic field is produced by electric currents that are induced within the conductive liquid outer core as a result of slow convective movements within it as the Earth rotates. This is known as the geodynamo theory (Roberts and Glatzmaier, 2000; Kono and Roberts, 2002; Christensen, 2011). The currents in the Earth's core are more complex than an electric current (Lowrie, 2007; Mussett and Khan, 2007). The composition of the fluid outer core has been estimated from seismic and geochemical data, and this has determined that the main constituent is liquid iron with smaller amounts of other less dense elements (Lowrie, 2007). The geomagnetic field can be described in the terms of declination, D, inclination, I, and the total field vector, B (Figure 3.2). A freely suspended magnetised needle will align itself along the total field vector. The total field vector, B, has both a vertical component, Z, and a horizontal component, H, which is in the direction of magnetic North. The dip of the total field vector is the inclination, I, of the field, and the horizontal angle between the magnetic and geographic North is the declination, D (Kearey *et al.*, 2002). The total field vector can vary in strength from around 25,000 nT in equatorial regions to values of 70,000 nT at the poles. The angle of inclination varies across the Earth. Within the Northern hemisphere the magnetic field generally dips down towards the North and eventually becomes vertical at the North pole (Kearey *et al.*, 2002), with an inclination of 90° (Reynolds, 1997). Conversely, in the southern hemisphere the dip is generally upwards towards the North. The point of zero inclination can be found approximately along the geographic equator, which is also known as the magnetic equator (Kearey *et al.*, 2002).

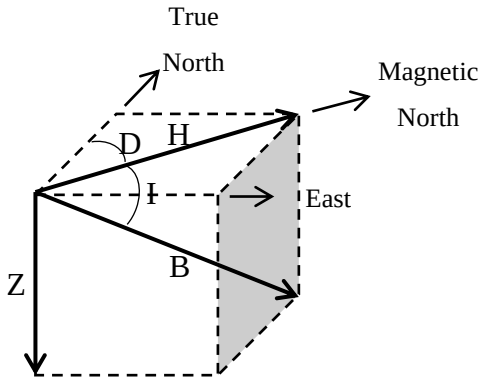

Figure 3.2: *A schematic diagram showing the elements of the magnetic field: B - Total Field Vector, Z - Vertical component of B towards magnetic north, H - Horizontal component of B towards magnetic north, I - Inclination of the field, D - Declination (After Kearey et al., 2002; Reynolds, 1997).*

The Earth's magnetic field is variable and changes over long and short term time periods. Over long-term time periods, the geomagnetic and magnetic pole positions can drift over time. This is known as the secular variation in the magnetic field (Reynolds, 1997). These changes are caused by the slow change of the circulation patterns founds within the Earth's core (Kearey *et al.*, 2002). Furthermore, the intensity of the main magnetic field is decreasing at a rate of around 5% per century (Reynolds, 1997). Also in addition to long-term secular variation in the magnetic field, the magnetic field can also undergo a collapse and reversal on a time scale of around 100,000 years (Nabighian *et al.*, 2005). The magnetic field can also change over a daily period, which are called diurnal variations. These are caused by changes in the strength and direction of currents in the ionosphere (a region of the Earth's upper atmosphere located between 80 km and 600 km above the Earth) (Kearey *et al.*, 2002; Reynolds, 1997). The ionosphere is composed of ionised molecules which release swarms of electrons that form powerful, horizontal, ring-like electrical currents. These currents act as sources of external magnetic fields that are detected at the surface of the Earth (Lowrie, 2007). As the Earth rotates beneath the ionosphere, the observed intensity of the geomagnetic field fluctuates with a range of amplitude of about 10 – 30 nT at the Earth's surface over the period of one day (Lowrie, 2007).

3.2.2 Basic Concepts

This section will detail the main basic concepts of magnetism. It will look at how a magnetic field is created, how materials can be magnetised, different types of magnetism, and how the magnetisation of a material can change.

3.2.2.1 Field Strength and Flux Density

A magnetic field can be produced in two ways: (i) when an electrical charge is in motion, such as when there is an electrical current flowing through a conductor, or (ii) by a permanent magnet. In the case of a permanent magnet, there is no electrical current producing the magnetic field. Instead, there are orbital motions and spins of

electrons within the material of the permanent magnet which produce a magnetisation within the material, and a magnetic field outside (Jiles, 1998).

A magnetic field exists around a (permanent) bar magnet with the field lines converging at the poles of the magnet (Figure 3.3) (Reynolds, 1997). Magnetic poles always exist in pairs of opposite sense, to form a dipole. When one of the poles is sufficiently far removed from the other so that it no longer affects it, the single pole is referred to as a monopole (Reynolds, 1997). The closeness of the field lines around the magnet indicate its magnetic flux density, ***B***, which is generally measured in teslas (T) (Reynolds, 1997). The magnetic flux density or the magnetic field strength, ***B***, is represented by the number of magnetic lines of flux per unit area that pass through a plane that is perpendicular to the direction of the lines (Spaldin, 2011). Both the magnetic flux density and the magnetising field strength are field vectors, and as such are characterised both by magnitude and their direction in space (Callister, 2007).

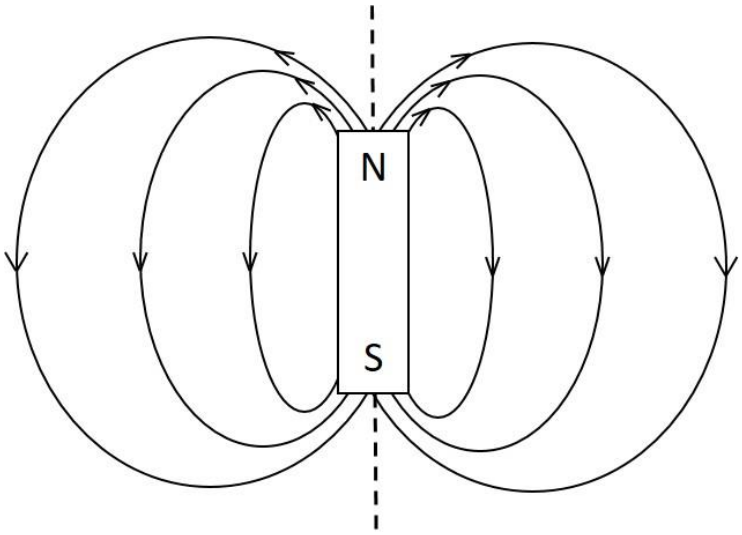

Figure 3.3: *The magnetic field around a bar magnet.*

3.2.2.2 Magnetic Moments

The macroscopic magnetic properties of materials are a result of the magnetic moments that are associated with spin of individual electrons (Callister, 2007; Coey, 2010). Magnetic moments quantify the magnitude and direction of the magnetism,

and hence the strength and orientation of the magnetic field generated (Spaldin, 2011). In an atom, each electron has a magnetic moment that comes from two sources: the orbital motion of an electron around the nucleus (Figure 3.4a) and its charge. As an electron is a moving charge, it may be considered to be a small current loop that is generating a very small magnetic field which has a magnetic moment along its axis of motion (Callister, 2007). The second source of the magnetic moment originates from electrons spinning around an axis (Figure 3.4b). The magnetic moment stems from this electron spin which is directed along the spin axis (Callister, 2007; Coey, 2010). Spin magnetic moments may only be either in an 'up' direction, or in an antiparallel 'down' direction (Coey, 2010). This means that each electron in an atom can be thought of as being a small magnet which has its own permanent orbital and spin magnetic moments (Coey, 2010; Callister, 2007).

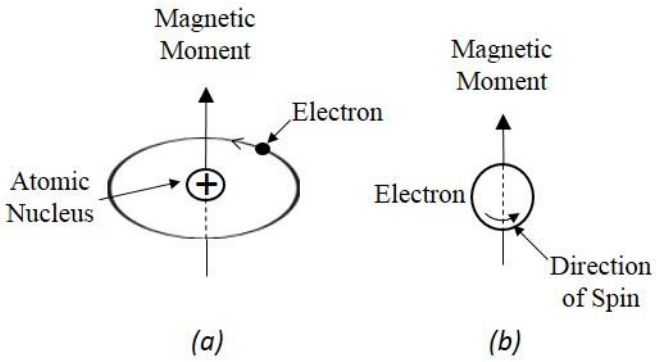

Figure 3.4: *The magnetic moments associated with (a) an orbiting electron, and (b) a spinning electron (After Callister, 2007).*

An electron's magnetic moment is gained from spin and this is known as the Bohr magneton, μ_B, which has a value of 9.27×10^{-24} A m^2 (Coey, 2010; Callister, 2007). For each electron in an atom, the spin magnetic moment is $\pm \mu_B$, with the plus sign for upwards spin, and the minus sign for downwards spin (Coey, 2010; Callister, 2007). In individual atoms, the orbital moments of some electron pairs can cancel each other out. This is also the case for spin moments where an upwards spin will cancel out one with a downwards spin (Coey, 2010; Callister, 2007). The net magnetic moment of an atom is calculated from the sum of the magnetic moments of each of the constituent electrons. This includes both spin and orbital contributions, and also the cancelling

out of the magnetic moments (Coey, 2010; Callister, 2007). For an atom that has completely filled electron shells, there will be a complete cancellation of both the spin and orbital moments. These materials are therefore unable to be permanently magnetised (Coey, 2010; Callister, 2007). The magnetic moments of electrons as described above controls the behaviour that is observed within different materials. This behaviour will be described in more detail in section 3.2.2.4.

3.2.2.3 Magnetic Permeability and Magnetic Susceptibility

Magnetic permeability measures the ability of a material to form and carry a magnetic field, therefore it is also the amount of magnetisation that the material gains when exposed to an applied magnetic field (Lowrie, 2007). The magnetic permeability (μ) is the ratio of the flux density, $\boldsymbol{B}$, to the magnetising field strength, $\boldsymbol{H}$, ($\mu = \boldsymbol{B} / \boldsymbol{H}$), where the magnetising field strength is the imposed magnetic field (Coey, 2010). The magnetic permeability of water and air is determined to be the same as the magnetic permeability of free space (a vacuum), and is therefore denoted to be μ_0, which has the value of $4\pi \times 10^{-7}$ Wb A^{-1} m^{-1} (Reynolds, 1997). For any other medium, the ratio of the magnetic permeability of a medium to that of free space is equal to the relative magnetic permeability, μ_r, so that $\mu_r = \mu/\mu_0$ (Reynolds, 1997).

When a material is exposed to a magnetic field, how responsive the material is to becoming magnetised is called the susceptibility (Reynolds, 1997; Milsom, 2003). The volume magnetic susceptibility is the ratio of the magnetisation of the medium, $\boldsymbol{M}$, to the magnetising field strength, $\boldsymbol{H}$, as follows:

$$\chi = \frac{\boldsymbol{M}}{\boldsymbol{H}} \tag{3.1}$$

Where;

χ = volume magnetic susceptibility,

$\boldsymbol{M}$ = the magnetisation of the medium (A/m),

$\boldsymbol{H}$ = magnetic field strength (A/m).

Magnetic susceptibility is dimensionless in SI units. The magnetisation of the medium, ***M***, is the magnetic dipole moment per the unit volume of the material (Lowrie, 2007). The susceptibility is measured by applying a known magnetic field to a sample and measuring the increased magnetism of the sample by the extra magnetic field it produces (Mussett and Khan, 2007). The magnetite susceptibility is related to the relative permeability as follows: $\chi = \mu_r - 1$. The magnetic flux density can therefore be related to ***M*** and ***H*** as: $\boldsymbol{B} = \mu_0(\boldsymbol{H} + \boldsymbol{M})$.

3.2.2.4 Magnetic Materials

Magnetic materials can be roughly categorised into three different classes depending on their magnetic susceptibility. These classes are; diamagnetic, paramagnetic, and ferromagnetic (Getzlaff, 2008; Parasnis, 1962). Diamagnetism is a property that is found in all materials. It is a very weak form of magnetism, which is non-permanent (Callister, 2007). Diamagnetism represents the special case in which the magnetic moments contributed by all electrons cancel each other out. Therefore the atom as a whole possesses a net zero magnetic moment (Anderson and Blotzer, 1999; Lanza and Meloni, 2006). An applied magnetic field however, can induce a moment within a diamagnetic material, with the induced moment opposing the applied field. The induced magnetic field is therefore in the direction opposite to the applied field and the susceptibility is less than or equal to zero (Anderson and Blotzer, 1999; Lanza and Meloni, 2006). Diamagnetism can often be masked by the stronger paramagnetic or ferromagnetic properties of a material (Lowrie, 2007). Examples of diamagnetic materials are nearly all organic substances, metals such as mercury, and superconductors, which are below the critical temperature (Getzlaff, 2008).

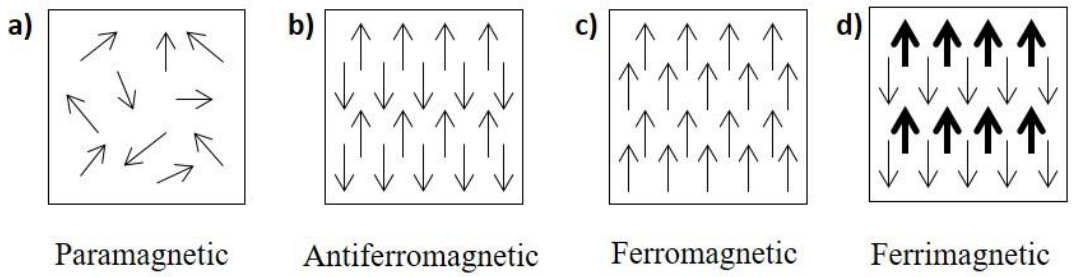

Figure 3.5: *Classes representing the magnetic ordering of magnetic minerals (After Spaldin, 2010).*

Paramagnetism occurs in materials which have atoms with randomly oriented magnetic moments in the absence of a field (see Figure 3.5a), and the magnetic interaction between the atoms is weak. If an external magnetic field is then applied, a slight alignment of these magnetic moments can occur resulting in a small induced internal magnetic field. This induced magnetisation is in the direction of the applied magnetic field and is proportional to the strength of the applied field (Lowrie, 2007). The materials that normally exhibit paramagnetism are atoms and molecules that have an odd number of electrons, so that there is an unpaired electron spin, which gives rise to the initial net magnetic moment (Jiles, 1998). Paramagnetic materials have a magnetic susceptibility of > 0. Examples of paramagnetic materials are platinum, aluminium, and oxygen. Many rocks have also been classed as paramagnetic, such as, gneiss, pegmatite, and dolomites (Parasnis, 1962).

Ferromagnetic materials can be further split into truly ferromagnetic, antiferromagnetic, and ferrimagnetic. In ferromagnetic materials the atoms have a magnetic moment and the interaction between neighbouring atoms is so strong that they align themselves in the same direction (see Figure 3.5c). The region within which the magnetic moments are aligned is called a domain. The net magnetic field within a domain may be large, but in the bulk sample, the magnetic field in the many domains will be randomly oriented and thus the material may be unmagnetised. An externally applied magnetic field can cause ferromagnets to become magnetised, this is discussed in the following sections. All ferromagnetic metals such as cobalt, iron, and nickel will become paramagnetic above their Curie point (Jiles, 1998). Their Curie point is

the temperature above which the spontaneous alignment of magnetic moments in a ferromagnetic or ferromagnetic material is lost (Harrison and Feinberg, 2009). Antiferromagnetic metals such as chromium and manganese will also become paramagnetic above their transition temperatures of 35°C and -173°C, respectively (Jiles, 1998). Ferromagnets are used to produce permanent magnets once magnetised and some examples of ferromagnetic materials are magnetic steels, cunife alloys (Cu-Ni-Fe), alnico alloys (Al-Ni-Co), and hexagonal ferrites ($BaO\text{-}6Fe_2O_3$) (Callister, 2007). The most commercially available rare earth permanent magnets are Samarium-Cobalt ($SmCo_5$) and Neodymium-Iron-Boron ($Nd_2Fe_{14}bB$) (Callister, 2007).

Antiferromagnetic materials are formed when the magnetic moments within a material are aligned antiparallel to each other, causing them to cancel each other out (see Figure 3.5b). resulting in a net zero magnetic moment (Parasnis, 1962). The magnetic susceptibility of an antiferromagnetic material is weak and positive, and remnant magnetism is not possible. The antiferromagnetic alignment breaks down at the Néel temperature. The Néel temperature is the temperature above which the spontaneous alignment of magnetic moments in an antiferromagnetic material is lost (Harrison and Feinberg, 2009). For many antiferromagnetic materials, the Néel temperature is below room temperature, and above this paramagnetic behaviour is shown (Lowrie, 2007).

Ferrimagnetic materials have atoms with opposing magnetic moments of unequal magnitude (see Figure 3.5d). This results in a net magnetic moment, even in the absence of a magnetic field. Above the Curie temperature, the internal molecular structure breaks down and the mineral behaves paramagnetically (Lowrie, 2007). A large number of the constituents of a rock are ferrimagnetic, such as magnetite, titanomagnetite, and ilmenite (Parasnis, 1962).

3.2.2.4.1 Applications of Magnetic Materials

Currently, magnetic materials and minerals have been applied to many different areas such as in pollution studies (Botsou *et al.*, 2011; Wang *et al.*, 2015), identifying areas of past human occupation (Herries and Fisher, 2010), and for localised drug delivery (Kempe and Kempe, 2010; Mangual *et al.*, 2010; Chomoucka *et al.*, 2010; Cherry and Eaton, 2014). They are also used in a wide range of electrical applications such as in electrical power generation (Sakuraba, Y., 2016), receipt of radio signals, microwaves and electromagnets (Jiles, 1998). However, the active introduction of magnetic minerals is not presently common practice in civil engineering. This thesis investigates for the first time the active introduction of magnetic minerals into cement grouts to aid detection.

3.2.2.5 Domains and Hysteresis

All ferromagnetic or ferrimagnetic materials that are at a temperature which is below its Curie temperature, are composed of regions. These regions are small in volume, and they have a mutual alignment, in the same direction, of all the magnetic dipole moments (Figure 3.6) (Callister, 2007; Spaldin 2011). Each region is called a domain and on the application of an external applied field these can be magnetised to their saturation magnetisation, which is the point at which a material cannot become more magnetised (Jiles, 1998). Adjacent domains are separated by domain boundaries or walls. Domain boundaries are the interfaces between domains in which the spontaneous magnetisation has different directions (Cullity and Graham, 2009). At or within the boundary, the magnetisation changes direction from one easy crystallographic direction to another (Cullity and Graham, 2009; Callister, 2007). Normally, the domains are microscopic in size, and for a polycrystalline material each grain may consist of more than one domain (Callister, 2007). The magnitude of the magnetic field for the entire solid material is the sum of the magnetisations of all the domains, with each domain contribution being weighted by its volume. Therefore, for an unmagnetised material, the sum of all the magnetisation of the domains is zero (Callister, 2007; Spaldin, 2011).

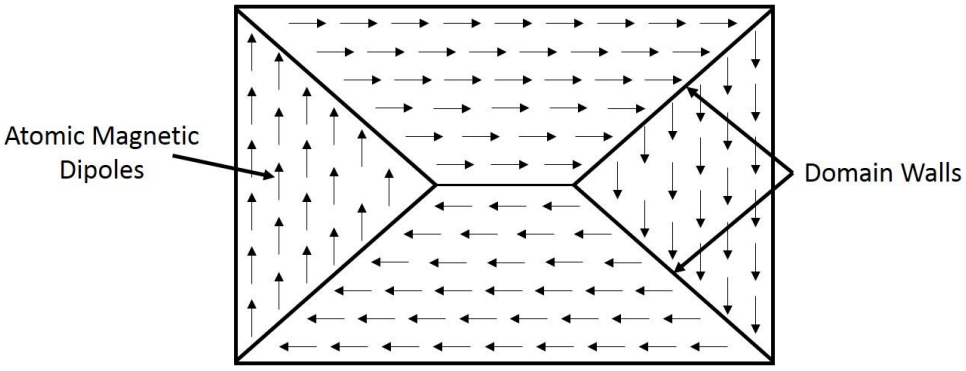

Figure 3.6: *A schematic representation of magnetic domains in a ferromagnetic or ferrimagnetic material (After Callister, 2007).*

Figure 3.7 presents a curve illustrating how the magnetic flux density, ***B*** of an initially unmagnetised ferromagnet increases in response to an increasing magnetic field strength ***H*** (Callister, 2007). As the magnetic field strength increases, the flux density begins to increase slowly at first in response to increasing magnetic field strength. The flux density then increases more rapidly before the curve levels off. This is the point at which the flux density becomes independent of the magnetic field strength (Callister, 2007). The maximum value of flux density is the saturation flux density, and the corresponding magnetisation is the saturation magnetisation value (Callister, 2007).

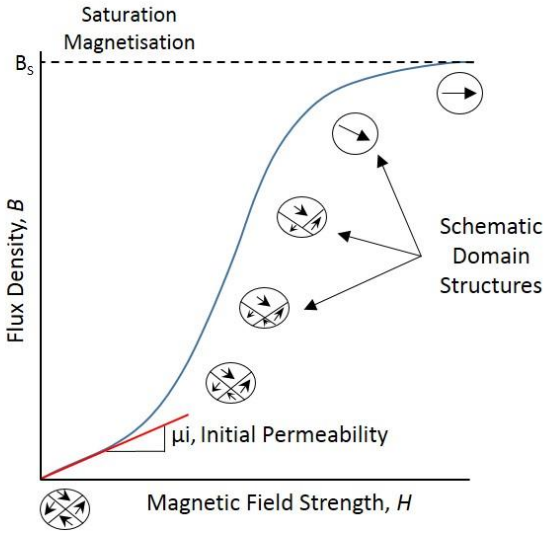

Figure 3.7: ***B*** *versus* ***H*** *curve showing the behaviour of an initially unmagnetised ferromagnetic or ferrimagnetic material (After Callister, 2007).*

As an increasing magnetic field is applied, the domains within the material change shape and size by the movement of the domain boundaries. The domains that are oriented in a favourable direction to the applied field grow at the expense of those domains in an unfavourable direction (Callister, 2007; Spaldin, 2011). This process continues with the increasing magnetic field strength until the material becomes a single domain that is almost perfectly aligned with the magnetising field (Callister, 2007; Spaldin, 2011).

Hysteresis can be found in ferromagnetic materials, and is the nonlinear response of magnetisation to an imposed magnetic field (Coey, 2010). Figure 3.8 presents the hysteresis loop of a ferromagnetic material. When the magnetic field strength is reduced, after the material has reached saturation point, it does not retrace its original path (Callister, 2007). This is because the magnetic flux density decreases at a lower rate than the applied magnetic field. At an applied magnetic field of zero, a residual magnetic flux density field can remain, this is called the remanence, see Figure 3.8 (Callister, 2007; Jiles, 1998). The existence of remanence is due to the fact that there are still parts of the domains which remain oriented. To be able to reduce the magnetic flux density value to zero, the magnetic field strength needs to be applied in a direction opposite to the previously applied field direction (Callister, 2007). This is called coercivity or coercive force ($-H_c$). A material that has a coercivity of less than 1000 Am^{-1} is considered to be magnetically soft (Jiles, 1998). Hard magnetic materials are used in the production of permanent magnets. With the continuation of the applied field in this reversed direction, the saturation point can again be achieved, but this time with a magnetic flux density in the opposite direction (Telford *et al.*, 1990; Callister, 2007). A second reversal of the applied field can be used so that the initial saturation point can again be reached. This completes the hysteresis loop, exhibiting both the points of negative remanence and positive coercivity (Telford *et al.*, 1990; Callister, 2007).

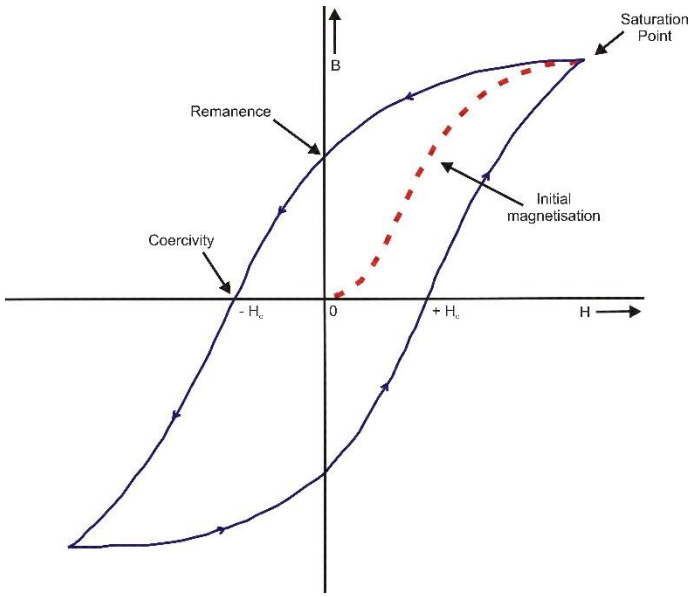

Figure 3.8: *A hysteresis loop of a ferromagnetic material (After Callister, 2007).*

The hysteresis behaviour and the permanent magnetisation of a material can be explained by the motion of the domain walls. When the magnetic field direction is reversed at the saturation point of the material, the process by which the domain structure changes is also reversed (Callister, 2007; Spaldin, 2011). This results in firstly the single domain rotating within the reversed field. Then domains which have their magnetic moments aligned with the new magnetic field form and grow in size at the expense of the domains present from the previous magnetic field (Callister, 2007; Spaldin, 2011). When the new reversed applied field reaches zero, there are still some domains that are oriented in the previous direction of the magnetic field, which results in the existence of remanence within the material (Callister, 2007; Spaldin, 2011).

3.3 Magnetic Field Sensors

In order to detect magnetic anomalies in the ground, equipment / devices capable of measuring magnetic properties in the field are necessary. Magnetic measurements were first used for large scale investigations into geological structures in 1925, but since then magnetic observations have been successfully employed in locating geological faults (Khalil, 2016), intrusions of igneous rocks (Galindo-Zaldívar *et al*., 2013), meteorites (Folco *et al*., 2006), and buried magnetic objects such as pipelines

and metal drums (Sheinker and Moldwin, 2016; Marchetti *et al.*, 2002). The magnetic flux density can be measured using several different technologies, with distinct applications requiring techniques with unique properties (Macintyre, 1999). The applications can range from sensing the presence and any changes in the magnetic field, to taking precise measurements of both the scalar and vector properties of a magnetic field (Macintyre, 1999). Magnetic field sensors can be split into two different types, vector or scalar sensors (Figure 3.9). The vector type sensors measure both the magnitude and direction of the magnetic field and can be further divided into sensors that can measure low magnetic field (< 1 mT (milliTesla)), and high magnetic fields (> 1 mT). The scalar sensors measure only the magnitude of the magnetic field (or magnetic flux density) (Selvåg, 2006). The instruments that are used to measure low magnetic fields are commonly called magnetometers, and high magnetic field instruments are called gaussmeters (Macintyre, 1999).

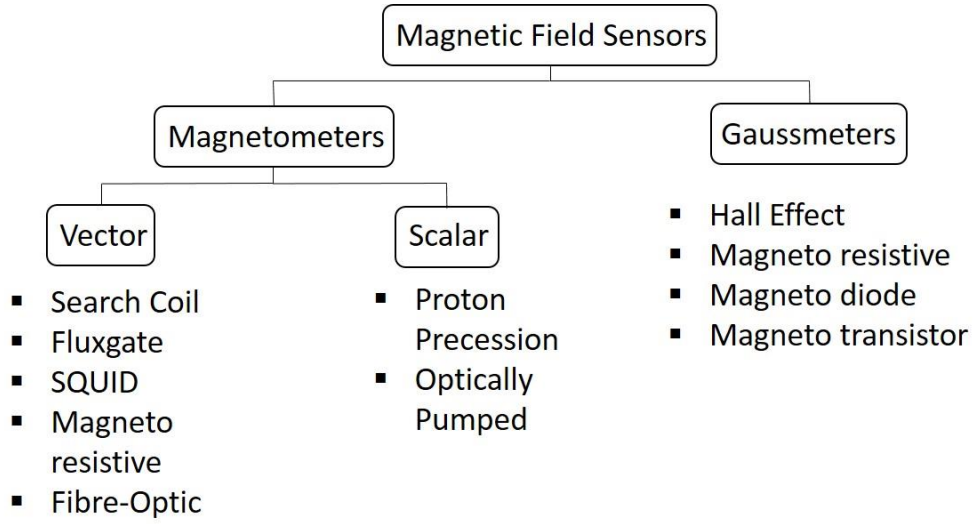

Figure 3.9: *Classification of different magnetic field sensors (After Macintyre, 1999).*

There are several different types of vector magnetic field sensors, however the main types used are induction coil (search coil), and fluxgate magnetometers, with fluxgate magnetometers being the most widely used. These two types of magnetometers are reliable, and also relatively less expensive than the other low field vector measuring instruments (Macintyre, 1999). Induction coil magnetometers are made up of a conventional wire coil that surrounds a permeable magnetic core. This measures the

rate of change of the magnetic field intensity in the direction parallel to the coil axis (Selvåg, 2006). They are mainly used for sensing AC magnetic fields and the relative motion of magnetic objects.

The first fluxgate magnetometers were produced for use in airborne submarine detection during World War II (Redford and Sumner, 1964). For total field measurements to be recorded, three sensors need to be used and these sensors are fixed at right angles to each other (Lowrie, 2007). Fluxgate magnetometers consist of two strips of a magnetic alloy, which is normally a nickel-iron alloy. These strips are wound around the primary coils in opposite directions. When a current flows into these coils, the strips of magnetic alloy become magnetised in opposite directions (Milsom, 2003; Lowrie, 2007). A secondary coil is wound around the primary pair, and this detects any changes between the magnetic flux of the cores (Lowrie, 2007). Variations in the electrical properties of the circuits with magnetisation of the cores, can be converted into voltages which are proportional to the external magnetic field. Measurements can therefore be taken of the magnetic field component in any direction (Milsom, 2003). The two current major applications of the fluxgate magnetometer are in airborne systems where they are used to perform heading corrections and also in downhole applications (e.g. foundation depth determination (Jo *et al.*, 2003)) and the detection of unexploded ordnance (Zhang *et al.*, 2007)) where they are the main instrument used (Nabighian *et al.*, 2005). The main advantage of a fluxgate magnetometer over an induction coil sensor is that a fluxgate magnetometer will measure the magnetic field in any direction whereas an induction coil sensor will only measure in one direction.

SQUID (Superconducting Quantum Interference Device) magnetometers are vector magnetic field sensors. This type of magnetometer is used for measuring a magnetic field at low frequencies due to its sensitivity (Selvåg, 2006). This magnetometer is based on the interactions between electric currents and magnetic fields that are observed when materials are cooled to a temperature close to absolute zero (Macintyre, 1999; Selvåg, 2006). SQUID magnetometers measure the change in the magnetic field from an arbitrary field level. They do not measure the absolute value of the magnetic

field (Macintyre, 1999). These magnetometers are expensive due to the special thermal control systems required to cool the materials. They are also less rugged and less reliable than other magnetometers (Macintyre, 1999). One of the most important applications of these magnetometers is in biomedical research, however, they are also used in palaeomagnetics, to measure the remnant magnetism in rocks, and in magnetotellurics, which are Earth resistivity measurements (Macintyre, 1999). Due to the requirement that the materials to be measured are at a temperature close to absolute zero, these magnetometers are lab-based instruments.

There are three different types of scalar magnetic field sensors, proton precession, overhauser, and optically pumped. Scalar magnetometers measure the magnetic field by exploiting the atomic and nuclear properties of the material (Macintyre, 1999). The most widely used of the three types of scalar magnetometers are the proton precession and the optically pumped. Both of these magnetometers have an extremely high resolution and accuracy, and are also generally insensitive to orientation (Macintyre, 1999). They both however have several limitations. These limitations include that they require the magnetic field to be uniform throughout the sensing element, and that they can also have a limited measurement range of 20 μT to 100 μT for the magnitude of the magnetic field, however this range would still be sufficient for detecting anomalies in the Earth's magnetic field (Macintyre, 1999).

Proton precessions magnetometers were introduced in the mid-1950s and by the mid-1960s had superseded flux-gate magnetometers for the majority of exploration applications (Nabighian *et al.*, 2005). They are the most popular instrument for measuring the scalar magnetic flux density (Macintyre, 1999). Proton precession magnetometers make use of the small magnetic moment of the hydrogen nucleus (proton). The magnetometer is composed of a sensing element which is made up of a bottle containing a hydrocarbon fluid with a low freezing point, and a coil of copper wire which is wound around it (Milsom, 2003). A polarising current is then passed through the copper wire coil which creates a strong magnetic field, along which the moments of the protons in the hydrogen atoms will become aligned (Milsom, 2003). When the current is removed, the spin of the proton causes them to precess about the

direction of the ambient or the Earth's magnetic field. These precessing protons then generate a small signal whose frequency is proportional to the magnetic flux density (Breiner, 1999). Proton precession magnetometers are used in mineral and oil exploration, weapons detection, volcanology, archaeology, and magnetic observations (Hrvoic, 2011).

A variant of the proton precession magnetometer, the Overhauser magnetometer uses radio frequency excitation and displays continuous oscillation. This magnetometer can be operated continuously, unlike the proton precession magnetometer (Selvåg, 2006). The Overhauser magnetometer is widely used in subsea environments and is also used for airborne and ground surveys (Nabighian *et al.*, 2005).

Optically pumped magnetometers can also be referred to as an alkali-vapour magnetometer. The main principle of its operation is based on the mechanical model of an atom (Lowrie, 2007). These magnetometers are composed of a photon emitter, an absorption chamber, a buffer gas, and a photon detector (Smith, 1997). A polarised light beam is passed through the adsorption chamber which contains a buffer gas such as rubidium, or more commonly caesium vapour. This light then falls on a photoelectric cell which measures the intensity of the light beam (Lowrie, 2007). Alkali-vapour magnetometers are the dominant instrument that are used for magnetic surveys in airborne, shipborne, and ground exploration (Nabighian *et al.*, 2005).

Caesium vapour magnetometers are part of the alkali metal range of magnetometers. The properties of a caesium atom allow for the displacement of electrons by applying photons (Smith, 1997). Caesium can exist at nine different energy levels; however, the photons only have an effect at three of these levels. This therefore makes it possible for the photons to pass through the caesium vapour unhindered, no longer resulting in the transfer of electrons. This gives the baseline state from which subsequent measurements are made (Smith, 1997). When an external AC magnetic field is applied, the difference in the energy levels of the electrons is established by the ambient magnetic field. This new field allows the photons to transfer electrons again

and this is measured by the amount of light that reaches the photon detector. It is this measurement that determines the magnetic field strength (Smith, 1997).

There are several different types of Gaussmeters, which measure strong magnetic fields. They are the Hall effect, magnetoresistive, magnetodiode, and magnetotransistor. These Gaussmeters can measure flux densities that range from 50 μT to 30 T (Macintyre, 1999). As the focus of this thesis is on detecting small anomalies within the magnetic field these types of Gaussmeters are not suitable for this application.

The development of magnetic sensors is an ongoing area of research such as the development of chip-scale magnetometers (MEMS devices) (Prouty and Johnson, 2010; Schwindt *et al*., 2004; Romalis, 2007). These devices will provide a sensitive magnetometer (from 10^{-15} to > 10^{-3} T) that is only millimetres in size which increases the portability of the device (Schwindt *et al*., 2004). Additionally, power consumption of these devices is much reduced compared to other magnetic sensors (Romalis, 2007). The increase in portability due to its small size will impact on both magnetic detection methods and the applications that they can be used in. This section has presented a wide range of different magnetic sensors, and the applications in which they can be used will now be discussed further.

3.4 Magnetic Surveying

The main purpose of a magnetic survey is to identify areas which have anomalous magnetisations. Anomalous magnetisations can be caused by localised mineralisation, subsurface structures, or anthropogenic activity (Lowrie, 2007). Magnetic surveying can be undertaken on land, in the air, at sea, in space, and down boreholes (Nabighian *et al.*, 2005; Lowrie, 2007). The magnetic measurements that are acquired from each method focus on lateral variations in the magnetisation of the Earth's crust. The measurements gained via a borehole additionally focus on the vertical variations in the vicinity of the borehole (Nabighian *et al.*, 2005).

Undertaking ground-based surveys produces a detailed pattern of the magnetic field anomaly, if the anomaly is close to the ground surface (Lowrie, 2007). In ground-based surveys, a local base station is set up away from the survey area, which allows the diurnal variations to be mapped over the course of the survey (Reynolds, 1997). Magnetic measurements taken down a borehole can be of the magnetic susceptibility, the three components of the magnetic field, and also measurements of the total field. These measurements can be used to determine the magnetic properties of the rock, and can also be used to determine the location and orientation of any magnetic bodies that have been missed by the drilled boreholes (Nabighian *et al.*, 2005).

The surveying of magnetic anomalies can also be undertaken from an aircraft. The magnetometer is towed at a set distance behind the aircraft to undertake the survey. Airborne magnetometers generally have a higher sensitivity than those used in ground based surveying, which helps to compensate for any loss in resolution due to the increased distance between the magnetometer and the source of the anomaly (Lowrie, 2007).

The magnetic field over the oceans can also be surveyed from the air, but the majority of the marine magnetic record has been obtained via shipborne surveys (Lowrie, 2007). Generally, in these surveys a magnetometer is towed behind the ship at a distance (around 100 – 300 metres), so that any magnetisation from the ship does not interfere with the survey. At this distance the magnetometer is below the surface of the water and therefore the survey is undertaken at a depth of between 12 – 20 metres (Lowrie, 2007). These surveys can also be performed using a magnetometer that is mounted onto an Autonomous Underwater Vehicle (AUV) (Szitkar *et al.*, 2016).

Magnetic surveying was first undertaken in space in 1964, when a scalar magnetometer was launched on the Cosmos 49 mission (Nabighian *et al.*, 2005). Since 1970, satellite measurements of the geomagnetic field have been used to model the dynamics of the core field and its secular variations (Nabighian *et al.*, 2005). The models produced have been incorporated into the International Geomagnetic

Reference Field (IGRF) which provides more accurate information for processing exploration quality magnetic surveys (Nabighian *et al.,* 2005).

There are many different applications that a magnetics survey can be applied to. One of these applications is the detection of unexploded ordnance (UXO). UXO detection is undertaken using magnetic surveying as the outer shells of the bombs are composed of either iron or steel, and therefore are magnetised (Hiergeist *et al.,* 2015). In using the magnetic field produced by the UXO, the position of the UXO in the ground can be found by undertaking a walk over survey of the area using one or more fluxgate magnetometers (Hiergeist *et al.,* 2015). Fluxgate magnetometers are used within this application as they are lightweight, and also allow for multiple sensors to be used (Munschy *et al.,* 2007). UXO detection was undertaken using magnetic surveying on Chevallier Ranch located in Montana, USA. This ranch had been previously used for artillery and tank training in the 1940s and 1950s (Billings and Youmans, 2007). A total field walk over magnetic survey was undertaken using four caesium-vapour magnetometers. The area surveyed was 200 acres, and took place over a 2-month period (Billings and Youmans, 2007). Throughout the survey 1127 magnetic anomalies were identified, with 69 of the anomalies being UXO. In addition to the UXOs, 23 anomalies were detected from emplaced objects, 445 anomalies were attributed to shrapnel, 395 were found to be either from the geology or no obvious source, and the remaining 195 anomalies were from junk (Billings and Youmans, 2007). Figure 3.10 shows the detected magnetic field of a UXO from the Chevallier Ranch survey.

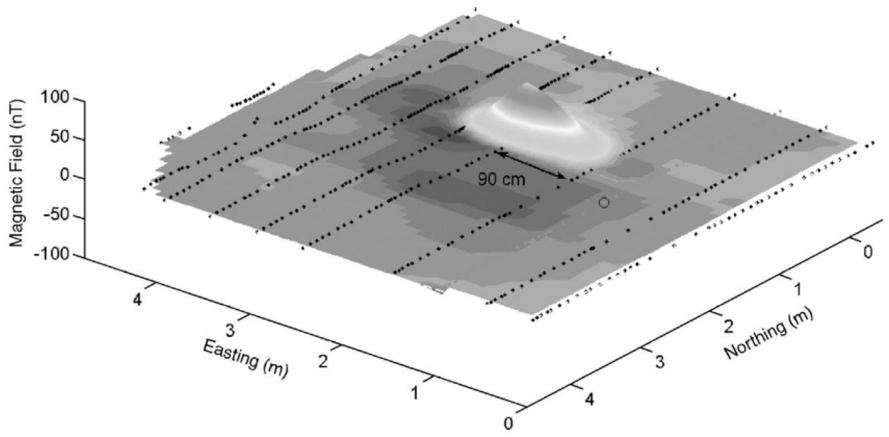

Figure 3.10: *The magnetic field of an UXO from the Chevallier Ranch, Montana (From Billings and Youmans, 2007).*

The detection of man-made structures, such as foundations and piles, can also be undertaken using magnetic surveying. Jo *et al*. (2003) outlined a method of using borehole magnetometry to determine the depth of foundations. In order for this method to be successful the foundations need to contain either reinforcement bars, steel casings, or embedded steel wires to produce a magnetic field that can be detected (Jo *et al*., 2003). The borehole magnetics survey was undertaken using a fluxgate magnetometer that was being raised in a borehole in the immediate proximity to the foundation. From this survey, it was concluded that as long as the background environment was not magnetically noisy, and there was sufficient ferromagnetic material embedded in the foundation, an accurate estimation of the depth of the foundation could be determined (Jo *et al.*, 2003).

Magnetic surveying is also used widely in geological exploration. It can be used to determine changes in the magnetisation of near-surface rocks, as well as being able to map the geology of an area, including the structural features (i.e. faults), and the depth to the basement rock (Gandhi and Sarkar, 2016). Magnetic surveys can detect mineralisations such as iron oxide, copper, and gold deposits, but they can also be used to locate favourable host rocks or environments such as carbonites, kimberlites, faulting, hydrothermal alteration, and the general geological mapping of potential prospective areas (Nabighian *et al.*, 2005). This type of surveying is often undertaken from the air as it is an economical way of investigating a large area in a short space of

time, and for this reason has become a routine part of the initial phases of a geophysical exploration of uncharted territory (Lowrie, 2007). An example of geological mapping using aeromagnetic surveying was discussed by Baptiste *et al.* (2016). Baptiste *et al.* used both aeromagnetic and gravity data to map an area around the French Paris Basin. Three magnetic surveys were collected from heights of between 85 m and 120 m above ground level, and conducted in a North – South orientation (Baptiste *et al*., 2016). Two different line spacing's were used over different regions. For the region of Brittany, a line-spacing of 500 m was used, which was reduced to 250 m over key areas, and over the regions of Pays de la Loire and Région Centre, a line-spacing of 1 km was used, reduced to 500 m over key areas (Baptiste *et al.*, 2016). Tie lines which run perpendicular to the main survey lines were spaced at every 10 km. Figure 3.11 gives an example of the magnetic data gained from this survey. The reds in the figure indicate areas where positive magnetic anomalies have been detected, whereas the blue and green areas indicate negative magnetic anomalies.

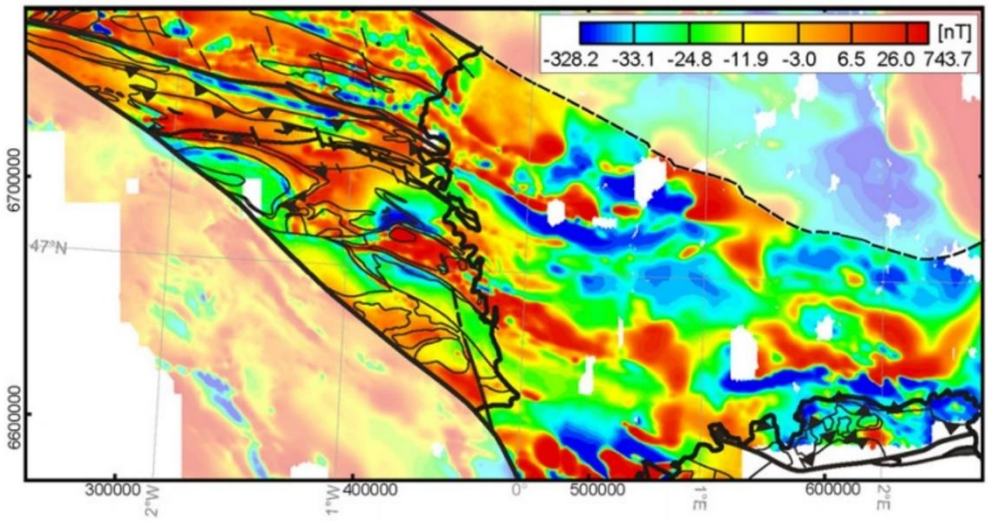

Figure 3.11: *An example of the magnetic anomaly data across the three survey areas, with the structural and lithological contours superimposed in black (From Baptiste et al., 2016).*

Geological mapping can also be undertaken underwater using an AUV. Szitkar *et al.* (2016) acquired near-seafloor magnetic data using a three-component fluxgate magnetometer that was attached to a AUV. This allowed data to be collected along

100 m profiles that were located at 70 m above the seafloor (Szitkar *et al*., 2016). This research was conducted along the East-Pacific Rise which is a mid ocean ridge that separates the Pacific oceanic plate from the Cocos and Nazca oceanic plates (Szitkar *et al*., 2016). The magnetic survey detected North-South trending elongated features that were identified as dykes (Szitkar *et al*., 2016).

The identification of buried archaeological features can also be achieved using magnetic surveying. Magnetic surveying has been used on archaeological sites around the world to determine the best locations to undertake excavations (Mekkawi *et al.*, 2013). Often magnetic surveys are used in conjunction with other geophysical methods such as electrical resistivity with both data sets being used to cross reference the results. These methods were used by Di Maio *et al.* (2016) at the archaeological site of Phaistos, located in Crete, Greece, to aid in the reconstruction of an ancient settlement at this site. The magnetic survey was used for preliminary exploration of the site, due to its fast data acquisition. These data were then used to identify areas for further analysis using other geophysical techniques (Di Maio *et al.*, 2016). Mekkawi *et al*. (2013) have also used magnetic surveying of archaeological sites in Egypt; a large proportion of the Egyptian archaeological features are composed of mud bricks which contain magnetic minerals (i.e. magnetite and hematite), therefore allowing them to be detected by magnetometers (Mekkawi *et al.*, 2013).

The nature of the application determines whether a ground-based, airborne, or seaborne survey is most appropriate. In the case of a ground-based survey, high resolution data can be obtained, however, this may be time consuming if the area is large. In the case of airborne and seaborne surveys a large area can be surveyed quickly, however, the resolution of the data gained may be lower.

3.5 Relevance to this Research

By introducing magnetic additives to grouts, this thesis investigates the potential for producing a magnetic grout which can be detected using commercially available magnetometers, over distances relevant to engineering works. The ability to detect a

grout post-injection would transform current grouting practice. Magnetic surveying has been used for many different applications, but is not a technique commonly used in ground engineering.

Within this research, a caesium vapour magnetometer will be used, as it is one of the most common types of magnetometer used for a ground-based survey. This type of magnetometer was chosen as it gives the option of either undertaking a detailed walkover survey with a fast measurement rate or taking single measurements at set points. Both of these methods were utilised within the field trials undertaken in this research and will be further described in Chapter 5. In using magnetic properties within a grout, as opposed to resistivity for example, variability over short distances, or between rock types can be minimised. Additionally, a magnetic field can be detected over long distances if it is strong enough. Chapter 4 presents experimental data on the engineering properties of magnetic grout mixes and Chapter 5 presents data from field trials that assess in-situ magnetic grout detectability, using a field magnetometer.

Chapter 4

Developing a Magnetic Grout

4.1 Introduction

This chapter focuses on the experimental laboratory work that has been undertaken to develop the magnetic grout. In order to investigate the usability of a magnetic cement grout, a series of tests were undertaken to investigate whether the properties of the cement grout, including the flowability, bleed, and setting time of the grout, were adversely affected by the addition of a magnetic additive. Additionally, magnetic susceptibility testing of the magnetic cement grout was undertaken to determine whether the addition of a magnetic additive would allow the cement grout to become detectable. This chapter also presents scanning electron microscope (SEM) and thin section images of different magnetic grout mixes.

4.2 Magnetic Cement Material

This section presents the magnetic properties of the magnetic cement material, focussing first on the magnetic susceptibility of the grout, before taking a closer look at the internal structure of the material by using thin section and SEM analysis.

4.2.1 Magnetic Susceptibility

The magnetic susceptibility (χ = **M** / **H,** where **M** is the magnetisation of the medium (A m^{-1}), and **H** is the magnetic field (A m^{-1})), is measured by applying a known magnetic field to a sample, and measuring the increased magnetism of the sample by the extra magnetic field it produces (Mussett and Khan, 2007).

4.2.1.1 Materials and Methods

For the magnetic susceptibility measurements, three different types of magnetic material were used. These materials are detailed below in Table 4.1. These materials (magnetite, maghemite, and iron filings) were chosen for testing, as they are all commercially readily available. Permanent magnet powders such as Samarium-Cobalt and Neodymium-Iron-Boron were also considered for testing within the cement mixtures, however these powders were not as readily available as the three magnetic materials chosen. Additionally, due to the availability of the magnetite, maghemite, and iron filings, they are also reasonably priced which allows for the end product of a magnetic grout to be economically viable. Within the testing of the magnetic cement material the magnetite was sourced from two different suppliers. Initially a synthetic magnetite from Sigma Aldrich was used, however due to the cost of this product a natural magnetite was sourced from Inoxia Ltd.

Table 4.1: *The different magnetic materials used.*

Magnetic Material	**Particle Size**	**Purity**	**Source**
Magnetite 1	< 5 µm	95 %	Sigma Aldrich
Magnetite 2 and 3	< 53 µm	95 %	Inoxia Ltd
Maghemite	< 5 µm	> 99 %	Sigma Aldrich
Iron Filings	< 20 µm	-	Sigma Aldrich

Throughout both the cement property testing and magnetic susceptibility testing two different types of cement were used. They are Procem 52,5N and Ultrafin 16 and a comparison of these cements can be seen in Table 4.2. Both of these cements are currently used in the grouting industry for rock fracture grouting.

Table 4.2: *A comparison of the two cements used.*

Cement	Cement Class	Particle Size	Source
Procem 52,5N– an Ordinary Portland Cement (OPC)	CEM 1	5 µm – 30 µm	Lafarge Tarmac
Ultrafin 16	CEM 1	95 % less than 16 µm	Cementa – part of the Heidelberg Cement Group

When preparing some of the cement samples, a superplasticiser and stabilising agent were also added to the cement mixtures. The superplasticiser used was Glenium 51. Glenium 51 is produced by BASF and is a polycarboxylic ether. It works by producing an electrostatic effect which stabilises the cement particles and their ability to disperse. This therefore allows less water to be used in the cement mixture resulting in a higher strength and durability of the cement being achieved. Where used, the dosage throughout the cement property testing was 1% of the total water content of the cement mixture, unless otherwise stated. The stabilising agent that was used was GroutAid. GroutAid is produced by Elkem, and is a silica fume (microsilica) based additive. The advantage of using GroutAid was that it improves the stability and strength properties of the cement. Where used, the dosage throughout the testing was 10% of the total water content of the cement mixture. However, as GroutAid is composed of 50% water and 50% silica, this water needs to be taken into account in the water to solids ratios used.

Magnetic susceptibility was measured using a Bartington MS3 Magnetic Susceptibility Meter, attached to a Bartington MS2B Dual Frequency Sensor (Figure 4.1). This system operated by generating a low frequency and low intensity AC magnetic field around the sensor. When a magnetic sample is placed in the sensor, the change in the magnetisation is detected by the system and converted into magnetic susceptibility readings. The Bartington MS2B Dual Frequency Sensor allows 10 mL samples to be analysed.

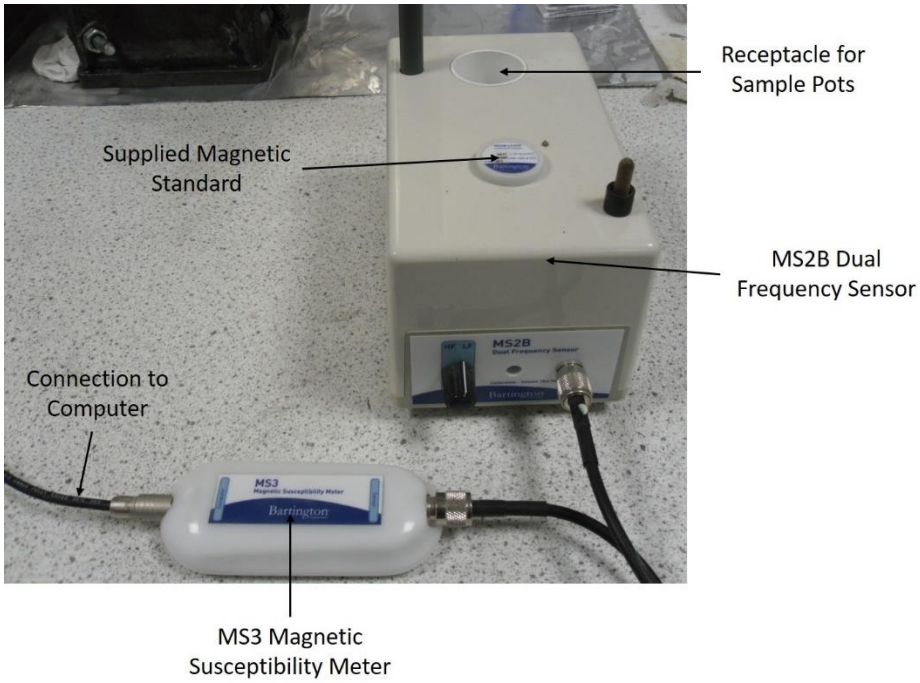

Figure 4.1: *The Bartington MS3 Magnetic Susceptibility Meter and the Bartington MS2B Dual Frequency Sensor used to measure magnetic susceptibility.*

To undertake the magnetic susceptibility measurements, the magnetic susceptibility of the cement materials were first established before magnetic materials were added to the mixture. This was achieved by hand mixing batches of both the pure OPC and the Ultrafin cement. These batches were small, with 50g of cement used each time. A 10 mL sample of each of the cement mixtures was decanted into a plastic sample pot, which was tapped to ensure that there were no air bubbles present, and the top was then scraped flat. The samples were placed into the Bartington MS2B Dual Frequency Sensor and measurements of magnetic susceptibility were recorded every 5 minutes for a duration of 24 hours.

After the magnetic susceptibility of the individual cements was established, differing amount of magnetic materials were added to both cements. These samples were created by mixing Magnetite, Maghemite, and Iron Filings at different percentages with the cement. Throughout all of the cement mixtures containing the magnetic materials, the percentage of the magnetic material (MM%) used is defined by the

following equation: $MM\% = (M_{MM} / M_C) \times 100$, where M_{MM} is the dry mass of the magnetic material, and M_C is the dry mass of the cement.

Table 4.3 details the different grout mixtures used for all of the magnetic susceptibility experiments.

Table 4.3: *Grout mixtures used for the magnetic susceptibility experiments.*

Grout Mix	Description (Batch Number)	Mass of Cement (g)	Mass of Water (g)	Mass of Superplasticiser (SA) (g)	Mass of Stabilising Agent (SA) (g)	Magnetic Material (Batch Number)	Mass of Magnetic Material (g)	% of Magnetic Material	Total Mass of Water (g)	Total Mass of Solids (g)	Water to Cement Ratio (WCR)	Water to Solids Ratio (WSR)
1	Pure OPC (1)	50	25	0	0	-	0	0	25	50	0.5	0.5
2	Pure OPC (1)	50	25	0	0	Magnetite (1)	0.5	1	25	50.5	0.5	0.5
3	Pure OPC (1)	50	25	0	0	Magnetite (1)	1.25	2.5	25	51.25	0.5	0.49
4	Pure OPC (1)	50	25	0	0	Magnetite (1)	2.5	5	25	52.5	0.5	0.48
5	Pure OPC (1)	50	25	0	0	Magnetite (1)	5	10	25	55	0.5	0.45
6	Pure OPC (1)	50	25	0	0	Magnetite (1)	10	20	25	60	0.5	0.42
7	Pure OPC (1)	50	25	0	0	Iron Filings	2.5	5	25	52.5	0.5	0.48
8	Pure OPC (1)	50	25	0	0	Maghemite	2.5	5	25	52.5	0.5	0.48
9	Pure OPC (2)	50	25	0	0	-	0	0	25	50	0.5	0.5
10	Pure OPC (2)	50	25	0	0	Magnetite (2)	0.5	1	25	50.5	0.5	0.5
11	Pure OPC (2)	50	25	0	0	Magnetite (2)	1.25	2.5	25	51.25	0.5	0.49
12	Pure OPC (2)	50	25	0	0	Magnetite (2)	2.5	5	25	52.5	0.5	0.48
13	Pure OPC (2)	50	25	0	0	Magnetite (2)	5	10	25	55	0.5	0.45
14	Pure OPC (2)	50	25	0	0	Magnetite (2)	10	20	25	60	0.5	0.42
15	OPC (2) + SP	50	25	0.25	0	-	0	0	25	50	0.5	0.5
16	OPC (2) + SP	50	25.5	0.25	0	Magnetite (2)	0.5	1	25.25	50.5	0.51	0.5
17	OPC (2) + SP	50	25.62	0.26	0	Magnetite (2)	1.25	2.5	25.62	51.25	0.51	0.5
18	OPC (2) +SP	50	26.25	0.26	0	Magnetite (2)	2.5	5.	26.25	52.5	0.53	0.5

Grout Mix	Description (Batch Number)	Mass of Cement (g)	Mass of Water (g)	Mass of Superplasticiser (SA) (g)	Mass of Stabilising Agent (SA) (g)	Magnetic Material (Batch Number)	Mass of Magnetic Material (g)	% of Magnetic Material	Total Mass of Water (g)	Total Mass of Solids (g)	Water to Cement Ratio (WCR)	Water to Solids Ratio (WSR)
19	OPC (2) + SP	50	27.5	0.27	0	Magnetite (2)	5	10	27.5	55	0.55	0.5
20	OPC + SP	50	30	0.3	0	Magnetite (2)	10	20	30	60	0.6	0.5
21	OPC (2) + SA	50	23.75	0	2.5	-	0	0	25	50	0.5	0.5
22	OPC (2) + SA	50	23.99	0	2.52	Magnetite (2)	0.5	1	22.25	50.5	0.51	0.5
23	OPC (2) + SA	50	24.34	0	2.56	Magnetite (2)	1.25	2.5	25.62	51.25	0.51	0.5
24	OPC (2) + SA	50	24.94	0	2.62	Magnetite (2)	2.5	5	26.25	52.5	0.53	0.5
25	OPC (2) + SA	50	26.12	0	2.75	Magnetite (2)	5	10	27.5	55	0.55	0.5
26	OPC (2) + SA	50	28.5	0	3.0	Magnetite (2)	10	20	30	60	0.6	0.5
27	OPC (2) + SP + SA	50	23.75	0.25	2.5	-	0	0	25	50	0.5	0.5
28	OPC (2) + SP + SA	50	23.99	0.25	2.52	Magnetite (2)	0.5	1	25.25	50.5	0.51	0.5
29	OPC (2) + SP + SA	50	24.34	0.26	0.56	Magnetite (2)	1.25	2.5	25.62	51.25	0.51	0.5
30	OPC (2) + SP + SA	50	23.94	0.26	2.62	Magnetite (2)	2.5	5	26.25	52.5	0.53	0.5
31	OPC (2) + SP + SA	50	26.12	0.27	2.75	Magnetite (2)	5	10	27.5	55	0.55	0.5
32	OPC (2) + SP + SA	50	28.5	0.3	3.0	Magnetite (2)	10	20	30	60	0.60	0.5

Grout Mix	Description (Batch Number)	Mass of Cement (g)	Mass of Water (g)	Mass of Superplasticiser (SA) (g)	Mass of Stabilising Agent (SA) (g)	Magnetic Material (Batch Number)	Mass of Magnetic Material (g)	% of Magnetic Material	Total Mass of Water (g)	Total Mass of Solids (g)	Water to Cement Ratio (WCR)	Water to Solids Ratio (WSR)
33	Pure Ultrafin (1)	50	33.3	0	0	-	0	0	33.3	50	0.67	0.67
34	Pure Ultrafin (1)	50	33.7	0	0	Magnetite (1)	0.5	1	33.7	50.5	0.67	0.67
35	Pure Ultrafin (1)	50	34.16	0	0	Magnetite (1)	1.25	2.5	34.2	51.25	0.68	0.67
36	Pure Ultrafin (1)	50	35	0	0	Magnetite (1)	2.5	5	35	52.5	0.70	0.67
37	Pure Ultrafin (1)	50	36.7	0	0	Magnetite (1)	5	10	36.7	55	0.73	0.67
38	Pure Ultrafin (1)	50	40	0	0	Magnetite (1)	10	20	40	60	0.80	0.67
39	Pure Ultrafin (2)	50	33.3	0	0	-	0	0	33.3	50	0.67	0.67
40	Pure Ultrafin (2)	50	33.7	0	0	Magnetite (2)	0.5	1	33.7	50.5	0.67	0.67
41	Pure Ultrafin (2)	50	34.16	0	0	Magnetite (2)	1.25	2.5	34.2	51.25	0.68	0.67
42	Pure Ultrafin (2)	50	35	0	0	Magnetite (2)	2.5	5	35	52.5	0.70	0.67
43	Pure Ultrafin (2)	50	36.7	0	0	Magnetite (2)	5	10	36.7	55	0.73	0.67
44	Pure Ultrafin (2)	50	40	0	0	Magnetite (2)	10	20	40	60	0.80	0.67

Grout Mix	Description (Batch Number)	Mass of Cement (g)	Mass of Water (g)	Mass of Superplasticiser (SA) (g)	Mass of Stabilising Agent (SA) (g)	Magnetic Material (Batch Number)	Mass of Magnetic Material (g)	% of Magnetic Material	Total Mass of Water (g)	Total Mass of Solids (g)	Water to Cement Ratio (WCR)	Water to Solids Ratio (WSR)
45	Ultrafin (2) + SP	50	33.33	0.33	0	-	0	0	33.3	50	0.67	0.67
46	Ultrafin (2) + SP	50	33.7	0.34	0	Magnetite (2)	0.5	1	33.7	50.5	0.67	0.67
47	Ultrafin (2) + SP	50	34.17	0.34	0	Magnetite (2)	1.25	2.5	34.12	51.25	0.68	0.67
48	Ultrafin (2) + SP	50	35	0.35	0	Magnetite (2)	2.5	5	35	52.5	0.70	0.67
49	Ultrafin (2) + SP	50	36.7	0.37	0	Magnetite (3)	5	10	36.7	55	0.73	0.67
50	Ultrafin (2) + SP	50	40	0.4	0	Magnetite (3)	10	20	40	60	0.80	0.67
51	Ultrafin (2) + SA	50	31.64	0	3.33	-	0	0	33.3	50	0.67	0.67
52	Ultrafin (2) + SA	50	23.01	0	3.37	Magnetite (3)	0.5	1	33.7	50.5	0.67	0.67
53	Ultrafin (2) + SA	50	32.46	0	3.42	Magnetite (3)	1.25	2.5	34.2	51.25	0.68	0.67
54	Ultrafin (2) + SA	50	33.25	0	3.5	Magnetite (3)	2.5	5	35	52.5	0.70	0.67
55	Ultrafin (2) + SA	50	34.87	0	3.67	Magnetite (3)	5	10	36.7	55	0.73	0.67
56	Ultrafin (2) + SA	50	38.0	0	4.0	Magnetite (3)	10	20	40.0	60	0.80	0.67
57	Ultrafin (2) + SP + SA	50	31.64	0.33	3.33	-	0	0	33.3	50	0.67	0.67
58	Ultrafin (2) + SP + SA	50	32.01	0.34	3.37	Magnetite (3)	0.5	1	33.7	50.5	0.67	0.67
59	Ultrafin (2) + SP + SA	50	32.46	0.34	3.42	Magnetite (3)	1.25	2.5	34.2	51.25	0.68	0.67
60	Ultrafin (2) + SP + SA	50	33.25	0.35	3.5	Magnetite (3)	2.5	5	35	52.5	0.70	0.67

Grout Mix	Description (Batch Number)	Mass of Cement (g)	Mass of Water (g)	Mass of Superplasticiser (SA) (g)	Mass of Stabilising Agent (SA) (g)	Magnetic Material (Batch Number)	Mass of Magnetic Material (g)	% of Magnetic Material	Total Mass of Water (g)	Total Mass of Solids (g)	Water to Cement Ratio (WCR)	Water to Solids Ratio (WSR)
61	Ultrafin (2) + SP + SA	50	34.87	0.37	3.67	Magnetite (3)	5	10	36.7	55	0.73	0.67
62	Ultrafin (2) + SP + SA	50	38.0	0.4	4	Magnetite (3)	10	20	40.0	60	0.80	0.67

4.2.1.2 Results

To gain the magnetic susceptibility results, the samples were placed in the MS2B Dual Frequency Sensor for 24 hours, with measurements being collected every 5 minutes. An example of the data collected over the 24-hour period for a cement sample can be seen in Figure 4.2. Some variation in the magnetic susceptibility can be seen; it is likely that this is due to changes in the background magnetic susceptibility as a result of the use of electrical equipment in the vicinity of the sensor. For consistency, for all subsequent tests, the value obtained at 24 hours is reported. All of the grout mixtures used for the magnetic susceptibility testing can be found in Table 4.3.

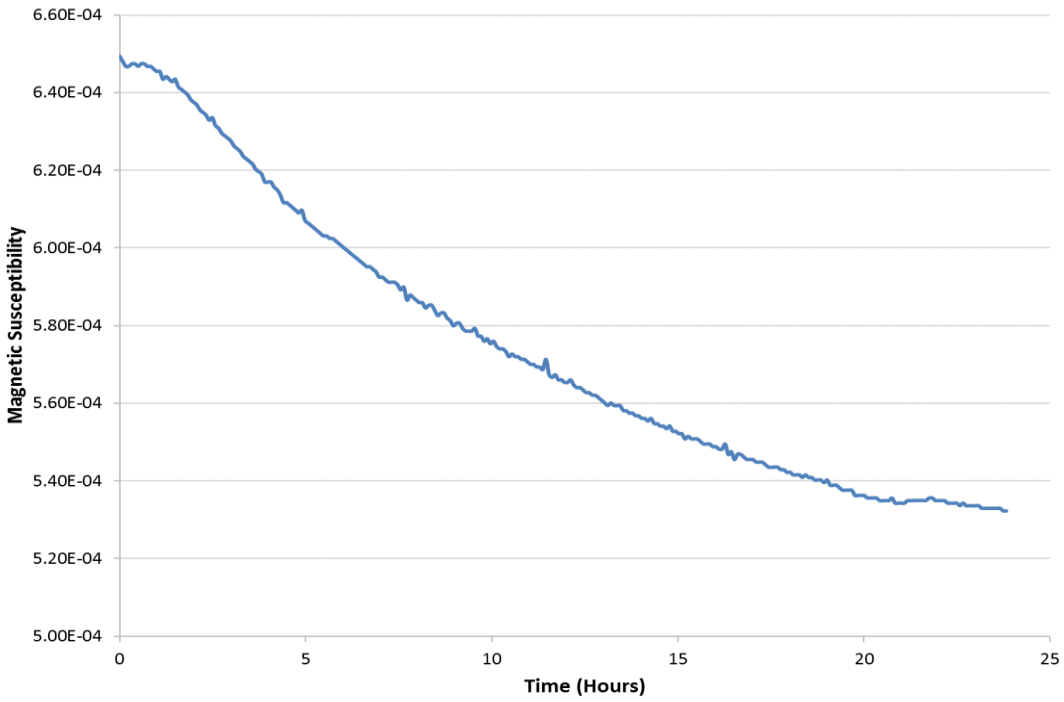

Figure 4.2: *Magnetic susceptibility data collected over a 24-hour period.*

The magnetic susceptibilities of both the pure OPC and the pure Ultrafin cement were 7.81 x 10^{-4} and 2.23 x 10^{-4} respectively. A comparison of the magnetic susceptibility of the magnetic materials of magnetite, maghemite, and iron filings added to OPC is presented in Figure 4.3. The grout mixtures used are from 1 to 8 for OPC and from 33 to 38 for Ultrafin in Table 4.3. The addition of 5 % maghemite to the OPC mixture resulted in a slight increase in the magnetic susceptibility of the cement to 1.92 x 10^{-3}. This value of magnetic susceptibility is much lower than that produced when only 1% magnetite is added to the cement. The addition of 5 % iron filings to the OPC resulted in a magnetic susceptibility value of 8.64 x 10^{-3}. This value is similar to the results gained when 1% magnetite is added to the OPC (8.28 x 10^{-3}) and 2.5% magnetite is added to the Ultrafin cement (8.48 x 10^{-3}). To increase the magnetic susceptibility of both cements, large percentages of both maghemite and iron filings would have to be added to the cement mixture to achieve the same level of magnetic susceptibility that has been recorded with the magnetite. Iron filings and maghemite were therefore not added to the Ultrafin cement as it could be seen from the OPC results that the magnetic susceptibility of these materials at the percentages tested would be too small to be detected on a larger scale. Consequently, based on these initial susceptibility data,

magnetite was chosen as the sole magnetic material to be taken forward. This is because the lower the percentage of magnetic material within the grout, the more likely that usability of the grout can be maintained, as well as ensuring costs are kept to a minimum.

The magnetic susceptibility results of the OPC and Ultrafin cement with different percentages of magnetic material are plotted in Figure 4.3. With the addition of magnetite to both the OPC and Ultrafin, the magnetic susceptibility increases linearly with increasing percentage of magnetite within the cement mixture. A straight line was fitted to sets of data, with an R^2 value of 0.9992 for the OPC and of an R^2 value of 0.9986 for the Ultrafin. For the calculation with the Ultrafin cement, the magnetic susceptibility value recorded for the cement with 20% magnetite was excluded due to this point being an outlier. Despite the same mass of magnetite being added to each sample, the magnetic susceptibility values recorded for the two types of cement are not the same. The magnetic susceptibilities of the OPC-magnetite mixtures are higher than those made with the Ultrafin; this difference in susceptibility increases as the percentage of magnetite in the samples increases (Figure 4.3). This result was unexpected, as it was anticipated that the magnetite would not react with the cement mixtures.

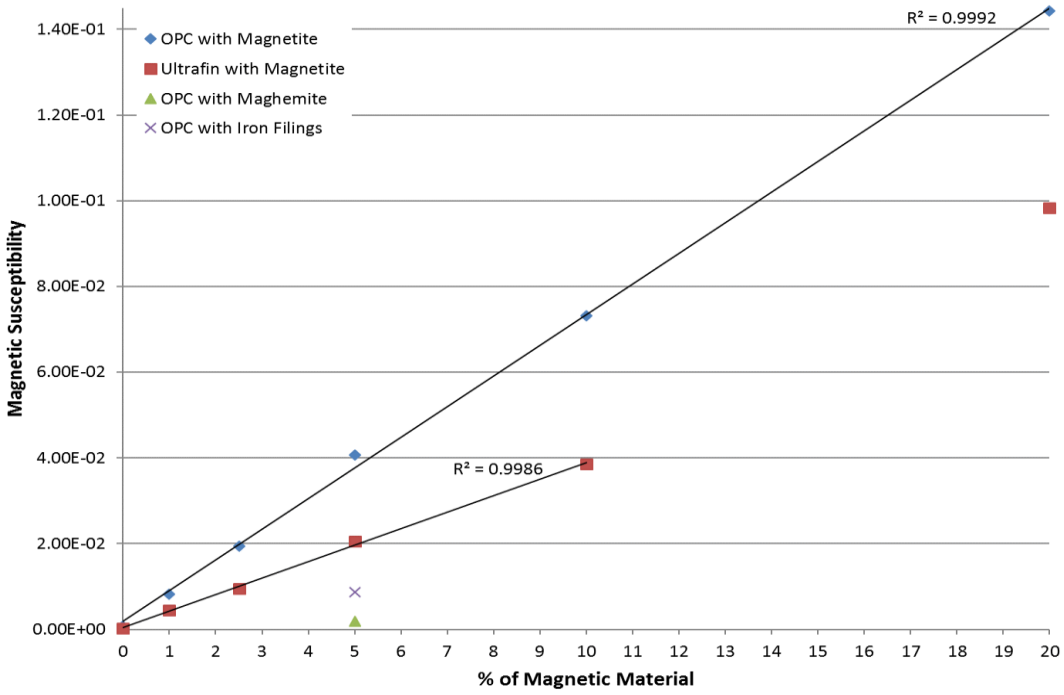

Figure 4.3: *Magnetic susceptibility of OPC with different percentages of magnetite, maghemite, and iron filings, and magnetic susceptibility of Ultrafin with magnetite.*

A comparison of the data in Figure 4.3, with the susceptibility of pure magnetite was undertaken. A 10ml sample containing 100% magnetite was tested and the magnetic susceptibility result gained is compared to those from the magnetic cement mixtures in Figure 4.4. Figure 4.4 shows that the magnetic susceptibility of the Ultrafin-magnetite cement mix generally follows that expected up to 10% magnetite, based purely on the percentage of magnetite within the sample. The magnetic susceptibility value for 20% magnetite is higher than expected and is therefore likely to be anomalous. Whereas, the samples made using OPC have a greater magnetic susceptibility than that expected from the pure magnetite throughout all of the experiments. The results suggest that with the addition of the magnetite to the cement mixture a reaction is occurring which produces a cement mixture that is more magnetically susceptible than pure magnetite.

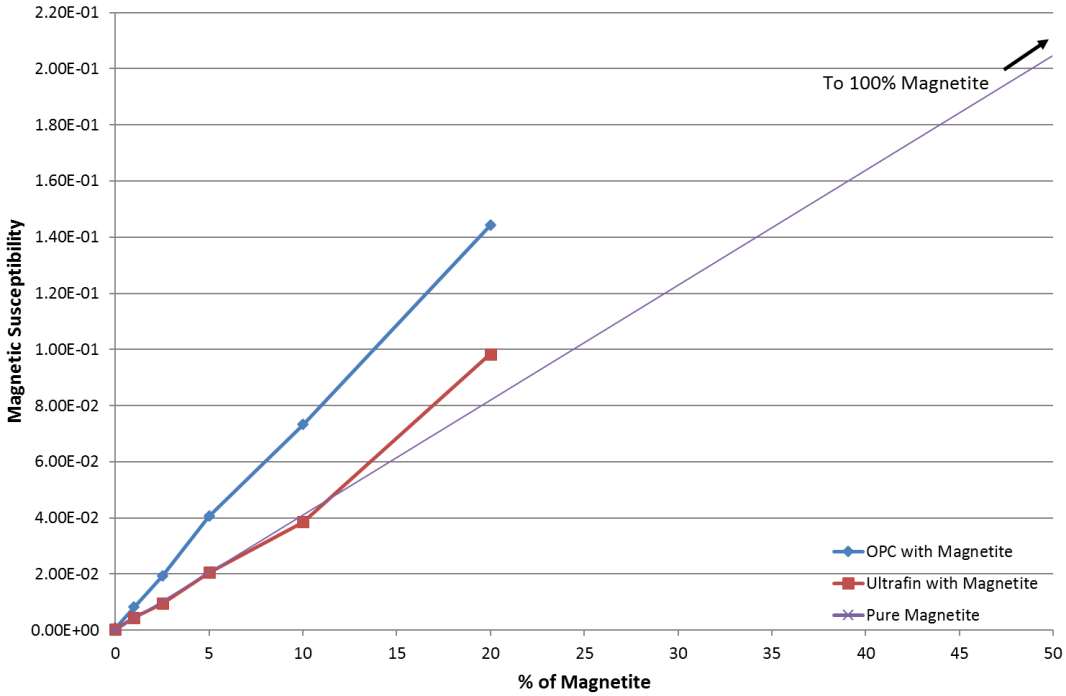

Figure 4.4: *A comparison of the magnetic susceptibility of pure magnetite with magnetic susceptibility of the magnetic cement mixtures.*

Further magnetic susceptibility measurements were undertaken on both cements, with the addition of a superplasticiser and/or a stabilising agent. In testing the magnetic susceptibility of mixtures containing just superplasticiser or stabilising agent, it could be determined whether the individual additives had any effect on the magnetic properties of the cement. As discussed previously, 1% superplasticiser, and 10% stabilising agent were added to the cement mixture. Within these magnetic susceptibility measurements a new batch of OPC was used and as such is referred to as OPC 2. The grout mixtures used are from 9 to 32 in Table 4.3. Figure 4.5 shows the magnetic susceptibility result for samples using OPC. The results do not differ greatly from those gained using only OPC with magnetite. The addition of both the superplasticiser and the stabilising agent reduces the measured magnetic susceptibility. As the percentage of magnetite increases, this susceptibility reduction increases. The addition of the stabilising agent has a lesser effect than that of the superplasticiser.

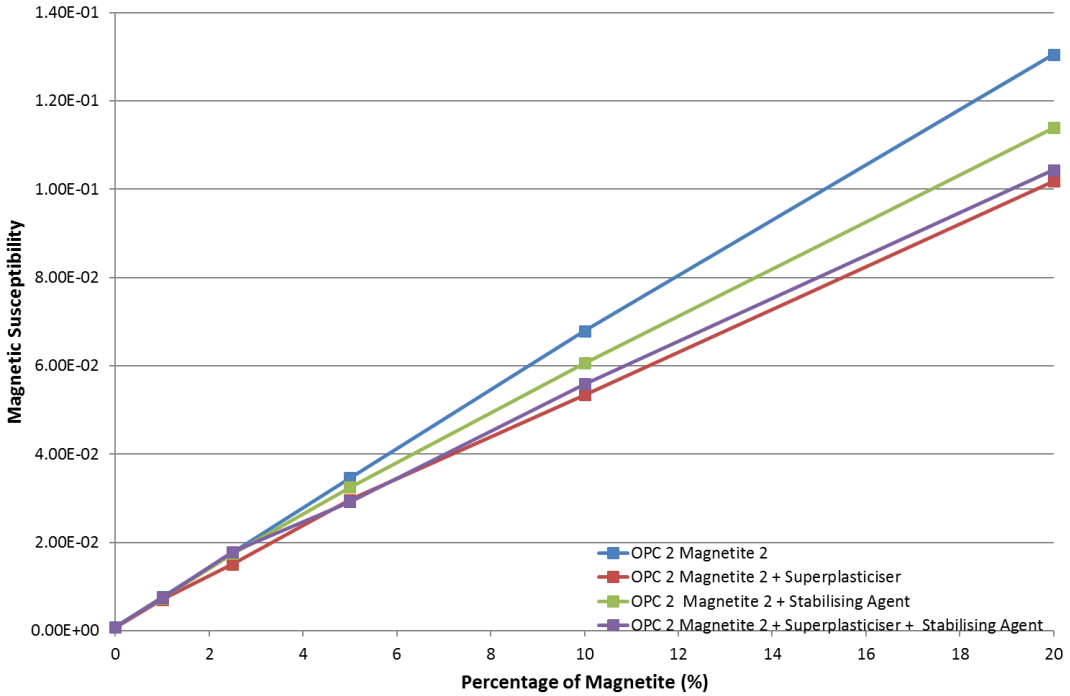

Figure 4.5: *Magnetic susceptibility of OPC with magnetite, with some mixtures containing superplasticiser, stabilising agent, and a mixture of both.*

In the Ultrafin mixtures, two different magnetite batches (magnetite 2 and magnetite 3) were used in the experiments, as the first batch ran out. The grout mixtures used are 39 to 62 in Table 4.3**.** In the mixture of Ultrafin cement with superplasticiser, magnetite 2 was used for the measurements with 1%, 2.5%, and 5% magnetite. These measurements follow closely the results gained from the Ultrafin cement with magnetite mixture. Magnetite 3 was then used for the mixtures with 10% and 20% magnetite to complete the data set. Due to this change in magnetite, there is a step in the results gained, caused by variation in the magnetic susceptibility of the natural magnetite.

The mixtures of Ultrafin cement with magnetite and stabilising agent, and Ultrafin cement with magnetite, superplasticiser, and stabilising agent were both completed using magnetite 3. Addition of both the stabilising agent and the superplasticiser did not cause any significant changes in the magnetic susceptibility of the final Ultrafin-magnetite cement mix. The difference in the magnetic susceptibility between the

Ultrafin cement and magnetite and the cement mixtures with stabilising agent and superplasticiser can be attributed to the change in the batch of magnetite from 2 to 3.

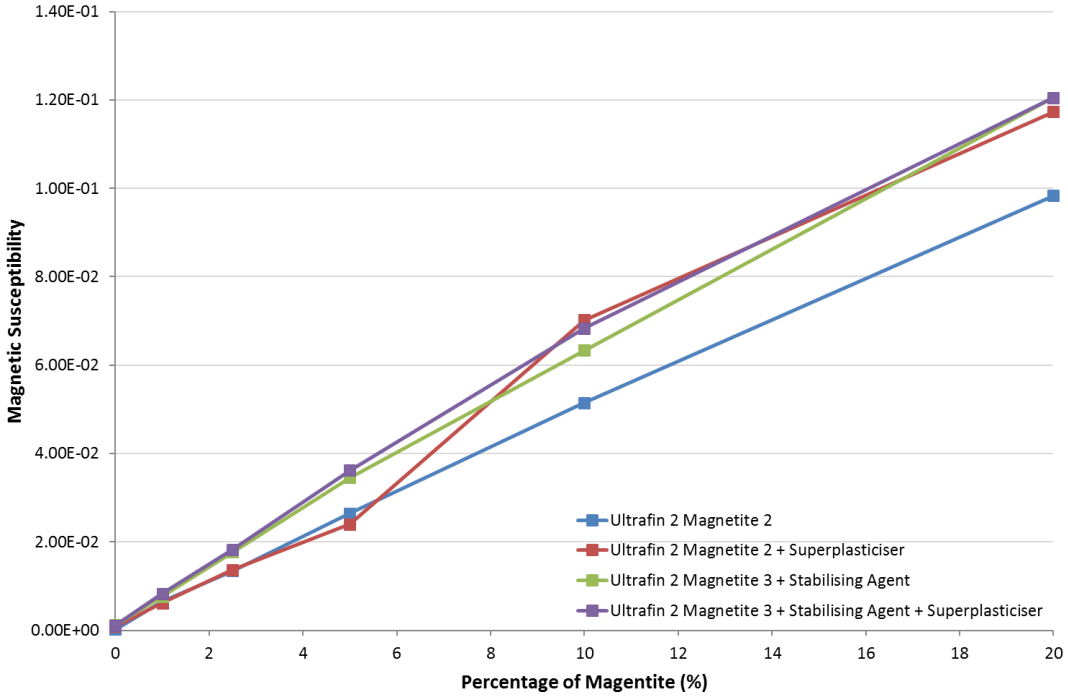

Figure 4.6: *Magnetic susceptibility of Ultrafin cement with magnetite. with some mixtures containing superplasticiser, stabilising agent, and a mixture of both.*

4.2.1.3 Discussion

In initially testing the magnetic susceptibility of a range of magnetic materials, magnetite, maghemite, and iron filings, the variability in the magnetic susceptibility of the different materials could be easily identified: magnetite has the highest magnetic susceptibility above maghemite and then iron filings. Hence, magnetite was the logical choice to take forward into further testing of the magnetic grout material. Due to its higher magnetic susceptibility, less magnetite will be needed to be added to the cement to achieve the level at which it can be sufficiently detected. It is expected that introducing lower amounts of magnetic material will also have less of an effect on the engineering properties of the cement.

The magnetic susceptibility results gained for both the OPC and Ultrafin cements have shown that, with increasing magnetite content within the cement mixtures, the magnetic susceptibility also increases linearly. This was the expected outcome, however, the magnetic susceptibility values gained for both cements are not the same. The difference in the magnetic susceptibility value between the cements rises as the amount of magnetite increases. This is likely to be caused by the natural variation in the magnetisation of the magnetite becoming more pronounced as the mass of the magnetite increases.

The addition of superplasticiser and stabilising agent to the magnetic cement mixtures have slightly different effects to the magnetic susceptibility. In the OPC samples it appears that the addition of the additives reduces the magnetic susceptibility of the cement material. However, within the Ultrafin cement samples, the susceptibility increases. It is possible that any changes in the magnetic susceptibility can be attributable to variability in the individual batches of magnetite, and not to the addition of either the superplasticiser or stabilising agent.

4.2.2 Thin Section and SEM Analysis

Thin sections were prepared to determine (i) the composition of the cements, (ii) how well the magnetite is distributed within the samples, and (iii) whether any reactions could have occurred with the magnetite resulting in a change to the elemental composition of the cements. Six thin sections were produced from the magnetic cement samples used in the magnetic susceptibility tests. The thin sections were taken vertically down the centre line of the magnetic cement samples. Thin sections were created from the following cement mixtures, pure OPC, OPC with 10% magnetite, OPC with 20% magnetite, pure Ultrafin cement, Ultrafin cement with 10% magnetite, and Ultrafin cement with 20% magnetite. The thin sections were polished and were carbon coated prior to imaging using the SEM. Optical light microscopy analysis was undertaken which allowed the thin sections to be analysed using both plane polarised and cross polarised light. The SEM analysis was undertaken using a HITACHI S-3700 Tungsten Filament Scanning Electron Microscope. The images gained from the

SEM are in the form of secondary electron images (SE) and back-scattered electron images (BSE). Using these two methods it was possible to image the microstructure of the samples, and the distribution of magnetite within the cement mixtures.

4.2.2.1 Thin Section Analyses

Figure 4.7 to Figure 4.9 present (a) plane-polarised light, and (b) cross-polarised light photographs of pure OPC, OPC containing 10% magnetite, and OPC containing 20% magnetite respectively at 10x optical zoom. The pure OPC sample is generally well mixed (Figure 4.7). Within this sample there are some small minerals present which are orange and black in colour and can be seen in both the plane-polarised and cross-polarised light. The thin sections containing the 10% and 20% magnetite (Figure 4.8 and Figure 4.9 respectively) are much darker in appearance, when compared to the pure OPC thin section. This is because magnetite is an opaque mineral which does not allow light to pass through it, and therefore appears black in both the plane-polarised and cross-polarised light. The OPC with 10% magnetite is not quite as well mixed as the pure OPC mixture, with unmixed cement grains present throughout the thin section. The cement grains show some zoning features which may be a result of the cement hydration reaction. There are also some dark areas present potentially indicating a higher density of magnetite. In the cross-polarised light, the main matrix of the thin section shows a higher birefringence colour than that observed in the pure cement mixes. This may suggest that new minerals are present within the thin section. The OPC with 20% magnetite is very well mixed, with the magnetite evenly distributed throughout the thin section. Orange minerals are also present throughout the thin section, and can be seen in both plane-polarised and cross-polarised light. These orange minerals are potentially an oxide of iron that was already present in the cement, however, without further chemical analysis of the cement this cannot be verified.

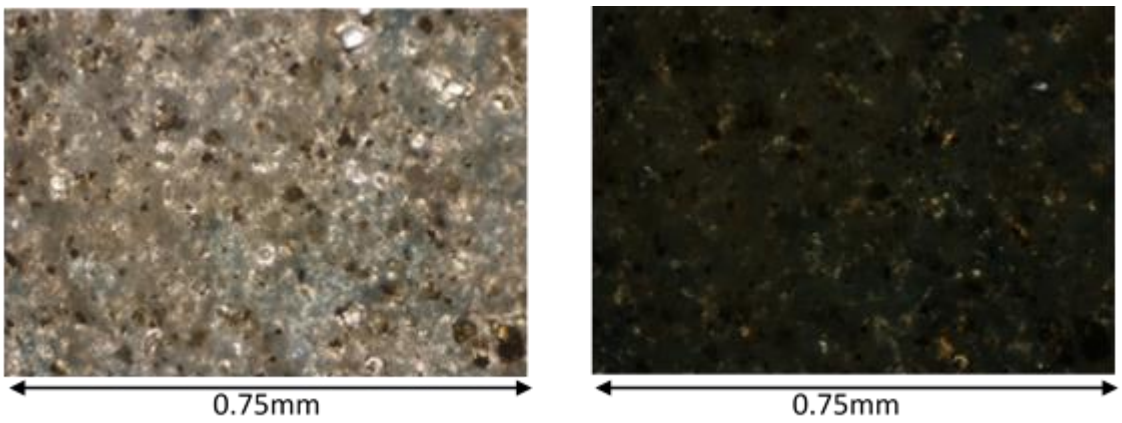

Figure 4.7: *a) Plane-polarised light, and b) cross-polarised light photographs of the thin section of pure OPC at 10x optical zoom.*

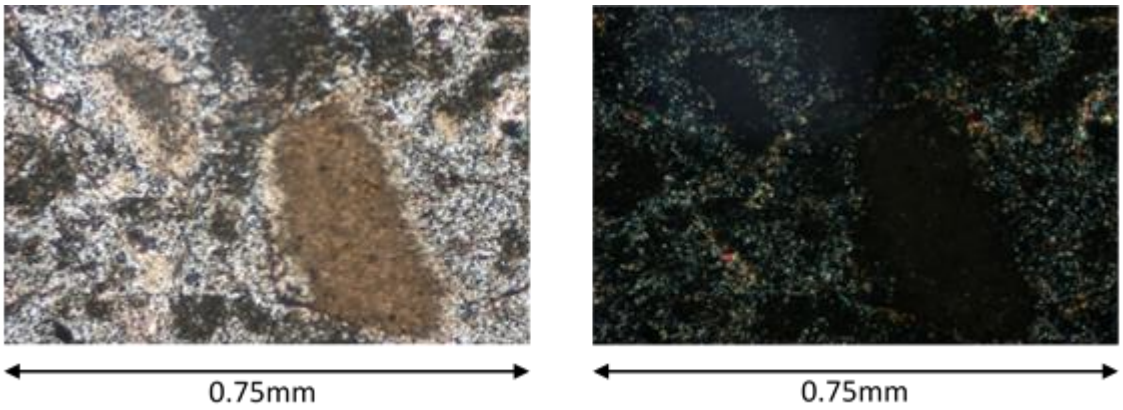

Figure 4.8: *a) Plane-polarised light, and b) cross-polarised light photographs of the thin section of OPC with 10% magnetite at 10x optical zoom.*

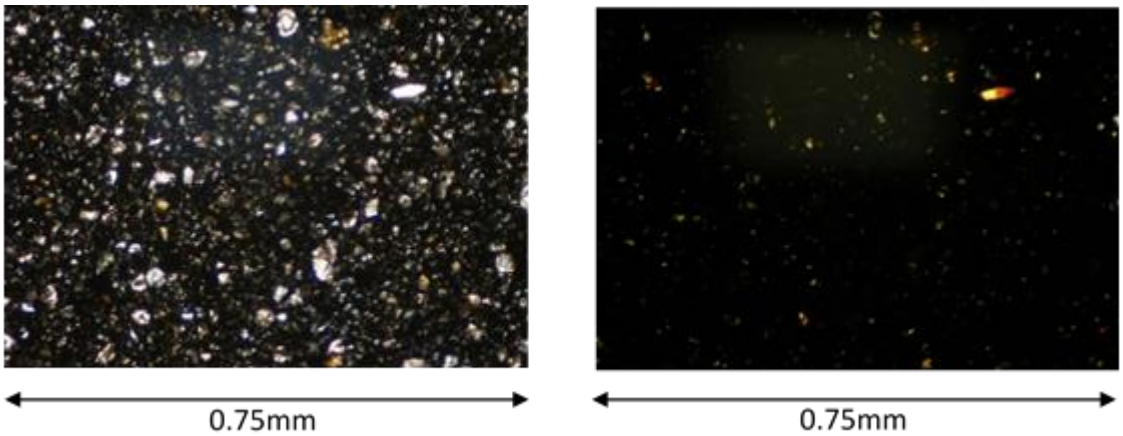

Figure 4.9: *a) Plane-polarised light, and b) cross-polarised light photographs of the thin section of OPC with 20% magnetite and 10x optical zoom.*

Figure 4.10 to Figure 4.12 present (a) plane-polarised light, and (b) cross-polarised light photographs of pure Ultrafin, Ultrafin cement containing 10% magnetite, and Ultrafin cement containing 20% magnetite at 10x optical zoom. The pure Ultrafin cement (Figure 4.10) contains small lumps of unmixed cement which have formed as a result of hand mixing the cement mixture. This thin section contains dark linear features, which do not appear to be aligned in any particular direction. The unmixed cement grains also have darker interiors and lighter edges. This could be a result of the hydration reaction of the cement with the edges of the cement particles having undergone a higher degree of hydration. The Ultrafin cement with 10% magnetite (Figure 4.11) is very well mixed with the magnetite largely evenly distributed throughout the thin section. There are some areas which are slightly darker in appearance which could be areas that have a higher density of magnetite. There are also some orange minerals present throughout the thin section which remain orange in cross-polarised light. These are again likely to be a form of iron oxide, however further analysis would need to be undertaken to confirm this. The Ultrafin cement with 20% magnetite (Figure 4.12) is not as well mixed, with large cement particles present throughout the thin section. These cement particles show some zoning features, with a dark cement and lighter edges. There are also some particles which are just composed of the lighter material. This lighter material also has a higher birefringence colour in crossed-polarised light.

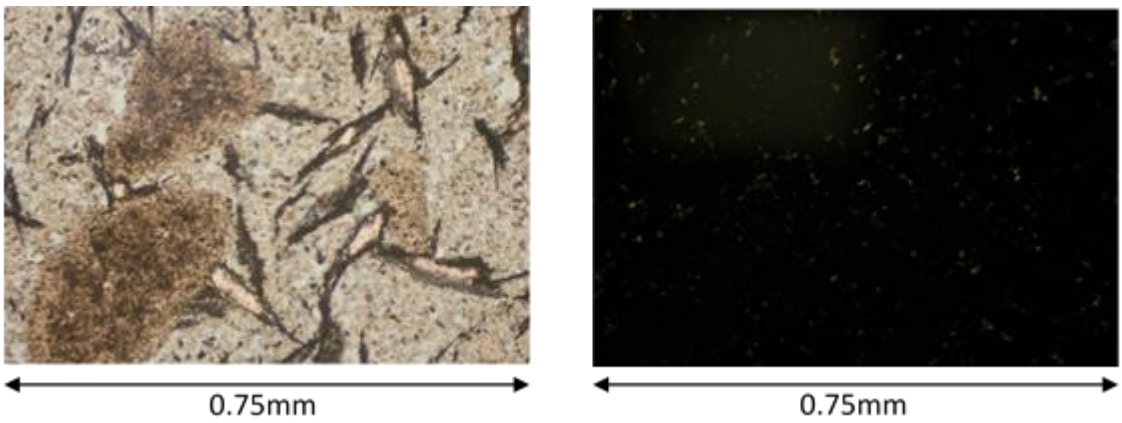

Figure 4.10: *a) Plane-polarised light, and b) cross-polarised light photographs of the thin section of pure Ultrafin cement at 10x optical zoom.*

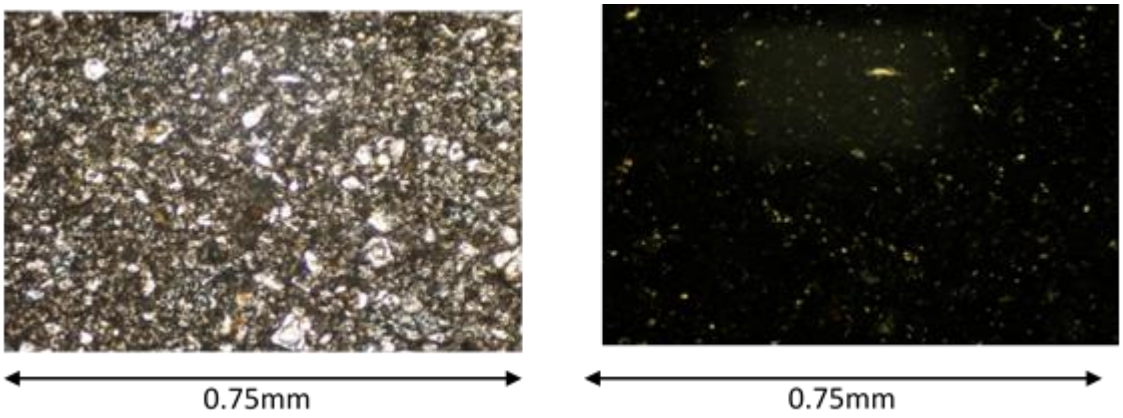

Figure 4.11: *a) Plane-polarised light, and b) cross-polarised light photographs of the thin section of Ultrafin with 10% magnetite at 10x optical zoom.*

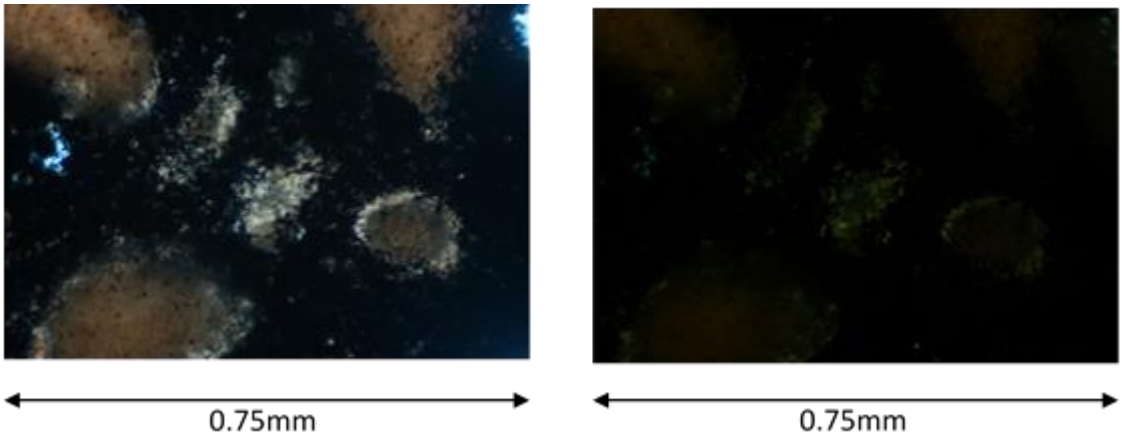

Figure 4.12: *a) Plane-polarised light, and b) cross-polarised light photographs of the thin section of Ultrafin cement with 20% magnetite at 10x optical zoom.*

4.2.2.2 SEM Analysis

SEM analysis was undertaken on all of the thin sections. Elemental analysis was undertaken using Oxford Inca 350 software, which reports the amount of a particular element in weight percent (wt %). This method does not detect hydrogen as the element is too light for the sensors to distinguish.

Image and elemental analyses were undertaken across the thin sections of the pure OPC, OPC with 10% Magnetite, and OPC with 20% Magnetite (Figure 4.13). Within the pure OPC sample (Figure 4.13a), the water and cement has been incorporated well together. This sample contains small amounts of iron naturally present within the cement, with the distribution of this iron, and the amount detected illustrated within Figure 4.13b and Figure 4.13c. The samples of OPC with 10% magnetite, and OPC with 20% magnetite appear to be generally well mixed (Figure 4.13d and Figure 4.13g). As the percentage of magnetite increases within the cement sample, the percentage of iron present also increases as expected. This can be seen in the bar charts, Figure 4.13f and Figure 4.13i. The distribution of iron throughout the samples which contained magnetite is generally evenly dispersed (Figure 4.13e and Figure 4.13h). There are some areas within both the sample of 10% and 20% magnetite where the magnetite is clustered together (indicated by brighter white areas), which is likely to be a result of the hand mixing of the samples. Throughout the OPC with 10% magnetite sample (Figure 4.13d) linear features are present. An elemental point analysis was undertaken on a linear feature indicating that they are mainly composed of Calcium and Oxygen, which suggests that they are a form of calcium oxide.

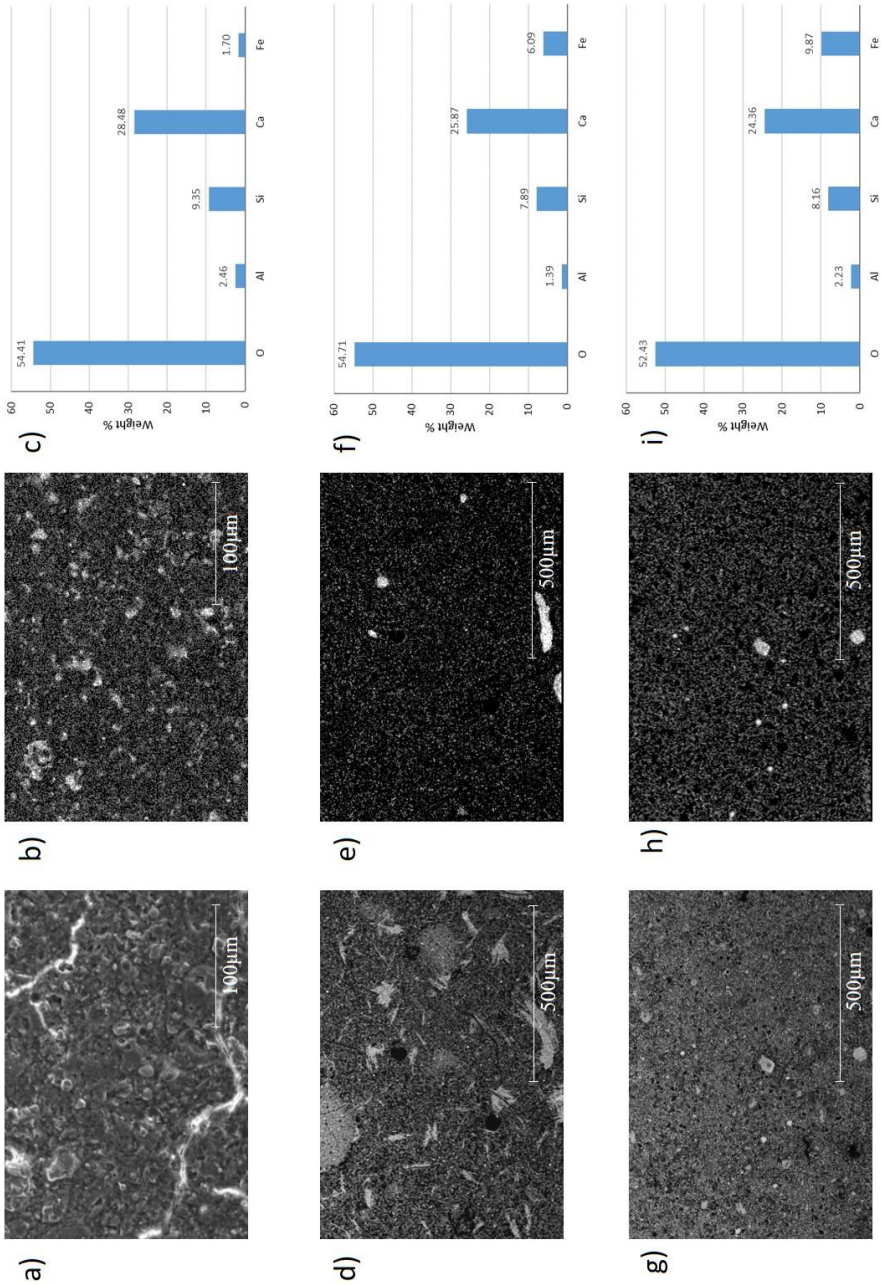

Figure 4.13: *a) Scanning electron image of pure OPC, b) elemental distribution of iron within the pure OPC sample, c) bar chart of elemental composition of pure OPC, d) backscattered electron image of OPC with 10% magnetite, e) elemental distribution of iron within the OPC with 10% magnetite sample, f) bar chart of elemental composition of OPC with 10% magnetite, g) backscattered electron image of OPC with 20% magnetite, h) elemental distribution on iron within the OPC with 20% magnetite sample, and i) bar chart of elemental composition of OPC with 20% magnetite.*

There are several areas within the OPC with 10% magnetite sample, that are less well mixed, and as a result contain areas of unmixed cement and magnetite. The areas of unmixed cement appear to contain desiccation cracks, which were formed as the sample dried out prior to preparation of thin sections (Figure 4.14). Four elemental point analyses were undertaken on one of these areas of unmixed cement, and the location of these is indicated by red crosses in Figure 4.14. The findings of the elemental analysis are that the weight percent of iron generally varies throughout, however there is a slightly higher percentage present at the edge of the unmixed cement area. Within some of the areas of unmixed magnetite, there appears to be a boundary present (Figure 4.15). Three small elemental area analyses were undertaken indicated by the red squares in Figure 4.15. Between all three areas of elemental analysis the weight percentage of iron varied, with the highest value being recorded as 48.24 wt%. Areas which have a higher concentration of iron present can also be found within the OPC with 20% magnetite sample with values being recorded up to 63.35 wt%.

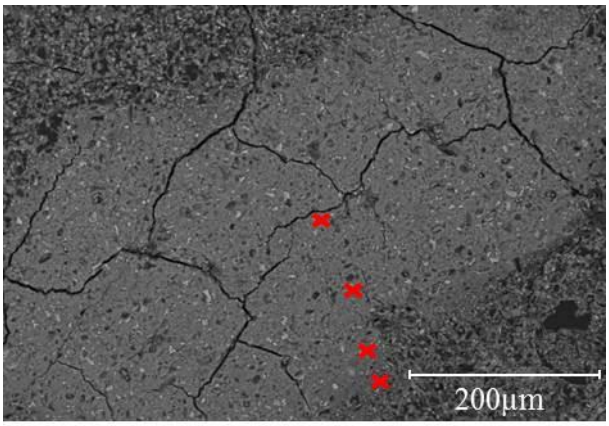

Figure 4.14: *A SEM back-scattered electron image of unmixed cement in the sample of OPC with 10% magnetite. The red crosses indicate the locations of where the elemental point analyses were undertaken.*

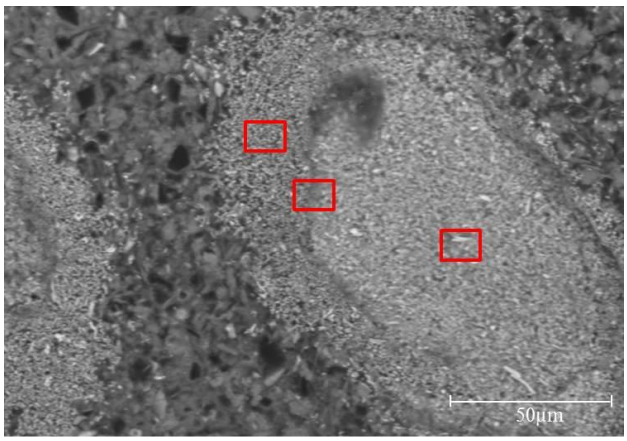

Figure 4.15: *A SEM back-scattered electron image of an unmixed area of magnetite in the sample of OPC with 10% magnetite. The red squares indicate the locations of the area analyses.*

The image and elemental analysis of pure Ultrafin cement, Ultrafin cement with 10% magnetite, and Ultrafin cement with 20% magnetite can be seen in Figure 4.16. Within the pure Ultrafin cement sample the water and cement have been well mixed (Figure 4.16a). From the elemental analysis (Figure 4.16c), the pure Ultrafin cement has a small percentage of iron present, with the iron being evenly distributed throughout the sample (Figure 4.16b). The samples of Ultrafin with 10% magnetite and Ultrafin cement with 20% magnetite are slightly less well mixed than the pure Ultrafin cement sample. This is likely to be a result of hand mixing the cement. Within both of these samples as the percentage of magnetite increases the percentage of iron present also increases. This can be seen from the bar charts in Figure 4.16f and Figure 4.16i. The distribution of iron throughout the samples which contained magnetite is generally evenly dispersed, however there are some areas that contain a higher percentage of iron (Figure 4.16e and Figure 4.16h). These are indicated by areas that are a brighter white in colour.

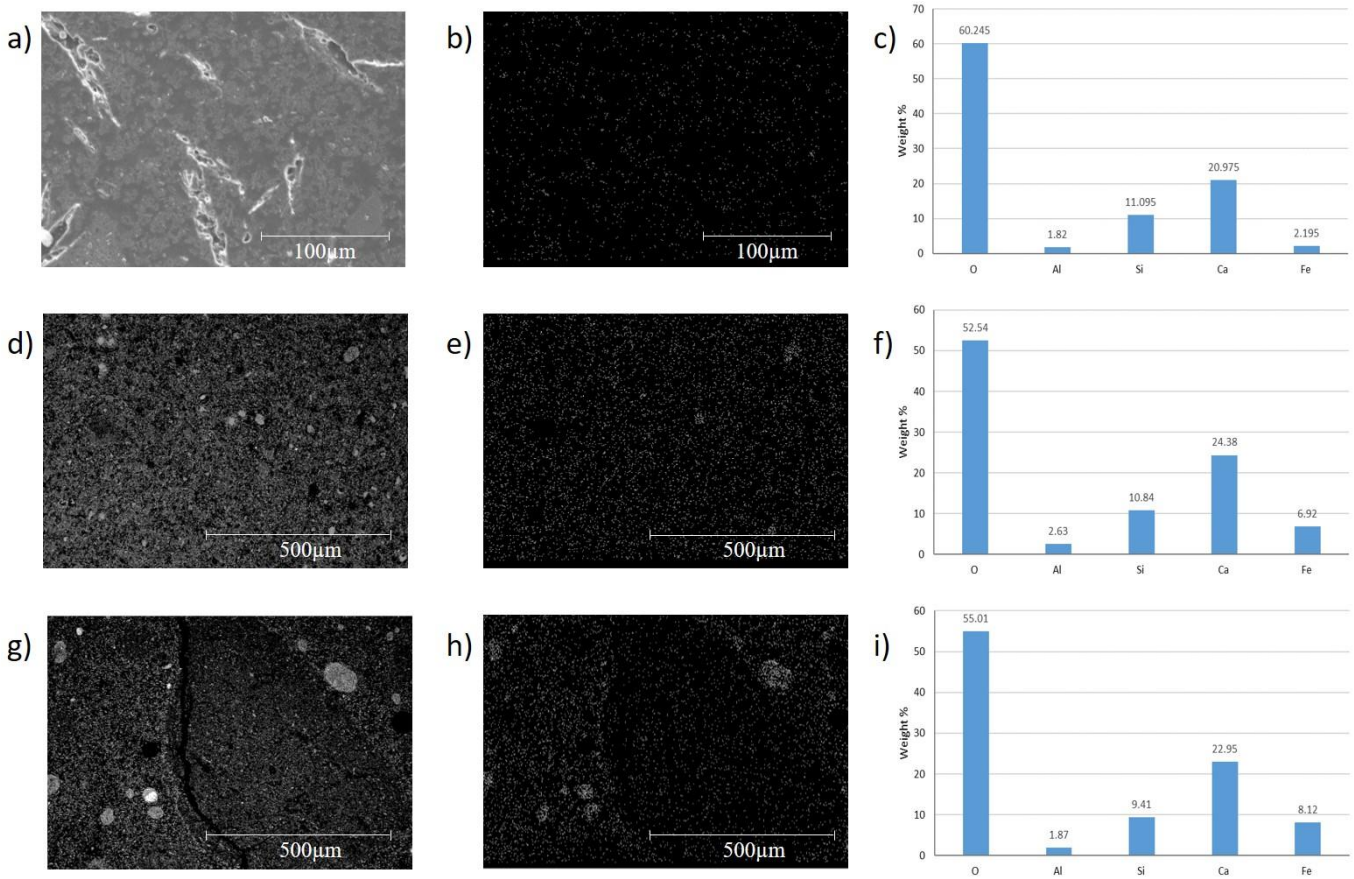

Figure 4.16: *a) Scanning electron image of pure Ultrafin cement, b) elemental distribution of iron within the pure Ultrafin cement sample, c) bar chart of elemental composition of pure Ultrafin cement, d) backscattered electron image of Ultrafin cement with 10% magnetite, e) elemental distribution of iron within the Ultrafin cement with 10% magnetite sample, f) bar chart of elemental composition of Ultrafin cement with 10% magnetite, g) backscattered electron image of Ultrafin cement with 20% magnetite, h) elemental distribution on iron within the Ultrafin cement with 20% magnetite sample, and i) bar chart of elemental composition of Ultrafin cement with 20% magnetite.*

4.2.2.3 Discussion

By closely examining the magnetic cement material, using both optical light microscopy and SEM analysis, the internal features of the material were characterised. The SEM analysis produced an elemental analysis of both the OPC and Ultrafin cement, which identified the similarities and differences between the cements. As expected both of the cements had high proportions of oxygen, calcium, and silicon identified as the main elements. These three elements (alongside hydrogen which cannot be detected here) are generally the main constituents of any cement. They form two of the main mineral phases in cement; alite and belite. Aluminium and iron were also identified within both cements. These elements combine with the calcium and oxygen to form the other two major mineral phases in cement; aluminate and ferrite. Within the pure OPC, there was more aluminium identified than iron, which suggests that a higher proportion of these elements would combine to produce a larger amount of aluminate than ferrite. However, in the pure Ultrafin cement a higher proportion of iron is identified, suggesting that there is a higher proportion of ferrite within the cement, rather than aluminate. There is also less aluminate present within the Ultrafin cement as it is classed as a sulphate resistant cement which requires a low aluminate content (Cementa, 2007).

Throughout the images of both cements, with and without added magnetite, unmixed cement, with what appears to be reaction rims, have been identified. These reaction rims are likely to be a result of the cement hydration reaction. The areas within the centre of the cement particles containing the reaction rims are generally darker in appearance, compared to the lighter edges. The central areas are more likely to contain un-reacted cement as they may not have had the opportunity to be in contact with the water within the mixture, and therefore have not hydrated. The reacted edges of the cement particles are likely to contain the minerals alite and belite, the main products of the hydration reaction, and may explain the lighter colour at the edge of the cement particles.

Cracking within the cement samples can be seen throughout the SEM images of both the OPC and Ultrafin cement mixtures. This cracking does not occur in any particular direction, and is indicative of desiccation cracking. This type of cracking occurs when the cement is drying and shrinks. Since desiccation cracking is present in all of the cement mixtures, this suggests that the addition of magnetite to the cement does not increase the chance of shrinkage as the cement is drying.

The magnetite present in the magnetic cement samples is generally evenly distributed throughout the cement. This can be seen in both the thin section images taken using the optical microscope and in the SEM images. There are however some areas within the cement samples, that contain only magnetite. This could be caused by the magnetic attraction of the magnetite particles to each other, forming clusters of the magnetite particles, or may just be due to poor mixing. Across all of the different cement samples (with and without magnetite), the weight percentage of iron varied (Table 4.4). The data within Table 4.4 was obtained by undertaking three random area elemental analyses for each cement sample. The size of these area analyses was 1.2 mm by 1.2 mm. From this data, the minimum and maximum iron wt% values were recorded, with an average value being calculated from all three area analyses. Within both the pure OPC and Pure Ultrafin cement samples, iron was present in low amounts, and was relatively evenly distributed throughout the samples. In introducing, and then increasing the amount of magnetite within the cement the weight percentage of iron increased. However, the amount of iron present generally did not correspond to the 10% or 20% magnetite added. This is because magnetite is composed of both iron and oxygen (Fe_3O_4) and therefore the oxygen component of the magnetite is detected separately. The maximum weight percentages of iron for both cements with 10% and 20% magnetite, have much increased values as these were taken at points where there was a high concentration of magnetite present.

Table 4.4: *Minimum and maximum and average weight percentages of iron within each cement sample.*

	Minimum wt% of Iron	**Maximum wt% of Iron**	**Average wt% of Iron**
Pure OPC	1.61	1.86	1.70
OPC with 10% Magnetite	4.82	7.16	6.09
OPC with 20% Magnetite	9.42	10.1	9.87
Pure Ultrafin Cement	1.82	2.57	2.20
Ultrafin with 10% Magnetite	6.44	7.34	6.92
Ultrafin with 20% Magnetite	7.04	9.80	8.12

Overall, in undertaking both the optical microscope, and SEM analysis of the OPC and Ultrafin grout mixtures it can be determined that the added magnetite is likely to be present throughout the grout mixture, and does not settle out to the bottom of the grout mixtures. In some areas of the grout mixtures however the magnetite has formed small clumps though this is possibly a result of the method used to mix the grout. This therefore indicates that with the addition of magnetite into the cementitious grout mixtures a usable magnetic grout (with the magnetite distributed throughout) could be developed.

4.3 Magnetic Cement Grout Properties

Following on from the magnetic susceptibility testing, and thin section and SEM analysis of the magnetic cement material, testing of the engineering properties of the magnetic cement grout were undertaken. This was done to determine whether the addition of magnetite, and also superplasticiser and stabilising agent resulted in any changes that would make the grout unusable in civil engineering practice.

4.3.1 Grout Mixtures

This section will detail the different cement grout mixtures tested within Table 4.5. These different cement grout mixtures represent the evolution of the properties testing of the magnetic cement grout. Initially, the properties of the pure cement grout mixtures were determined to provide a baseline for the experiments. Magnetite was then added to ascertain how this affected the properties, followed by the addition of superplasticiser and stabilising agents. In adjusting the water to solids ratios for these magnetic cement grout mixtures, the optimal engineering properties could be established.

Table 4.5: *Grout mixtures used within the cement properties experiments.*

Grout Mix	Description (Batch of Cement and Magnetite)	Mass of Cement (g)	Mass of Water (g)	Mass of Superplasticiser (SA) (g)	Mass of Stabilising Agent (SA) (g)	Mass of Magnetite (g)	% Magnetite	Total Mass of Water (g)	Total Mass of Solids (g)	Water to Cement Ratio (WCR)	Water to Solids Ratio (WSR)
63	Pure OPC (2)	2500	1250	0	0	0	0	1250	2500	0.5	0.5
64	OPC (2) + 5% Magnetite (2)	2500	1312.5	0	0	125	5	1312.5	2625	0.53	0.5
65	OPC (2) + SP + SA	2000	760	8	80	0	0	800	2000	0.4	0.4
66	OPC (2) + 5% Magnetite (2) + SP + SA	2000	798	8.4	84	100	5	840	2100	0.42	0.4
67	OPC (2) + 10% Magnetite (2) + SP + SA	2000	836	6.6	88	200	10	880	2200	0.44	0.4
68	Pure Ultrafin (2)	1875	1250	0	0	0	0	1250	1875	0.67	0.67
69	Ultrafin (2) + 5% Magnetite (2)	1875	1312.5	0	0	93.75	5	1312.5	1968.75	0.67	0.67
70	Ultrafin (2) + SP + SA	1875	1187.5	12.5	125	0	0	1250	1875	0.67	0.67
71	Ultrafin (2) + SP + SA	1875	890.62	9.38	93.75	0	0	937.5	1875	0.5	0.5
72	Ultrafin (2) + SP + SA	2000	904.76	9.52	95.24	0	0	952.38	2000	0.48	0.48
73	Ultrafin (2) + 5% Magnetite (2) + SP + SA	2000	950	10	100	100	5	1000	2100	0.5	0.48
74	Ultrafin (2) + 10% Magnetite (2) + SP + SA	2000	995.24	10.48	104.76	200	10	1047.62	2200	0.52	0.48

Grout Mix	Description (Batch of Cement and Magnetite)	Mass of Cement (g)	Mass of Water (g)	Mass of Superplasticiser (SA) (g)	Mass of Stabilising Agent (SA) (g)	Mass of Magnetite (g)	% Magnetite	Total Mass of Water (g)	Total Mass of Solids (g)	Water to Cement Ratio (WCR)	Water to Solids Ratio (WSR)
75	Pure OPC (2)	300	150	0	0	0	0	150	300	0.5	0.5
76	Pure OPC (2)	300	120	0	0	0	0	120	300	0.4	0.4
77	Pure OPC (2)	500	175.44	0	0	0	0	175.44	500	0.35	0.35
78	Pure OPC (2)	300	90.1	0	0	0	0	90.1	300	0.3	0.3
79	OPC (2) + SP + SA	200	76	0.8	8	0	0	80	200	0.4	0.4
80	OPC (2) + 5% Magnetite (3)	500	262.5	0	0	25	5	262.5	525	0.53	0.5
81	OPC (2) + 5% Magnetite (3) + SP + SA	200	79.8	0.84	8.4	10	5	84	210	0.42	0.4
82	Pure Ultrafin (2)	200	133.33	0	0	0	0	133.33	200	0.67	0.67
83	Ultrafin (2) + SP + SA	500	226.19	2.38	23.81	0	0	238.01	500	0.48	0.48
84	Ultrafin (2) + 5% Magnetite (3)	500	350	0	0	25	5	350	25	0.7	0.67
85	Ultrafin (2) + 5% Magnetite (3) + SP + SA	200	95	1	10	10	5	100	210	0.5	0.48
86	OPC (2) + SP + SA	300	114	1.2	12	0	0	120	300	0.4	0.4
87	OPC (2) + SP + SA	500	142.5	0.75	15	0	0	150	500	0.3	0.3
88	OPC (2) + SP + SA	500	142.5	1.125	15	0	0	150	500	0.3	0.3
89	OPC (2) + SP + SA	500	142.5	1.5	15	0	0	150	500	0.3	0.3

Grout Mix	Description (Batch of Cement and Magnetite)	Mass of Cement (g)	Mass of Water (g)	Mass of Superplasticiser (SA) (g)	Mass of Stabilising Agent (SA) (g)	Mass of Magnetite (g)	% Magnetite	Total Mass of Water (g)	Total Mass of Solids (g)	Water to Cement Ratio (WCR)	Water to Solids Ratio (WSR)
90	OPC (2) + SP + SA	500	118.75	1.25	12.5	0	0	125	500	0.25	0.25
90	OPC (2) + 5% Magnetite (3) + SP + SA	300	119.7	126	12.6	15	5	126	315	0.42	0.4
92	Pure Ultrafin (2)	300	200	0	0	0	0	200	300	0.67	0.67
93	Pure Ultrafin (2)	500	250	0	0	0	0	250	500	0.5	0.5
94	Pure Ultrafin (2)	500	200	0	0	0	0	200	500	0.4	0.4
95	Ultrafin (2) + 5% Magnetite (3) + SP + SA	300	142.5	1.5	15	15	5	150	315	0.5	0.48

4.3.2 Magnetic Cement Grout Properties Testing

This section will detail the methods used to determine the engineering (grout) properties of the magnetic cement followed by the results of these experiments.

4.3.2.1 Flowability

4.3.2.1.1 Method

The flowability of the cement grout was measured using a flow cone following ASTM International Standard C939 (ASTM, 2010). The test was undertaken to determine how the flowability of the cement grout changed with the addition of magnetite and

cement additives. The flow cone was mounted in a stand constructed of brick and a thick plastic sheet with a circle cut out in the centre to enable the cone to sit level (Figure 4.17a). Before the cement testing could commence, the cone was calibrated. This was undertaken by closing the outlet of the cone with a stopper and then introducing 1725mL of water into the cone. The point gauge was then adjusted to indicate the level of the water (Figure 4.17b). The water was then allowed to drain out of the cone.

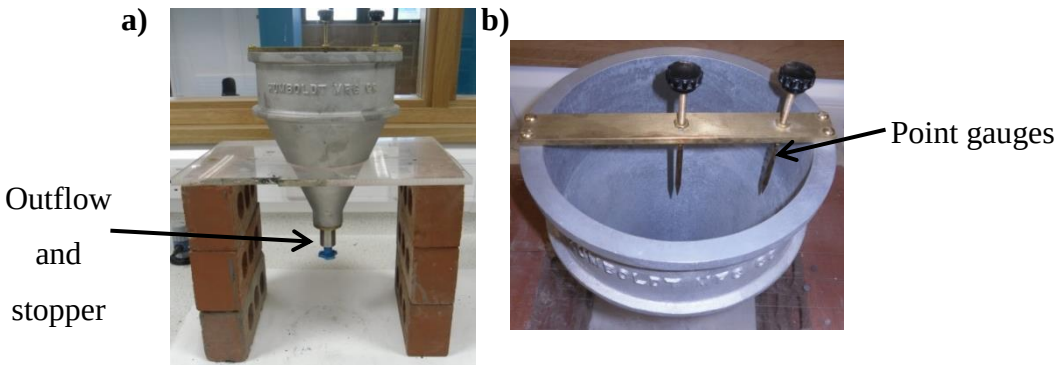

Figure 4.17: *(a) The flow cone mounted in its stand, (b) The location of the point gauges within the flow cone.*

For each flowability test, the cement mixture was introduced into the previously moistened flow cone, up to the level of the point gauge. The stopper was then removed from the outflow end of the flow cone and a stopwatch started simultaneously to measure the efflux time of the cement mixture. The stopwatch was stopped at the first break in continuous flow of the cement observed at the outlet. The time indicated by the stopwatch is the time of efflux of the cement mixture. This process was then repeated a further two times on the same cement mixture to ensure repeatability. In practice an efflux time of 30 – 35 seconds is desirable (personal communication A. Henderson, BAM Richies, 7th February 2013).

4.3.2.1.2 Results

For all the OPC and Ultrafin cements the flow cone test was repeated on the same sample three times with the values reported being the average of these three repeats.

The grout mixtures used in these experiments can be found in Table 4.5 and are the grout mixtures numbered 63 to 74.

The flowability results undertaken of the different magnetic cement mixtures (numbers 63 to 67) containing OPC have a range of flow time from 24 seconds to 71 seconds (Figure 4.18). However, the majority of the flow times fall between 30 and 45 seconds. Pure OPC was tested with a water to solids ratio of 0.5, and this produced a range of flow results between 29 and 45 seconds across three different grout batches, with an average flow time being 36 seconds. A grout mixture of OPC with 5% magnetite was also tested using a water to solids ratio of 0.5. The mixture of OPC with 5% magnetite has a larger range of flow values from 36 seconds to 71 seconds, with the higher flow value being a result of that batch of grout mixture beginning to set more rapidly than the other batches.

To investigate the effect of an increasing magnetite percentage on the flow of the grout mixture, grout mixtures containing superplasticiser and stabilising agent were examined at a water to solids ratio of 0.4 with 0% magnetite, 5% magnetite, and 10% magnetite. From Figure 4.18 it can be seen that the majority of the grout mixtures recorded flow times between 30 and 40 seconds which would be workable in practice.

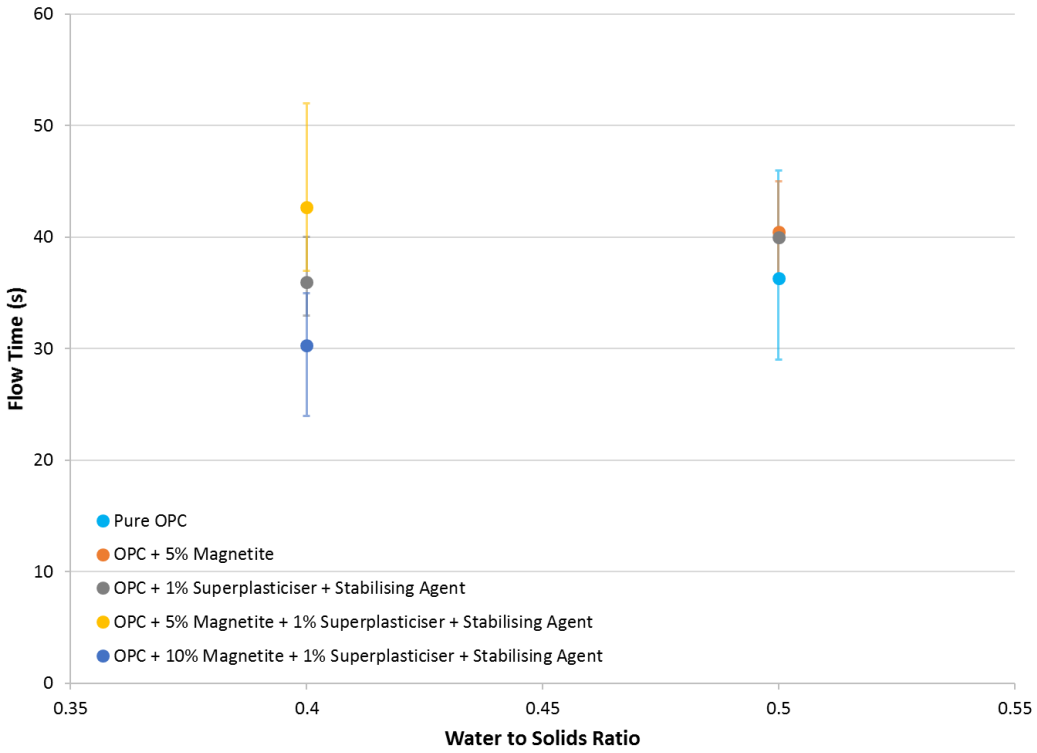

Figure 4.18: *Flow times of OPC grout mixtures with differing water to solids ratios.*

The flowability results undertaken of the different magnetic grout mixtures containing Ultrafin cement (numbers 68 to 74) have a range of flow times from 13 seconds to 50 seconds (Figure 4.19). The pure Ultrafin cement grout mixture was tested with a water to solids ratio of 0.67, and this produced flow values between 38 and 48 seconds. The water to solids ratio of 0.67 was chosen for the Ultrafin cement after experimentation with several different water to solids ratios (including the water to solids ratio of 0.5 which was used for the pure OPC) determined that this gave the optimum properties for the pure Ultrafin cement. To compare the effect of superplasticiser and stabilising agent on the Ultrafin cement, a grout mix was tested at the same water to solids ratio (0.67) as the pure Ultrafin. This grout mixture gave a much faster rate of flow. By decreasing the water to solids ratio for this grout mixture (to 0.5 and 0.48), the flow time increases as expected. This was also seen with the OPC grout mixtures. A grout mixture of Ultrafin with 5% magnetite was also tested at a water to solids ratio of 0.67, with the results gained being very similar to the pure Ultrafin grout mixtures.

To investigate the effect of an increasing magnetite percentage on the flow of the grout mixture, grout mixtures containing superplasticiser and stabilising agent were examined at a water to solids ratio of 0.48 with 0% magnetite, 5% magnetite, and 10% magnetite. From Figure 4.19, all of the grout mixtures had similar flow times which indicates that the addition of magnetite does not have an effect on the flow times apart from increasing the solids present in the grout mixture.

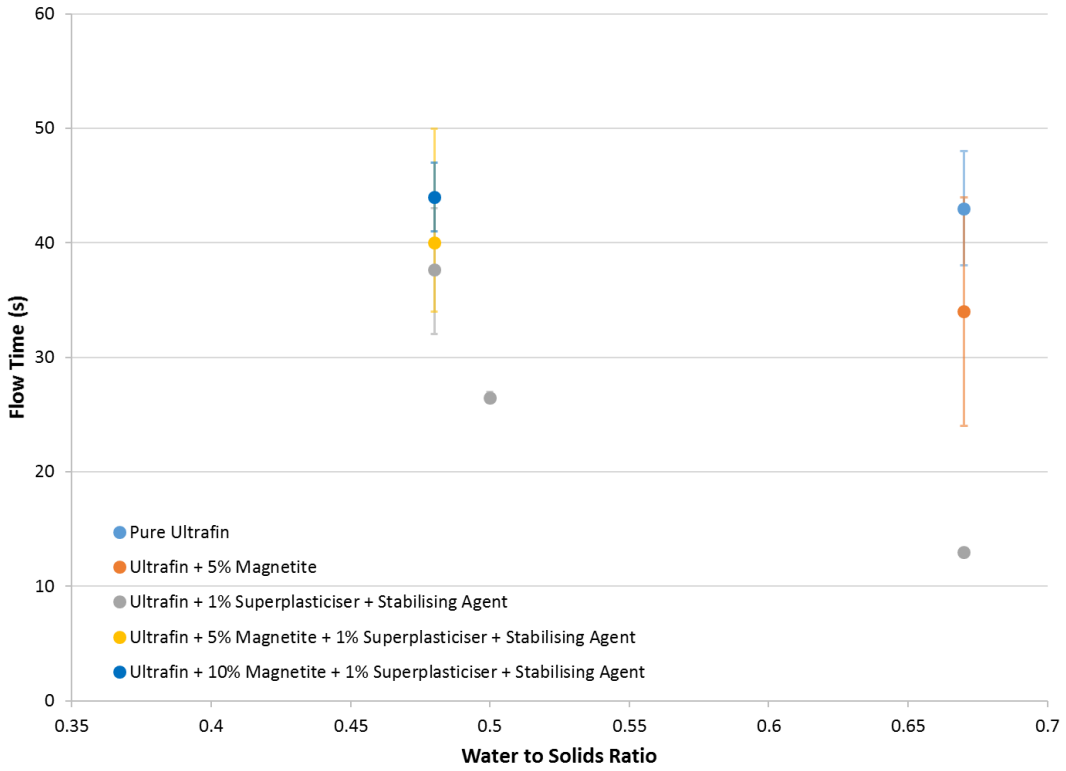

Figure 4.19: *Flow times of Ultrafin grout mixtures with differing water to solids ratios.*

4.3.2.2 Bleed

4.3.2.2.1 Method

The bleed of the cement mixtures was measured to determine the amount of separation occurring of the water from the solid particles in the grout mixture. Bleed was measured following the ASTM International Standard C232/C232M - 12 (ASTM,

2012). To undertake a bleed measurement, a 1000mL graduated cylinder was attached to a clamp stand with clamps holding the cylinder at both the top and bottom (Figure 4.20). This ensured that the cylinder would be level at all times.

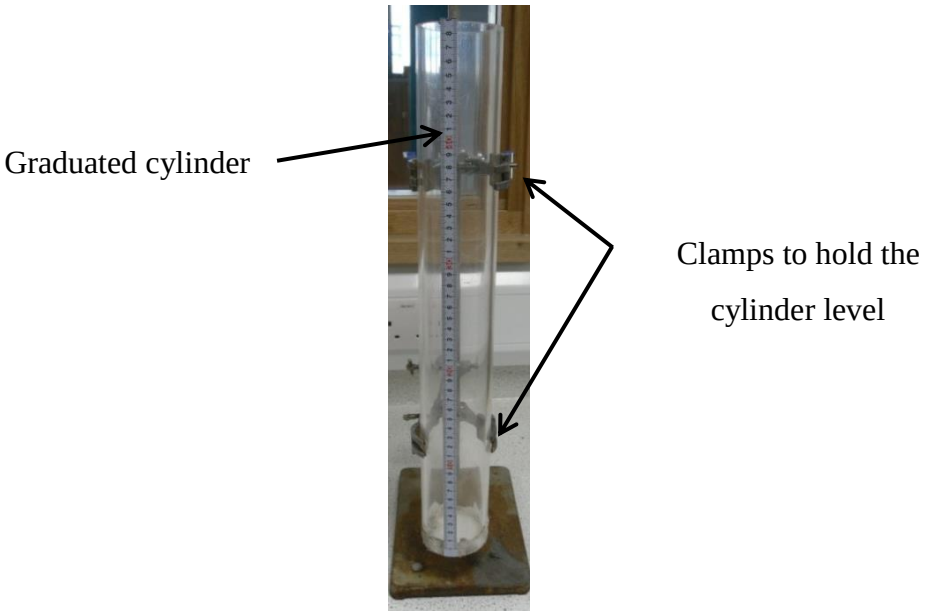

Figure 4.20: *The graduated cylinder used for the bleed tests.*

Once the cement mixture had been produced for the test, it was introduced into the cylinder until the volume of the sample reached a level of 800 ± 10 mL. The top of the cylinder was then covered to prevent any evaporation of the bleed water occurring. Readings of the height of the bleed water (the difference between the top of the cement and the top of the bleed water), were then taken at 15 minute intervals for 2 hours, or until two successive readings showed no further bleeding had occurred. At the conclusion of the test, the bleed water was decanted into a 25 mL graduated beaker by drawing the water off with a pipette. The final volume of the bleed water was recorded to the nearest 0.5 mL. In practice it is desirable that a grout mixture should not exhibit bleed < 1% of the total cement volume (personal communication, A. Henderson, BAM Richies, 7th February 2013), as this ensures that the grout mixture does not have a large amount of separation.

4.3.2.2.2 Results

Figure 4.21 presents the percentage bleed of OPC grout mixtures recorded. The quantities for the grout mixtures used can be found in Table 4.5 and correspond to grout mixture numbers 63 to 67. For each grout mixture, three tests were run with the average, minimum, and maximum values plotted in Figure 4.21. Grout mixtures at two different water to solids ratios 0.5 and 0.4 were tested as these gave flow times within the range of 30 and 45 seconds (Figure 4.18), meaning that they would be workable in practice. The Pure OPC and OPC + 5% magnetite tested (wsr = 0.5) both exhibited a higher percentage of bleed than the grout mixes tested at a water to solids ratio of 0.4. This is to be expected as they contained higher amounts of water in the grout mixture. Furthermore, all grouts tested at a water to solids ratio of 0.4 contained 10% stabilising agent which acts to reduce the bleed. The addition of 5% magnetite to the OPC slightly reduced the overall bleed exhibited, with both the Pure OPC and OPC + 5% magnetite resulted in no further increase in the volume of bleed water after 105 minutes. By comparing the three grout mixes, all prepared at a water to solids ratio of 0.4 (OPC + SP + SA, OPC + 5% + SP + SA, OPC + 10% + SP + SA) it is evident that the percentage of magnetite does not affect the overall bleed exhibited by the grout mix. The percentage bleed for all three was well below the maximum amount of 1% after 2 hours, used as a threshold in industrial practice.

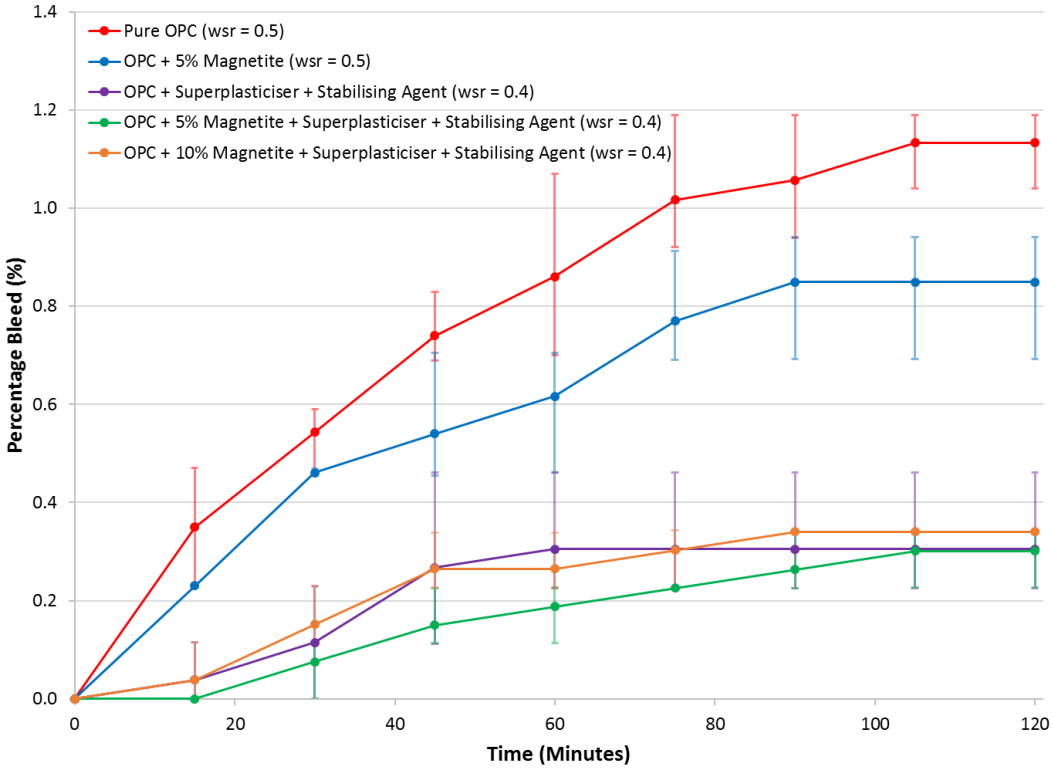

Figure 4.21: *Percentage bleed observed over 2 hours for OPC grout mixes.*

Figure 4.22 presents the bleed results for different Ultrafin grout cement mixtures over 2 hours. The quantities for the grout mixtures used can be found in Table 4.5 and correspond to grout mixture numbers 68 to 72. For each grout mixture, three tests were run with the average, minimum, and maximum values plotted in Figure 4.22. Overall, the Ultrafin cement produced much less bleed water than the OPC mixtures. Grout mixes at two different water to solids ratios of 0.67 and 0.48 were tested as these gave flow times within the range of 30 to 45 seconds (Figure 4.19), meaning that they would be workable in practice. The pure Ultrafin and Ultrafin + 5% magnetite tested (wsr = 0.67) both produced a higher percentage of bleed than the grout mixes with a water to solids ratio of 0.48. However, due to the higher amount of water in the grout mix this result was expected. Both of these grout mixes showed no further bleed after 30 minutes had elapsed. The further three grout mixes (Ultrafin + SP + SA, Ultrafin + 5% magnetite + SP + SA, and Ultrafin + 10% magnetite + SP + SA) tested at a water to solids ratio of 0.48 all contained 10 % stabilising agent, which acts on the grout mixture to reduce the amount of bleed. In all three cases the percentage bleed after 2 hours was 0 %.

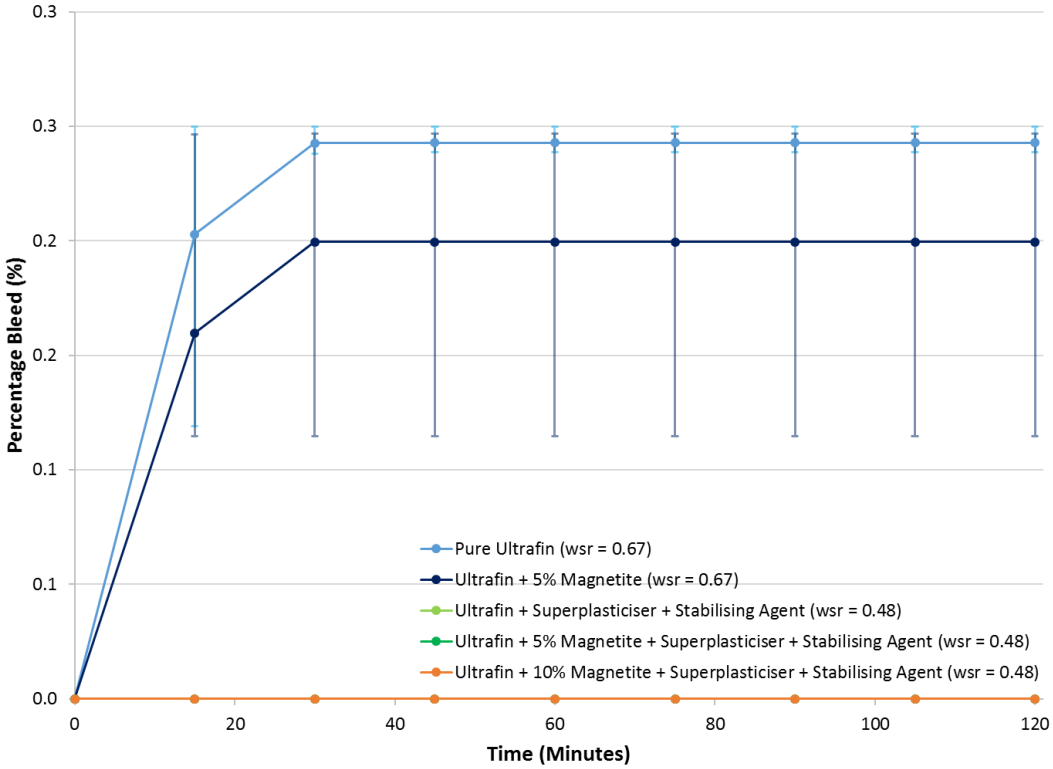

Figure 4.22: *Percentage bleed observed over 2 hours for Ultrafin grout mixes.*

4.3.2.3 Setting Time

4.3.2.3.1 Method

The setting time of the cement mixes were measured using a Vicat Needle as outlined in BS EN 196-3.2005 (BSI, 2005). The setting time of the cement mixes was tested to determine whether the addition of magnetite resulted in a change to the length of the setting time occurring.

The initial setting time is defined as the time at which the Vicat needle penetrates 6mm ± 3 mm into the cement from the top of the Vicat mould. Figure 4.23 gives a schematic diagram of the Vicat apparatus used in these experiments. The Vicat mould is shaped like a truncated cone and is 40 mm deep with an internal diameter of 75 mm. This mould was filled with the cement mixture. The mould was initially filled to excess and tapped to ensure that no air voids were present. The excess cement mixture was

then scraped off, leaving the cement in the mould with a smooth upper surface. The filled Vicat mould and base plate were then placed in a bowl with a small vial of water and covered in cling film to ensure that the humidity remained high during the setting of the cement. After a few hours had elapsed, the mould and the base plate were placed under the Vicat needle and the needle lowered until it was just in contact with the top of the cement mixture. The needle was maintained in this position for a few seconds to ensure that the Vicat apparatus was at rest. The needle was then released quickly, penetrating vertically into the cement mixture. The scale was read after the penetration had ceased, or 30 seconds after the release of the needle. This process was then repeated with each penetration occurring not less than 8 mm from the rim of the mould or 5 mm from each other. This repeated penetration was undertaken initially at 15 minute intervals, before the frequency was increased as the cement began to set. Between the penetrations the mould was kept in the bowl wrapped in cling film to ensure that the humidity remained high. The penetrations were repeated until penetration reached 6 ± 3mm.

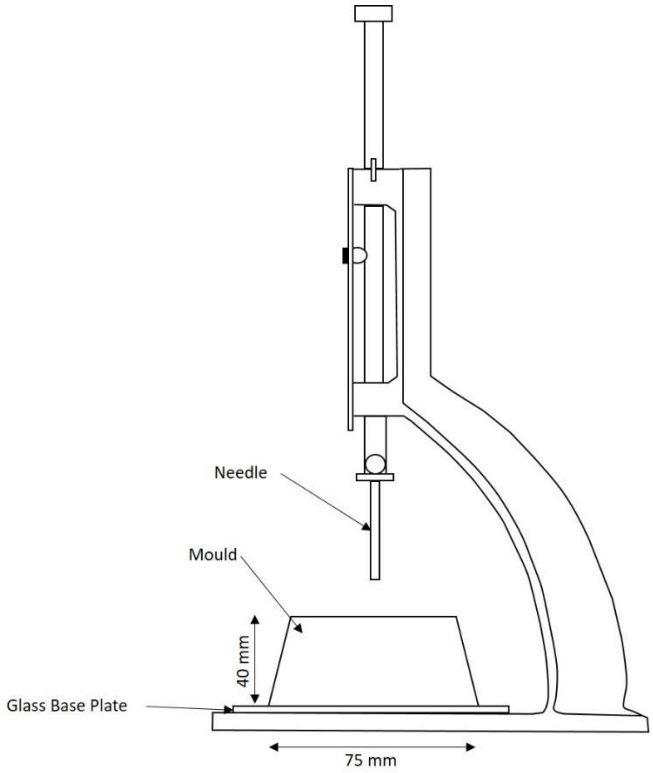

Figure 4.23: *A schematic diagram of the Vicat needle apparatus (After BSI, 2007).*

4.3.2.3.2 Results

Initial setting tests were undertaken on a range of mixtures of OPC (Figure 4.24). The quantities for the grout mixtures used within the initial setting time experiments can be found in Table 4.5 and correspond to grout mixture numbers 73 to 93. An ideal initial setting time for a cement grout is up to around 4 hours as this gives the time during which the cement remains plastic and is able to be mixed, transported, and injected into the subsurface. The OPC mixture that had the longest initial setting time of 260 minutes was with the water to solids ratio of 0.5. The initial setting time then reduced as the water to solids ratio reduced, however this was expected as the higher water content increases the setting time. An OPC mixture containing 5% magnetite was then tested with a water to solids ratio of 0.5. This produced an initial setting time that was essentially the same as the setting time of the pure OPC.

The addition of superplasticiser and stabilising agent to the OPC mixtures, generally gave an increased initial setting time. A mixture of OPC with 1% superplasticiser, and stabilising agent with a water to solids ratio of 0.4 gave an initial setting time of 375 minutes, whereas OPC with 5% magnetite, 1% superplasticiser, and stabilising agent at the same water to solids ratio gave an initial setting time of 515 minutes. This setting time however, is much too long for practical purposes.

To shorten the initial setting time achieved with the OPC mixtures containing superplasticiser and stabilising agent, the amount of superplasticiser was reduced. In decreasing the percentage of superplasticiser within the mixture from 1% to 0.5% the initial setting time reduced.

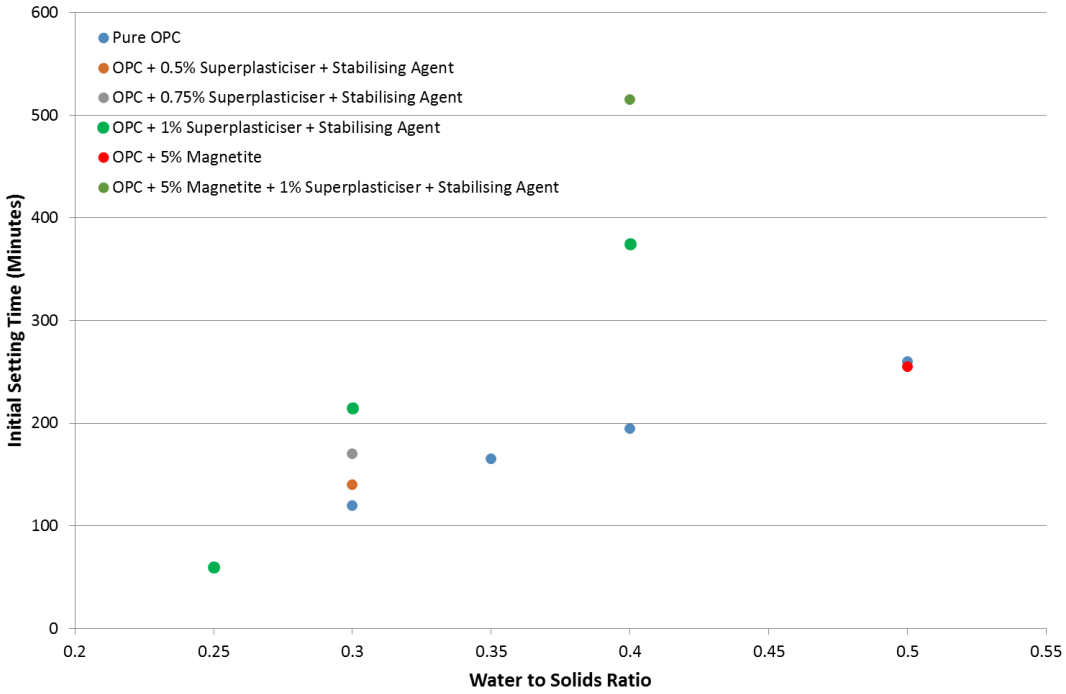

Figure 4.24: *Initial setting time of different mixtures of OPC.*

Initial setting time tests were also undertaken on a range of mixtures using Ultrafin cement (Figure 4.25). These mixtures were chosen as they produced workable grouts in the flow and bleed experiments. The pure Ultrafin cement was tested with three different water to solids ratios, 0.67, 0.5, and 0.4. In increasing the amount of water present within the cement mixture, the initial setting time increased as expected. The addition of 5% magnetite to the Ultrafin cement resulted in a slight increase in the initial setting time. This mixture had a water to solids ratio of 0.67.

Superplasticiser and stabilising agent were also added to the Ultrafin cement. The mixture of Ultrafin cement with 1% superplasticiser and stabilising agent was tested with a water to solids ratio of 0.48. This mixture recorded an initial setting time of 325 minutes. A mixture of Ultrafin cement with 5% magnetite, 1% superplasticiser and stabilising agent was also tested with a water to solids ratio of 0.48. This mixture recorded an initial setting time that was longer than the same mixture without the magnetite added. This is likely to be because of the lower amount of cement within the grout mixture.

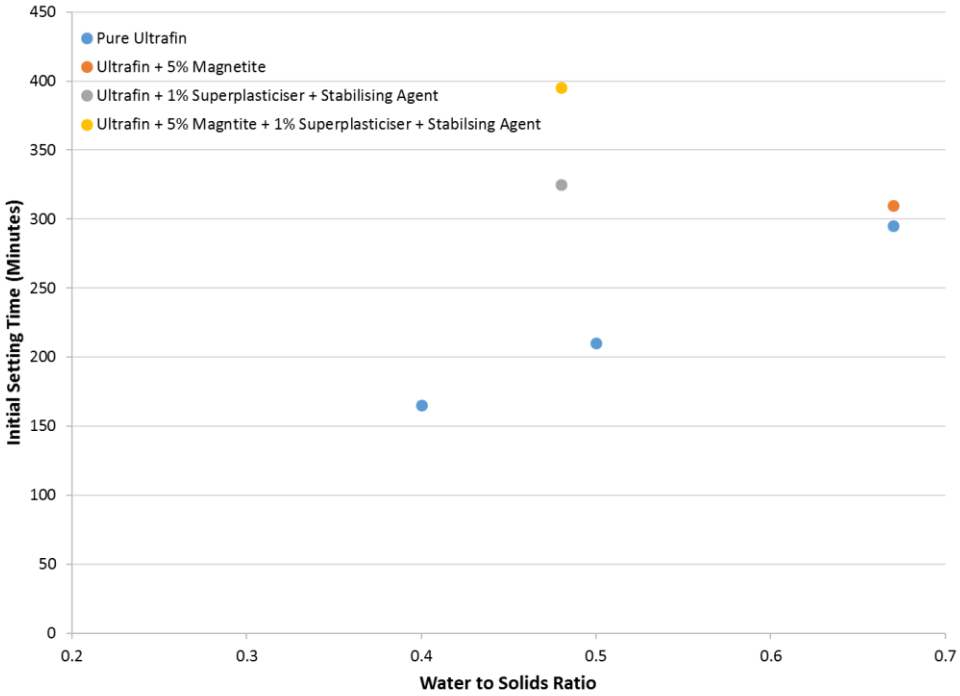

Figure 4.25: *Initial setting time of different mixtures of Ultrafin cement.*

4.3.2.4 Temperature

4.3.2.4.1 Method

The samples to test temperature variation within the magnetic cement were prepared following BS EN 196-7:2007 Part 7: Methods of taking and preparing samples of cement (BSI, 2007).

To take temperature measurements of the cement mixtures a temperature probe was used to take readings as the cement cured. This was undertaken by decanting the cement mixture into a plastic cup. The plastic cup held a maximum volume of 122 mL. A plastic tube was then placed into the centre of the cement mixture with the purpose of protecting the temperature probe from the cement. The plastic cup and its contents were then placed inside an insulated mug located within an insulated box in a cool box. The layers of insulation that these vessels provided ensured that the recorded temperature was the actual temperature of the cement mixture and was not influenced by changes in the temperature of the surrounding environment. The temperature probe

was then lowered into the plastic tube located in the centre of the cement mixture. A rubber bung was then placed in position over the cement mixture and all of the lids closed on both the insulated box and the cool box. Figure 4.26 shows a schematic diagram of the temperature experiment setup. To record the temperature of the cement as it cured the software TEMPer V24.4.5 was used. This software was set to take a temperature measurement at 10 minute intervals. The measurements were undertaken for around 50 hours, or until the cement temperature returned to room temperature. In undertaking temperature measurements of different grout mixtures, the effect of adding magnetic minerals, superplasticiser and stabilising agent on the cement curing temperature can be determined. The effect on curing temperature of varying the water content was also investigated. The curing temperature of the cement mixture affects how the strength of the material develops.

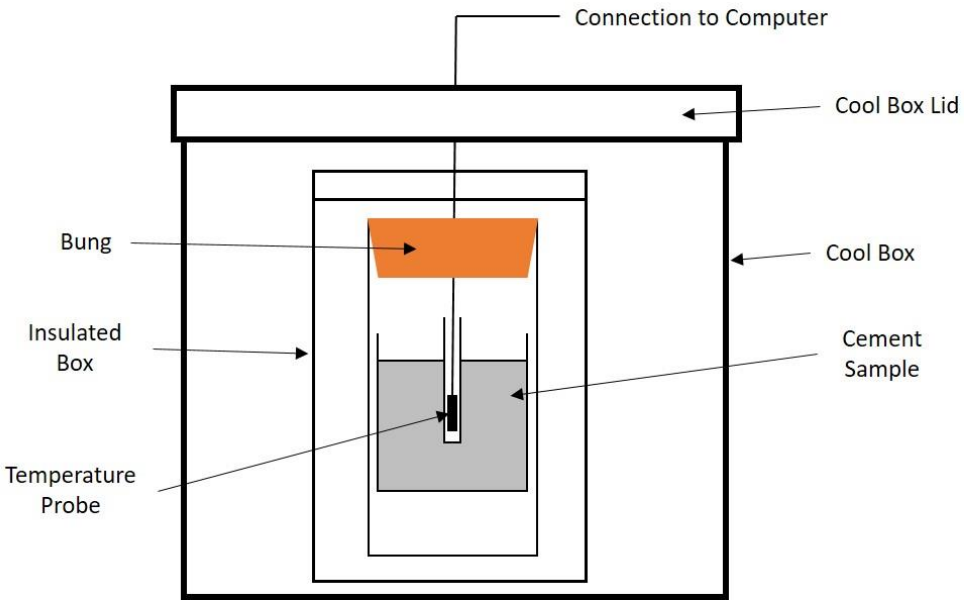

Figure 4.26: *Schematic diagram of the setup for the temperature experiments.*

Once recorded, temperature curves can be compared to the stages of the well-known general heat evolution curve of hydrating cements (Figure 4.27). The first stage of the cement heat evolution curve, occurs due to onset of the initial reaction, and can be seen as an initial increase in temperature followed by a temperature drop. This is then followed by a period of slow temperature decline, then rapid temperature rise (the acceleration period, Figure 4.27). The final stage is the decelerating period. Within

this stage the temperature of the cement mixture decreases, rapidly at first, before levelling off.

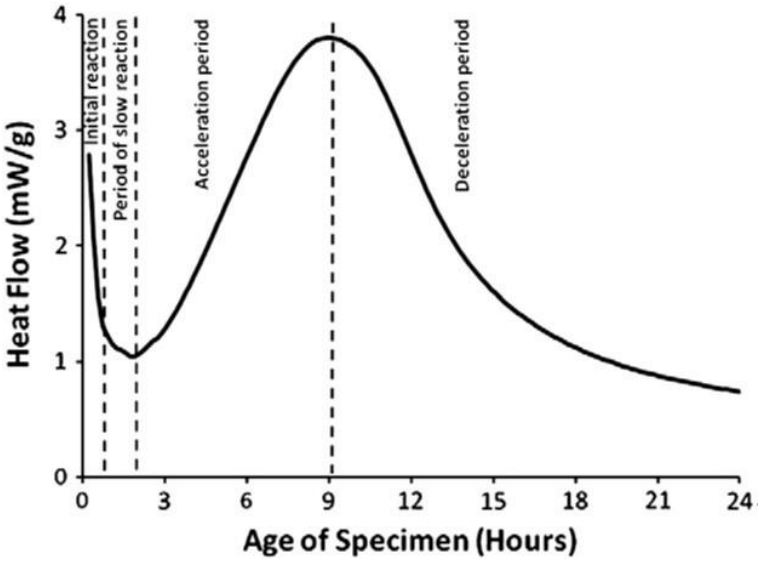

Figure 4.27: *An example of a heat evolution curve for cement (From Bullard et al., 2011).*

4.3.2.4.2 Results

The temperature testing was carried out on different mixtures of OPC. The temperature change within the cement is due to the heat of hydration of the cement, i.e. the hydration reactions occurring. To determine the temperature changes due solely to variations in the background temperature, a blank test was undertaken (i.e. without any cement sample present). Figure 4.28 shows the comparison of the background temperature recorded against a sample of pure OPC. This shows that the background temperature did fluctuate by around 1 degree over a 3-day period, but clearly shows that the setup is suitable for measuring the temperatures recorded during hydration of the OPC cement. The quantities for the grout mixtures used within the temperature experiments can be found in Table 4.5 and correspond to grout mixture numbers 73 to 83.

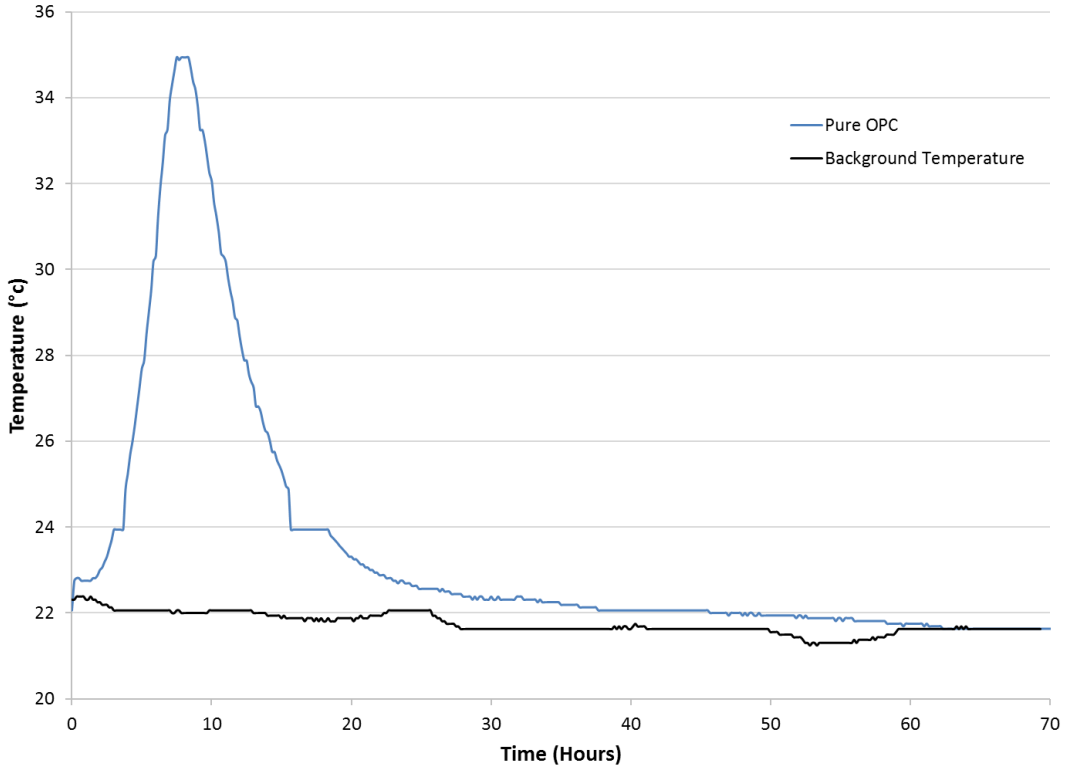

Figure 4.28: *A comparison of the background temperature against the temperature recorded for a sample of pure OPC.*

Pure OPC was tested with mixtures containing the following water to solids ratios – 0.5, 0.4, 0.35, and 0.3 (Figure 4.29). Two volumes of cement samples were tested (74 mL and 122 mL), to determine whether a greater cement mass present in the larger cement sample would result in higher temperatures. The cement mixture with the volume of 74 mL, and with the water to solids ratio of 0.5 (Figure 4.29a), recorded the lowest maximum temperature. At this volume, as the water to solids ratio decreases the maximum temperature which the cement mixtures reached increased. This is because the lower water to solids ratios contain more cement, leading to a higher amount of heat being generated. The shape of the temperature curves for all of the cement mixes follow the same trend.

Figure 4.29b presents the temperature results of the larger cement mixture (122 mL). With this increase in size the peak temperatures of all the cement mixtures has increased, however the same trend can be seen as with the previous smaller cement volume. The mixture with a 0.5 water to solids ratio has the lowest maximum

temperature (38.06°C), and the 0.3 water to solids ratio mixture recorded the highest (50.5°C). The increase in temperature for all the cement mixtures tested is likely to be a result of the increase in cement mass present in the sample, leading to a larger heat of hydration reaction, and therefore increased peak temperatures.

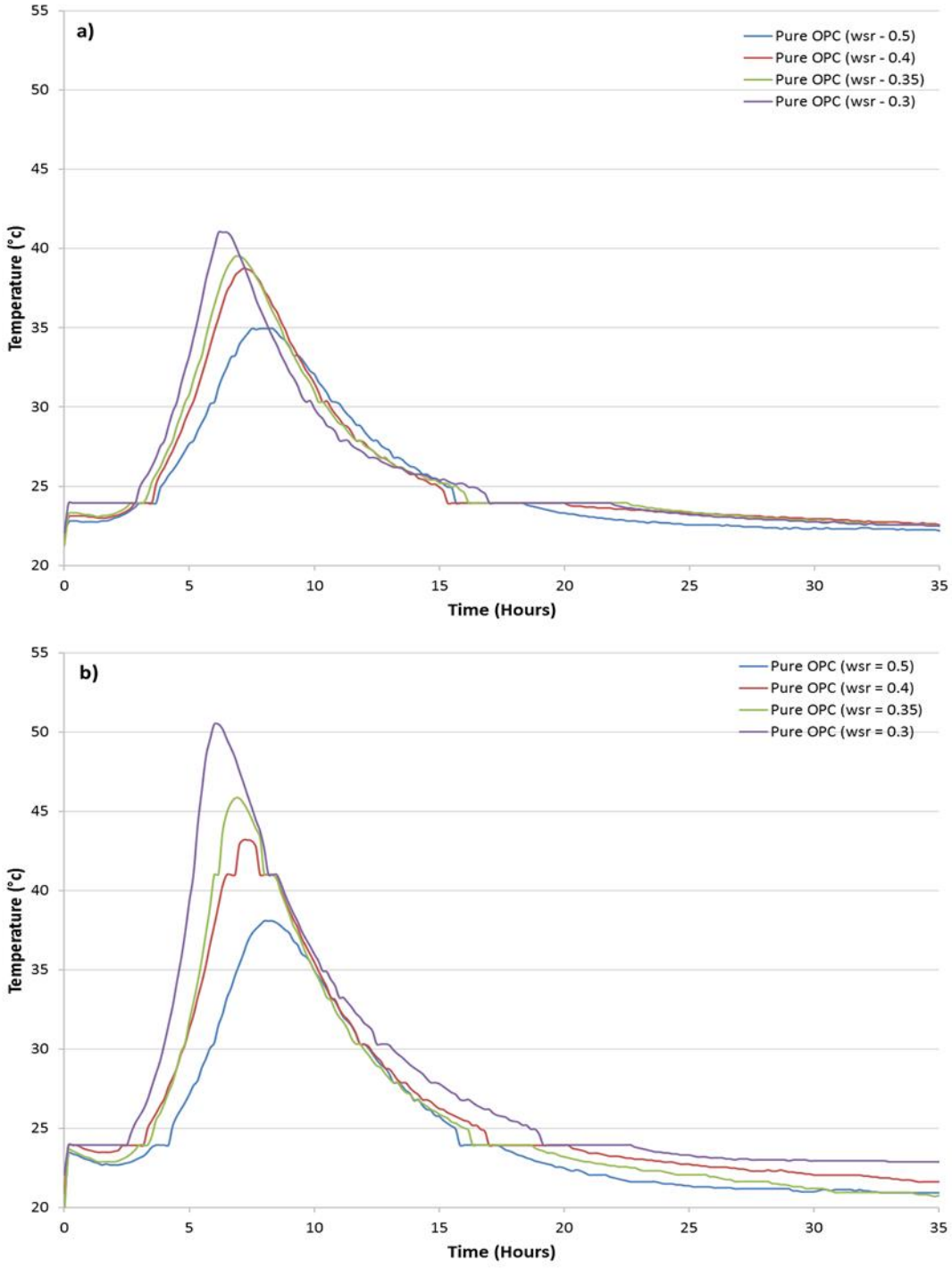

Figure 4.29: *a) Temperature curves of OPC grout mixtures with differing water to solids ratios with a volume of 74 mL, and b) Temperature curves of OPC grout mixtures with differing water to solids ratios with a volume of 122 mL.*

Figure 4.30 presents the temperature results of OPC grout mixtures. OPC with 5% magnetite was tested with a water to solids ratio of 0.5. This test resulted in a lower maximum temperature being achieved than with pure OPC. The maximum temperature recorded for this mixture was 33.25°C. This is due to some of the cement within the mixture being replaced with magnetite to maintain the water to solids ratio of 0.5. The temperature curve for this magnetic cement mixture did however follow a similar shaped trend to that which had been recorded for the pure OPC mixture. Additionally, cement mixtures containing superplasticiser and stabilising agent were also tested. These cement mixtures exhibit a delay in the peak temperature being reached of around 5 hours compared to the cement mixtures that do not contain superplasticiser and stabilising agent. This is because these admixtures delay the hydration reactions within the cement, which delays the occurrence of the peak reaction temperature. The OPC with superplasticiser and stabilising agent mixture recorded a peak temperature of 41°C, whereas the OPC with 5% magnetite, superplasticiser and stabilising agent recorded a peak temperature of 36°C.

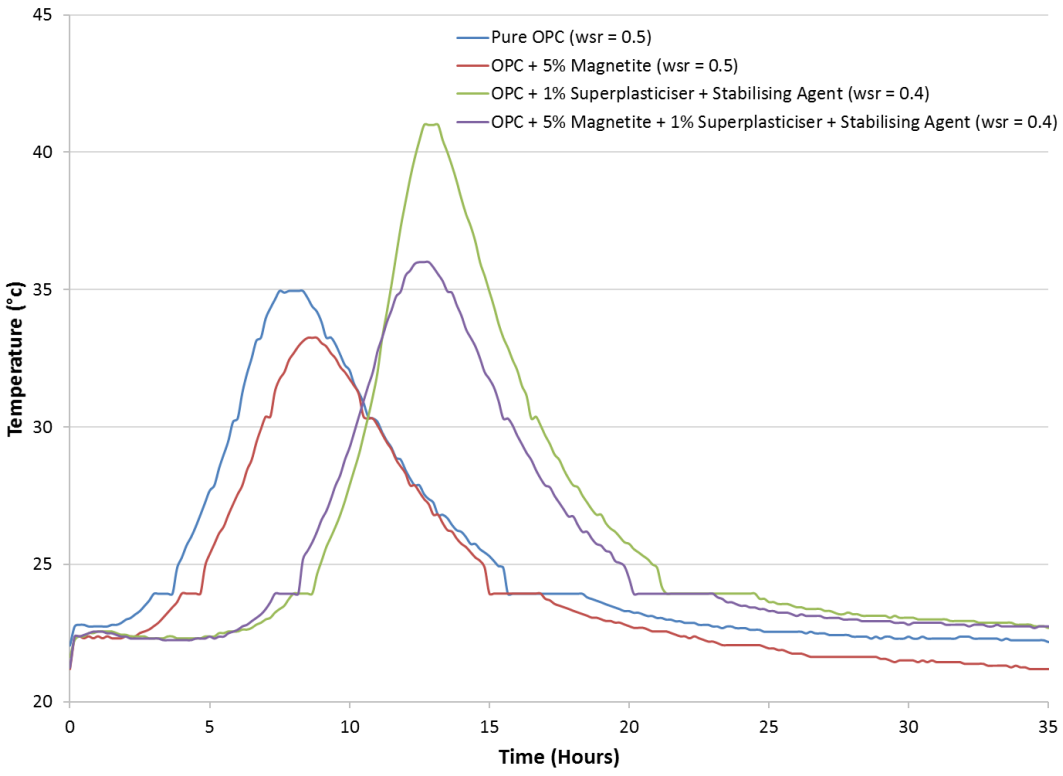

Figure 4.30: *Temperature curves for a range of different mixtures of OPC.*

Figure 4.31 presents the temperature curves of several different mixtures of Ultrafin cement. The temperature curves that have been produced from the cement mixtures follow closely with the same trend seen from the OPC mixtures tested. The pure Ultrafin cement mixture was tested with a water to solids ratio 0.67. This produced a maximum peak temperature of 38°C after 8 hours had elapsed. A mixture of Ultrafin cement with 5% magnetite was also tested. This mixture gave a lower peak temperature reading of 36.75°C at a slightly later time of 8 hours and 30 minutes. Two Ultrafin cement mixtures containing superplasticiser and stabilising agent were also tested for their temperature. These both resulted in very similar maximum temperatures being recorded. As was observed for the OPC grout mixes, the presence of both the superplasticiser and the stabilising agent increased the maximum temperature reached and delayed the time to reach the maximum temperature.

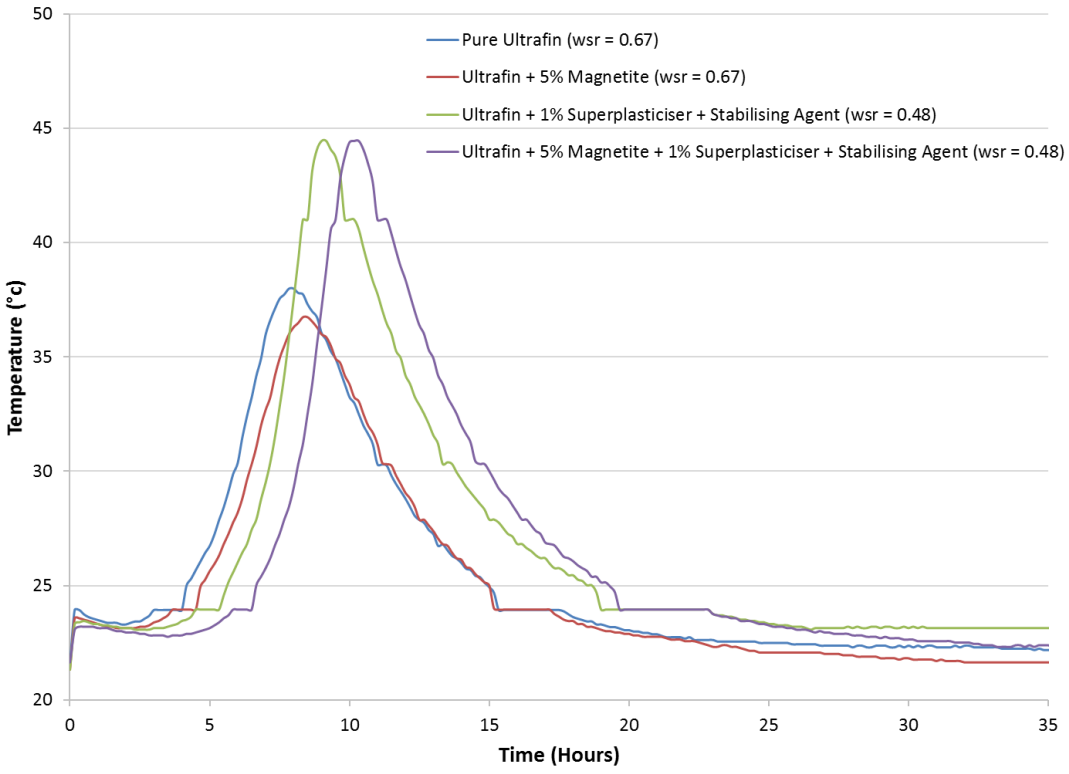

Figure 4.31: *Temperature curves for a range of different mixtures of Ultrafin cement.*

The temperature curves recorded for the majority of the OPC and Ultrafin cement mixtures follow the stages of the general heat evolution curve of hydrating cements seen in Figure 4.27. The first stage indicating the initial reaction, can be seen in the

initial increase in temperature and subsequent slight temperature drop which can be identified in virtually all of the temperature results gained from the two cements. The following stage, the period of slow reaction, can also be identified in all of the cement samples tested. In all but the normal and large volume sample of OPC with a water to solids ratio of 0.3, this stage is characterised by a dip in the temperature, followed by a rise back to the initial peak temperature seen in the first stage of the reaction. For two samples, the normal and large volume sample of OPC with the 0.3 water to solids ratio, the results do not contain this slight drop in temperature but keep a constant temperature across the whole of this stage. This period of slow reaction also varies in length, with the greatest time taken when a higher amount of water is present. This stage then leads onto the acceleration period, which can be identified in all of the experiments, as the part of the temperature curve that leads up to the peak temperature. This period also varies in length, with the cement mixtures containing the most water taking longer to reach their peak temperatures. The final stage is the decelerating period. Within this stage the temperature of the cement mixture decreases, rapidly at first, before levelling off at a slower rate back to room temperature. The time taken for the cement samples to reach room temperature is similar for all of the samples tested. However, the cement samples containing superplasticiser and stabilising agent reduce in temperature at a faster rate than the samples that do not contain the additives.

4.3.3 Discussion

In undertaking the testing of the properties of the magnetic cement material, it can be seen that the addition of magnetite, and also of superplasticiser and stabilising agent, to the cement mixture can result in significant changes to the grout properties occurring. The addition of superplasticiser and stabilising agent, resulted in less water being required within the cement mixtures. As superplasticisers cause cement particles to become more dispersed, this allows the same flowability of the cement mixture to be achieved with a lower amount of water. This also resulted in a significant reduction in the amount of bleed water produced as expected. This is due to the stabilising agent reducing the amount of segregation that occurs within the mixture. The reduction of bleed water can be especially seen within the Ultrafin cement mixtures, where none,

or negligible amounts of bleed were detected in all grout mixtures prepared with a stabilising agent. OPC mixtures also recorded a large decrease in bleed water when a stabilising agent was added to the mixture, with an average of 0.3% bleed water recorded after 2 hours.

The addition of superplasticiser resulted in an increase in the initial setting time. This result can be seen in both the OPC and Ultrafin cement mixtures. This increase in the initial setting time can be attributed to the dispersive effects of the superplasticiser on the cement particles. As the superplasticiser becomes adsorbed onto the surface of the cement particles the hydration reaction of the cement with the water is slower, leading to an increased initial setting time. In changing the concentration of superplasticiser used, the setting time can either be increased or decreased. The reduction in the setting time that corresponds to the decrease in the concentration of the superplasticiser is caused by less adsorption of the superplasticiser on the surface of the cement particles. This allows the cement mixture to undertake its hydration reaction at faster rates. The changes to the speed of the hydration reactions as a result of the superplasticiser adsorbing onto the surface of the cement particles, can also be seen via a delay in the peak temperature recorded in the temperature experiments.

In adding magnetite to the grout mixtures changes can be seen in all of the properties tested. In the case of the flow of the grout mixtures, the addition of magnetite mainly resulted in an increase in the solid mass of the mixture, however only slightly longer flow times were gained for grout mixtures with magnetite compared to the pure cement mixtures. The bleed of the grout mixtures containing magnetite produced similar results to grout mixtures containing just the pure cement. For both of these properties there were only small differences recorded between the magnetic and non-magnetic grout mixtures; any changes that were seen could be controlled by changing the water to solids ratio of the mixture.

The addition of magnetite to the grout mixtures used within the initial setting time experiments resulted in an increase in the time required to set. For the OPC cement mixtures, as the water to solids ratio decreased the setting time also decreased. This

trend was also seen within the Ultrafin cement mixes. The addition of 5% magnetite to the cement mixture resulted in only a slight increase in the initial setting time of both the pure OPC and Ultrafin cement mixtures at the same water to solids ratios of 0.5, and 0.67 respectively. This slight increase in the initial setting time will have been caused by the overall reduction of the cement material in the mixture due to the presence of magnetite that has replaced some of the cement.

The temperature experiments demonstrated that the addition of magnetite resulted in both lower peak temperatures being recorded and a delay in the peak temperature, when compared to the corresponding grout mixtures without magnetite. Hence, the hydrations reactions within the cement are occurring at a later time. Both the drop in temperature and the delay in the hydration reactions can be attributed to there being less cement available for the hydration reaction, since some of the cement has been replaced by magnetite.

4.4 Conclusion

In conclusion, adding magnetite to the OPC and Ultrafin cements results in changes to the grout properties, but a viable grout mixture can still be developed. In testing the magnetic susceptibility of the magnetic grout mixture, the susceptibility of the mixture increases with increasing magnetite. Whilst there is variation between mixes, both due to cement type and the addition of cement additives, the magnetic susceptibility remains close to that which would be predicted just from knowledge of the magnetite mass in each sample. During the magnetic susceptibility testing three different batches of magnetite were used; with the first batch being synthetic, and the following two batches being composed of natural magnetite. In changing the batch of magnetite some changes in the magnetic susceptibility can be seen between the results. Within the natural magnetite batches there will be variances in its magnetic susceptibility which could be seen in the change in batch of magnetic from 2 to 3 within the Ultrafin grout mixes in Figure 4.6. This change however can be attributed to the natural variation of the magnetite and not a result of the cement reacting differently.

In testing the properties of the grout mixture, one of the largest factors that needs to be considered is the water to cement ratio. When adding magnetite into the grout mixture, the mass of solids increases, which results in an increase in the flow time of the grout. In replacing some of the cement for magnetite, the water to solids ratio can be kept constant and similar properties of flow and bleed can be achieved. However, this does lead to an increase in the initial setting times, and delays in the hydration reactions. A delay to the hydration reactions however may be beneficial as this can lead to a better distribution of the hydration products within the grout, and therefore result in better strength development (Lothenbach *et al*., 2007).

Detailed optical microscopy and SEM analyses on thin sections of different versions of the grout mixture, have shown that the magnetite generally does not cluster together into large lumps or sink to the bottom of the cement sample, and is likely to be present throughout the grout mixture. The following chapter will make use of the magnetic grout mixes developed in this chapter to prepare samples for field trials. The field trials investigate the methods and feasibility of detection of the magnetic grout.

Chapter 5

Detecting the Magnetic Grout

5.1 Introduction

This chapter will focus on the two field trials undertaken as part of this research. It will detail the methods used for both trials including the production of the magnetic test samples, and the rationale of the different layouts of both trials. This chapter will also describe the results gained, how the results were analysed, and what conclusions can be drawn from the field trial results.

5.2 Field Trial 1

This section presents the results gained from field trial 1, which was conducted between the 21st and 29th October 2013.

5.2.1 Aims and Objectives of Field Trial 1

The main rationale for undertaking field trial 1 was to determine whether large samples of the magnetic grout could be detected at the surface and at depth using a magnetometer. The main research questions addressed in field trial 1 are:

- Following on from the laboratory magnetic susceptibility tests of small 10ml samples of the magnetic grout, will larger samples be able to be detected in the field?
- How does the magnetic field strength detected by the magnetometer vary with the percentage of magnetite added to the cement?
- Do different shapes of the larger magnetic grout samples result in detectably different magnetic fields?
- Can the magnetic cement samples be detected at the surface when buried?

5.2.2 Preliminary Testing for Field Trial 1

In undertaking field trial 1, several different challenges were encountered. Initially, finding a suitable location at which to undertake the field trial proved difficult. For the first two days of the trial (21st and 22nd October 2013) were undertaken at Rouken Glen Park, which is located 6 miles to the South of Glasgow City centre (Figure 5.1).

Figure 5.1: *Location of the field trial within Rouken Glen Park (Google Maps, 2016a).*

After preliminary analysis of the data collected, the site was found to be extremely magnetically noisy. This large variation in the background magnetic field is likely to be a result of historic activity within the park, such as the presence of a metal mill, and its use in World War II by the Army Royal Electrical and Mechanical Engineers (Rouken Glen Park, 2016). As a result of the large spatial variations in the magnetic field, it was extremely difficult to pick out the magnetic anomaly produced by any grout samples placed within the trial area. Figure 5.2 gives an example of the background magnetic results from a 5 m by 5 m magnetometer field survey at the Rouken Glen Park trial location. Several peaks in the magnetic field are apparent, which would make additional magnetic anomalies extremely hard to detect. Consequently, a different location for field trial 1 was found on the beach at Troon.

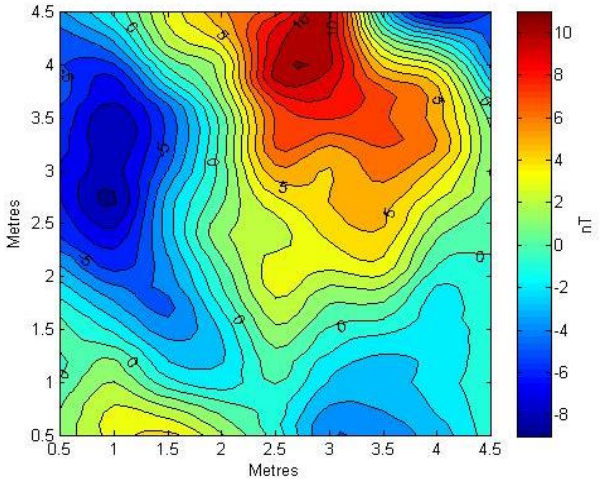

Figure 5.2: *A contour map showing the background magnetic field at Rouken Glen Park.*

Despite the difficulty in conducting a trial at Rouken Glen, lessons were learned that were used in design of the subsequent field trials. The need for accurate positioning of the magnetometer sensors is required to determine the grout location, as it is necessary to remove the background magnetic field, leaving only the grout signal. Consequently, an accurate knowledge of the 3D location of the magnetometer is critical. This poses two challenges, first knowing the relative coordinates of the magnetometer and, second, keeping the magnetometer at a constant distance above ground whilst conducting a walkover survey.

5.2.3 Location of Field Trial 1

Field trial 1 was undertaken along a stretch of beach at Troon (Figure 5.3). This location was chosen as sand is generally magnetically quiet, which is ideal for undertaking a magnetic survey. Additionally, in undertaking the trial on a beach it would be easy to bury the magnetic grout samples to different depths.

Figure 5.3: *a) A satellite image of the location of the field trial at Troon (Google Maps, 2016b), and b) A photograph from the field site looking towards Troon.*

5.2.4 Methods

This section will detail the equipment used in field trial 1, along with the production of the large magnetic grout samples, and the setup configuration of the trial.

5.2.4.1 Magnetic Grout Samples

Large magnetic grout samples of both OPC and Ultrafin cement were produced for use in field trial 1. The samples contained either 5% or 10% magnetite, which allowed variations in the strength of the detected magnetic field to be investigated. The OPC magnetic grout samples were produced with a water to cement ratio of 0.5, and the Ultrafin cement magnetic grout samples had a water to cement ratio of 0.67. These two water to cement ratios were chosen due to their engineering properties (without added superplasticiser and stabilising agent) that were established in Chapter 4 Section 4.3.3. To produce the samples, the cement and magnetite were mixed together thoroughly before the water was added to the mixture. This ensured that the magnetite was evenly distributed throughout the cement. Once the cement mixtures had been made they were decanted into rectangular and disc shaped moulds, which were then left over 3 days to cure. Table 5.1 details the dimensions of the magnetic grout samples produced.

Table 5.1: *Dimensions of the large magnetic grout samples.*

Ultrafin with 5% Magnetite						
	Width (cm)	**Length (cm)**	**Depth (cm)**	**Diameter (cm)**	**Volume (cm^3)**	**Mass (g)**
Rectangle	9.5	22.5	5	-	1069	1484
Disc 1	-	-	1.5	25.4	760	926
Disc 2	-	-	2.1	25.4	1064	1293
Ultrafin with 10% Magnetite						
	Width (cm)	**Length (cm)**	**Depth (cm)**	**Diameter (cm)**	**Volume (cm^3)**	**Mass (g)**
Rectangle 1	9.5	22.5	4.8	-	1026	1451
Rectangle 2	9.5	22.5	5.2	-	1112	1493
Rectangle 3	9.5	22.5	5	-	1069	1687
Disc 1	-	-	1.6	25.4	811	1028
Disc 2	-	-	1.7	25.4	861	1086
OPC with 5% Magnetite						
	Width (cm)	**Length (cm)**	**Depth (cm)**	**Diameter (cm)**	**Volume (cm^3)**	**Mass (g)**
Rectangle	9.5	22.5	6.5	-	1197	1975
Disc	-	-	1.7	25.4	861	1166

5.2.4.2 Magnetometer

The equipment used for detecting the magnetic field in field trial 1 was a G-858 MagMapper Magnetometer (Figure 5.4). This was hired for the duration of the trial from Geomatrix Earth Science Ltd. The G-858 is a high-performance caesium vapour magnetometer with a sensitivity of 0.01 nT.

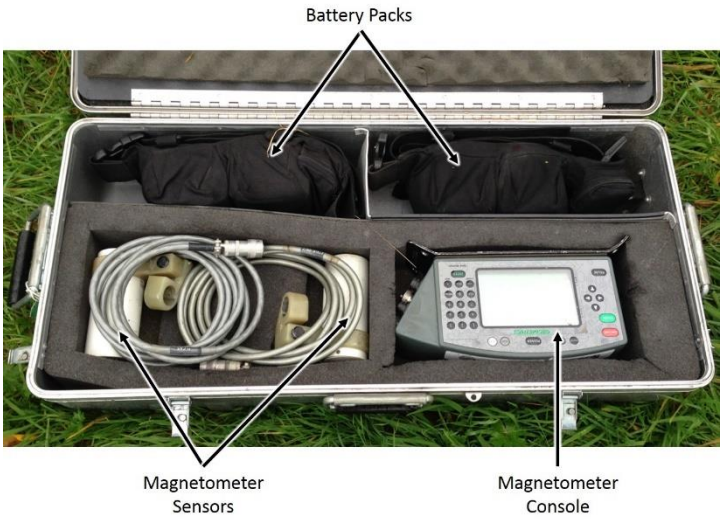

Figure 5.4: *A photograph of the magnetometer before it is set up.*

The G-858 can be used both as a gradiometer and a magnetometer depending on the orientation of the sensors, and whether one or two sensors are used. In using the G-858 as a gradiometer, the sensors are positioned vertically, one above the other (Figure 5.5). In this configuration both sensors take a magnetic field reading, at different distances from the ground surface. To determine the magnetic gradient, the difference between the two sensors is calculated. When the G-858 is used as a magnetometer, either one of the sensors can be used, and the two sensors are oriented either parallel or perpendicular to the ground surface.

Figure 5.5: *The G-858 MagMapper Magnetometer in use as a gradiometer.*

5.2.4.3 Field Trial 1 Setup

The first field trial was undertaken using a 5 m by 5 m square grid, which was measured out on the beach using tape measures (Figure 5.6). The data were collected along lines within this square spaced at 0.5 m apart. The data were collected using a unidirectional approach (i.e. all the lines were walked in the same direction each time). All lines were surveyed walking towards the North (Figure 5.7). The sensors were oriented vertically, with one sensor located above the other, in the gradiometer arrangement, with each sensor collecting data separately. The sensors collected data every 0.1 seconds.

Figure 5.6: *The layout of the 5 m by 5 m trial area on the beach at Troon.*

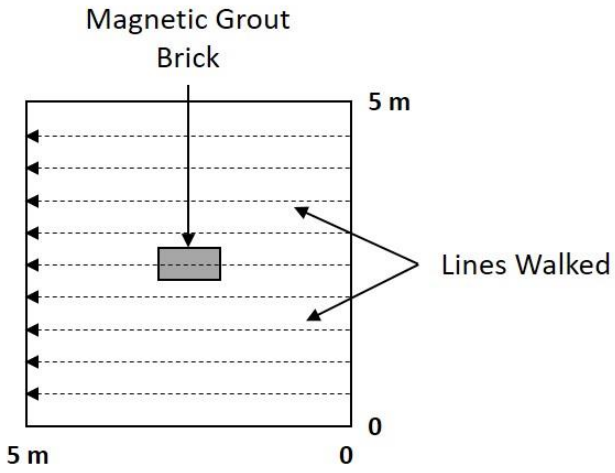

Figure 5.7: *A schematic diagram showing the lines along which the data was collected.*

Before the samples were placed within the 5m by 5m trial area, a background reading was taken of the trial area at the start of each day. This was done so that any anomalies present in the background magnetic field, prior to introducing the grout samples, could be removed from the data.

The magnetic grout samples were placed approximately in the centre of the trial area. Initially, the samples were tested at the ground surface. Three initial surveys were completed, each with a single rectangular sample for OPC with 5% magnetite, for Ultrafin cement with 5% magnetite, and for Ultrafin cement with 10% magnetite. These initial surveys were undertaken to determine whether the magnetic grout sample could be detected, and how the size of the magnetic anomaly changed with increasing magnetite content. Once these tests had been undertaken, a further test of three rectangular samples of Ultrafin cement with 10% magnetite was surveyed to explore the effect of increasing the volume of grout present (as opposed to the density). The samples of Ultrafin cement with 10% magnetite were chosen as from the initial surveys the 10% magnetite sample gave the best magnetic response. This latter survey was completed using two configurations: two rectangles located side by side and the third located across the top; and all three rectangles stacked on top of each other. After completing the surveys with the rectangular samples, disc shapes were then tested. This was to determine how changing the shape of the magnetic grout sample affected the detected magnetic anomaly. Two surveys were undertaken each with two stacked discs of Ultrafin cement with 5% magnetite, and Ultrafin cement with 10% magnetite.

After all the surface-based trials had been undertaken, three of the Ultrafin cement with 10% magnetite rectangular samples were buried to different depths within the sand (Figure 5.8). This was to determine how increasing distance from the magnetometer affected the strength of the magnetic anomaly detected. The configuration of the three rectangles was with two of the rectangles located side by side with the third located across the top. The depths the samples were buried to, from the ground surface, were 0 cm (top of the sample was level with the ground surface), 6.5 cm, 15 cm, 30 cm, and 40 cm. These depths equate to the following distances from

the bottom sensor of the magnetometer, 50.35 cm, 58.35 cm, 66.85 cm, 81.85 cm, and 91.85 cm.

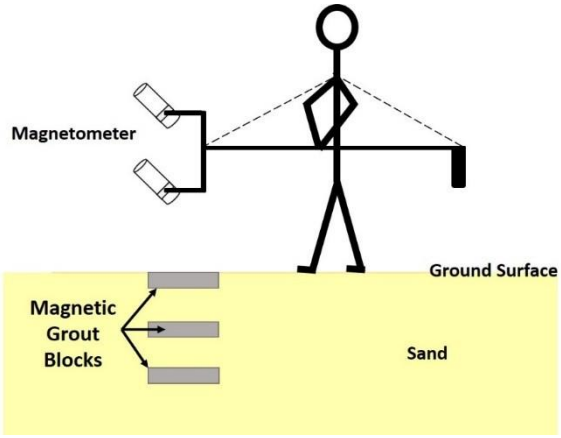

Figure 5.8: *A schematic diagram showing the walk over survey of the buried magnetic grout rectangles.*

5.2.5 Data Analysis for Field Trial 1

This section will detail how the data gained from field trial 1 was analysed.

5.2.5.1 Formation of Contour Maps

To be able to easily visualise and compare the data gained from field trial 1, contour maps were produced of the data. By producing contour maps it was possible to determine and to compare the location and intensity of the magnetic anomaly detected from the magnetic grout samples. The following step by step process to form the contour maps was undertaken to produce the clearest image of the magnetic anomaly as part of the proof of concept stage of this research.

To produce the contour maps, the field data results were imported into Matlab for each of the trials undertaken. Initially a contour map of the magnetic field was created for each field trial, including the background magnetic field taken on each day the trials were undertaken. As both magnetometer sensors were collecting data at the same time,

two sets of magnetic field data were processed. An example of the contour maps generated from the upper and lower magnetometer sensor can be seen in Figure 5.9.

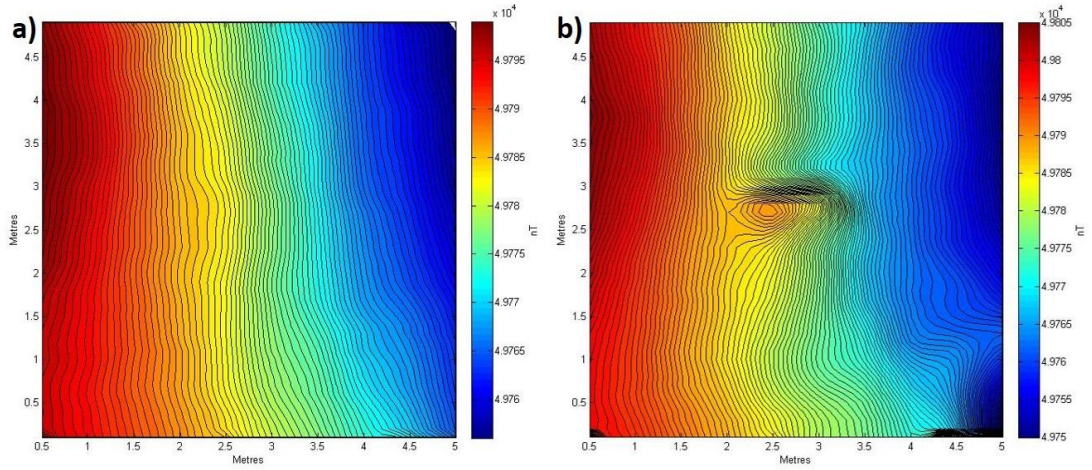

Figure 5.9: *Two contour maps showing a) the magnetic field data collected from the upper sensor, and b) the magnetic field data collected from the lower sensor for the same survey.*

From the contour maps produced from the upper and lower magnetometer sensor, it can be seen that the magnetic grout sample is present in the centre of the lower sensor data, but not in the upper sensor data. To produce a clearer image of the magnetic field of the magnetic grout sample, the upper sensor data was subtracted from the lower sensor data. An example of one of the contour maps produced using this method can be seen in Figure 5.10.

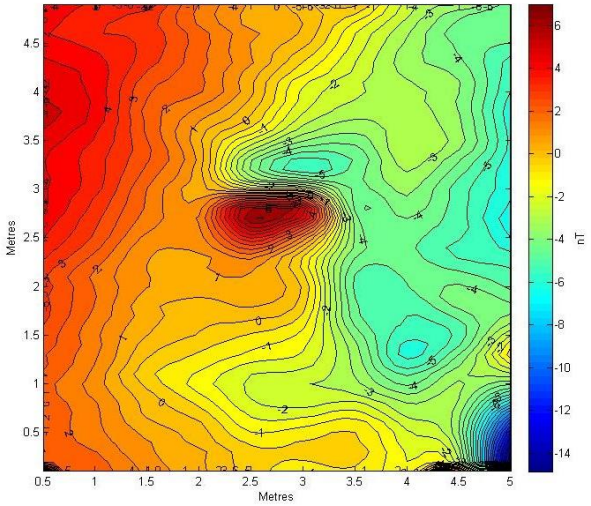

Figure 5.10: *An example of a contour plot of the raw magnetic field data containing a magnetic grout sample at the centre.*

Figure 5.10 above shows that even by subtracting the upper sensor, which should represent a background magnetic field at that data point, from the lower sensor, the magnetic grout sample is still not very clear within the contour plot. To gain a clearer view of just the magnetic field generated by the magnetic grout sample, instead of removing the field recorded by the upper sensor, the data recorded by the lower sensor prior to the introduction of the grout sample were removed (Figure 5.11). This was achieved by subtracting the magnetic field data collected by the lower sensor of the magnetometer when the magnetic grout sample was present, from the magnetic field data collected by the lower sensor of the background magnetic field. As demonstrated in Figure 5.11, this gave a much clearer image of the magnetic anomaly generated by the grout sample only.

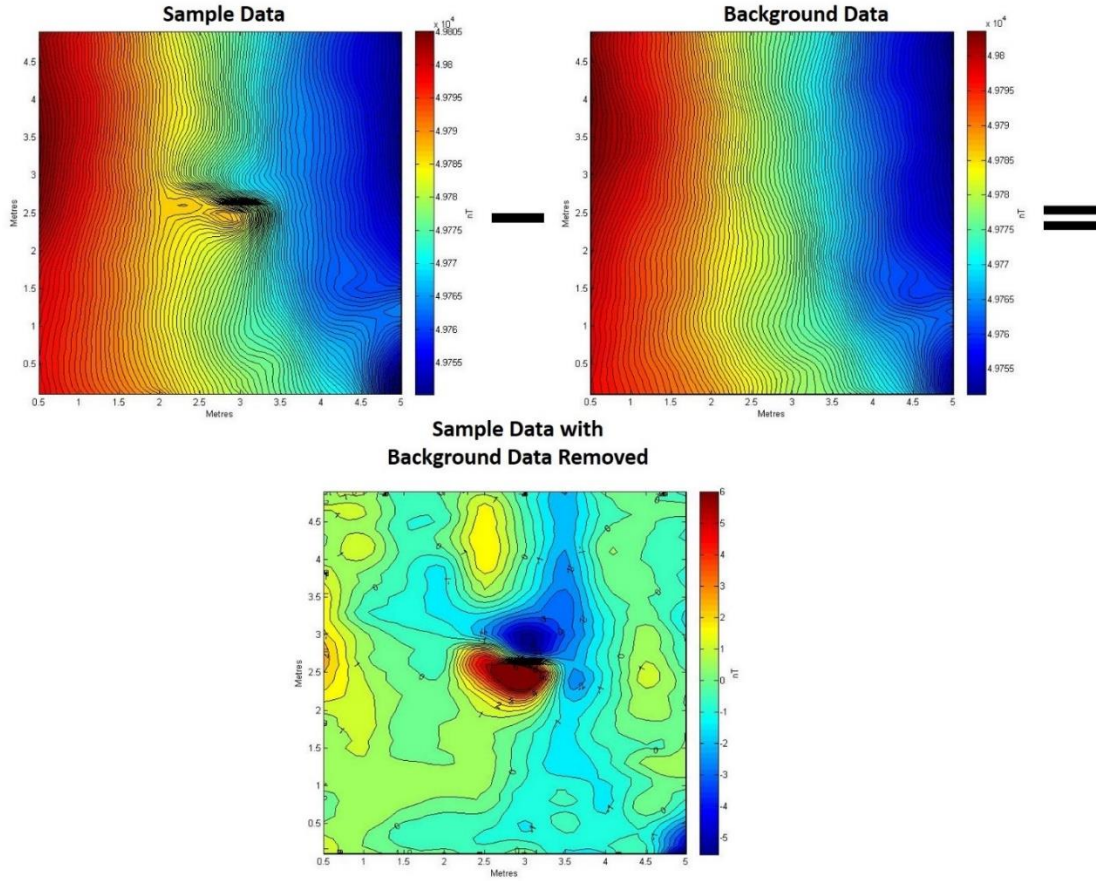

Figure 5.11: *The process of removing the lower sensor background magnetic field data from the lower sensor data containing the magnetic field of the magnetic grout sample.*

In most cases, this method of subtracting the lower sensor of the magnetometer when the magnetic grout sample was present, from the magnetic field data collected by the lower sensor of the background magnetic field, produced the clearest image of the magnetic field generated by the samples. However, in some instances, the resulting magnetic field, including the anomaly, was negative (Figure 5.12) due to error in the vertical alignment of the sensors. To remove this effect of vertical misalignment, for each survey (i.e. before and after the grout was emplaced), the lower sensor data were first removed from that of the upper sensor data. Then, the resulting survey data from the background field data were removed from the survey data taken with the grout emplaced. Figure 5.13 shows one of the contour maps produced using this method. In taking the difference of the upper and lower sensors before subtracting the background field data from the field data taken with the grout emplaced, the contour

maps produced are much more consistent. This method of data processing is used in the production of all subsequent contour maps for field trial 1.

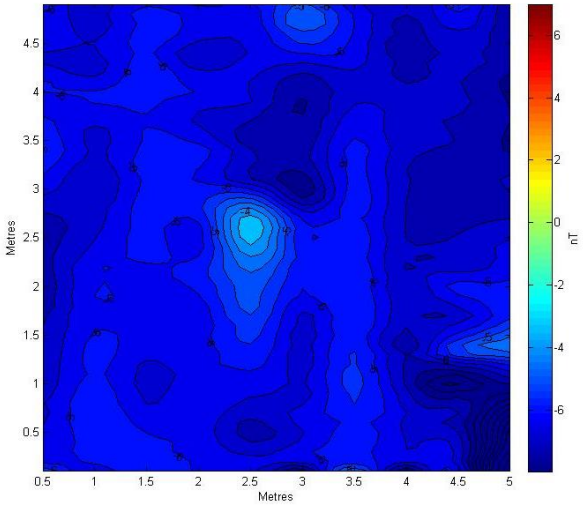

Figure 5.12: *A contour map containing entirely negative magnetic field values produced by removing the lower sensor data of the background magnetic field from the lower sensor data of the magnetic field of the magnetic grout sample.*

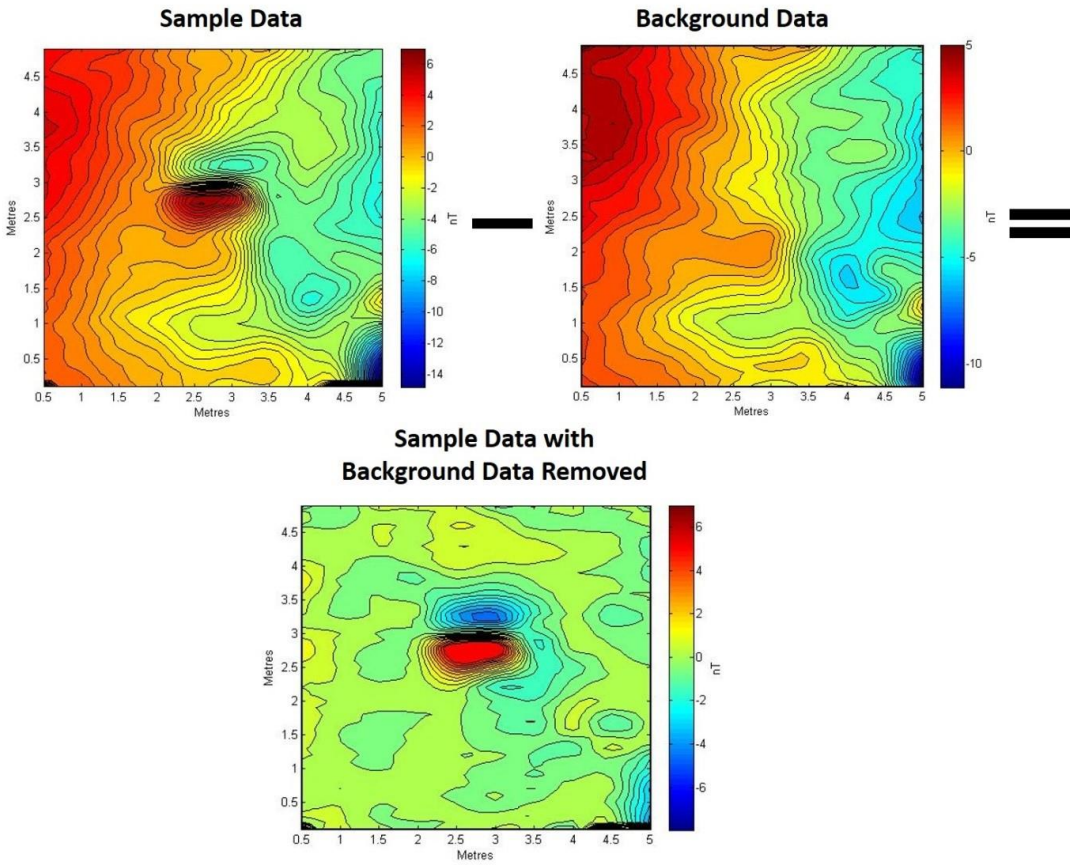

Figure 5.13: *The process of removing the difference in the upper and lower magnetic field data of the background from the difference in the upper and lower magnetic field data of the magnetic grout sample.*

To ensure that contour maps produced for each of the trials can be easily compared with each other, all the contours use the same scale. The minimum and maximum contour values are -8 nT and 7 nT respectively. These values were chosen as they represented the highest and lowest values measured in this field trial.

Finally, the scaling of the x axis on each of the trials' contour maps was changed to begin at 0.5 m instead of the original 0 m. This was the position of the magnetometer with respect to the grid, when undertaking the data collection.

5.2.6 Results from Field Trial 1

5.2.6.1 At the Ground Surface

Figure 5.14 shows the survey results for one rectangle of OPC with 5% magnetite, and one rectangle of Ultrafin cement with 5% magnetite. The rectangle of OPC with 5% magnetite (Figure 5.14a) shows a marked anomaly in the region where the rectangle was located. The offset seen between the positioning of the grout samples (the rectangle on Figure 5.14a) and the anomaly itself can be attributed to the fact that the exact horizontal location of the magnetometers during the walkover survey is not known. The shape of the magnetic anomaly created is relatively circular, with a slight elongation towards the North and South ends. The data taken from the 2.5 m walkover line is also plotted in Figure 5.14b, which shows that the maximum value recorded for this sample is 3.369 nT.

For comparison, similar results for the rectangle of Ultrafin cement with 5% magnetite is shown in Figure 5.14c and Figure 5.14d. Once again, the magnetic anomaly produced by the sample is clearly apparent but in this case, has a slightly lower peak of 2.554 nT. The shape of the magnetic anomaly is very similar to that of OPC with 5% magnetite. The variation in the peak recorded magnetic field may be due to a lateral difference in the location of the recordings with respect to the grout sample; if the magnetometer does not pass directly over the sample then the value of the recorded field will be lower. However, this variation may also be a result of the difference in the magnetic susceptibility between the grout mixes. In Chapter 4, Section 4.2.1.2, the Ultrafin cement with 5% magnetite recorded a lower magnetic susceptibility than the OPC mixture containing 5% magnetite which could contribute to a lower magnetic field being detected.

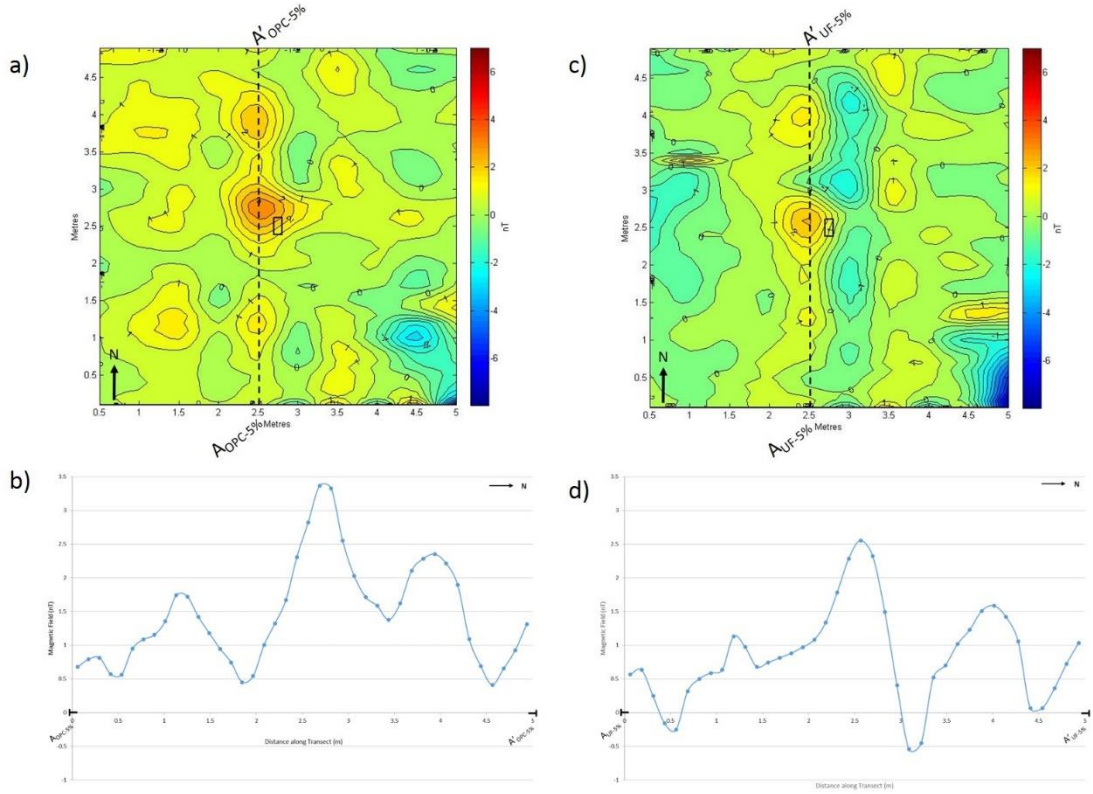

Figure 5.14: *a) Contour map of one rectangle of OPC with 5% magnetite, b) a graph of the response along the 2.5 m line of OPC with 5% magnetite, c) contour map of one rectangle of Ultrafin cement with 5% magnetite, and d) a graph of the response along the 2.5 m line of Ultrafin with 5% magnetite.*

Figure 5.15 shows the survey results for the rectangles containing Ultrafin cement with 5% magnetite and the rectangle of Ultrafin cement with 10% magnetite. Doubling the mass of magnetite within the sample produces an anomaly that is more than twice the size, with the peak recorded value rising from 2.554 nT to 7.152 nT (Figure 5.15b and Figure 5.15d). This more than doubling of the anomaly is likely due to uncertainty in the magnetometer location with respect to the samples, meaning that the true peak value is not being recorded. A comparison of the contour maps and graph in Figure 5.15 shows the anomalies to be similar in shape.

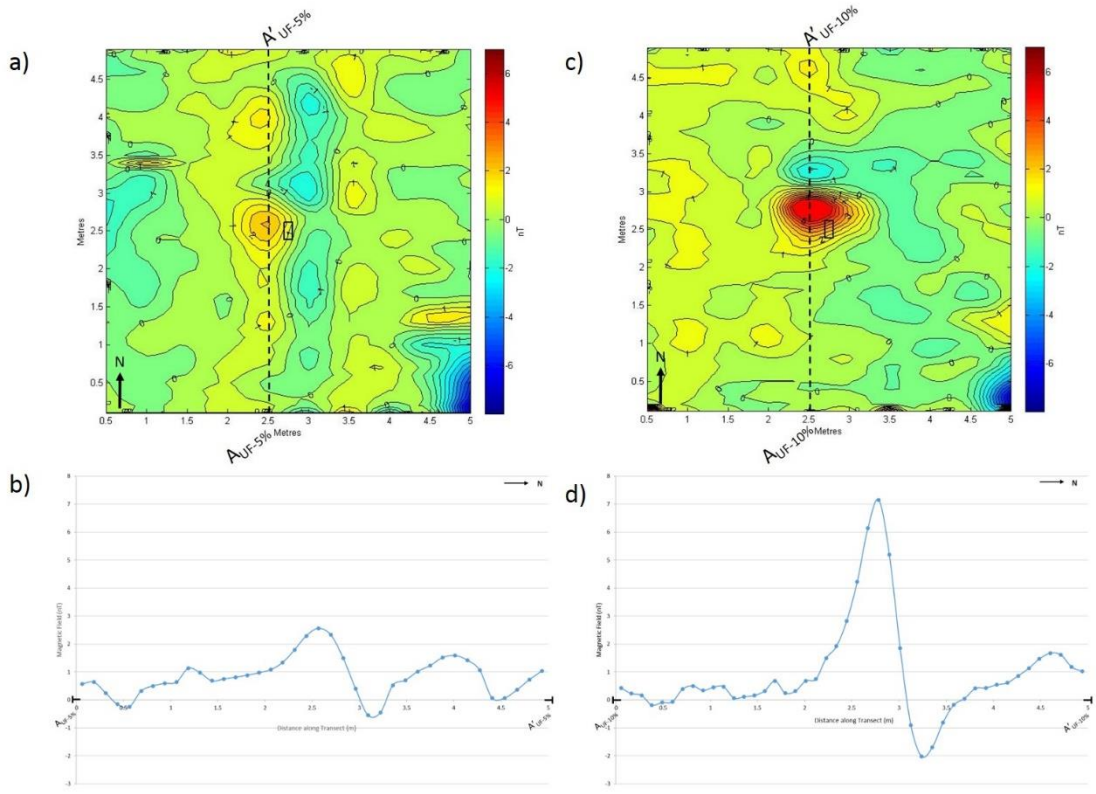

Figure 5.15: *a) Contour map of one rectangle of Ultrafin cement with 5% magnetite, b) a graph of the response along the 2.5 m line of Ultrafin cement with 5% magnetite, c) contour map of one rectangle of Ultrafin cement with 10% magnetite, and d) a graph of the response along the 2.5 m line of Ultrafin cement with 10% magnetite.*

The number of rectangular samples within the trial area containing Ultrafin cement with 10% magnetite was then increased to three (Figure 5.16). These three rectangles were arranged in two different formations. The first formation was with two rectangles placed side by side with one located across the top edge of the two rectangles (Figure 5.16a). The second formation was with the three rectangles stacked on top of each other (Figure 5.16d). From the contour map of the results gained from the three Ultrafin cement rectangles with 10% magnetite in the first formation (Figure 5.16b) the magnetic anomaly is easily identified. The maximum recorded magnetic field value for this sample is 20.034 nT (Figure 5.16c). This compares to a peak recorded value of 7.152 nT for a single rectangle containing the same percentage of magnetite, so as expected the anomaly is approximately three times the size. There is also a dipole present, with the dipole axis orientated along the North East – South West axis.

The stacked second formation of the three Ultrafin cement with 10% magnetite rectangles can be seen in Figure 5.16d. Figure 5.16e shows the magnetic field recorded for the magnetic grout samples in this formation. The maximum magnetic field recorded for this sample formation is 8.807 nT. This value is much lower than that recorded for the flat formation of three rectangles. Again, this may be due to errors in the magnetometer location. For the stacked bricks, the anomaly will be smaller in diameter and hence it is easier to miss the peak in a walkover survey in which adjacent walkovers are 0.5m apart. The contoured dipole on Figure 5.16e is oriented along the North – South axis, rather than along the North East – South West axis as seen in the flat formation. This dipole can also be clearly seen within the graph of the magnetic response in Figure 5.16f. It is not clear whether this reorientation of the dipole is a figment of the location errors in the magnetometer readings or is due to different stacking geometries of the grouted samples.

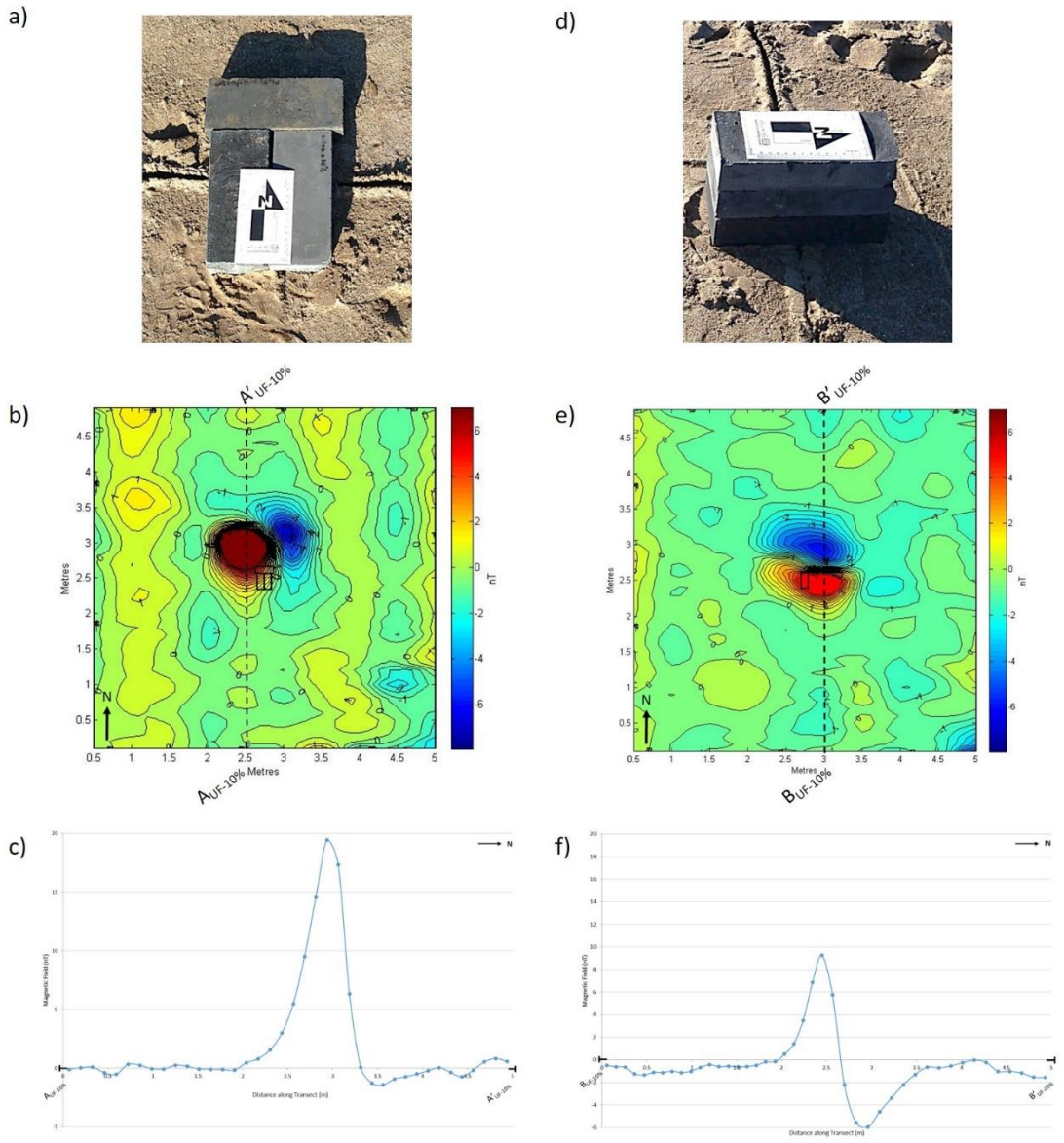

Figure 5.16: *a) A photograph showing three Ultrafin cement with 10% magnetite rectangles, with two rectangles placed side by side and one across the top, b) a contour map of the three rectangles with 10% magnetite in the same formation as in (a), c) a graph showing the magnetic response along the 2.5 m line for three Ultrafin cement with 10% magnetite rectangles in the same formation as in (a), d) a photograph showing three Ultrafin cement with 10% magnetite rectangles stacked, e) a contour map of the three rectangles with 10% magnetite in the same formation as (d), and f) a graph showing the magnetic response along the 3 m line for three Ultrafin cement with 10% magnetite rectangles in the same formation as (d).*

The shape of the magnetic grout samples was then changed from a rectangle to a disc. Figure 5.17a shows the magnetic field recorded when two discs of Ultrafin cement with 5% magnetite were stacked on top of each other in the field trial area. The peak magnetic field value recorded for this sample was 2.822 nT. The magnetic anomaly recorded is slightly larger than the peak anomaly (2.554 nT) recorded for the one rectangle of Ultrafin cement with 5% magnetite. The shape of the magnetic anomaly is relatively rounded with a slight elongation present to the North and South. There is also a gradual increase in the magnetic field up to the peak magnetic field value recorded. The magnetic response line across the centre of the magnetic anomaly produced by two stacked discs of Ultrafin cement with 5% magnetite can be seen in Figure 5.17b.

Figure 5.17c shows the magnetic field recorded when two discs of Ultrafin cement with 10% magnetite were present in the field trial area. The peak magnetic field value which was recorded for this sample was 2.019 nT. This value is much less than the peak anomaly recorded for one rectangle of Ultrafin cement with 10% magnetite (7.152 nT). This is possibly due to the peak magnetic anomaly being missed in the walkover survey. The shape of the magnetic anomaly for this magnetic grout sample is elongated to the East and West, however the general size of the anomaly is similar to the discs containing 5% magnetite. The magnetic response line across the centre of the magnetic anomaly produced by two stacked discs of Ultrafin cement with 10% magnetite can be seen in Figure 5.17d.

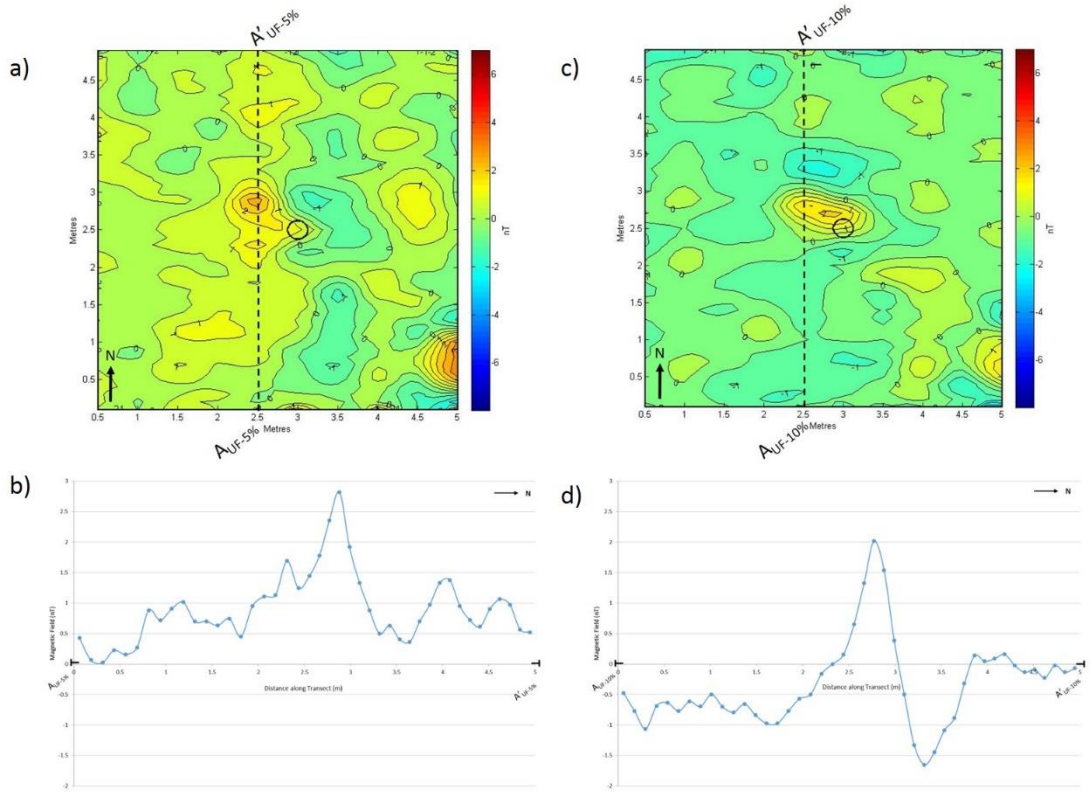

Figure 5.17: *a) A contour map of the magnetic response of two stacked discs of Ultrafin cement with 5% magnetite, b) a graph of the magnetic response along the 2.5 m line of the two stacked discs of Ultrafin cement with 5% magnetite, c) a contour map of the magnetic response of two stacked discs of Ultrafin cement with 10% magnetite, and d) a graph of the magnetic response along the 2.5 m line of the two stacked discs of Ultrafin cement with 10% magnetite.*

5.2.6.2 At Depth

In burying the three rectangles of Ultrafin cement with 10% magnetite to different distances from the lower sensor of the magnetometer, the distance at which the magnetic grout rectangles can be detected can be determined. Figure 5.18a shows the three magnetic grout rectangles located on the surface of the ground, with the top surface of the samples at a distance of 46.85 cm from the lower magnetometer sensor. These data have previously been presented in Figure 5.16b, and are reproduced here so they can be easily compared with the other data sets. Additionally, Figure 5.19a shows the magnetic response along the 2.5 m line for the three Ultrafin cement with

10% magnetite rectangles at 46.85 cm from the lower sensor. These data have also previously been presented in Figure 5.16c, and are included here to allow for easy comparison.

From Figure 5.18 and Figure 5.19 it can be seen that with increasing distance from the lower magnetometer sensor, the detected magnetic field from the three magnetic grout rectangles decreases. The peak magnetic anomaly values recorded at each distance are as follows: at 46.85 cm – 20.034 nT, at 50.35 cm – 4.950 nT, at 58.35 cm – 8.238 nT, at 66.85 cm – 5.491 nT, at 81.85 cm – 4.293 nT, and at 91.85 cm – 4.717 nT. The lower peak magnetic anomaly recorded at 50.35 cm is likely to have been caused by the walkover survey missing the peak magnetic field produced by the three discs. In Figure 5.18a a strong dipole is present, with an axis orientated in a North East – South West direction. Dipoles are not clearly present within the other magnetic responses at greater distances from the magnetometer sensor.

Additionally, as the distance between the lower magnetometer sensor and the three magnetic grout rectangles increases, the size of the magnetic anomaly detected decreases as expected. This can be seen in both the contour maps in Figure 5.18, and within the graphs in Figure 5.19. The shape of the anomaly also changes from being relatively rounded to elongated within the samples located at a greater distance (Figure 5.18e and f). This change in shape is also visible within the graphs with narrow peaks present when the magnetic grout rectangles were located closer to the magnetometer, and wider peaks when they were located further away.

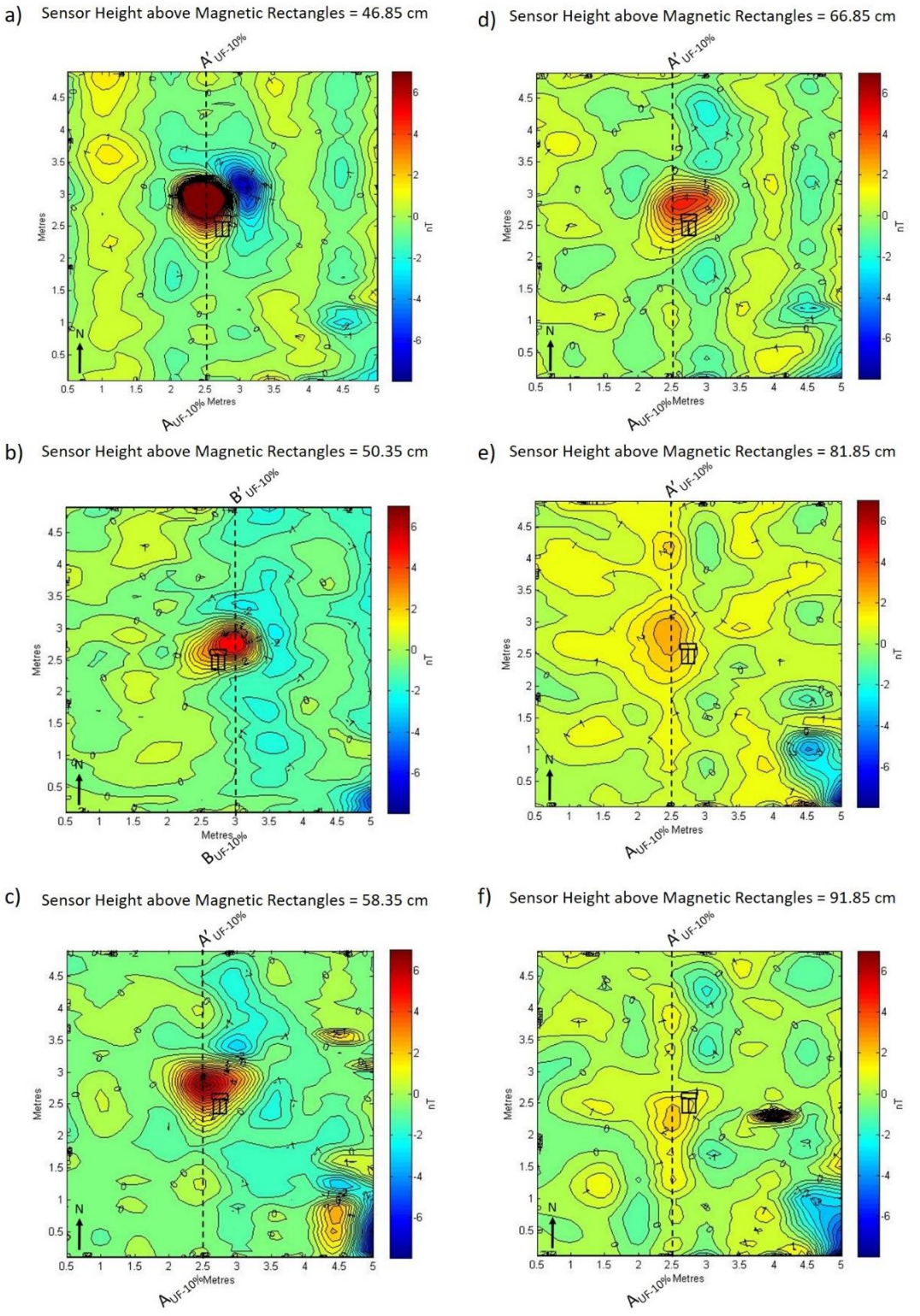

Figure 5.18: *Contour maps of 3 rectangles of Ultrafin cement with 10% magnetite, arranged with two rectangles placed side by side and one across the top at distances from the lower magnetometer sensor of, a) 46.85 cm, b) 50.35 cm, c) 58.35 cm, d), 66.85 cm, e) 81.85 cm, and f) 91.85 cm.*

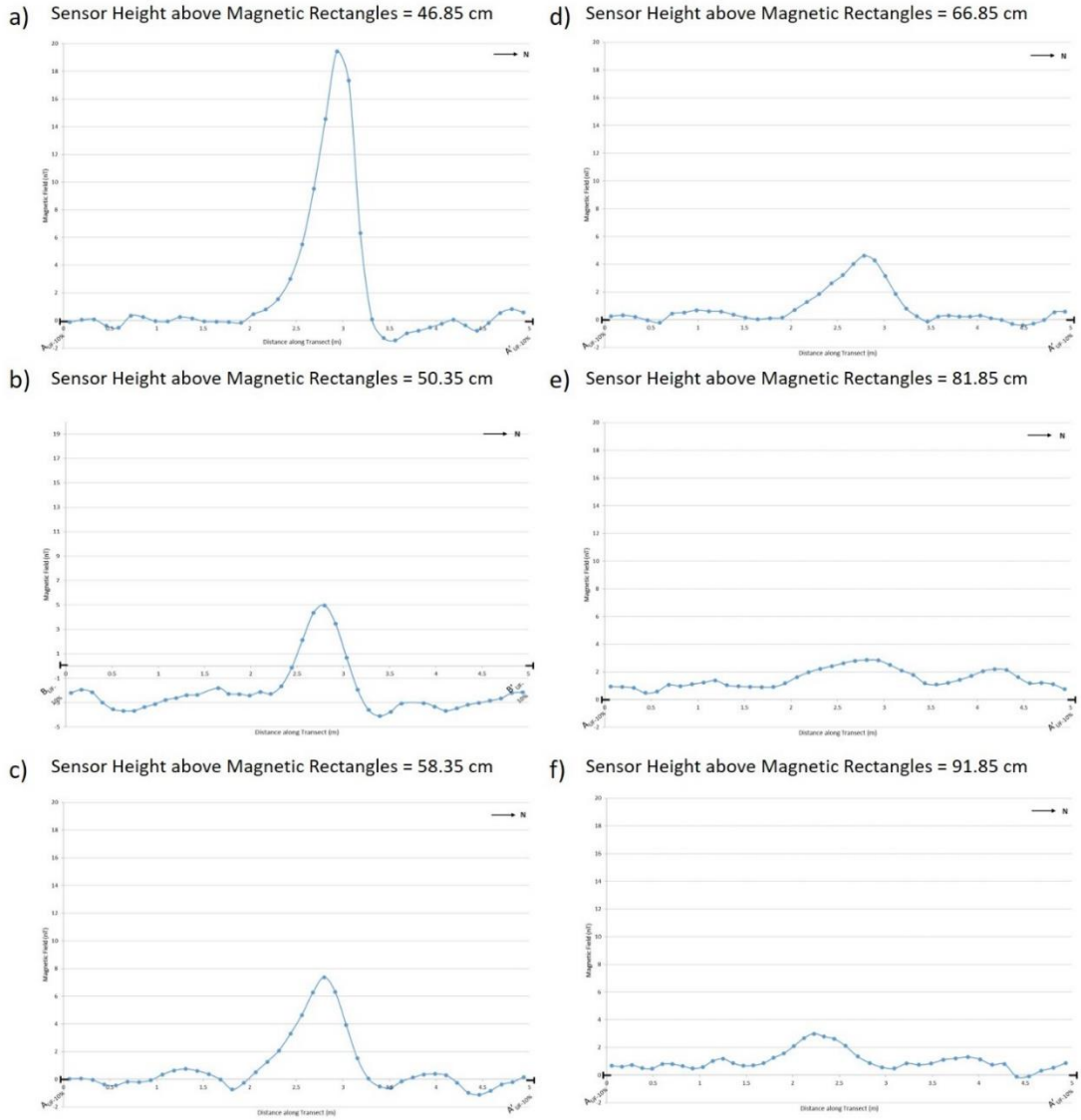

Figure 5.19: *Graphs showing the magnetic response along the 2.5 m line (and 3 m line for (b)) for three Ultrafin cement with 10% magnetite rectangles arranged with two rectangles placed side by side and one across the top at distances from the lower magnetometer sensor of, a) 46.85 cm, b) 50.35 cm, c) 58.35 cm, d), 66.85 cm, e) 81.85 cm, and f) 91.85 cm.*

5.2.7 Discussion of Field Trial 1 Results

From the results detailed in the previous section, it can be seen that the large magnetic grout samples tested can be detected in the field. However, the size and shape of the magnetic anomaly signal that is recorded is dependent on several factors.

The first of these factors is the percentage of magnetite that is contained within the magnetic grout sample. Figure 5.20 shows a comparison of the mass of magnetite contained within the magnetic grout samples to the peak magnetic anomaly detected. From this, the largest peak magnetic anomaly is gained from the sample containing the largest mass of magnetite as expected. These results confirm for the rectangular grout samples that the larger the mass (and therefore the percentage) of magnetite contained within the magnetic grout, the larger the magnetic field of the grout itself. For the disc shaped grout samples a smaller peak magnetic anomaly is recorded for the discs containing 10% magnetite compared to the discs with 5% magnetite. This result is likely to be a consequence of the peak magnetic field being missed during the collection of the data for the discs containing 10% magnetite. This is because the sensor could have passed to either side of the magnetic grout discs rather than over the centre of the discs, which would result in a lower peak field being recorded.

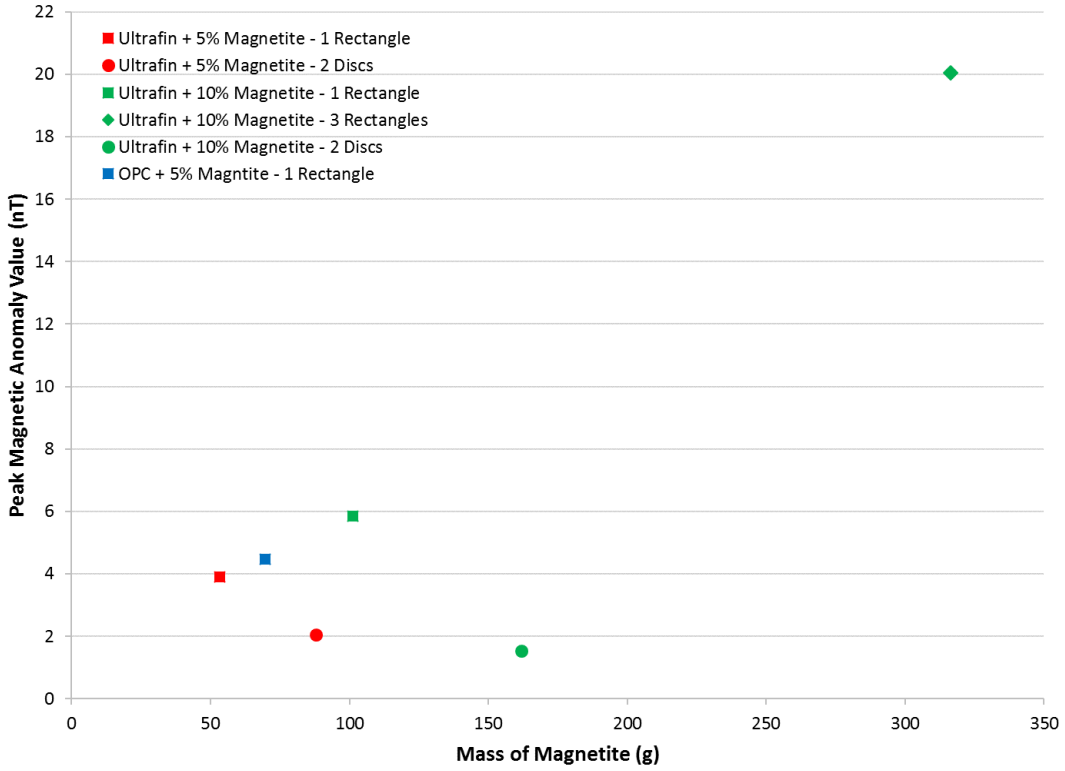

Figure 5.20: *A comparison of the mass of magnetite to the peak magnetic anomaly value.*

Another factor that determines the magnetic anomaly signal recorded is the shape of the magnetic grout sample. In this field trial, two shapes were tested, a rectangular brick and a disc. When trialled both shapes produced magnetic anomalies that could be easily seen above the background magnetic field, however they produced different magnetic anomaly shapes. The rectangular brick shapes produced a magnetic anomaly that was generally rounded in appearance, with the single rectangle containing 10% magnetite producing a wider circular anomaly than the sample containing 5% magnetite. Due to the width of the single magnetic grout bricks used (9.5 cm), they are likely to only have been detected along the transect line that passed directly over the sample due to the 0.5 m line spacing. When three of the bricks were present, the width of the magnetic grout sample was increased to 22.5 cm, and is therefore likely to be additionally detected by the transect lines to either side of the magnetic grout sample.

The magnetic grout samples shaped as discs produced a more oval shaped magnetic anomaly than the rectangular samples. The magnetic anomalies produced were elongated in an East – West orientation. The difference in the shape of the magnetic anomalies produced can be attributed to the fact that the discs were much wider (diameter of 25.4 cm) than the single rectangles and therefore the magnetic anomaly produced by the discs was picked up by more than one transect line, so the contour shape is more accurate. The discs also produced smaller magnetic anomalies than the rectangles containing the same amount of magnetite. This is likely to have been caused by the fact that the discs were much wider than the rectangles meaning that the mass of magnetite was spread out over a larger area.

The final factor that affects the magnetic anomaly signal is the distance that the magnetic grout sample is located away from the magnetometer sensors. The results in Figure 5.18 and Figure 5.19 show that by increasing the distance away from the magnetometer sensor, the smaller the detected magnetic field from the magnetic grout sample. This can be seen in both the value of the magnetic field, and in the width of the magnetic anomaly. Figure 5.21 below shows the peak magnetic field values gained as the distance between the magnetic grout sample and the magnetometer sensor increased. There is a general decrease in the magnetic field value, apart from the value gained at a distance of 50.5 cm, where a lower than expected value was recorded. This is likely to be because the peak magnetic field of the magnetic grout sample at this distance was missed in the walkover survey. Overall, however there is a marked decrease in the magnetic field value of 15.317 nT for the sample over 45 cm.

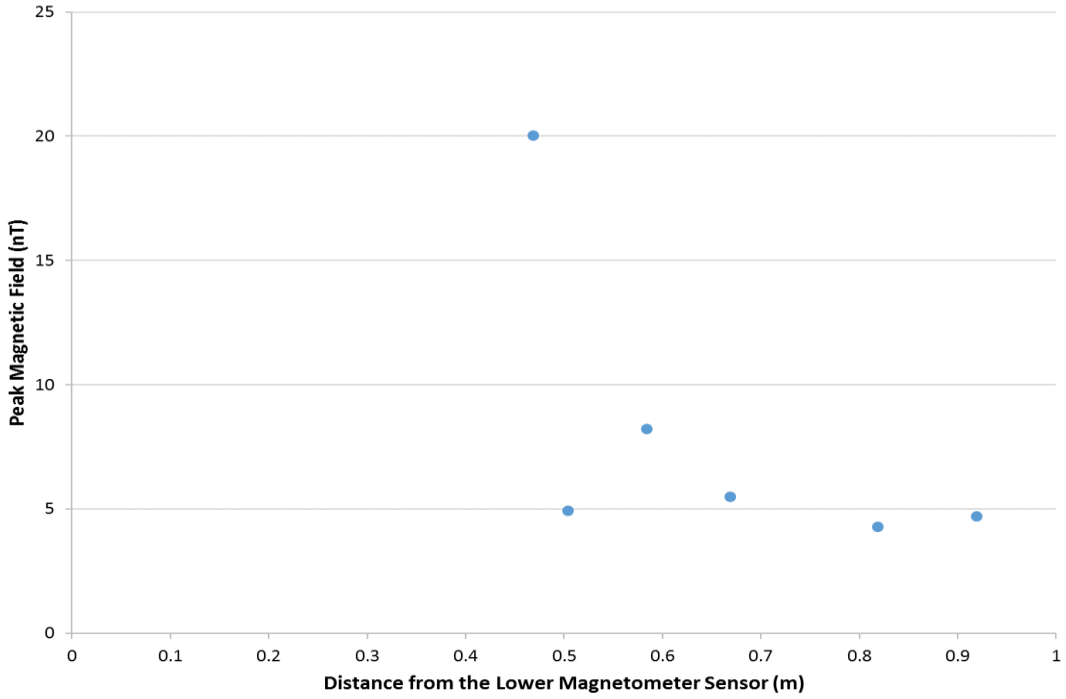

Figure 5.21: *The relationship between distance and the peak magnetic anomaly.*

5.2.8 Comparison of Results with Theory

The magnetic field of a dipole (such as a bar magnet) decays following the inverse cube law:

$$\frac{1}{r^3} \tag{5.1}$$

Where:

r = distance.

A graph of this decay (Figure 5.22) was plotted with the peak values gained from the field trial results (with the anomalous value at 0.5m distance removed from the data).

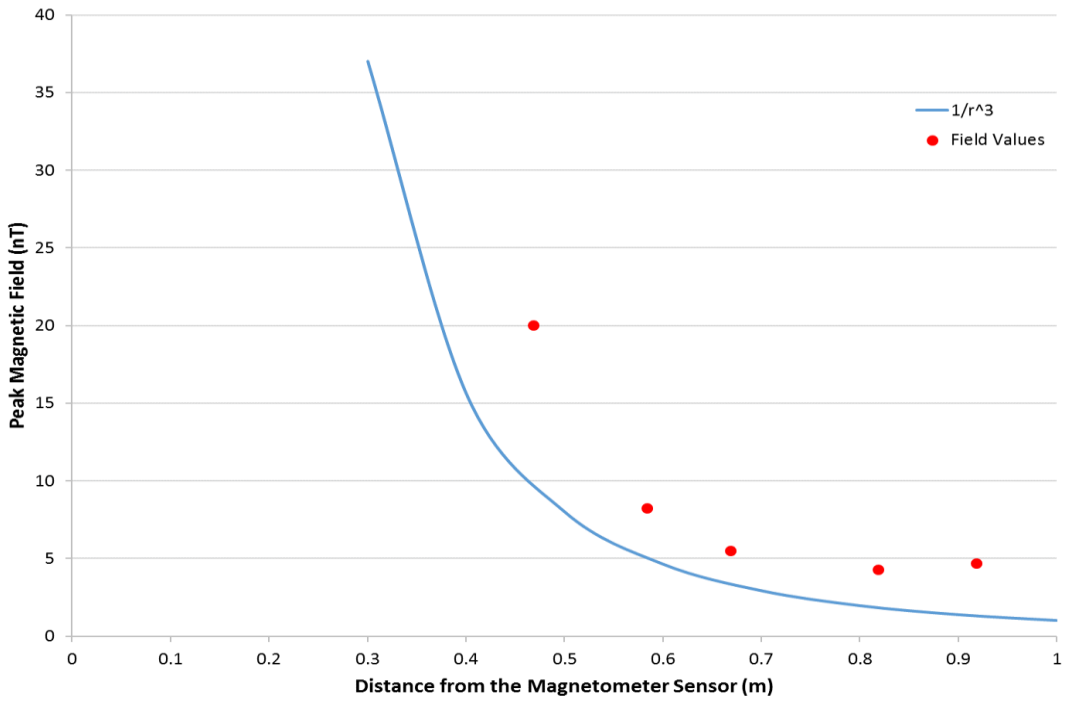

Figure 5.22: *A comparison of the decay of $1/r^3$ to the peak field trial values.*

In comparing the results of a magnetic decay following the inverse cube law to the peak magnetic field results gained at different depths during field trial 1, it can be seen that all of the field trial results are located above the inverse cube line. This is especially seen for the last two points where the magnetometer sensor was at a distance of 0.73 m and 0.83 m from the magnetic grout sample. At this point the inverse cube line continues to drop down towards a value of 1, whereas the field trial results level off, suggesting that the field trial results do not exactly decay by the inverse cube law. This difference between the field trial results and the inverse cube line could be related to the effect of the Earth's magnetic field on the field trial results. As the Earth's magnetic field is inclined at an angle of 69.467° (calculated using the online magnetic field calculator provided by Geomatrix Earth Science Ltd on their website (Geomatrix Earth Science Ltd, 2016)), and not vertical as is presumed by the equation, the magnetic field values gained will differ from the theoretical results. This difference could also be a result of measurement error in the horizontal positioning of the magnetometer, resulting in some background field value remaining at distance within the data even after the initial magnetic field survey (with no grout present) has been removed.

5.2.9 Conclusions of Field Trial 1

Overall, the results of field trial 1 have shown that it is possible to upscale the small 10 ml magnetic grout samples used in the laboratory experiments to larger samples that are detectable in the field. In trialling magnetic grout mixtures containing both 5% and 10% magnetite, a marked difference can be seen in the resulting magnetic signal achieved. With the magnetic grout mixtures containing 10% magnetite producing a larger magnetic signal. In using different shapes during this trial, it has been possible to determine whether different shapes have any effect on the shape of the magnetic anomaly produced by the magnetic grout. As seen from the field trial results slightly different shaped magnetic anomalies were produced for the rectangular and disc shaped magnetic grout samples, although it is hard to determine the accuracy of these shapes due to the 0.5 m spacing used for data collection in the walkover survey.

This trial has also shown that the magnetic grout can be detected when buried, with a magnetic signal still being detected at the furthest distance measured from the magnetometer sensors in this field trial (91.85 cm). In burying the magnetic grout samples at different distances away from the magnetometer sensors, it can be seen that the peak magnetic field diminishes towards the background field value, with increasing distance from the magnetometer sensors.

In comparing the field trial results to the $1/r^3$ model, similarities in the trend of both data sets can be easily seen. This suggests that the magnetic field values obtained during the field trial decay following a $1/r^3$ law. However, a difference between the model and the field data sets is apparent for the values recorded at the largest distance from the magnetic grout samples. This is likely to be a result of error in the removal of the background field.

Field trial 1 has provided proof of concept for development of a magnetic grout that is detectable at depth.

5.3 Field Trial 2

This section will present the results gained from field trial 2 which was undertaken between the 29th September and 4th October 2015.

5.3.1 Aims and Objectives of Field Trial 2

The main aim of field trial 2 was to determine the decay of the magnetic field with distance from the magnetic grout sample. The following were the main objectives of field trial 2:

- To ascertain the maximum horizontal distance at which a certain volume of magnetic grout can be detected.
- To determine more accurately, the shape of the magnetic field around the magnetic grout sample.
- To establish how the magnetic field of the magnetic grout sample changed with vertical distance.

To fulfil the aims and objectives of this field trial, three different trial set-ups were utilised. The first trial set-up was composed of a single 13 m long transect line located to the South of the magnetic grout. At each measurement location, magnetometer readings were taken at four different vertical heights. The aims of this set-up were to determine the maximum horizontal distance at which the magnetic grout could be detected and how the magnetic field changed with vertical distance. The second trial set-up had four 1 m transect lines that radiated out from the magnetic grout in approximately, North, South, East, and West orientations. At each measurement location, magnetometer readings were taken at six different vertical heights. The aims of this set up were to determine how the shape of the magnetic field changed with orientation around the magnetic grout, and how the magnetic field changed with vertical height. The third trial set-up was comprised of six 3 m transect lines that radiated out from the magnetic grout in approximately, North, South, North-West, North-East, South-West, and South-East orientations. At each measurement location,

magnetometer readings were taken at two vertical heights. This set up built upon the findings of the previous two set ups with the aims being to determine the shape of the magnetic field around the magnetic grout, and how the magnetic field changed with height. Further detail of these three set-ups can be found in Section 5.3.3.3.

5.3.2 Location of Field Trial 2

Field trial 2 was undertaken at a similar location to field trial 1, on the beach at Troon (Figure 5.23). This location was again chosen for field trial 2 since it had already been established in field trial 1 that the area was generally magnetically quiet. Also, the sand allowed the different trial configurations to be easily setup.

Figure 5.23: *A satellite image showing the location of Field Trial 2 at Troon (Google Maps, 2016b).*

5.3.3 Methods

This section will detail how the large magnetic grout samples were produced, the equipment used throughout the duration of the trial, and the set-up of the trial positions.

5.3.3.1 Magnetic Grout Samples

Larger identical magnetic grout samples, each in the shape of a disc with a hole in the centre, were produced for use in field trial 2. The shape of a disc was chosen so that the trial could simulate the shape of a borehole, as this is the likely scenario in which the magnetic grout would be used. All the samples were produced using Ultrafin cement and contained 10% magnetite. The magnetite used in the production of these samples was magnetite 3, as the two previous batches had been depleted. The samples were produced with a water to solids ratio of 0.48, and also contained superplasticiser and stabilising agent. The amount of superplasticiser used was 1% of the total water within the cement mixture, with the dose of the stabilising agent being 10% of the total used, with 50% of the stabilising agent itself contributing to the overall water content. This mixture was chosen due to its favourable engineering properties that were established in Chapter 4, Section 4.3.3. Five magnetic cement discs were produced in a large batch, with the overall mixture being as follows:

Ultrafin cement – 50 kg
Water – 24.7 kg
Magnetite – 5 kg
Superplasticiser (Glenium 51) – 0.26 kg
Stabilising Agent (GroutAid) – 2.6 kg

The procedure used for producing the cement mixture is as follows: Firstly the Ultrafin cement and magnetite powders are thoroughly mixed together before any of the other components of the cement mixture are added. This is to ensure that the magnetite is evenly distributed throughout the dry cement powder. The water is then added to the mixture and is mixed until the water has penetrated throughout all the dry materials. At this stage in the mixing process, the cement mixture is extremely thick, and is not of a pourable consistency. The addition of the superplasticiser and stabilising agent loosens the consistency of the mixture, and allows it to become a viable grout mixture.

Once the grout has been thoroughly mixed, it is evenly distributed between five ready prepared identical moulds and left to set. The moulds used in this trial were 40 cm diameter baking tins. To ensure that the cement discs could be easily removed from the tins, they were firstly greased and then layered with a bin liner, before being greased again and lined with plastic sheeting on both the bottom and sides of the tin. To enable a hole to be cast in the centre of the disc a piece of wooden doweling was thoroughly greased and placed in the centre of the tin. The tins were then given a final layer of grease before the cement mixture was poured into the tins, being careful not to change the position of the wooden doweling (Figure 5.24). The samples were left for four days before they were turned out of the moulds. The wooden doweling was then removed from the centre of the grouted discs.

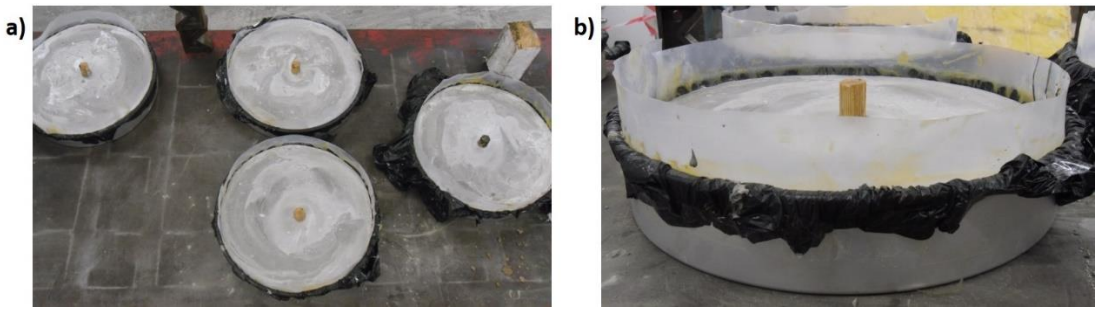

Figure 5.24: *Photographs of a) four of the five magnetic cement discs curing within their moulds, and b) a side view of a magnetic cement disc within its mould.*

The magnetic susceptibility of this grout mixture was tested following the same procedure used in Chapter 4, Section 4.2.1.1, with the susceptibility being recorded as 0.0727.

5.3.3.2 Equipment

The equipment used in field trial 2 was the same as that used previously in field trial 1. A G-858 MagMapper Magnetometer was hired for the duration of the trial from Geomatrix Earth Science Ltd. It is provided with two separate sensors which can be used simultaneously as a gradiometer, or independently as separate magnetometers.

In this trial both sensors were used as individual magnetometers in a vertical orientation.

To minimise the location errors that were the source of so much uncertainty in Field trial 1, a Trimble S6 Total Station (Figure 5.25) was also used to survey the positions at which the magnetic measurements were taken. This ensured that errors in the relative locations of the magnetometer between surveys were minimised.

Figure 5.25: *A photograph showing the Trimble S6 Total Station used in the field trial.*

5.3.3.3 Trial Setup

This section will detail the three different setups which were utilised at Troon over the trial period.

Throughout field trial 2, both magnetometer sensors were placed on a wooden pole on which a vertical height scale had been measured and marked, so that each sensor could be accurately located. During the trial the magnetometer sensors were sited so that the top of the sensor holder was always aligned with the marked vertical height position on the pole. Additionally, the sensors were always oriented such that they pointed towards North. Each of the different trial setups were allocated different combinations of vertical heights for magnetic measurements to be taken at, and these are explained in more detail below. For each measurement location within a survey (both horizontal

and vertical) a background measurement was taken, before the magnetic grout discs were put in place. This ensured that as before, the background magnetic field could be removed from the magnetic field data collected with the magnetic grout discs present. In each of the three different sampling arrangements discussed below, the 5 magnetic grout discs were stacked on top of each other to create a single anomaly.

For the first setup, a transect line was laid out on the South side of the stack of magnetic grout sample discs (Figure 5.26). Along this transect line, measurement locations were marked out at the following positions; 0.5 m, 1 m, 1.5 m, 2 m, 3 m, 4 m, 5 m, 7 m, 9 m, 11 m, and 13 m. At each of these measurement locations a magnetometer reading was taken at four vertical heights above ground level; 0.2 m, 0.35 m, 0.5 m, and 0.65 m. Figure 5.27 shows a photograph of data being collected along the transect line to the South of the magnetic grout discs.

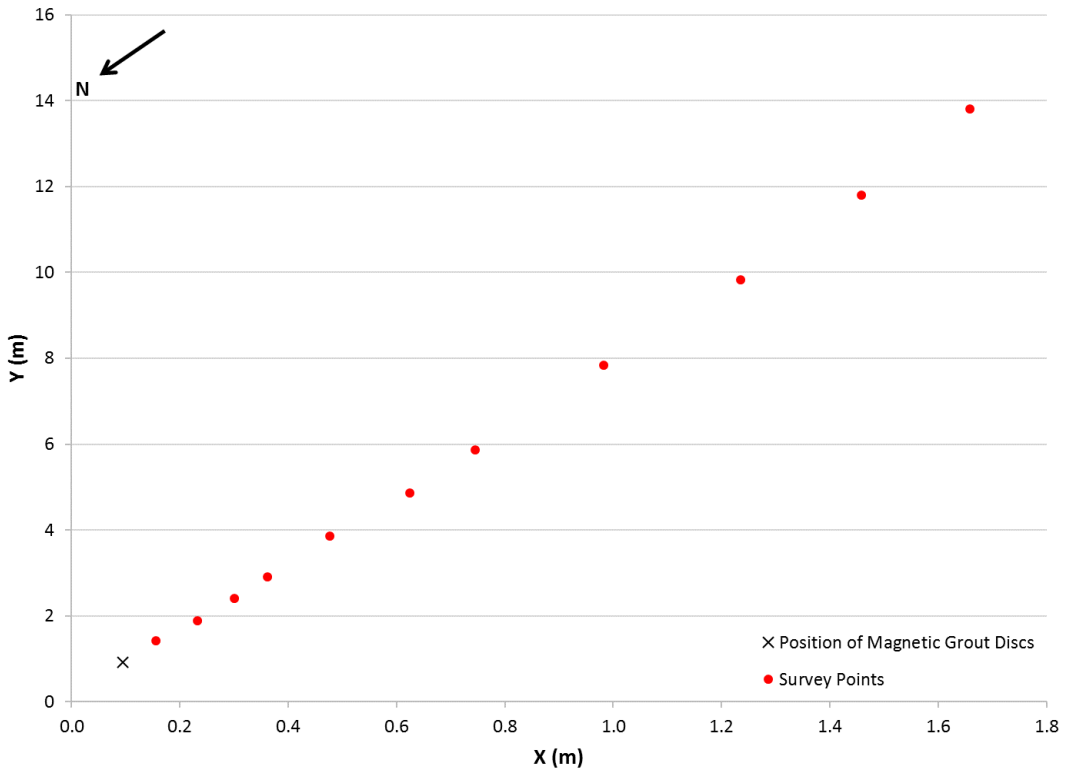

Figure 5.26: *The location of the survey points for trial setup 1.*

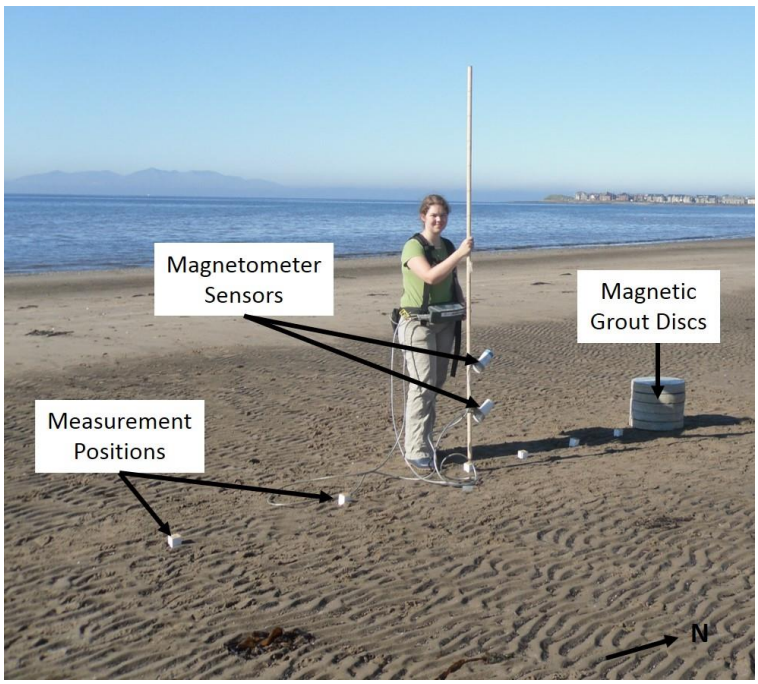

Figure 5.27: *A photograph showing data being collected during trial setup 1.*

The second trial setup was laid out with transect lines radiating from the stack of magnetic grout sample discs in approximately North, South, East, and West directions (Figure 5.28). Along each transect line, measurement locations were marked out at the following positons, 0.5 m, 0.75 m, and 1 m. For each of these measurement locations, magnetometer readings were taken at vertical heights above ground level of 0.1 m, 0.2 m, 0.35 m, 0.5 m, 0.65 m, and 0.8 m.

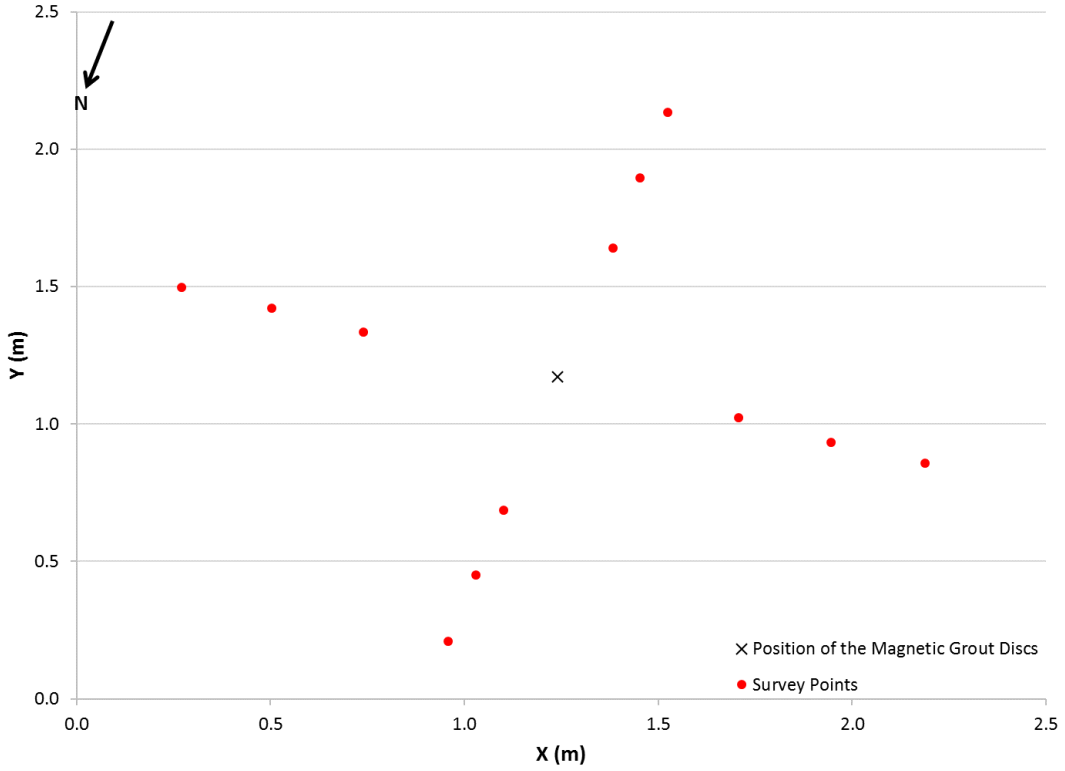

Figure 5.28: *The location of the survey points for the second trial setup.*

The third trial setup was laid out with the transect lines radiating from the stack of magnetic grout sample discs in North, South, North-West, North-East, South-West, and South-East directions (Figure 5.29). Along each transect line, measurement locations were marked out at the following positions, 0.5 m, 1 m, 1.5 m, 2 m, and 3 m. At each of these measurement locations a magnetometer reading was taken at the vertical heights above ground level of 0.35 m, and 0.8 m. Figure 5.30 shows a photograph of this trial setup before the magnetic grout discs were placed in position.

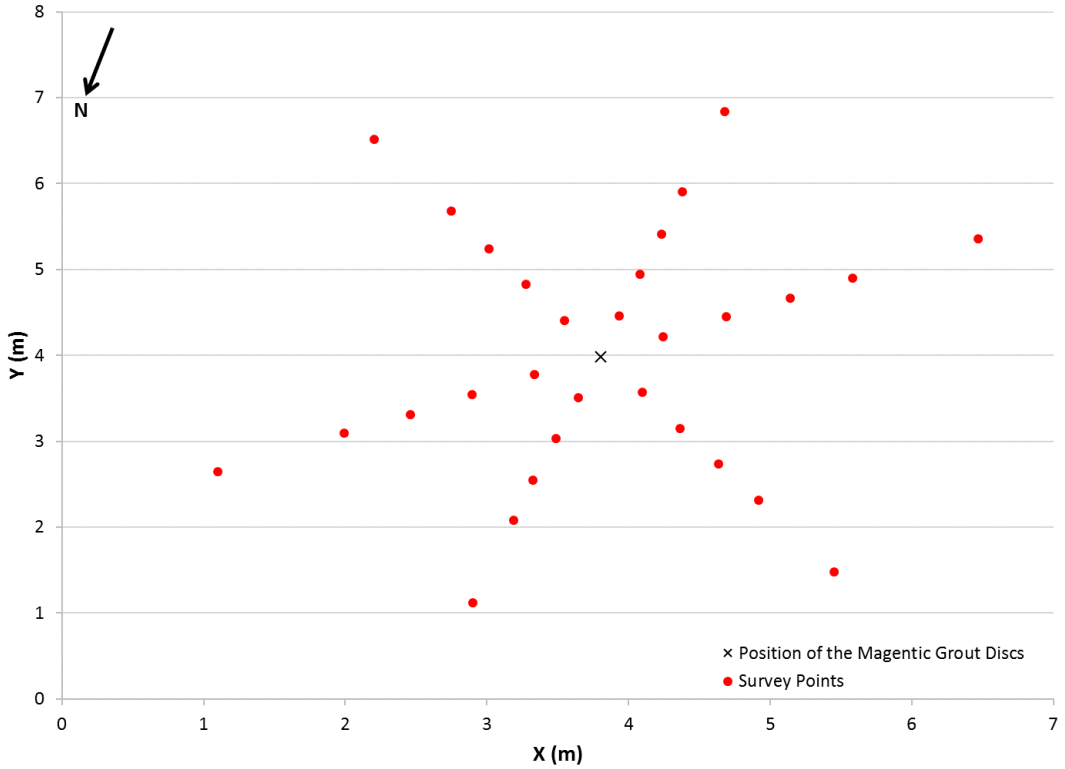

Figure 5.29: *The location of the survey points for the third trial setup.*

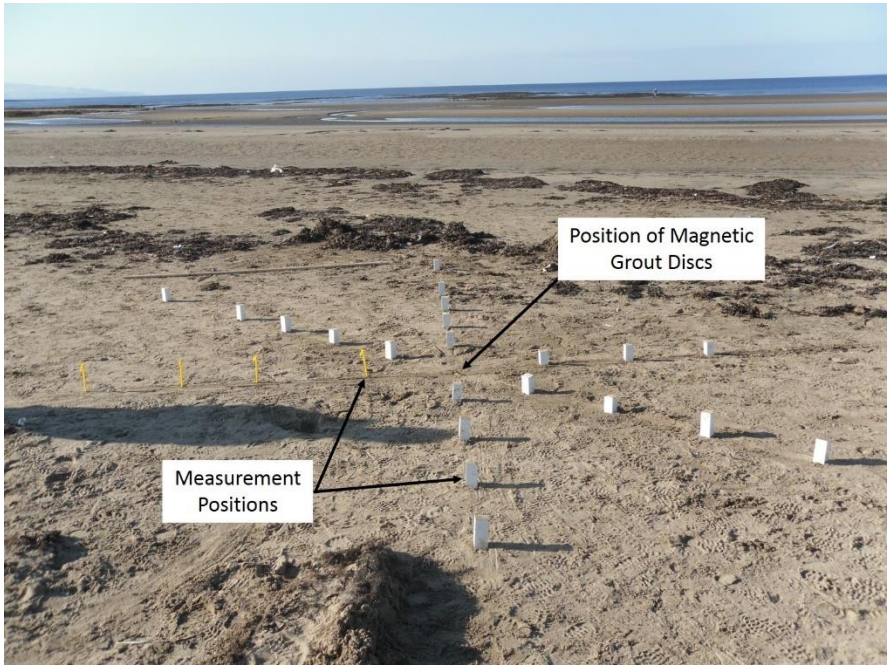

Figure 5.30: *A photograph showing the measurement positions of trial setup 3. (NB: The position markers were subsequently hammered down level to the sand surface).*

For each of the setups detailed above, the location of each measurement position (e.g. Figure 5.30) was surveyed, before any magnetic field measurements were taken. Every time a magnetic measurement was taken, a new survey measurement was obtained to ensure that the background data collected and the measurements acquired with the magnetic grout samples in situ were as accurate as possible.

The surveying was undertaken by firstly setting up a reference point that was adjacent to the total station. This reference point was located at a height of 0.1 m from the ground level and was given the arbitrary values of Easting – 500 m, Northing – 1000 m, and Elevation – 100 m. All the measurement location points were then surveyed in relation to this reference point. To gain both the location of the measurement points and the elevation of the magnetometer sensor, a target was placed on the pole holding the sensors in place. This target was located at a height of 1.2 m for all three survey setups. In using the automatic target recognition function on the total station, the total station was able to follow the target to each measurement position before a survey measurement was taken.

5.3.4 Data Analysis for Field Trial 2

This section will detail how the raw magnetic field data gained from field trial 2 were analysed.

The first stage of data analysis was to process the raw magnetic field data gained from the background measurements, and the sample measurements which were taken when the magnetic grout discs were present. To gain a clearer view of the magnetic field produced only by the magnetic grout discs, the background field data were again removed from each dataset collected. The results could then be used to plot transect lines, and anomaly response graphs, and also for the contour maps detailed below.

The magnetic data were combined with the survey data to identify the exact locations of every reading taken. Before this could be achieved, several steps needed to be undertaken to process the survey data. In undertaking the surveying, arbitrary values

for the Easting (500 m), Northing (1000 m), and Elevation (100 m) were set for the base station reference point. This reference point was different on each day of the field trial. All of the survey points gained therefore reference this point and have values around these numbers. At each magnetic measurement point, the elevation of the height of the target which was located 1.2 m above ground level was recorded. To gain the correct elevation of the sensor positions the difference between the height of the target and the sensor position was calculated. The difference values can be seen in Table 5.2.

Table 5.2: *The calculated differences between the target height and the sensor position.*

Sensor Positon (m)	**Difference between Target Height and Sensor Position (m)**
0.1	1.1
0.2	1
0.35	0.85
0.5	0.7
0.65	0.55
0.8	0.4

These differences are then subtracted from the target elevation value to gain the actual elevations of the sensor positions. These calculated elevations of the sensor positions are then subtracted from the target elevation value. Finally, to gain the correct elevation for each sensor positon 0.1 m was added back onto the sensor position elevation as the reference point located adjacent to the total station was at an elevation of 0.1 m above sea level.

As each sensor position had a very slightly different elevation value (although the intention was to survey at the same height), to be consistent throughout the thesis, the sensor height positions were averaged to give an average elevation for each sensor

position in the vertical. The final average values for the heights of the magnetometer sensors were: 0.085 m, 0.186 m, 0.336 m, 0.486 m, 0.636 m, and 0.786 m.

5.3.4.1 Formation of Contour Maps

Contour maps were produced to better visualise and compare the data gained at the different vertical heights. To produce the contour maps, the background field data without the discs present were once again removed from each set of survey data. This allowed for a clear view of the magnetic field generated by the grout discs. The data for each vertical height in trial setup 2 and 3 were then imported into Matlab, along with the corresponding X and Y coordinates for each position. These data were then contoured to produced anomaly maps such as that in Figure 5.31 below.

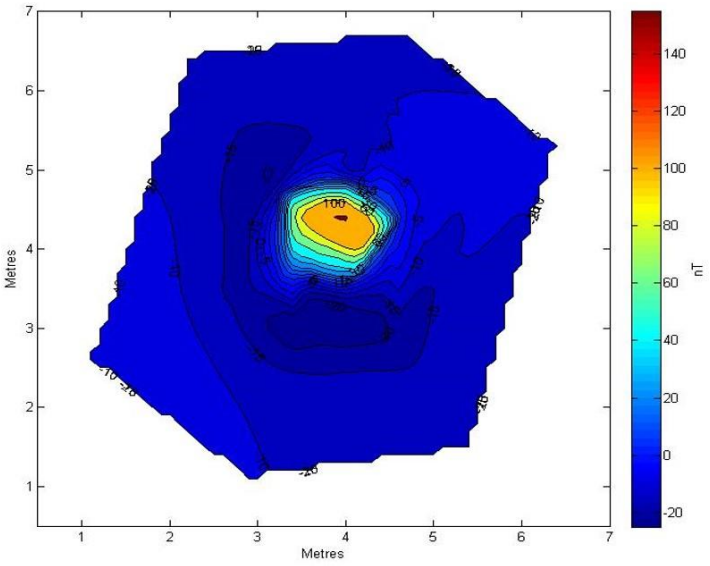

Figure 5.31: *A contour map showing the data being interpolated across the central area.*

From Figure 5.31 it can be seen that the data have been interpolated across the central area of the contour map produced. In this area, it was not possible to collect data, as this is the location of the magnetic grout discs. To produce a contour map without interpolating across the central area, new data points were created with coordinates located in this area. These points were assigned with the value 'NaN' (in Matlab this stands for 'Not a Number'). Additionally, further data points were created around the

edge of the magnetic grout disc from data produced using a model. Figure 5.32 shows the position of the new points assigned with the value 'NaN', and also the points at the edge of the magnetic grout discs, in relation to the original data points.

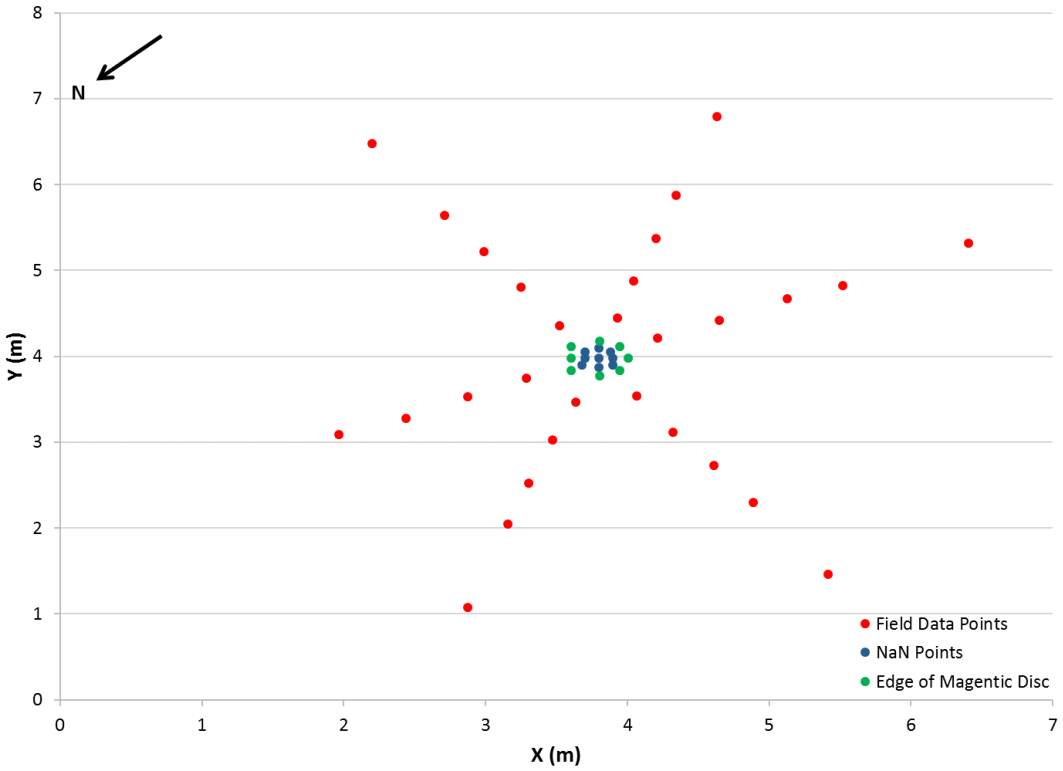

Figure 5.32: *The location of NaN data points in relation to the field data points.*

The data set including the new points was then imported back into Matlab, and was again used to produce a contour map. Figure 5.33 gives an example of the contour map produced with the central area of no data removed.

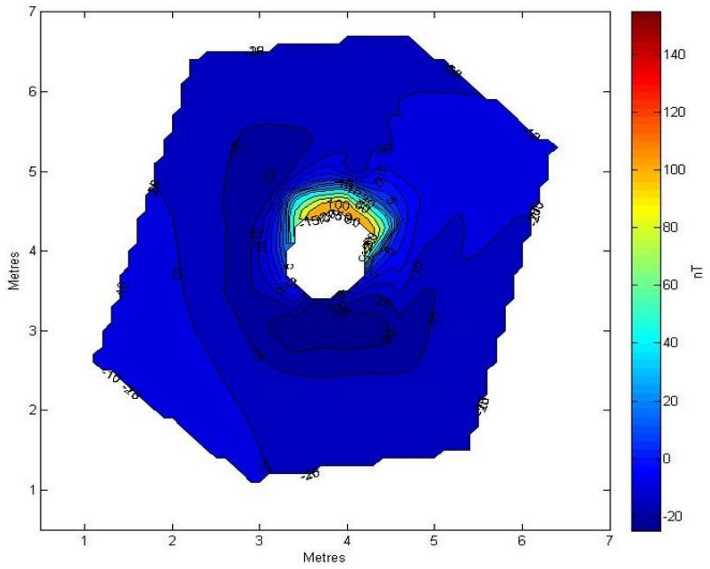

Figure 5.33: *A contour map produced with the additional NaN values, and data points surrounding the edge of the magnetic grout disc.*

The contour map is not entirely accurate at the boundaries, as interpolation beyond the measured points is not possible. Since it is known that theoretically, at distance, the magnetic field generated by the grouted samples must tend to zero, additional points with a value of zero were added to each dataset prior to interpolating at a distance of 5 m from the grout discs. The distance of 5 m was chosen for these points as this was a distance at which the magnetic field from the magnetic grout discs could not be detected in the field trial. Figure 5.34 shows the location of the additional zero value data points in relation to the original field trial data points, and Figure 5.35 shows an example of a contour map produced using this data set.

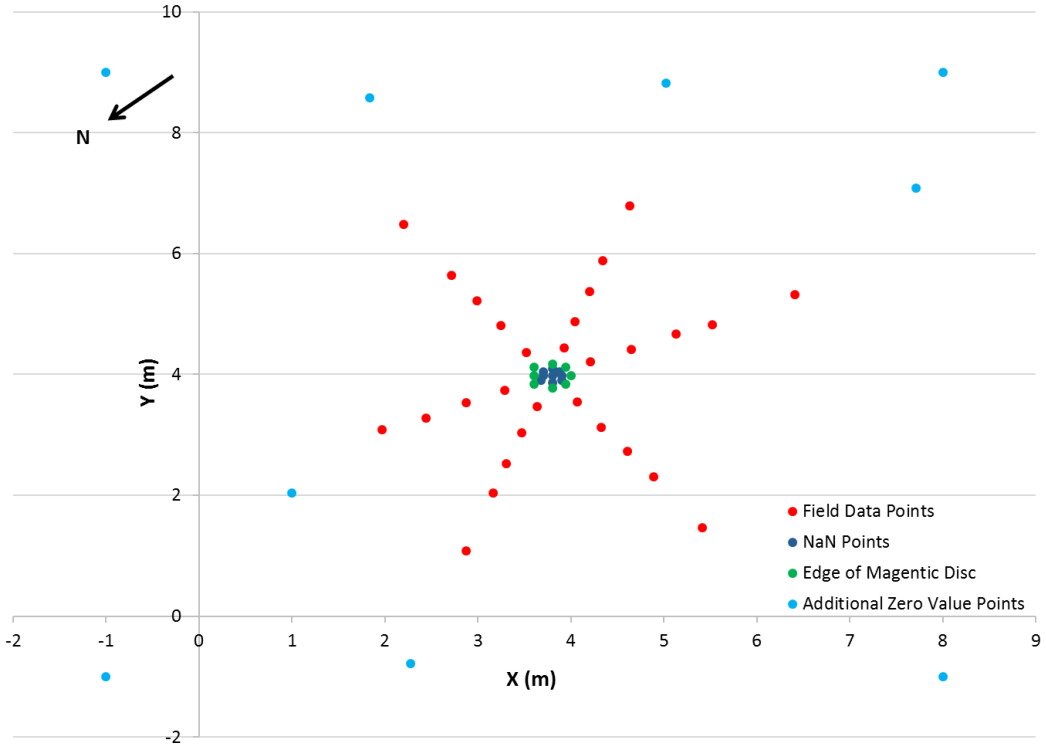

Figure 5.34: *The location of the additional zero value points.*

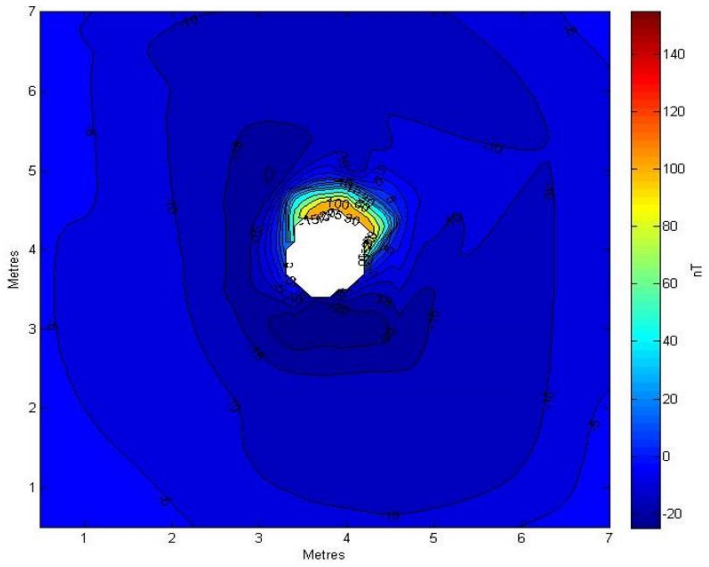

Figure 5.35: *A contour map produced with the data set containing the additional zero value points.*

The final stage in the creation of the contour maps was to focus in on the area that contained the actual data points from the trial. To achieve this the axis were set at

0.2 m to 2.2 m for trial setup 2, and 0 m to 7 m for trial setup 3. By setting the axis to these values, the extent of the area containing the points with data collected in the trial can be seen and the areas where zero values were artificially added to aid the interpolation process, are excluded. The data points that mark the locations of the magnetic data collected in the field were also highlighted in white.

To ensure that the contour maps produced for each of the trial setups could be easily compared to each other, all the contours were scaled to be the same. For trial setup 2 the minimum and maximum values used were -400 nT and 400 nT, and for trial setup 3 they were - 325 nT and 155 nT. These values were chosen as they best represented the data gained from each of the trial setups. Figure 5.36a, b gives an example of the final contour maps produced for trial setups 2 and 3 respectively.

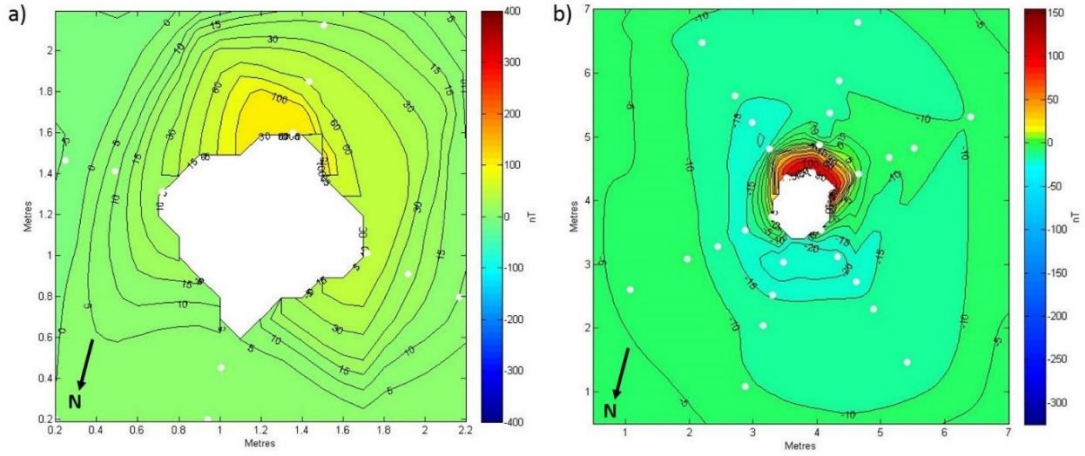

Figure 5.36: *Final contour maps from a) trial setup 2, and b) trial setup 3.*

5.3.5 Results of Field Trial 2

This section will focus on the results gained from field trial 2. It will firstly look at the trial setup (trial setup 1) where one transect line was laid out to the South of the magnetic field discs to a length of 13 m from the centre of the magnetic grout discs. Trial setup 2 contains the magnetic field data from transect lines running to the North, South, East, and West of the magnetic grout discs. These transect lines continue to a distance of 1 m from the centre of the magnetic grout discs. Trial setup 3 contained

the magnetic field data obtained from transect lines running to the North, South, North West, North East, South West, and South East of the magnetic grout discs. These transect lines ran to a distance of 3 m from the centre of the magnetic grout discs.

This section will then move on to look at a comparison of the data obtained during field trial 2 and data produced by a model.

5.3.5.1 Trial Setup 1

The graph showing the magnetic field for the transect line located to the South of the five cement discs can be seen in Figure 5.37. From this graph, it can be seen that, as expected, the magnetic field decays rapidly with distance away from the magnetic grout discs. The largest magnetic field response can be seen at a horizontal distance of 0.5 m from the magnetic grout discs. The largest positive (481.555 nT) and negative (-3334.258 nT) magnetic anomalies were recorded at this horizontal distance.

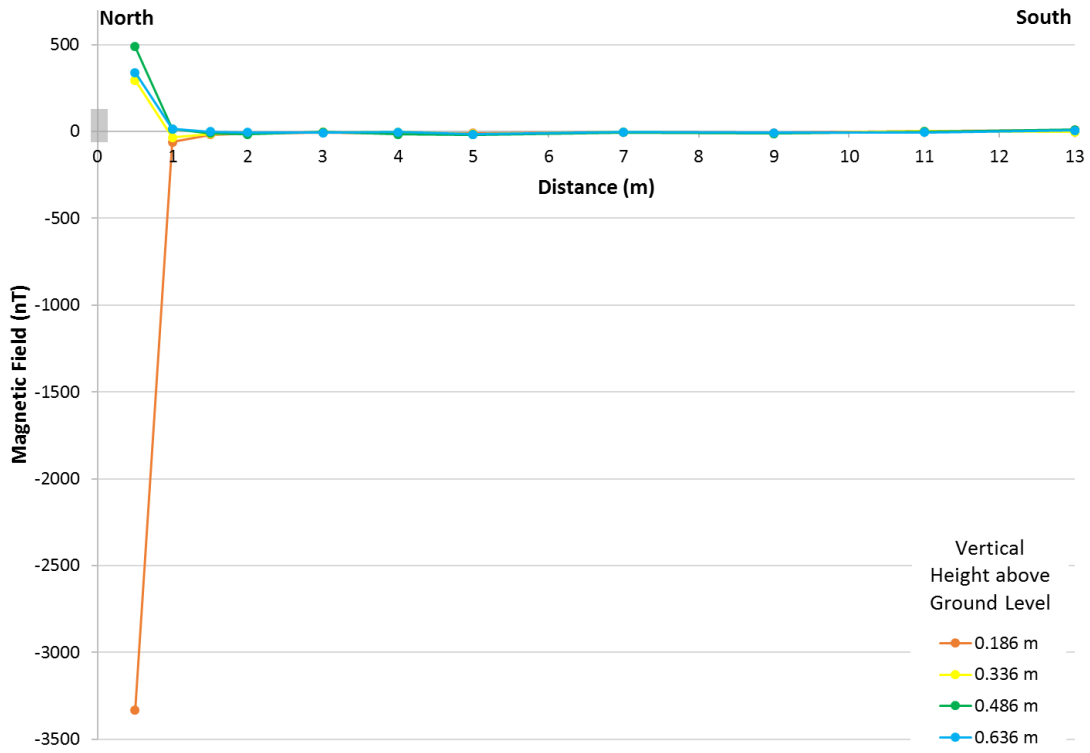

Figure 5.37: *The magnetic field of one transect line located to the South of the five magnetic grout discs.*

Figure 5.38 and Figure 5.39 (an enlarged view) present the vertical magnetic response of the magnetic grout discs from the same data as plotted in Figure 5.37. This graph shows the location of the magnetic measurements in relation to the height of the magnetic grout discs. The largest negative magnetic anomaly was produced at an elevation that is within the vertical height of the sample. As vertical height increased above the top of the stack of magnetic grout discs, the magnetic anomaly produced became positive, with the largest positive anomaly being produced at a vertical height of 0.486 m above ground level (0.15 m above the top of the magnetic grout discs). As the horizontal distance from the grout discs increases the magnitude of the magnetic anomaly produced at the different vertical heights decreases rapidly.

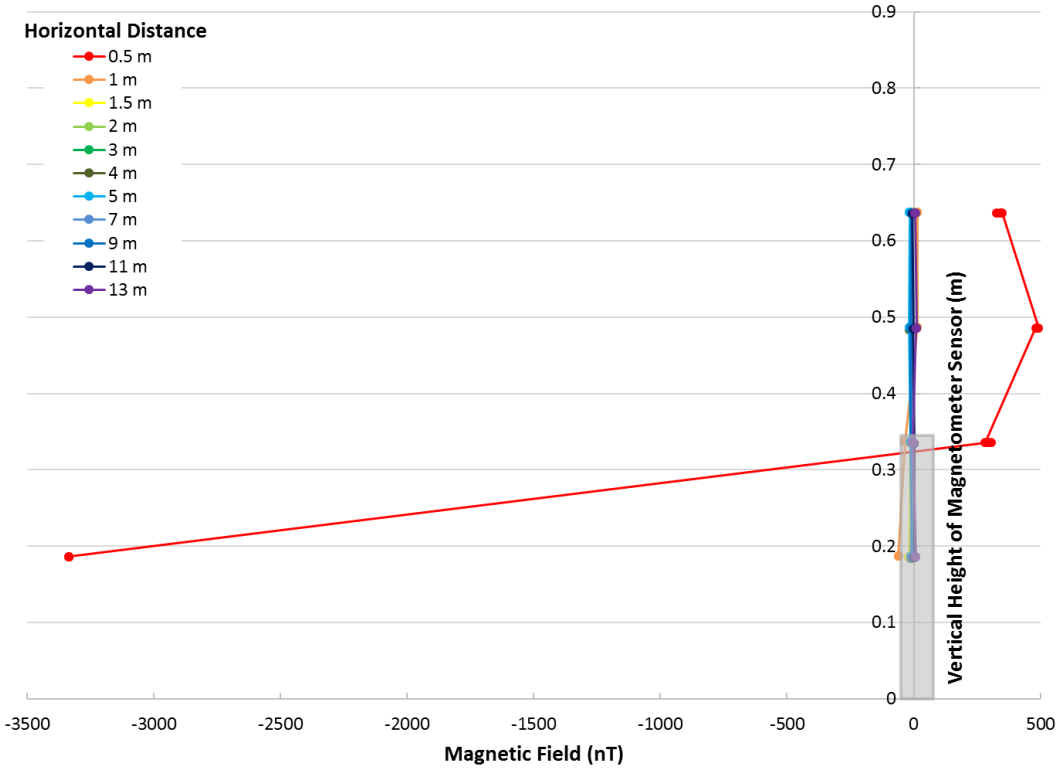

Figure 5.38: *The vertical magnetic response to the South of the magnetic grout discs.*

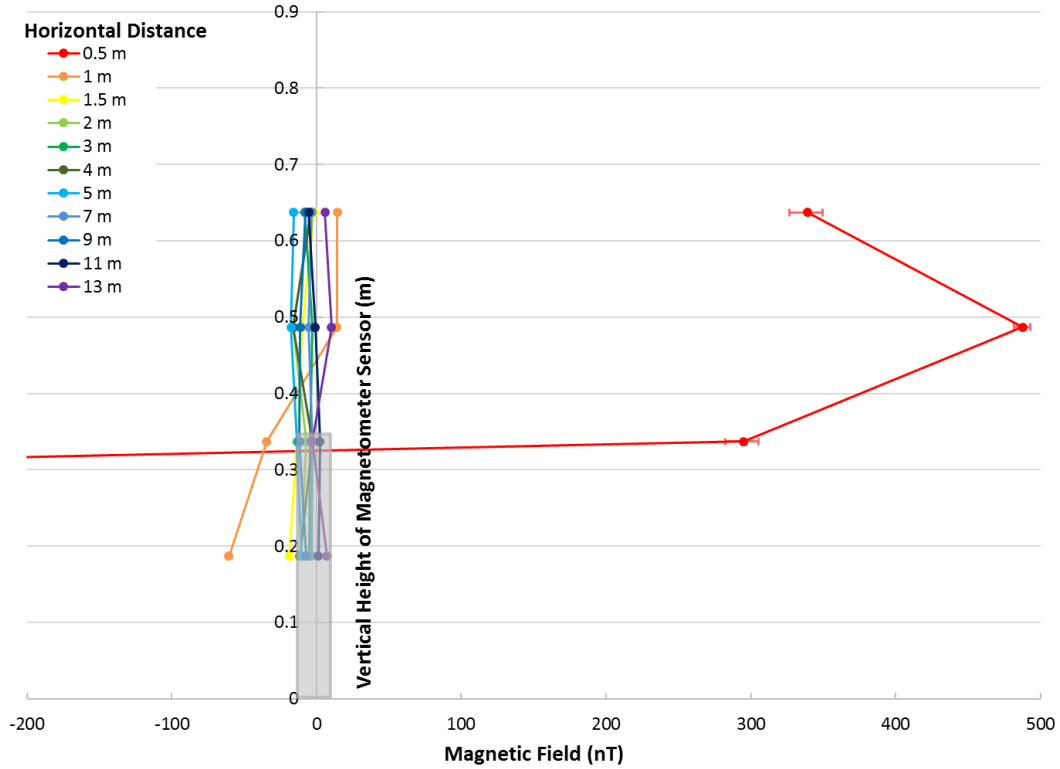

Figure 5.39: *The vertical magnetic response to the South of the magnetic grout discs. This graph shows a more detailed view of the results presented in Figure 5.38.*

5.3.5.2 Trial Setup 2

For the second trial setup, measurements were taken in four different directions, North, East, South, and West, with magnetic field measurements being taken at horizontal distances of 0.5 m, 0.75 m, and 1 m from the magnetic grout discs. Figure 5.40 and Figure 5.41 shows the magnetic response recorded along the North-South line, with the centre of the magnetic discs being located at point 0,0. Figure 5.41 shows an enlarged view of the results shown in Figure 5.40. From these graphs, it can be seen that the magnetic field decays rapidly as the distance from the magnetic grout discs is increased. There is a larger range of the size of the magnetic field anomaly present to the South of the magnetic grout discs than to the North, with a significant negative anomaly (-5871.229 nT) being recorded at a vertical height of 0.085 m above ground level. The largest positive magnetic anomaly was located at a vertical height of 0.486 m above ground level with a value of 305.54 nT, also to the South. To the North of the magnetic grout discs, the magnetic field anomaly recorded is mainly negative at all vertical heights above ground level, apart from at 0.786 m which is slightly positive.

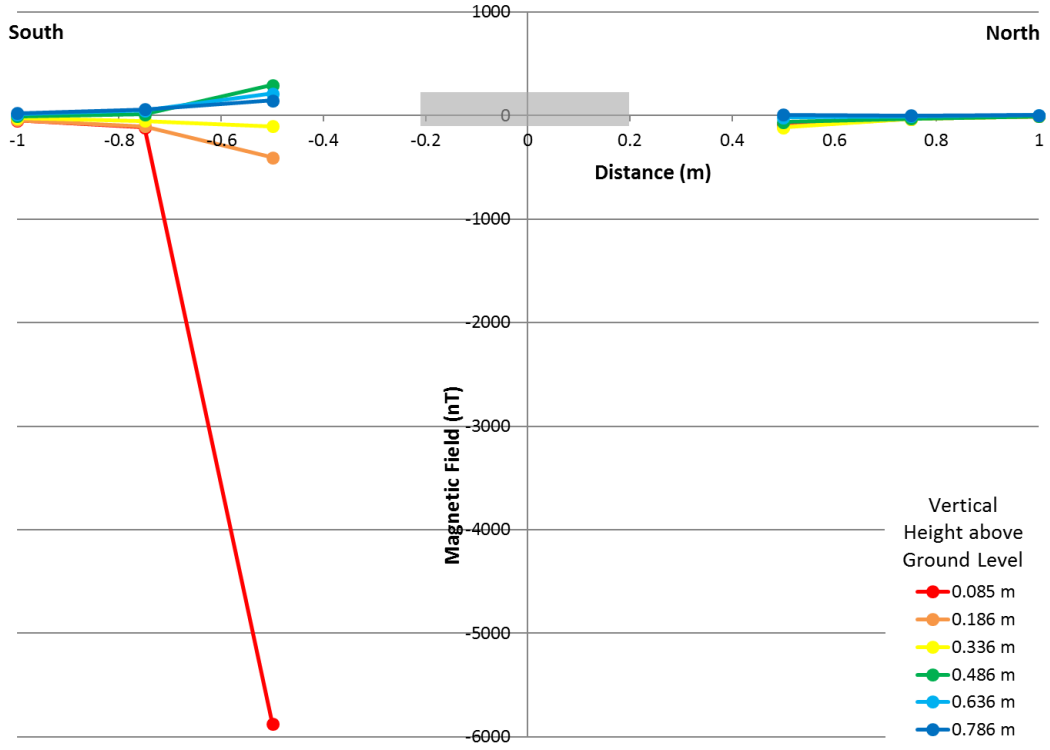

Figure 5.40: *The magnetic response along the North-South line, with the centre of the sample located at 0,0.*

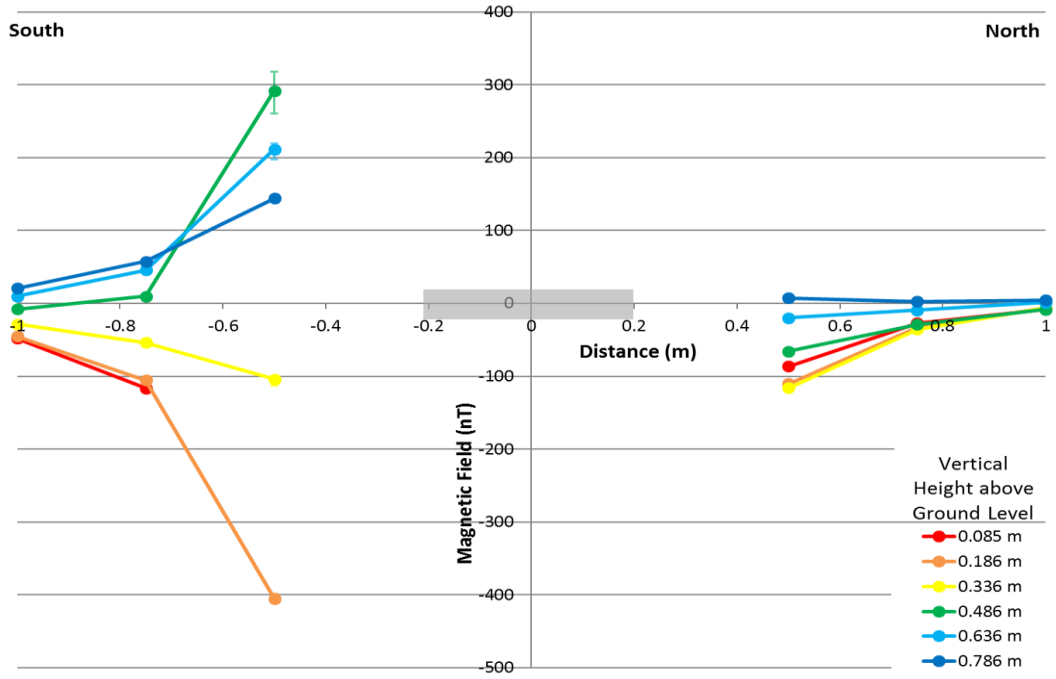

Figure 5.41: *The magnetic response along the North-South line, with the centre of the sample located at 0,0. This graph shows a more detailed view of the results presented in Figure 5.40.*

The graph in Figure 5.42 shows the shape of the magnetic anomaly formed over the vertical, to the North of the magnetic grout discs. The largest response to the magnetic grout discs can be seen when the magnetic field measurements were taken at a horizontal distance of 0.5 m from the discs. As the horizontal distance increases away from the magnetic grout discs, the size of the magnetic field anomaly decreases at all of the vertical height positions. The largest magnetic response was produced at a vertical height which corresponds with the height of the top of the magnetic grout discs. As the vertical height above the magnetic grout discs increases the magnetic anomaly produced changes from being negative to positive.

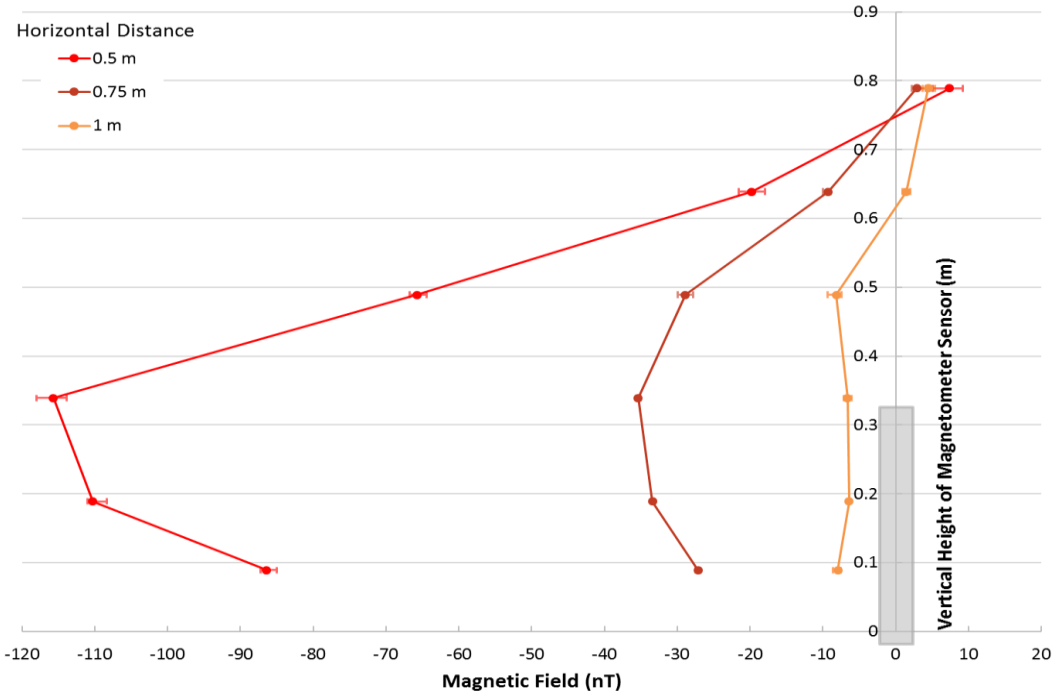

Figure 5.42: *The vertical magnetic response to the North of the magnetic grout discs.*

To the South of the magnetic grout discs (Figure 5.43), the shape of the vertical magnetic response is different to that seen in the North (Figure 5.42). The largest change in the vertical magnetic anomaly produced by the magnetic grout discs can be seen at a horizontal distance of 0.5 m. At the other two horizontal distances, there is a much smaller change in the vertical magnetic anomaly and it generally changes from being negative to positive in value as the vertical height increases.

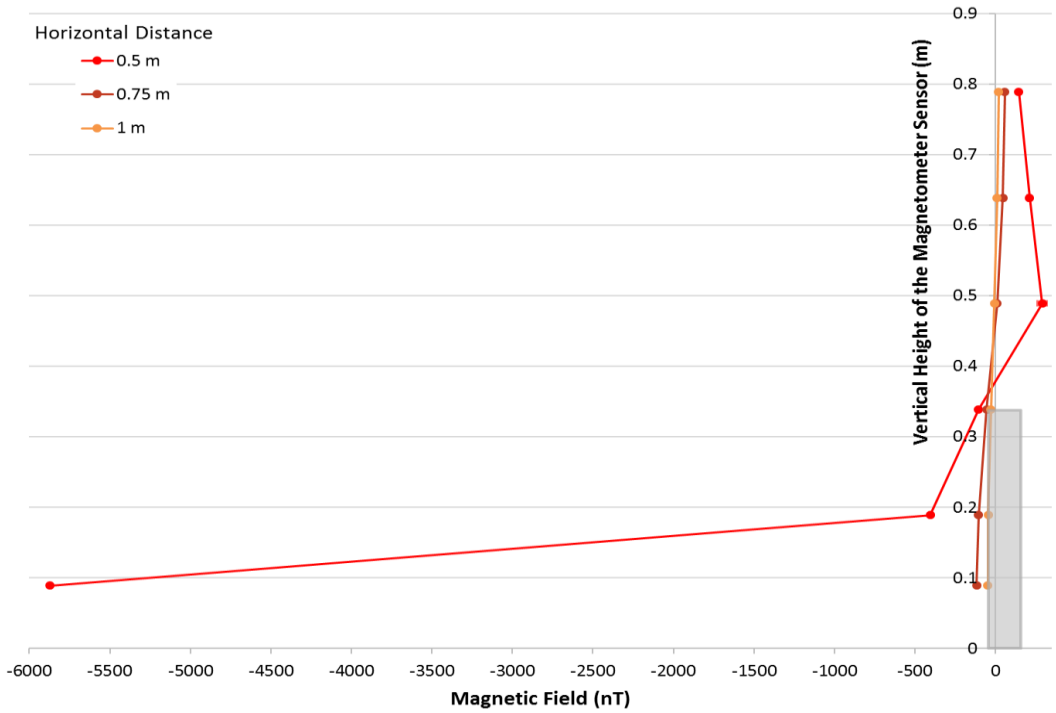

Figure 5.43: *The vertical magnetic response to the South of the magnetic grout discs.*

The East-West magnetic response line gained during the second trial setup can be seen in Figure 5.44. The measurements taken to the West of the magnetic grout discs have a larger range of magnetic field values compared to the East of the discs, however this range is not as large as was seen in the measurements to the South (Figure 5.40). As with the North-South cross-section in Figure 5.40 , the magnetic field decays rapidly as distance from the magnetic grout discs is increased. The largest positive (52.622 nT) and negative (-230.567 nT) anomalies were both detected to the West of the magnetic grout discs at vertical heights of 0.786 m and 0.186 m respectively.

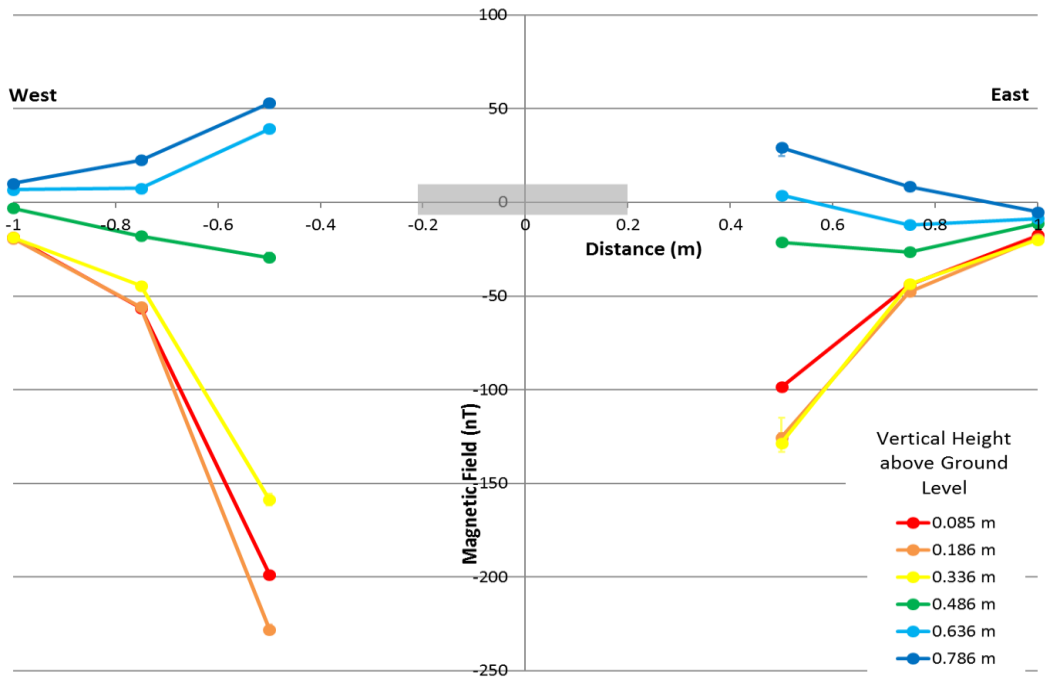

Figure 5.44: *The magnetic response along the East-West line, with the centre of the sample located at 0,0.*

Figure 5.45 presents the vertical magnetic response recorded to the East of the magnetic grout discs. The response seen follows a similar trend to that seen previously in other orientations around the magnetic grout discs. The largest magnetic response from the magnetic grout discs can be seen at a horizontal distance of 0.5 m, at a vertical height of 0.336 m above ground level. This vertical height corresponds to the top of the stack of magnetic grout discs. As the vertical height above the magnetic grout discs increases, the magnetic anomaly produced changes from being negative to positive for horizontal distances of 0.5 m and 0.75 m.

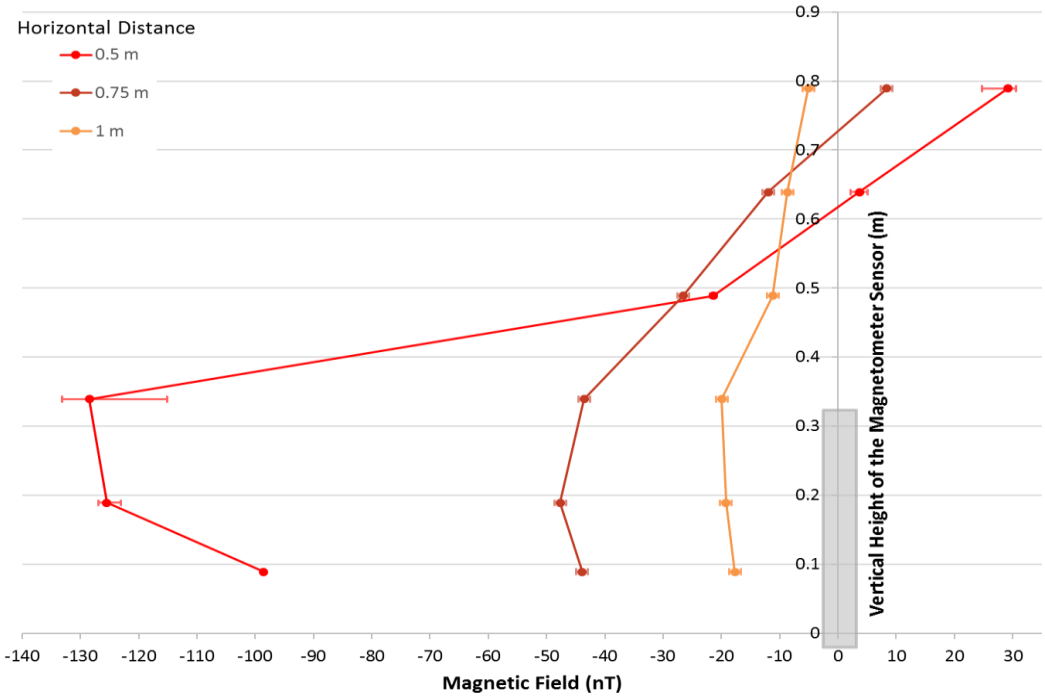

Figure 5.45: *The vertical magnetic response to the East of the magnetic grout discs.*

The magnetic response to the West of the magnetic grout discs is presented in Figure 5.46. This response is similar to that seen to the North and East of the magnetic grout discs in Figure 5.42 and Figure 5.45 respectively. The largest magnetic response is at a horizontal distance of 0.5 m from the magnetic grout discs with a vertical height of 0.186 m. This vertical height corresponds to around the midpoint of the magnetic grout discs. As the horizontal distance from the magnetic grout discs increases, the size of the magnetic anomaly produced decreases.

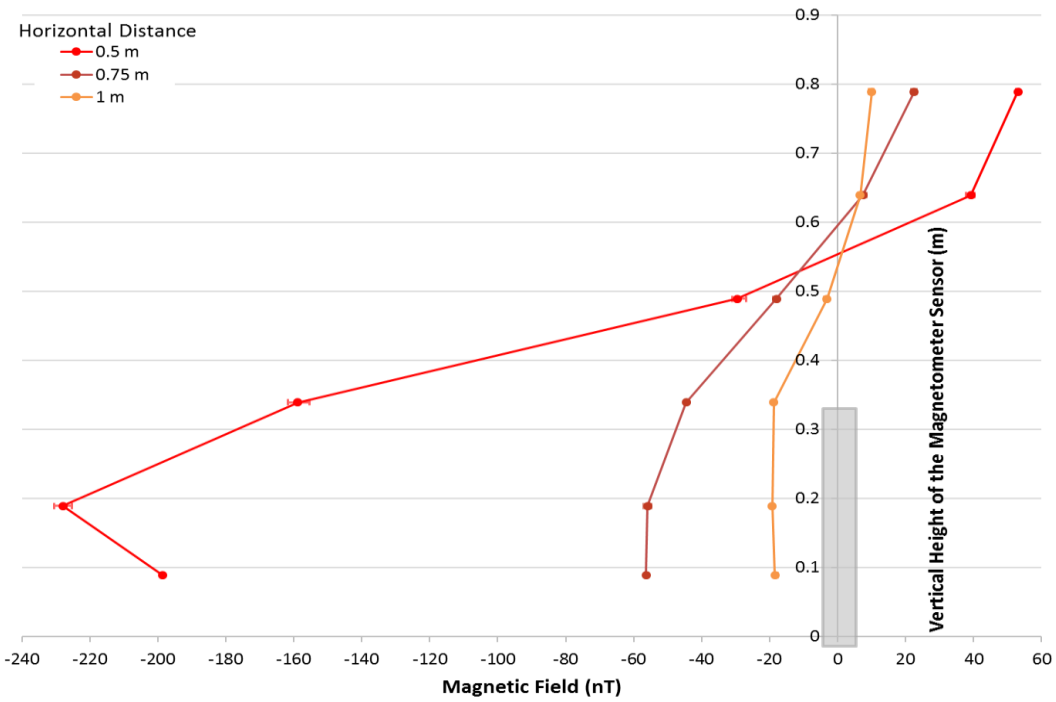

Figure 5.46: *The vertical magnetic response to the West of the magnetic grout discs.*

5.3.5.2.1 Trial Setup 2 Contour Maps

Figure 5.47 shows contour maps produced from the data gained from trial setup 2. At all of the vertical heights the largest magnetic response is toward the South of the magnetic grout discs. The largest negative magnetic field values were recorded at the lowest vertical height of 0.085 m above ground level, with the negative anomaly being present over 3 m away to the South of the magnetic grout discs. As the vertical height increased the magnetic anomaly remained negative for heights that are within the vertical range of the magnetic grout discs. Above the height of the discs a positive magnetic anomaly was recorded oriented toward the South. The largest positive magnetic anomalies were seen at a vertical height of 0.486 m above ground level. Additionally, at vertical heights of 0.486 m and 0.636 m a magnetic dipole is recorded, with the negative lobe of the magnetic anomaly oriented toward the North. As the vertical height continued to increase the value of the positive magnetic anomaly decreased.

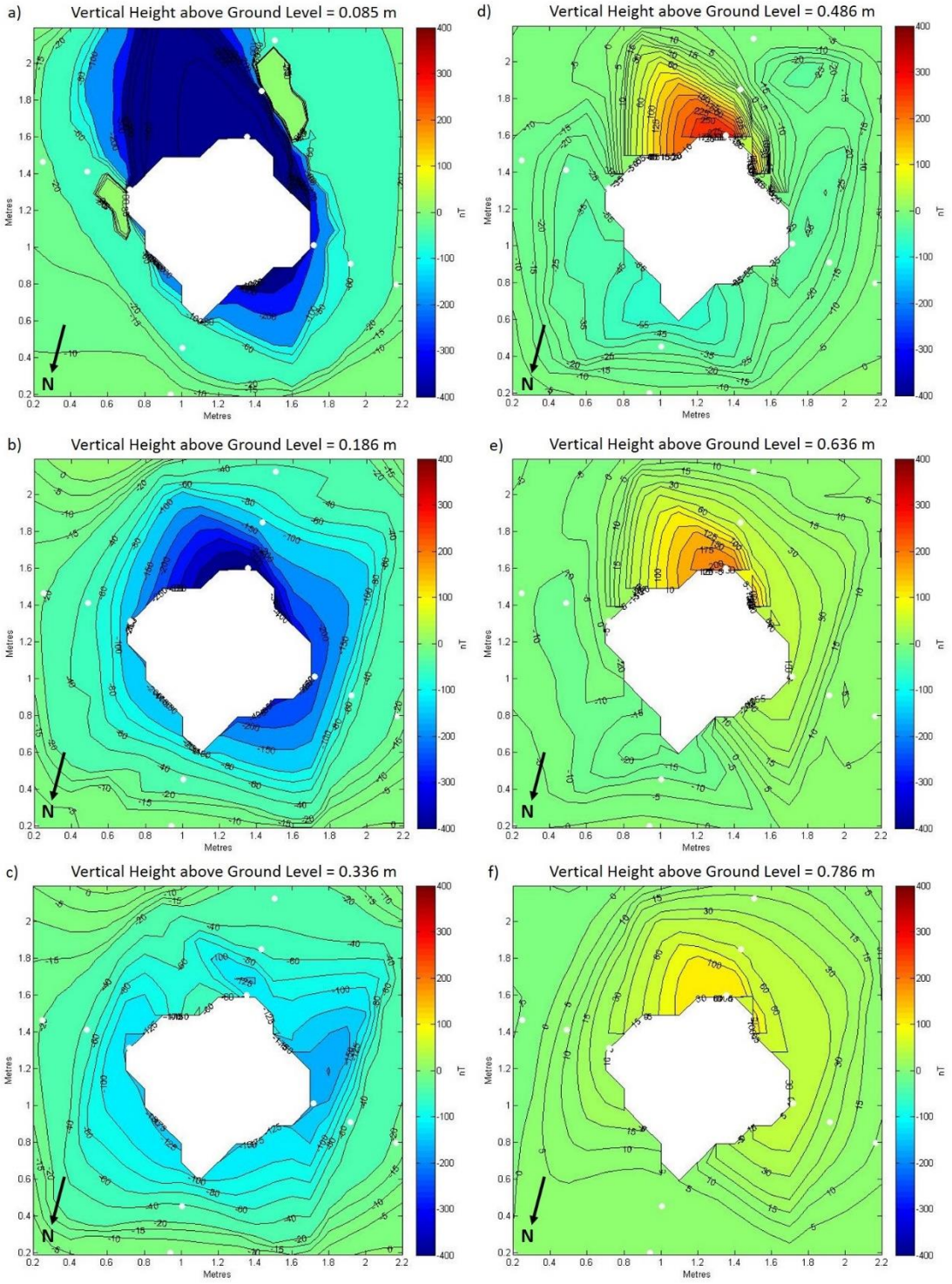

Figure 5.47: *Contour maps of the data gained from the five magnetic grout discs from trial setup 2, with the magnetometer sensor positioned at a) 0.085 m, b) 0.186 m, c) 0.336 m, d) 0.486 m, e) 0.636 m, and f) 0.786 m above ground level.*

5.3.5.3 Trial Setup 3

For the third trial setup, six transect lines were laid out with measurements taken in the following directions: North, South, North West, North East, South West and South East. Figure 5.48 shows the magnetic response gained along the North - South transect line. The measurements taken to the South of the magnetic grout discs have a larger range of magnetic field values compared to the North of the discs. From the graph, it can be seen that the magnetic field decays rapidly with increasing distance from the magnetic grout discs. Once again, the largest positive (158.893 nT) and negative (-281.608 nT) anomalies were detected to the South of the magnetic grout discs.

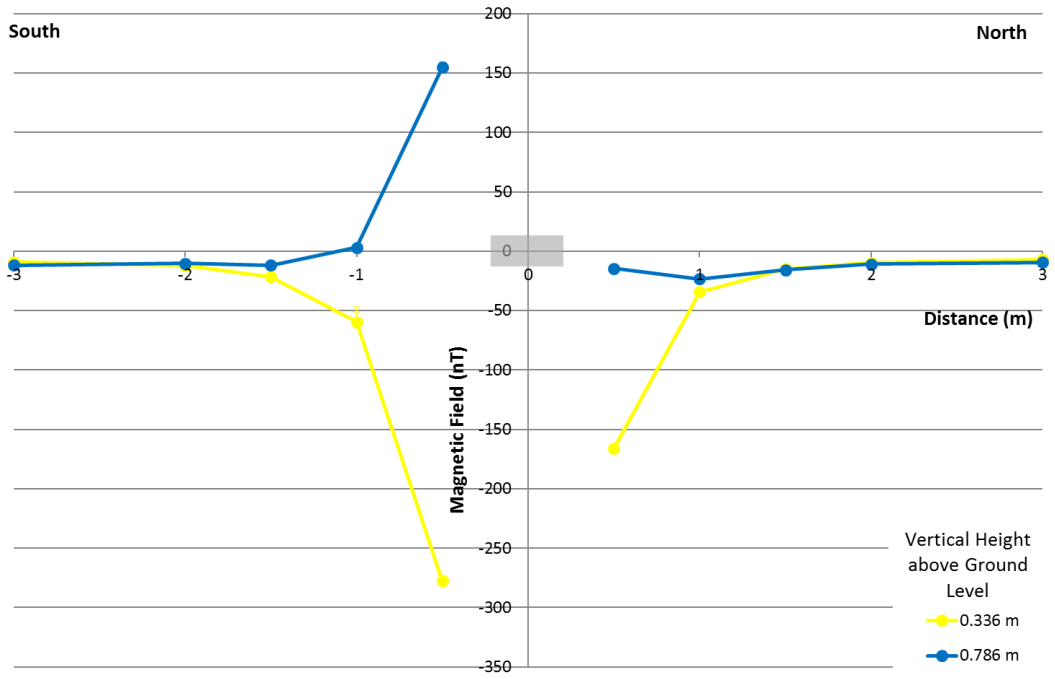

Figure 5.48: *The magnetic response along the North-South line, with the centre of the sample located at 0,0.*

Figure 5.49 presents the magnetic response of the magnetic grout discs to the North. Due to the magnetometer sensor only being positioned at two vertical heights the shape of the vertical magnetic anomaly is not as well defined in the other two trial setups. This graph does however show that as the horizontal distance from the magnetic grout discs increases, the difference in the magnetic field value between the two heights

decreases. This is expected since the magnetic field produced by discs decreases with distance.

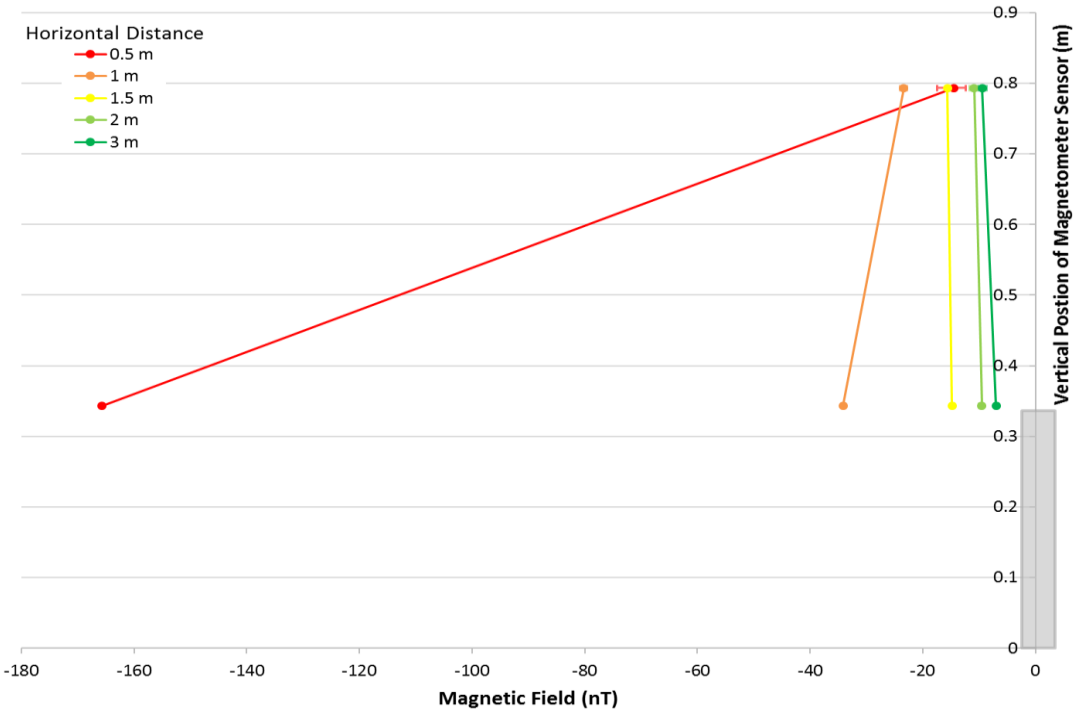

Figure 5.49: *The vertical magnetic response to the North of the magnetic grout discs.*

The magnetic response to the South of the magnetic grout discs is presented in Figure 5.50. This magnetic response is similar to that seen toward the North, however there is a larger difference in the magnetic field values obtained close to the discs. Once again, as the horizontal distance increases, the magnetic field detected decreases leading to a smaller difference in the magnetic field reading taken at both vertical heights.

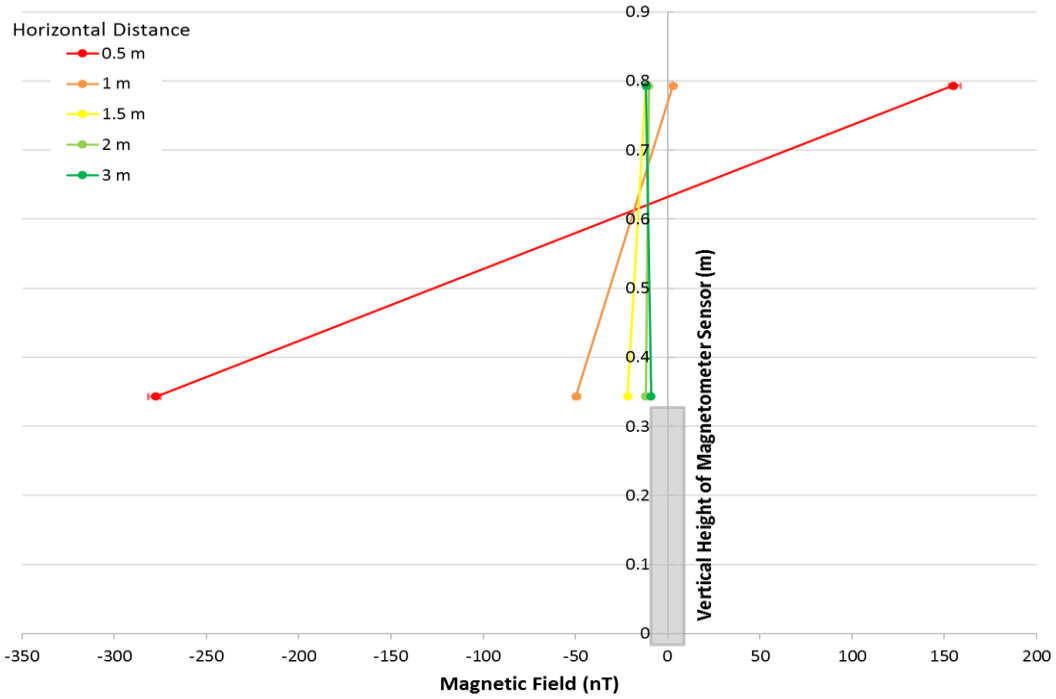

Figure 5.50: *The vertical magnetic response to the South of the magnetic grout discs.*

Figure 5.51 presents the magnetic response along the South West – North East transect line. This graph is very similar to the results obtained along the South – North transect line (Figure 5.48), with the largest magnetic response being recorded to the South West. As has been seen previously, as the distance from the magnetic grout discs increases, the magnetic field decays rapidly away. The largest positive (134.258 nT) and negative (-247.803 nT) anomalies are both found to the South West of the magnetic grout discs. These values are slightly less than the anomalies recorded to the South.

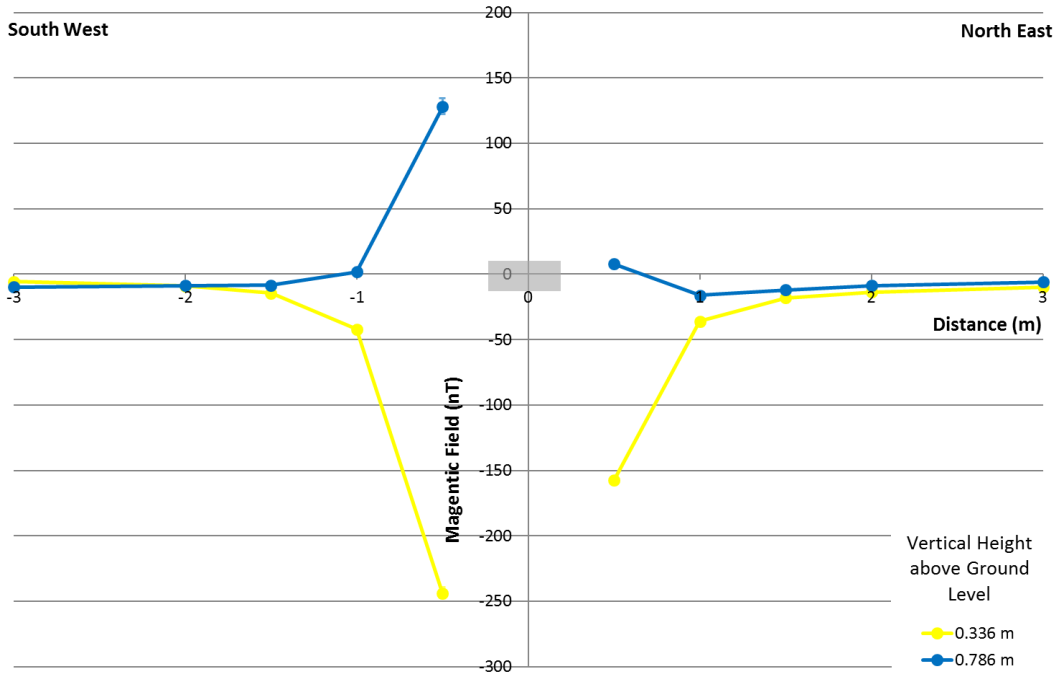

Figure 5.51: *The magnetic response along the South West - North East line, with the centre of the sample located at 0,0.*

Figure 5.52 presents the magnetic response along the North West – South East transect line. The data that was collected along this transect line has a similar trend to that in the previous two transect lines. As the horizontal distance increases from the magnetic grout discs, the magnetic field value decreases rapidly. The largest positive (106.682 nT) and negative (-325.438 nT) magnetic anomalies can be seen to the South East of the magnetic grout discs. This negative magnetic anomaly is much larger than that seen in the other two transects.

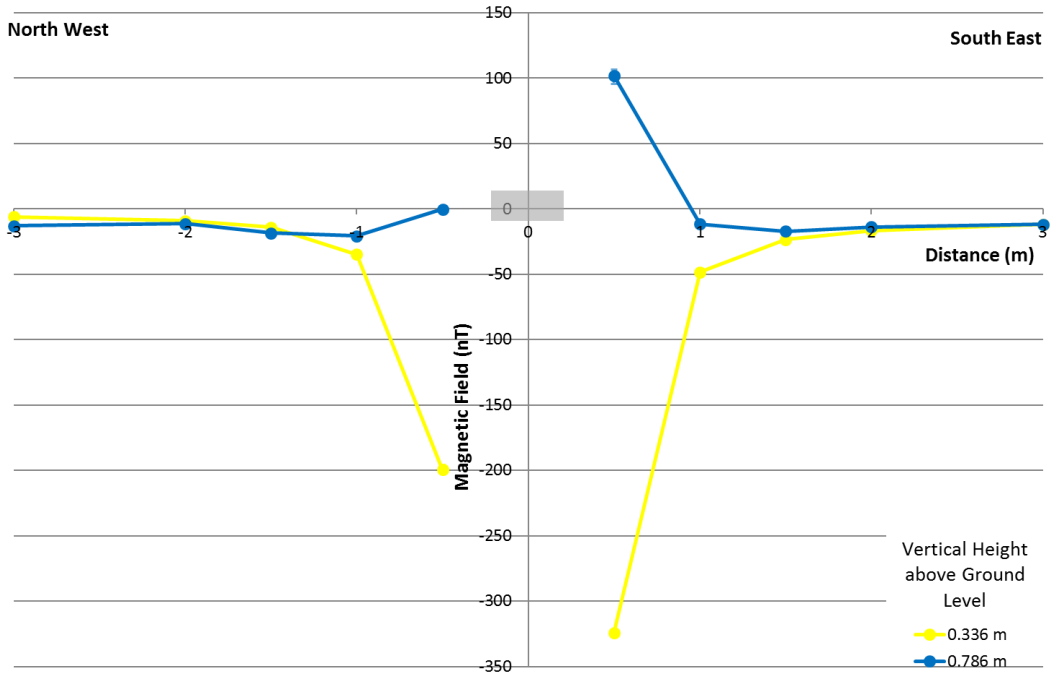

Figure 5.52: *The magnetic response along the North West - South East line, with the centre of the sample located at 0,0.*

5.3.5.3.1 Trial Setup 3 Contour Maps

Figure 5.53a presents the magnetic field recorded at a vertical height of 0.336 m above ground. At this height, the magnetometer sensor is located just above the top of the magnetic grout discs. From Figure 5.53a it can be seen that the negative magnetic anomaly produced generally decreases evenly around the discs. Towards the South, South East, and South West of the discs, the largest magnetic anomaly is located. From the area closest to the magnetic grout discs the size of the magnetic anomaly decreases rapidly in an approximately radial fashion with increasing distance.

Figure 5.53b shows the magnetic field gained when the magnetometer sensor was 0.786 m above ground level. To the South, South East, and South West of the magnetic grout discs, the magnetic anomaly produced is positive. As the horizontal distance from the discs increases, the magnetic field rapidly decreases to almost background levels within 1 m. After the horizontal distance of 1 m, the decrease is more gradual. To the North of the magnetic grout discs, the anomaly produced is negative in value.

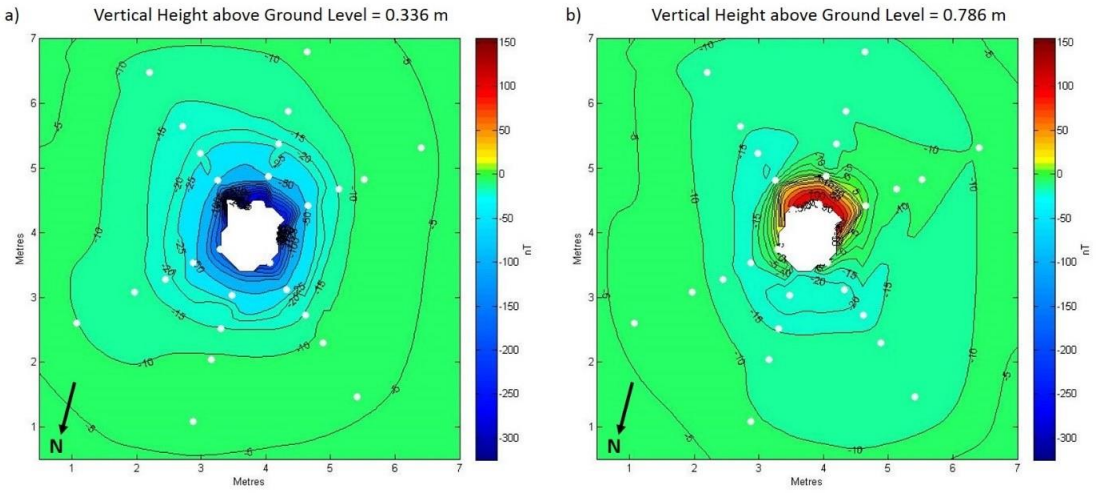

Figure 5.53: *Contour maps showing the magnetic field around the magnetic grout discs when the magnetometer sensor was positioned at a) 0.336 m, and b) 0.786 m.*

5.3.6 Discussion of Field Trial 2 Results

From the results gained from Field Trial 2, it can be seen that the magnetic grout discs are clearly detectable. The strength of the magnetic field detected from the discs is dependent on several different factors. These factors are; the height above the ground of the magnetometer sensors with respect to the vertical location of the discs, the horizontal distance from the discs, and the compass orientation at which the measurements were undertaken.

At vertical heights that are within the vertical range of the discs, i.e. at 0.1 m and 0.2 m above the base of the stack of discs, very large negative magnetic field measurements were recorded. Whereas, above the top of the discs, at vertical heights of 0.5m, 0.65 m and 0.8 m above ground, smaller positive magnetic field measurements were recorded. This change in the magnetic field values with the height above ground level can be attributed not only to the relative vertical location of the discs, but also to the inclination of the Earth's magnetic field and how this affects the shape of the magnetic anomaly produced by the magnetic grout discs. The Earth's magnetic field is inclined at an angle of 69.467° to the horizontal at the field site at Troon. This value was calculated using the online magnetic field calculator provided by Geomatrix Earth Science Ltd on their website (Geomatrix Earth Science Ltd, 2016). Figure 5.54 shows

a schematic representation of the magnetic field that may be produced by the discs. The field recorded by the magnetometer, is the field in Figure 5.54, superimposed on the Earth's magnetic field, which comprises parallel field lines oriented at a declination and inclination of 0.59° and 69.467° respectively. Field lines in Figure 5.54 that have a direction (shown by the arrows) that is the opposite direction to the Earth's magnetic field, produce negative magnetic field recordings. Whereas, where the field is travelling in the same direction as the Earth's magnetic field, the total recorded field is enhanced and positive total field values are measured. Visual inspection of the schematic in Figure 5.54 shows that the magnetic field lines at the top of the sample are in line with the Earth's magnetic field (where the magnetic field lines enter into the magnetic grout discs), whereas at the base of the sample the magnetic field is opposite to the Earth's magnetic field (where the magnetic field lines exit the magnetic grout discs). This accounts for the change in the size of the anomaly in the recorded field data. Similarly, superposition of the anomaly created by the samples onto the Earth's magnetic field, is what causes the positive values to be recorded along transects extending to the South and the negative values to the North.

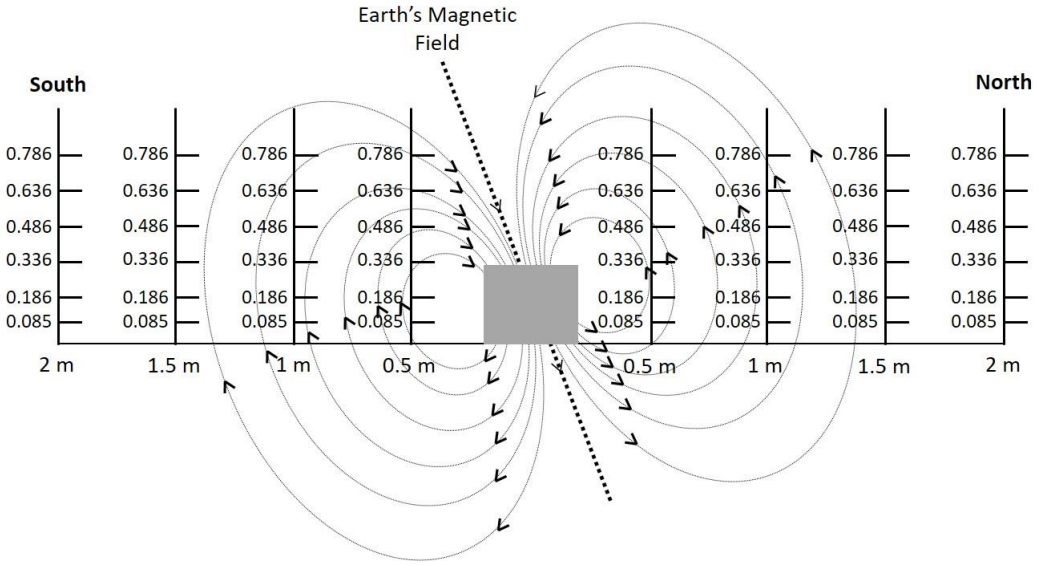

Figure 5.54: *A schematic diagram showing the location of the magnetometer sensors in relation to the magnetic field of the magnetic grout discs.*

In taking measurements at increasing distances from the magnetic grout discs, the furthest point at which the magnetic field from the discs can be detected can be established. All of the results gained in field trial 2 have shown that, as the distance from the magnetic grout disc stack increases, the magnetic field values obtained become smaller, until they can no longer be detected. The maximum distance at which the magnetic grout disc stack could be detected was generally between 1.5 m and 2 m, although this is dependent on orientation and vertical alignment.

5.3.7 Comparison of Field Trial 2 Results with a Model

The results from field trial 2 were compared with a model determining the anomalous magnetic field for a sphere determined by Borglin *et al*. (1998) at the Earnest Orlando Lawrence Berkeley Laboratory. This model assumes that the induced magnetisation is directly proportional to the inducing field and the magnetic susceptibility of the material (Borglin *et al.,* 1998).

In this study Borglin *et al.* (1998) investigated using ferrofluids to be able to trace the location of liquids that had been injected into the subsurface. Several different geometrical shapes were included in this study including a sphere, a disc, a rectangular horizontal slab, and a cylinder (Borglin *et al.*, 1998). Before experiments were undertaken, calculations which were based on the principles of magnetics were undertaken to determine the maximum detection depths of the geometrical shapes (Borglin *et al.,* 1998). Experiments were then undertaken using a three-axis miniature fluxgate magnetometer, with the vertical component of the magnetic field anomaly being reported. The results gained from these experiments match closely to the theoretical detection depths calculated for each geometrical shape (Borglin *et al.*, 1998).

In using the spherical model, the magnetic field anomaly of a magnetised sphere can be calculated by assuming the sphere to be a magnetic dipole whose moment, M, is the product of the spherical volume, V, and its magnetisation. The dipole axis of the sphere

is orientated along the direction of the inducing field (Borglin *et al*., 1998). This gives the equation:

$$M = Vk_mF_0 \tag{5.2}$$

Where:

M = the magnetic moment of the sphere,

V = the spherical volume,

k_m = the magnetic susceptibility of the sphere,

F_0 = local ambient magnetic field.

For this model, the sphere is exposed to a vertical inducing field of 47,000 nT, with the volume of the sphere being 3.3 m^3, with a magnetic susceptibility of 0.014 (Borglin *et al.*, 1998).

The magnetic field of the sphere is located using a total field magnetometer which measures the vertical component of the magnetic field of the sphere (Borglin *et al*., 1998). In using the centre of the sphere (located at a depth, *h*) as the origin of the coordinate system, the observable magnetic anomaly along a traverse line over the sphere is given by the following equation:

$$\Delta F = \frac{M}{4\pi r_d^3}\frac{2h^2 - x^2}{r_d^2}, \tag{5.3}$$

Where:

$$r_d^2 = h^2 + x^2. \tag{5.4}$$

Where:

ΔF = the observable magnetic anomaly,

M = the magnetic moment,

h = depth of the sphere,

x = transverse distance.

The results gained from three spheres, located at depths of 3 m, 5 m, and 10 m are presented in Figure 5.55. This graph was produced to verify the calculations against their published results. The plot is identical to their published calculations; as expected, as the distance from the sphere increases, the size of the magnetic anomaly decreases.

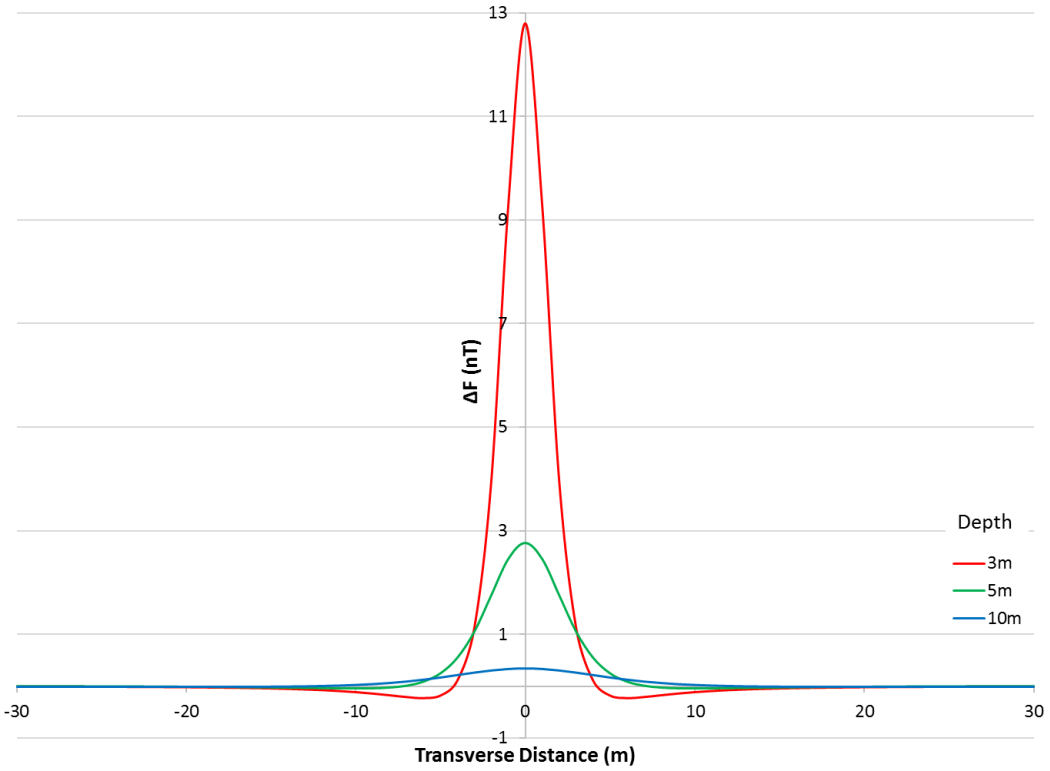

Figure 5.55: *The magnetic response along transverse profiles over a sphere located at three different depths using the model variable values (After: Borglin et al., 1998).*

The model variables were then adjusted to utilise data values from field trial 2. The sphere was exposed to a background magnetic field of 49,715 nT, with the volume of the sphere being 0.0421 m^3, and assuming a magnetic susceptibility of 0.0727 (Section 5.3.3.1). This produces an equivalent sphere with a diameter of 43cm.

The model predictions were compared to the results gained in field trial 2, for all three trial setups. As the magnetic grout discs in the field trial were not buried, the heights at which the magnetometer sensors were located above the centre of the sample were

used to generate model predictions. This resulted in vertical heights of - 0.0675 m, 0.0325 m, 0.1825 m, 0.3325 m, 0.4825 m, and 0.6325 m.

For the first trial setup, where a transect line was laid out to the South side of the stack of magnetic grout discs to a horizontal distance of 13 m, the magnetometer sensors were located at 0.0325 m, 0.1825 m, 0.3325 m, and 0.4825 m. Figure 5.56 shows a comparison between the model predictions and the field trial measurements. In general, the magnitude of the magnetic field close to the discs is much greater than that which is predicted by the model. When the magnetometer sensors were positioned at 0.0325 m (Figure 5.56a), the largest magnetic anomaly can be seen for both the model and field trial data. Both the model and field data produce a negative magnetic anomaly at this height. In increasing the height of the magnetometer sensor, the size of the magnetic anomaly produced significantly decreases. At a sensor height of 0.1825 m (Figure 5.56b), a positive magnetic anomaly is produced from the field trial data, however the model produces a negative anomaly. As the height of the sensor continues to increase, the magnetic anomaly produced from both the model and field trial data becomes positive in value. Additionally, the difference between the values gained decreases with increasing height.

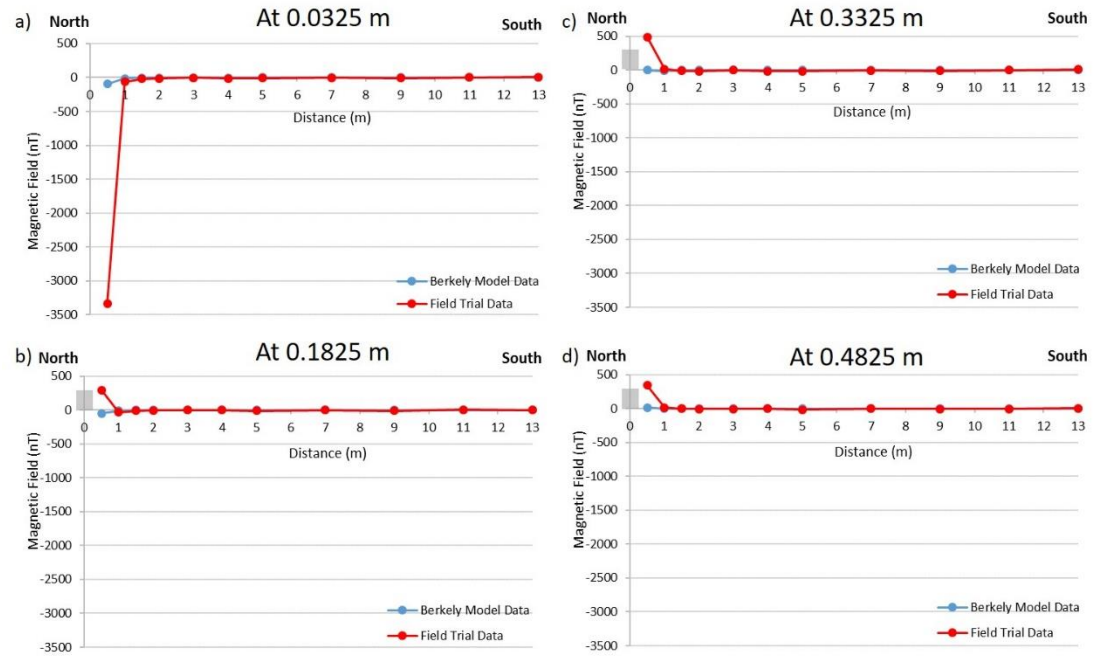

Figure 5.56: *A comparison of field trial data with the model data for field trial setup 1 with the magnetometer sensor located at a) 0.0325 m, b) 0.1825 m, c) 0.3325 m, and d) 0.4825 m.*

For the second trial setup, where the transect lines radiated out from the stack of magnetic grout discs to the North, South, East, and West, the magnetometer sensors were located at -0.0675 m, 0.0325 m, 0.1825 m, 0.3325 m, 0.4825 m, and 0.6325 m. Figure 5.57 shows the graphs of the comparison between the model and field data across the South – North transect line, and Figure 5.58 shows the comparison graphs across the West – East transect line.

These results (Figure 5.57 and Figure 5.58) again show that the trends of both the field trial and model data are very similar to each other. From both the South – North, and West – East transect lines, it can be seen that in general the magnetic anomaly produced from the field trial data is larger than the anomaly produced by the model data. At a sensor height of -0.0675 m, the field trial data gained at a horizontal distance of 0.5 m to the South of the magnetic grout discs (Figure 5.57a) produced a much larger negative magnetic anomaly than the model. For both the field trial and model data, the largest magnetic response can be seen closest to the magnetic grout discs. In increasing the horizontal distance from the discs, the size of the magnetic anomaly

produced decreases. Additionally, as the height of the magnetometer sensor increased, the magnetic anomaly produced becomes positive.

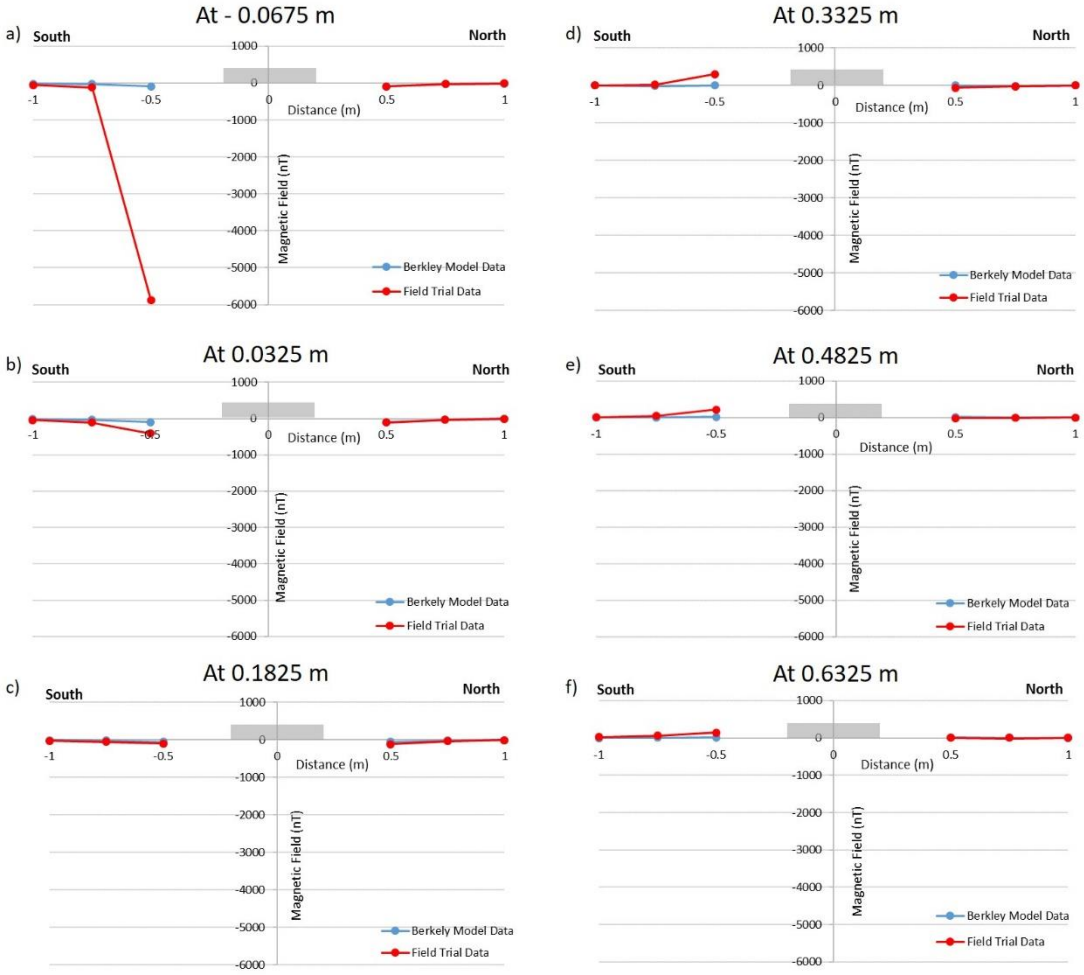

Figure 5.57: *A comparison between the model and field trial data across the South - North transect for trial setup 2, with the magnetometer sensors located at a) -0.0675 m, b) 0.0325 m, c) 0.1825 m, d) 0.3325 m, e) 0.4825 m, and f) 0.6325 m.*

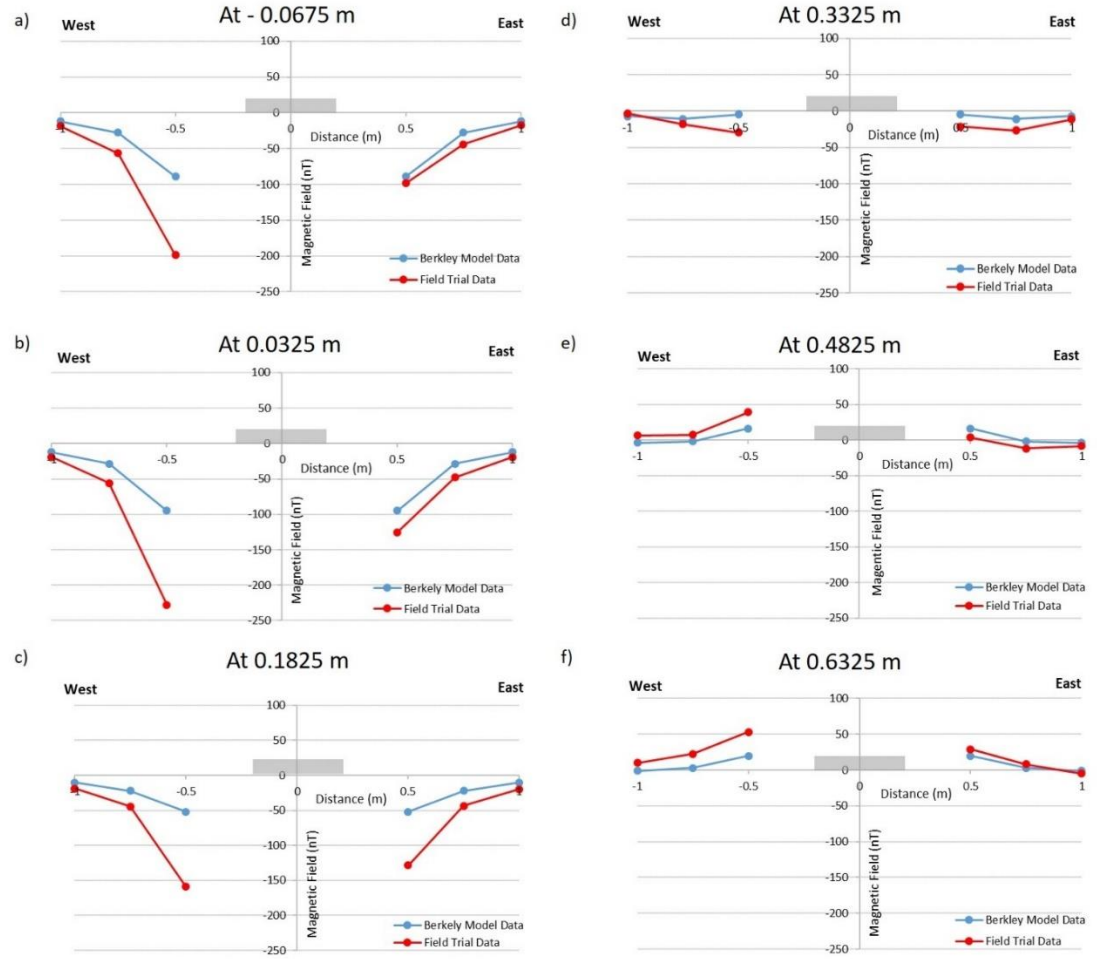

Figure 5.58: *A comparison between the model and field trial data across the West - East transect for trial setup 2, with the magnetometer sensors located at a) -0.0675 m, b) 0.0325 m, c) 0.1825 m, d) 0.3325 m, e) 0.4825 m, and f) 0.6325 m.*

For the third trial setup, where the transect lines radiated out from the stack of magnetic grout discs to the North, South, North West, North East, South West, and South East, the magnetometer sensors were located at 0.1825 m and 0.6325 m. The three figures below (Figure 5.59, Figure 5.60, and Figure 5.61) compare the model and field trial results across the South – North transect line, the South West – North East transect line, and the North West – South East transect line respectively.

The results from trial setup 3 again show a very similar trend between the field trial data and the model. For all of the transect lines with a sensor height of 0.1825 m, the magnetic anomaly produced is negative, whereas at the height of 0.6325 m the

anomaly is generally positive. As with the results from the other trial setups, the largest magnetic response can be seen at the closest horizontal distance of 0.5 m to the magnetic grout discs. Generally, throughout all of the results gained from trial setup 3, the field data produces a larger magnetic anomaly response than the model data. As the horizontal distance from the magnetic grout discs increases, the size of the magnetic anomaly produced decreases.

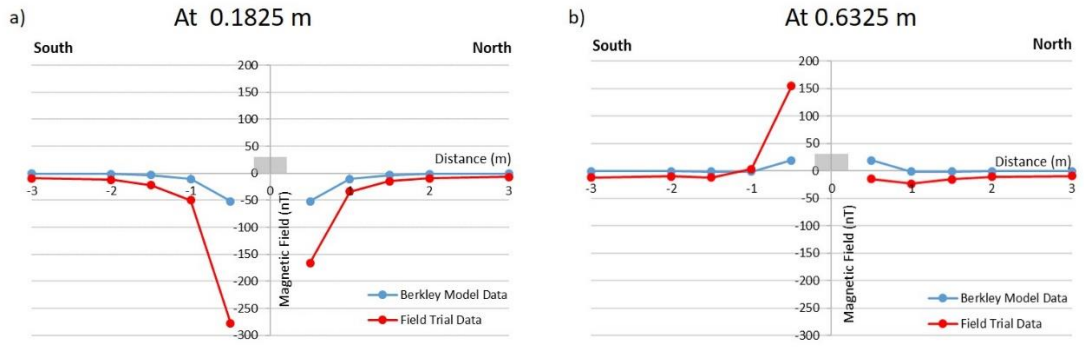

Figure 5.59: *A comparison between the model and field trial data across the South - North transect for trial setup 3, with the magnetometer sensors located at a) 0.1825 m, b) 0.6325 m.*

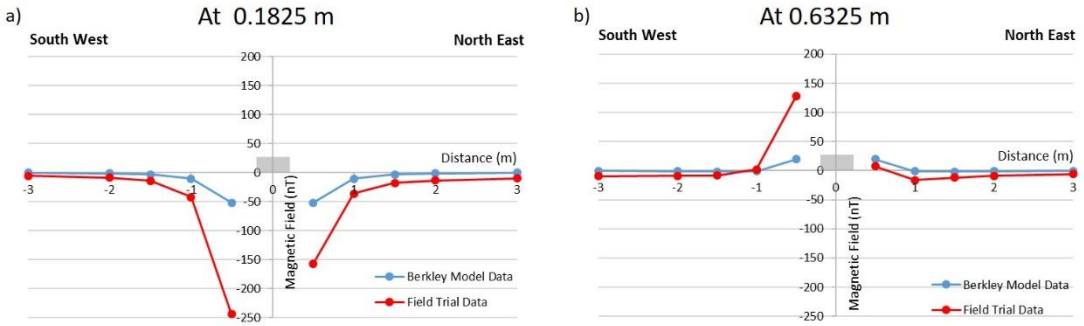

Figure 5.60: *A comparison between the model and field trial data across the South West – North East transect for trial setup 3, with the magnetometer sensors located at a) 0.1825 m, b) 0.6325 m.*

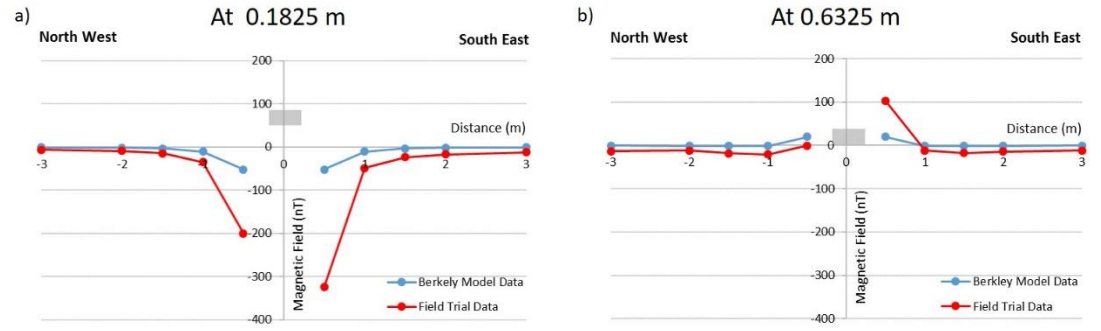

Figure 5.61: *A comparison between the model and field trial data across the North West – South East transect for trial setup 3, with the magnetometer sensors located at a) 0.1825 m, b) 0.6325 m.*

In comparing the data gained from field trial 2, to data produced using a model which determines the anomalous magnetic field for a sphere by Borglin *et al.* (1998), both similarities and differences can be seen. Similar trends in the magnetic response of both the field and model data can be seen across all three trial setups. The size of the magnetic anomaly produced by the model data decreases with distance from the magnetic grout discs in the same way as the field data. The only difference between the data is in the size of the magnetic anomaly produced. The differences between the data sets could be attributed to the fact that the model assumes that the background magnetic field is vertical. However, in the case of the field data the background magnetic field is inclined to 69.467°. This therefore means that there is no variation in the model data, and the values gained are the same for each different orientation. Additionally, the larger magnetic anomaly produced in the field trial could be a result of the magnetometer used reporting the total magnetic field as opposed to the model only reporting the vertical component of the magnetic field. Hence, larger magnetic field values would be obtained in the field trial compared to the model data.

5.3.8 Conclusions of Field Trial 2

Overall, the results from field trial 2 have shown that it is possible to determine the decay of the magnetic field with distance from the stack of magnetic grout discs. In undertaking three different trial setups that obtained magnetic measurements at different distances from the magnetic grout discs, the maximum distance at which they

could be detected was around 1.5 m to 2 m. Additionally, the rate of decay of the magnetic field can be easily seen in all orientations around the magnetic grout discs. In undertaking measurements in different orientations around the magnetic grout disc stack, it has been possible to determine the shape of the magnetic field. In general, the largest positive magnetic anomalies were seen towards the South of the magnetic grout discs, with the largest negative anomalies present to the North. The location of these anomalies can be attributed to the inclination of the Earth's magnetic field.

In collecting magnetic measurements at different vertical heights the effect of the Earth's inclined magnetic field on the magnetic field of the magnetic grout discs can be easily seen. In increasing the vertical height of the magnetometer sensor it was possible to see a large amount of variability over a 0.7 m distance. In general, the lower vertical heights produced negative magnetic anomalies, and the higher vertical heights produced positive anomalies. These results fit with the concept that the magnetic field at the base of the magnetic grout discs is taking away from the Earth's magnetic field and the magnetic field at the top is adding to it.

In comparing the field trial results with data from a model similar trends in the magnetic response could be seen across all three trial set ups. The main difference between the two data sets is the magnitude of the magnetic anomalies produced, however this could be a result of the model assuming that the background magnetic field is vertical.

5.4 Overall Conclusions

In conclusion, in undertaking two field trials with the magnetic grout mixture, a detectable grout has been developed. Field trial 1 provided the proof of concept that it was possible to detect the magnetic grout outside of a laboratory environment and also at depth. This trial confirmed that in using a higher percentage of magnetite the larger the magnetic anomaly produced. Additionally, in burying the magnetic grout samples they could still be detected at just under 1 m away from the magnetometer sensors. In undertaking field trial 2, the results of the first field trial were built upon.

In taking magnetic measurements at all orientations around the magnetic grout discs, it has been possible to see the rate of decay of the magnetic field in all directions. Also, vertical changes in the magnetic field have been established, and this has enabled a much better understanding of how the magnetic field changes with distance and with height. The following chapter will discuss the potential use of the detectable magnetic grout in industry.

Chapter 6

Application to Industry

6.1 Introduction

During a grouting campaign, the lack of information on grout location leads to large uncertainty in the grouting process and highly conservative designs. To reduce this uncertainty, there have been several previous attempts at detecting the location of the injected grout, with each using a different method. These methods have included using several different geophysical methods and also down-hole monitoring. However, none have proved conclusive in determining grout location.

This thesis has looked at determining whether the addition of magnetite to a traditional cementitious grout results in a usable grout that has the potential to be detected once injected into the subsurface. This research has found that the largest factor that needs to be considered for the properties of the grout mixture is the water to solids ratio. The addition of magnetite into the grout mixture increases the amount of solids present, however by replacing some of the cement with the magnetite the water to solids ratio can be kept constant. This allows similar properties of flow and bleed of the grout mixture to be achieved. However, this change does lead to increased initial setting times and a delay in the hydration reactions occurring. To assess detectability of the magnetic grout field trials have been conducted using grouted samples placed both at the surface and buried. These trials demonstrate that the position of the magnetic grout can be identified. Furthermore, from the magnetic field data gained it is possible to determine the size and shape of the injected grout, and therefore in industry the integrity of a grout curtain, for example, could potentially be established.

6.2 How could this technique influence and / or change current practice?

The development of magnetic grout has the potential to influence how the current practice of grouting is undertaken. In current grouting practice limits to both the maximum grouting pressure and the maximum grout volume are set before grouting commences. These limits are then used to curtail grout injection. This method of grout control was discussed in Chapter 2, Section 2.5. In using these variables it is impossible to know if the intended volume of rock has been grouted, or whether for example, all the grout has travelled down one individual large aperture fracture away from the intended grout location. This results in large inefficiencies in the grouting process, designs are over conservative, leading to wasted material and unnecessary drilling of boreholes. Additionally, in using these simplistic limits it is not possible to *optimise* design of the grouting campaign, as the grouting operation progresses.

In combining the current practice of using a maximum grouting pressure and maximum grout volume used in the GIN technique (as described in Chapter 2, Section 2.5) with the magnetic grout it would be possible to monitor the grout penetration in real time. This would lead to significant reductions in project uncertainty, less wastage of material and a consequent reduction in costs. Additionally, the ability to image the grouted rock volume will result in increased confidence in the final construction project and a much-reduced risk of subsequent ground failure.

From the two field trials conducted, the magnetic grout could be detected up to distances of 2 m. From the results of field trial 2, using the stack of magnetic grout discs, the largest magnetic anomalies (both positive and negative) were found along the North – South orientation. This therefore corresponds to the orientation along which the grout could be detected at the greatest distance. When comparing the field trial results with a model of the magnetic field produced by a sphere (of the same volume and magnetic susceptibility of the magnetic grout discs used in the field trial (see Chapter 5, Section 5.3.6)) determined by Borglin *et al*. (1998), similar trends in the size of the magnetic anomaly produced can be clearly seen. Additionally, the

distance at which the model predicts the magnetic grout can be detected is very similar to that achieved in the field trial.

The distance at which the magnetic grout can be detected is dependent on the volume of the magnetic grout. Within the field trial a set volume of magnetic grout was used, with this volume being further used within the modelling. By increasing the volume of the magnetic grout larger detection distances could be achieved. Within a typical grouting campaign a much larger volume of grout is likely to be injected for a single borehole interval. For example, in a recent grouting campaign conducted by BAM Ritchies (pers. Com.) 354 litres of grout was injected over an interval of 3 m. If this is assumed to be typical, applying this volume within the model of Borglin *et al*. (1998) for the magnetic field produced by a sphere (and keeping the same magnetic susceptibility of 0.0727 as used previously in Chapter 5, Section 5.3.6) the maximum distance at which the magnetic grout could be detected increases to 6 m. In this scenario, monitoring boreholes could be located at distances of 1 m, 2 m, 4 m, and 6 m from the injection borehole to gain a clear understanding of the decay of the magnetic field produced by the magnetic grout.

To further the understanding of the detectability of the magnetic grout within an engineering environment, a borehole injection grouting trial should be undertaken. The results of such a trial could be used to design protocols for grout use, including appropriate locations for monitoring boreholes and design of the accompanying detection system.

When conducting a grouting campaign, the magnetic grout would be best applied during the first phase of grouting. This would allow the initial penetration distance of the grout within the rock fractures to be assessed. Using fluxgate magnetometers, instead of a caesium vapour magnetometer as used in the two field trials presented here, magnetic measurements can be taken in any direction which would enable the location and shape of the injected magnetic grout to be more easily determined. After grout injection, magnetic readings within the monitoring boreholes could be taken at different vertical heights within each monitoring borehole. This would give an

indication of how the magnetic field of the magnetic grout decays as the distance between the grout and the magnetometer increases. As in the two field trials undertaken in this thesis, a background magnetic reading should always be undertaken prior to the injection of the magnetic grout. The background readings must be taken at exactly the same depths as the readings taken during, and after, grout injection to ensure that the background magnetic field can be removed accurately.

After injection of grout into the subsurface, the shape of the grout will be dependent on the initial rock conditions. When injecting into a planar rock fracture, the most likely grout shape produced will be a disc, rather than the cylindrical shapes used within field trial 2. A disc shape volume within each fracture represents a 'best-guess' outcome of a grouting campaign, however, the actual shape produced will be unpredictable and controlled by the initial aperture profile within each fracture. Thus, it could be irregular.

To predict grout detection thresholds, different models can be used, the accuracy of which will be dependent on the actual shape of the injected grout. The magnetic field of a dipole which decays following the inverse cube law ($1/r^3$), can give a good indication of the distance over which the magnetic grout may be detectable. The inverse cube law was compared with the results of the first field trial, and the rate of decay in field strength was found to be similar (see Chapter 5, Section 5.2.8). To give an indication of the anomalous magnetic field of a disc shape, which is more likely if the grout is injected into a fracture, the following equation from Borglin *et al.* (1998) can be used:

$$\Delta F_{max} = \frac{M}{2\pi\,(z^2 + r^2)^{\frac{3}{2}}} \tag{6.1}$$

Where:

$$M = V\,k_m F_0 \tag{6.2}$$

Where:

ΔF_{max} = maximum magnetic anomaly,

M = magnetic moment of the disc,

z = depth to the disc,

r = radius of the disc,

V = volume of the disc,

k_m = magnetic susceptibility of the disc,

F_0 = local ambient magnetic field.

Applying this equation, the maximum magnetic anomaly of the magnetic grout disc can be calculated, and therefore the distance at which it can be detected can be determined. Note, this equation assumes that the background magnetic field is vertical, rather than inclined. In comparing this model, with the previous spherical model, both shapes with the same volume produce a maximum detection distance of 6 m (Figure 6.1). This maximum detection distance of 6 m is calculated assuming that the realistic detection limit of the magnetometer used is 1 nT. However, depending on the thickness of the disc produced within the borehole (due to the presence of and size of individual fractures) the magnetic field detected close to the disc varies. This can be seen in Figure 6.1 where, as the thickness of the disc decreases the magnitude of the magnetic field at a distance of 1 m from the disc, also decreases. To confirm this, monitoring boreholes could be located in the same position as for the spherical model, with an additional borehole located at 0.5 m to detect variability within individual fractures close to the injection borehole.

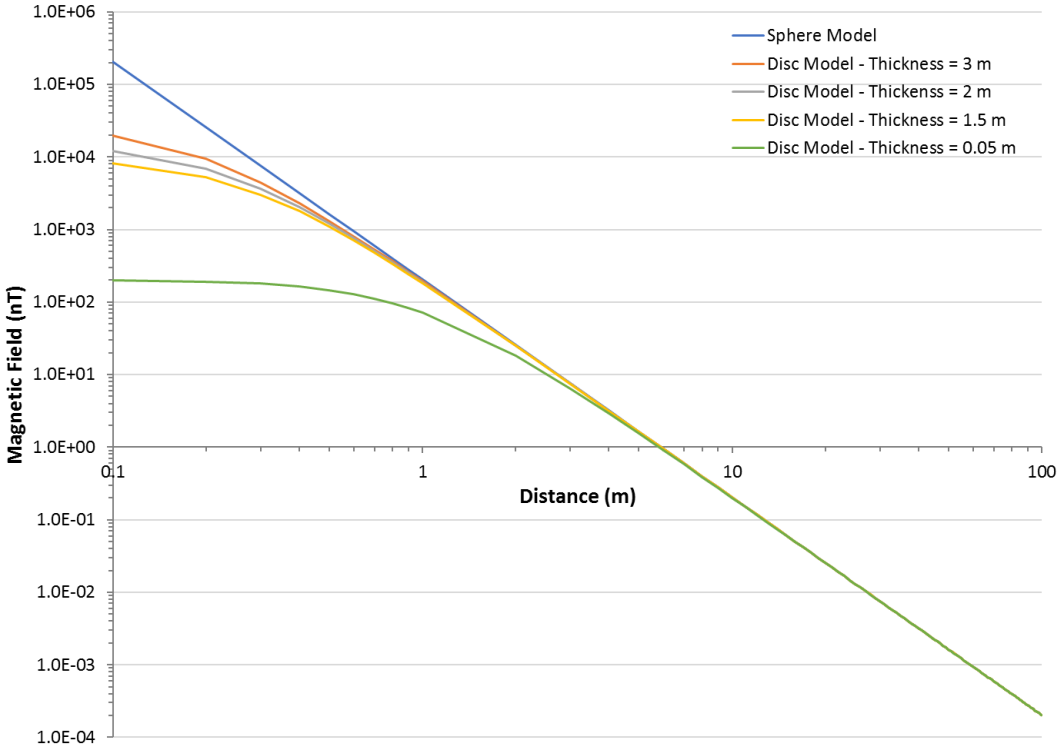

Figure 6.1: *A comparison of magnetic field of 354 litres of injection grout modelled in the shape of a sphere and a disc.*

When injecting magnetic grout, one of the factors that will need to be considered is the penetrability of the grout. The addition of magnetite into a cementitious grout has not greatly changed the engineering properties as seen in Chapter 4. With a particle size of < 53 µm, the magnetite does have a larger particle size than the cements (up to 30 µm). This will lead to a reduced penetrability. As the penetrability of the magnetic grout has not been tested within this thesis, this should be further investigated before borehole injection is undertaken.

6.3 Applications of the Technique

One of the main applications of the magnetic grout is in the production of grout curtains. Grout curtains are used in a number of engineering scenarios, for example, beneath dams, and in nuclear waste repositories (as discussed in further detail in Chapter 2). The use of magnetic grout in scenarios such as these could enable any gaps in the grout curtain to be identified, which is critical to secure hydraulic

containment around the site. In practice to reduce costs, magnetic grout could just be used within an initial known volume of grout (followed by normal cement) within each interval. This would still enable the distance to which the grout has penetrated to be determined, and hence the integrity of the grout curtain. Any optimisation of the grouting design could then be performed based on data gathered from phase 1. To reduce costs, further grouting stages could either take the same approach or simply be undertaken in non-magnetic grout.

A further application of the magnetic grout could be tracking the location of grout injected behind tunnel linings. Attempts to detect grout behind tunnel linings have already been made using GPR (Zhang *et al.*, 2010), but success was limited (further details of this study can be found in Chapter 2, Section 2.7.3). Use of the detectable grout would enable a far more complete picture of the geometry of the grout shape to be determined. This would therefore enable gaps in the grout to be determined. Furthermore, the magnetic grout could be used to fill in fractures behind the tunnel lining, within the rock walls of tunnels forming a secondary grout curtain. In knowing the integrity of the grout curtain formed, groundwater ingress could be prevented.

For use of detectable grout in applications such as ground stabilisation, and compensation grouting under buildings to prevent subsidence, knowing the extent of the grouted rock volume will reduce risk of future ground failure. Furthermore, it will enable an informed decision to be made on when to stop grouting, so that grout wastage does not occur. Detectable grout could also be used in the filling of sinkholes, where the geometry of the hole formed is not previously known.

6.4 Limitations of the Technique

As with any technique, there are several limitations to the usage of the magnetic grout. One of the main limitations is that the magnetic grout needs to be more magnetic than the background magnetic field. As seen in the field trial undertaken at Rouken Glen Park areas that have had previous historical use may be problematic (see Chapter 5, Section 5.2.2). This is because at these sites it is presumed the historical use of the

site left behind magnetic items, which resulted in a much higher background magnetic field being recorded than expected. Additionally, the large amount of variability in the background magnetic field makes it difficult to pick out the magnetic anomaly produced by the magnetic grout. Depending on the size and the depth of the historic magnetic anomalies, the distance at which they will disturb detection of an injected grout, will vary. It is probable, however, that buried magnetic items from historical use will only be present in the top few metres of the soil. As grouting is undertaken at much greater depths, it is unlikely that such items would cause significant detectability problems in most engineering projects. If it is found that the background magnetic field is larger than the magnetic field produced by the magnetic grout, the magnetite within the grout may need to be changed to a more magnetic material.

Another limitation to using the detectable grout is its use close to power utilities, and mobile on-site metallic equipment, since they may result in significant fluctuations in the background magnetic field. This would lead to a difficulty in detecting the magnetic grout as the background signal could not be accurately removed to reveal the anomaly produced by the injected grout only.

A further limitation to using a detectable grout is that to accurately know where the magnetic grout is located, a good positioning system (GPS) must be deployed. This will ensure that the precise location of both the background and magnetic grout magnetic measurements are known. This is important when removing the background magnetic field values and will affect the accuracy with which the grout front can be located.

6.5 Limitations of this Thesis

There are several limitations to the work undertaken within this thesis on developing the magnetic grout material.

Firstly, strength testing and penetration testing of the magnetic grout were not undertaken. The strength of the cementitious grout is an important factor within

engineering projects, and should be determined by future research. Penetration testing of the magnetic grout has also not been undertaken. In going forward with the magnetic grout material, it is imperative to ensure that the magnetic grout does not unduly compromise grout penetrability.

There have been no experiments to determine the durability of the magnetic grout. The durability of the magnetic grout is important, for example, the long-term integrity of a grout curtain may be crucial. Durability measurements have previously been undertaken on pure cement mixtures, however the addition of magnetite into the cement may alter its durability, as the presence of magnetite may provide a pathway for groundwater and its constituents to degrade the integrity of the cement. To gain a representative measure of the durability of the magnetic grout, a durability experiment would have taken longer than the length of this research project.

In undertaking the field trials, only precast magnetic grout shapes were used. This was advantageous during the proof of concept stage of the research, where the precise location of the magnetic grout allowed the magnetic field to be predicted. The magnetic grout now needs to be taken to the next stage and trialled by subsurface injection. In doing this, it will give a better indication of how the detection system using the magnetometer can image both the size and shape of the magnetic grout in a subsurface fractured environment.

Chapter 7

Conclusions and Future Work

7.1 Introduction

This thesis has developed a detectable grout material by adding the magnetic mineral magnetite into two commercially available cementitious grouts. The main aim of the thesis was to investigate the potential for use of magnetic minerals in cementitious grouts to enable the detection of grouts in the subsurface. This aim was then split down into the following three objectives:

1. Does the addition of magnetic minerals into a cementitious grout mixture sufficiently change its magnetic properties to enable it to become detectable? How are magnetic properties influenced by type and concentration of magnetic minerals in the grout mix?

2. Can a workable grout, in terms of cement grout properties, be achieved using magnetic additives?

3. Can the location of magnetic grouts be detected in the environment? What survey methods can be used to detect grouts present at depth? Over what distances are magnetite-based magnetic grouts detectable?

This chapter will be split into two sections; realisation of objectives, and future work. The realisation of objectives section will focus on how each objective has been addressed within this research, and the future work section will give an indication of where further research could be undertaken.

7.2 Realisation of Objectives

The first objective of determining whether the addition of magnetic minerals into a cementitious grout mixture sufficiently change its magnetic properties to enable it to become detectable was established by undertaking magnetic susceptibility testing of the grout. In determining the magnetic susceptibility for both the pure OPC and Ultrafin cements before and after magnetic minerals had been added, changes in the magnetic properties of the grout mixtures could be established. Initially, several magnetic materials (magnetite, maghemite, and iron filings) were tested, to determine the most magnetic material to take forward, with magnetite being identified as having the highest magnetic susceptibility above the other two materials. Magnetite was therefore the logical choice to take forward for the remainder of the research.

When increasing the magnetite content of both cements, their magnetic susceptibilities were found to increase linearly. However, the magnetic susceptibility of the two cements were not the same. With the addition of superplasticiser and stabilising agent to the cement mixtures there was a slight reduction in the magnetic susceptibility within the OPC cement. However, there was virtually no loss in magnetic susceptibility in the Ultrafin cement mixtures.

In addition to the magnetic susceptibility testing the magnetic grout material was examined using optical light microscopy and SEM analysis. In using these methods, the general distribution of the magnetite within the grout could be estimated, with the magnetite being found throughout the mixtures. There were however some areas where the magnetite had clustered together, potentially caused by the hand mixing of the cement samples. Additionally, in undertaking the SEM analysis of the samples the elemental composition of the two different cements was determined. The main elements identified in both the OPC and Ultrafin cements were Oxygen, Calcium, and Silicon, which corresponds with the main mineral phases of any cement: alite and belite.

The second objective of determining whether a magnetic grout could be produced with workable properties was addressed by undertaking a series of laboratory testing on the grout material. In testing the engineering properties of the magnetic grout, the addition of magnetite, and also the superplasticiser and stabilising agent, resulted in significant changes to the grout properties occurring. The addition of magnetite to both the OPC and Ultrafin cements resulted in an increase in the flow times but a decrease in the amount of bleed water produced by the grout mixtures, in comparison to the times recorded for the pure cement mixtures. This change in both the flow times and the amount of bleed water is likely to have been caused by the different water to solid ratios used resulting in an overall increase in the percentage of solids within the mixture. The subsequent addition of superplasticiser and stabilising agent to the cement mixtures led to a reduction in the amount of water required as the superplasticiser disperses the cement particles, and the stabilising agent reduces the amount of segregation that occurs within the cement mixture. This resulted in the flow time of both cement mixtures being similar to the recorded values for the pure cement mixtures. However, there was a much more significant reduction in the amount of bleed water produced.

For both the pure OPC and Ultrafin cement the initial setting time was largely controlled by the water to solids ratio of the cement mixture. As the water to solids ratio decreases, the setting time also decreases. This is because the hydration reaction is completed faster, due to the smaller amounts of water present. In adding magnetite into the cement mixture, the initial setting time slightly increased. This increase would have been caused by the combination of a reduction in the amount of cement material present and the presence of magnetite within the mixture. The addition of superplasticiser and stabilising agent to the magnetic cement mixture resulted in an increase in the initial setting time. This result was seen for both the OPC and Ultrafin cements. This increase is due to the dispersive effects of the superplasticiser on the cement particles.

Temperature testing of the curing pure cement mixtures found that in decreasing the water to solids ratio of the cement mixtures, a higher curing temperature was achieved.

The temperature changes can be attributed to the way the hydration reaction responds to differing amounts of water in the cement mixture. In adding magnetite into the cement mixtures, a drop in temperature occurred. This temperature drop is likely to have been caused by decreasing amounts of cement in the mixture leading to a smaller hydration reaction taking place. The addition of superplasticiser and stabilising agent to the magnetic cement resulted in the peak temperatures occurring later, suggesting that the cement hydration reactions are being inhibited. This is most likely being caused by the superplasticiser, as it is designed to increase the workability and penetrability of the cement mixture.

From the results detailed above, a workable magnetic grout was then developed. The main factor that needs to be considered in producing the magnetic grout is the water to solids ratio, as this controls many of the engineering properties. In adding magnetite into the cementitious grout mixture some of the cement mass is replaced, however, the water to solids ratio is kept constant resulting in similar flow and bleed being achieved. The reduction in the mass of cement does however affect the initial setting time, which needs to be considered in relation to the desired penetration distance during grouting. In summary, the engineering property tests show that the magnetic grout mixture can be adapted to meet any project specific grout property requirements. The recommended magnetic grout mixture would ideally contain a superplasticiser and stabilising agent as these, in combination with the water to solids ratio, can be used to produce a magnetic grout mixture with optimum workable properties.

The third objective of establishing whether the location of the magnetic grouts in the environment could be detected was determined by undertaking two different field trials. These field trials showed that shown it is possible to detect the location of the magnetic grout, at distance, in the field. Field trial 1 established that it was possible to upscale the small magnetic grout samples used in the laboratory to larger samples that could be detected in the field. In trialling magnetic grout mixtures containing both 5% and 10% magnetite, a noticeable difference was seen in the magnetic response achieved with, as expected, the higher percentage of magnetite resulting in a larger magnetic response. In changing the shape of the magnetic grout sample, only slightly

different magnetic anomaly shapes were produced. Additionally, in burying the magnetic grout samples, it was determined that they could still be detected at distances of up to 1 m from the magnetometer sensor. As expected, the field trial results showed that the peak magnetic field diminishes with increasing distance of the grouted object from the magnetometer sensors. This field trial provided proof of concept that the grout was detectable.

Field trial 2 added to the information on the detectability of the magnetic grout gained in field trial 1. In this field trial, magnetic measurements were taken in all orientations around the magnetic grout discs at different distances. This allowed the rate of decay of the magnetic field to be seen in all directions, as well as the shape of the magnetic field produced by the magnetic grout discs. Additionally, in undertaking vertical magnetic measurements a better understanding of how the magnetic field changes with height has also been gained. In general, the lower vertical heights above ground level produced negative magnetic anomalies and the higher vertical heights produced positive magnetic anomalies. The results from field trial 2 have enabled a better understanding of the shape of the magnetic field and also of how the magnetic field changes with distance from the magnetic grout discs.

From both field trials, the maximum distance at which the detectable grout could be detected was 3 m. However, by increasing the volume of detectable grout to a volume typical of an industrial application, the distance at which it can be detected is increased. Hence, for the volumes of the detectable grout commensurate with a real-world engineering scenario, modelling predicts (See Chapter 6, Section 6.2) a maximum detectable distance of 6 m.

7.3 Future Work

Following on from the work undertaken in this thesis there are several areas suitable for further research.

As part of this thesis, extensive testing of the magnetic grout properties has been undertaken. The flow, bleed, setting time, and curing temperature of the grout has been tested and an understanding gained of how these properties are affected by the addition of the magnetic additive to the grout mixture. To further the understanding of how the addition of a magnetic additive to the grout effects its properties, the strength of the magnetic grout material should be tested. The strength of grout is formed during the hydration reactions of the cement. The speed at which the cement reacts with water to form the alite constituent of cement, contributes to the early strength. In adding a magnetic additive to the grout mixture, it has been seen during both the temperature and setting time tests that the magnetic cement does not reach the same temperature as for a pure cement mixture, nor does the temperature rise as rapidly. This therefore could indicate that the strength of the magnetic grout mixture has been adversely affected by the addition of the magnetic additive.

Using magnetite as the magnetic additive within the grout, the furthest detection distance achieved within this thesis was 3 m. The amount of magnetic additive within the magnetic grout mixture to enable detection at this distance was 10% of the cement mass. To both increase the detection distance of the magnetic grout material, and also decrease the amount of magnetic additive added into the mixture, different magnetic additives could be tested. An option of increasing the magnetic field generated by the additives is the use of permanent magnet powders. Permanent magnets, such as neodymium, and samarium-cobalt magnets, are much stronger than magnetite. This implies that to achieve the same field strength, a much smaller amount of the permanent magnet powder would be required. By trialling the addition of different magnetic additives to the grout mixture, all the property tests undertaken in this thesis could be carried out on a new range of magnetic grout mixtures. This would allow

comparisons to be undertaken and the grout material to be optimised for both cost and performance.

Both of the field trials undertaken and discussed in this thesis have focused on determining the distance at which the magnetic grout mixture can be detected. To further the understanding of the detectability of the magnetic grout mixture in the field, a borehole trial should be undertaken. This would mimic the conditions under which the magnetic grout would be used on engineering projects. The trial would follow a similar procedure to that used here, with a background reading for the site being undertaken before the injection of the magnetic grout takes place. By injecting the magnetic grout via a borehole, real time monitoring of the grout spread could also be undertaken. This would give a good indication of the location of the grout, informing the decision to stop grouting once the design grout volume has been achieved.

7.4 Overall Conclusions

Overall, this thesis has investigated the production of a magnetic grout material that is detectable. In using a combination of laboratory experiments and field trials, the magnetic grout material has provided sufficient proof of concept that magnetic grout has workable engineering properties and that once injected, the location and shape of the resulting grouted rock volume can be detected. This detectable grout has the potential both to increase confidence in the integrity of grouted rock volumes and to reduce the inefficiencies currently present in the grouting industry, by enabling in-situ real-time optimisation of grouting campaigns.

References

Anderson, J.P. and Blotzer, R.J. (1999) Permeability and Hysteresis Measurement. In: ed. Webster, J.G. *The Measurement, Instrumentation and Sensors Handbook.* CRC Press. Pages: 1448 – 1456.

ASTM C939 – 10 (2010) Standard Test Method for Flow of Grout for Preplaced – Aggregate Concrete (Flow Cone Method).

ASTM C232/C232M – 12 (2012) Standard Test Method for Bleeding of Concrete.

Baptiste, J., Martelet, G., Faure, M., Beccaletto, L., Reninger, P.-A., Perrin, J., and Chen, Y. (2016) Mapping of a buried basement combining aeromagnetic, gravity and petrophysical data: The substratum of Southwest Paris Basin, France. *Tectonophysics*, **683**, 333-348.

Barton, G. (2013) Stabilisation of Mine Workings at the National Indoor Sports Arena and Velodrome [PowerPoint Presentation]. Available at: http://www.strath.ac.uk/media/departments/civilengineering/research/seminars/Graham_Barton_16.10.2013_Stabilising_Mineworking_at_NISA.pdf (Accessed 28th October 2013).

Billings, S. and Youmans, C. (2007) Experiences with unexploded ordnance discrimination using magnetometry at a live-site in Montana. *Journal of Applied Geophysics*¸ **61**, 194-205.

Blundell, S. (2012) Magnetism A Very Short Introduction. Oxford University Press.

Borglin, S.E., Moridis, G.J., and Becker, A. (1998) Magnetic Detection of Ferrofluid Injection Zones. Earnest Orlando Lawrence Berkeley National Laboratory.

Botsou, F., Karageorgis, A.P., Dassenakis, E. and Scoullos, M. (2011) Assessment of heavy metal contamination and mineral magnetic characterisation of the Asopos River sediments (Central Greece). *Marine Pollution Bulletin,* **62,** 547-563.

Breiner, S. (1999) Applications Manual for Portable Magnetometers. Geometrics.

British Standards Institution (2007) *BS EN 196-7:2007 Methods of Testing Cement – Part 7: Methods of taking and preparing samples of cement*, London British Standards Institution.

British Standards Institution (2008) *EN 196-3:2005+A1:2008 Methods of Testing Cement – Part 3: Determination of setting times and soundness,* London British Standards Institution.

British Standards Institution (2011) *BS EN 197-1 Cement Part 1: Composition, specifications and conformity criteria for common cements,* London British Standards Institution.

Bullard, J.W., Jennings, H.M., Livingston, R.A., Nonat, A., Scherer, G.W., Schweitzer, J.S., Scrivener, K.L., and Thomas, J.J. (2011) Mechanisms of cement hydration. *Cement and Concrete Research,* **41**, 1208-1223.

Bye, G.C. (1999) *Portland Cement.* Second Edition, Thomas Telford.

Callister, W.D. (2007) Materials Science and Engineering. John Wiley & Sons, Inc.

Cementa (2007) Ultrafin 16.

Chen, Y., Nishiyama, T., Terada, M. and Iwamoto, Y. (2000) A fluorescent approach to the identification of grout injected into fissures and pore spaces. *Engineering Geology,* **56,** 395-401.

Cherry, E.M. and Eaton, J.K. (2014) A comprehensive model of magnetic particle motion during magnetic drug targeting. *International Journal of Multiphase Flow*, **59,** 173-185.

Christensen, U.R. (2011) Geodynamo models: Tools for understandings properties of Earth's magnetic field. *Physics of the Earths and Planetary Interiors*, **187,** 157-169.

Chomoucka, J., Drbohlavova, J., Huska, D., Adam, V., Kizek, R., and Hubalek, J. (2010) Magnetic nanoparticles and targeted drug delivering. *Pharmacological Research*, **62,** 144-149.

Coey, J.M.D. (2010) Magnetism and Magnetic Materials. Cambridge University Press.

Cullity, B.D. and Graham, C.D. (2009) Introduction to Magnetic Materials. IEEE Press, Wiley.

Dhir, R.K. and Jackson, N. (1980) Concrete In: Jackson, N. ed. Civil Engineering Materials.

Di Maio, R., La Manna, M., and Piegari, E. (2016) 3D Reconstruction of Buried Structures from Magnetic, Electromagnetic and ERT Data: Example from the Archaeological Site of Phaistos (Crete, Greece). *Archaeological Prospection*, **23**, 3-13.

Donaldson Associates (2012) Pre-excavation Grouting Strategy Report. Drainage Services Department Harbour Area Treatment Scheme Stage 2A.

Draganović, A. (2009) *Bleeding and Filtration of Cement-based Grout*. Doctoral Thesis. Royal Institute of Technology, Stockholm.

Draganović, A. and Stille, H. (2011) Filtration and penetrability of cement-based grout: Study performed with a short slot. *Tunnelling and Underground Space Technology*, **26,** 548-559.

Dunlop, D.J. (1990) Developments in Rock Magnetism. *Reports on Progress in Physics*, **53,** 707-792.

Emmelin, A., Brantberger, M., Eriksson, M., Gustafson, G and Stille, H. (2007) Rock Grouting – Current competence and development for the final repository. Swedish Nuclear Fuel and Waste Management Co.

Folco, L., Rochette, P., Gattacceca, J. and Perchiazzi, N. (2006) In situ identification, pairing, and classification of meteorites from Antarctica through magnetic susceptibility measurements. *Meteoritics and Planetary Science*, **41**, 343-353.

Fransson, Å. (2008) Grouting design based on characterization of the fractured rock. Presentation and demonstration of a methodology. SWECO Environment and Chalmers University of Technology.

Funehag, J. and Gustafson, G. (2008) Design of grouting with silica sol in hard rock – New design criteria tested in the field, Part II. *Tunnelling and Underground Space Technology*, **23**, 9-17.

Galíndez, J.M. and Molinero, J. (2010) Assessment of the long-term stability of cementitious barriers of radioactive waste repositories by using digital-image-based microstructure generation and reactive transport modelling. *Cement and Concrete Research*, **40,** 1278-1289.

Galindo-Zaldívar, J., Ruiz-Constán, A., Pedrera, A., Ghidella, M., Montes, M., Nozal, F. and Rodríguez-Fernandez, L.R. (2013) Magnetic anomalies in Bahia Esperanza: A window of magmatic arc intrusions and glacier erosion over the northeastern Antarctic Peninsula. *Tectonophysics*, **585**, 68-76.

Gandhi, S.M. and Sarkar, B.C. (2016) Essentials of Mineral Exploration and Evaluation. Elsevier.

Gani, M.S.J. (1997) *Cement and Concrete*. Chapman and Hall.

Getzlaff, M. (2008) Fundamentals of Magnetism. Springer.

Geomatrix Earth Science Ltd (2016) Magnetic Field Calculator https://www.geomatrix.co.uk/tools/magnetic-field-calculator/ [Online] (Accessed: January 2016).

Google Maps (2016a) Rouken Glen Park (Satellite) [Online] (Accessed: 20th May 2016).

Google Maps (2016b) The beach at Troon (Satellite) [Online] (Accessed: 20th May 2016).

Gustafson, G. (2012) *Hydrogeology for Rock Engineers*.

Håkansson, U., Hässler, L., and Stille, H. (1992) Rheological Properties of Microfine Cement Grouts. *Tunnelling and Underground Space Technology*, **7,** 453-458.

Hallal, A., Kadri, E.H., Ezziane, K., Kadri, A., and Khelafi, H. (2010) Combined effect of mineral admixtures with superplasticizers on the fluidity of the blended cement paste. *Construction and Building Materials*, **24**, 1418-1423.

Harrison, R.J. and Feinberg, J.M. (2009) Mineral Magnetism: Providing New Insights into Geoscience Processes. *Elements*, **5,** 209-215.

Healy, P.R. and Head, J.M. (1984) *Construction over abandoned mineworkings*. Construction Industry Research and Information Association, Special Publication 32.

Henderson, A.E., Robertson, I.A., Whitfield, J.M., Garrard, G.F.G., Swannell, N.G. and Fisch, H. (2008) A New Method for Real-Time Monitoring of Grout Spread through Fractured Rocks. *MRS Proceedings,* **1107.**

Henn, R.W. (1996) *Practical Guide to Grouting of Underground Structures*. Thomas Telford.

Herries, A.I.R. and Fisher, E.C. (2010) Multidimensional GIS modelling of magnetic mineralogy as a proxy for fire use and spatial patterning: Evidence from the Middle Stone Age bearing sea caves of Pinnacle Point 13B (Western Cape, South Africa), *Journal of Human Evolution,* **59,** 306-320.

Hiergeist, R., Ketzler, R., Harcken, H., Lüdke, J., Albrecht, M., Brand, T., and Fischer, A. (2015) A novel test ground for the equipment qualification of magnetic gradient sensors used for unexploded bomb detection. *Journal of Applied Geophysics,* **112,** 242- 248.

Høien, A.H. and Nilsen, B. (2014) Rock Mass Grouting in the Løren Tunnel: Case Study with the Main Focus on the Groutability and Feasibility of Drill Parameter Interpretation. *Rock Mechanics and Rock Engineering,* **47,** 967-983.

Hollmén, K. (2008) R20 Programme: The Development of Grouting Technique – Stop Criteria and Field Tests. Posiva Working Report 2007-101.

Hrvoic, I. (2011) Magnetometers. In: ed. Gupta, H.K. Encyclopaedia of Solid Earth Geophysics. Springer.

ITA Working Group (1991) Damaging Effects of Water on Tunnels during their Working Life. *Tunnelling and Underground Space Technology*, **6**, 11-76.

Jiles, D. (1998) Introduction to Magnetism and Magnetic Materials. Chapman and Hall.

Jo, C.H., Cha, Y.H. and Choi, J.H. (2003) A Borehole magnetic logging tool for estimating unknown foundation depths. Presented at the 3rd International Conference on Applied Geophysics, Hotel Royal Plaza, Orlando, Florida, December 8th -12th 2003.

Kearey, P., Brooks, M. and Hill, I. (2002) An Introduction to Geophysical Exploration. Blackwell Science.

Kempe, H. and Kempe, M. (2010) The use of magnetic nanoparticles for implant-assisted magnetic drug targeting in thrombolytic therapy, *Biomaterials*, **31,** 9499-9510.

Khalil, M.H. (2016) Subsurface faults detection based on magnetic anomalies investigation: A field example at Taba protectorate, South Sinai. *Journal of Applied Geophysics*, **131,** 123-132.

Knappett, J.A. and Craig, R.F. (2012) Craig's Soil Mechanics. Eighth Edition, Spon Press.

Kono, M. and Roberts P.H. (2002) Recent geodynamo simulations and observations of the geomagnetic field. *Reviews of Geophysics*, **40,** 4-1-4-53.

Lanza, R. and Meloni, A. (2006) The Earth's Magnetism. An Introduction for Geologists. Springer.

Lombardi, G. (1996) Selecting the Grouting Intensity. *The International Journal on Hydropower and Dams,* **4,** 62-66.

Lombardi, G. and Deere, D. (1993) Grouting design and control using the GIN Principle. *Water Power and Dam Construction,* 15-22.

Lothenbach, B., Winnefeld, F., Alder, C., Wieland, E., and Lunk, P. (2007) Effect of temperature on the pore solution, microstructure and hydration products of Portland cement pastes. *Cement and Concrete Research,* **37**, 483-491.

Lowrie, W. (2007) Fundamentals of Geophysics. Cambridge University Press.

Macintyre, S.A. (1999) Magnetic Field Measurement. In: ed. Webster, J.G. *The Measurement, Instrumentation and Sensors Handbook.* CRC Press. Pages: 1414 – 1446.

Majer, E.L. (1989) The Application of High Frequency Seismic Monitoring Methods for the Mapping of Grout Injections. *International Journal of Rock Mechanics and Mining Sciences & Geomechanics Abstracts,* **26,** 249-256.

Mangual J.O., Li, S., Ploehn, H.J., Ebner, A.D., and Ritter, J.A. (2010) Biodegradable nanocomposite magnetite stent for implant-assisted magnetic drug targeting. *Journal of Magnetism and Magnetic Materials,* **322,** 3094-3100.

Marchetti M., Cafarella, L., Di Mauro, D. and Zirizzotti, A. (2002) Ground magnetometric surveys and integrated geophysical methods for solid buried waste detection: a case study. *Annals of Geophysics,* **45**, 563-573.

Mekkawi, M., Arafa-Hamed, T., and Abdellatif, T. (2013) Detailed magnetic survey at Dahsour archaeological sites Southwest Cairo, Egypt. *NRIAG Journal of Astronomy and Geophysics,* **2**, 175-183.

Milsom, J. (2003) Field Geophysics – The Geological Field Guide Series. Third Edition, Wiley.

Munschy, M., Boulanger, D., Ulrich, P., and Bouiflane, M. (2007) Magnetic mapping for the detection of characterization of UXO: Use of multi-sensor fluxgate 3-axis magnetometers and methods of interpretation. *Journal of Applied Geophysics,* **61**¸ 168-183.

Mussett, A.E. and Khan, M.A. (2007) Looking Into the Earth: An Introduction to Geological Geophysics. Cambridge University Press.

Nabighian, M.N., Grauch, V.J.S., Hansen, R.O., LaFehr, T.R., Li, Y., Peirce, J.W., Phillips, J.D., and Ruder, M.E. (2005) The historical development of the magnetic method in exploration, *Geophysics*, **70**, 33-61.

Neville, A.M. (1973) *Properties of Concrete.* Pitman Publishing.

Nicholson, P.G. (2015) *Soil Improvement and Ground Modification Methods*. Elsevier.

Nkinamubanzi, P.-C., Mantellato, S., and Flatt, R.J. (2016) Superplasticizers in practice. In: Aïtcin, P.-C., and Flatt, R. eds. *Science and Technology of Concrete Admixtures*. Woodhead Publishing, pp 353-377.

Parasnis, D.S. (1962) Principles of Applied Geophysics. Chapman and Hall, London.

Prouty, M. and Johnson, R. (2010) Small, Low Power, High Performance Magnetometers. EGM 2010 International Workshop: Adding new value to Electromagnetic, Gravity and Magnetic Methods for Exploration. Capri, Italy, April 11-14.

Rawlings, C.G., Hellawell, E.E., and Kilkenny, W.M. (2000) Grouting for Ground Engineering. Construction Industry Research and Information Association, Publication C514.

Reford, M.S and Sumner, J.S. (1964) Aeromagnetics, Geophysics, 29, 482-516. In: Nabighian, M.N., Grauch, V.J.S., Hansen, R.O., LaFehr, T.R., Li, Y., Peirce, J.W., Phillips, J.D., and Ruder, M.E. (2005) The historical development of the magnetic method in exploration, *Geophysics*, **70**, 33-61.

Reynolds, J.M. (1997) An Introduction to Applied and Environmental Geophysics. Wiley.

Roberts, P.H. and Glatzmaier, G.A. (2000) Geodynamo theory and simulations. *Reviews of Modern Physics*, **72**, 1081-1123.

Romalis, M.V. (2007) Atomic sensors: Chip-scale magnetometers. *Nature Photonics*, **1**, 613-614.

Rosquoët, F., Alexis, A., Khelidj, A., and Phelipot, A. (2003) Experimental study of cement grout: Rheological behaviour and sedimentation. *Cement and Concrete Research*, **33**, 713 – 722.

Rouken Glen Park (2016) Park History [Online] Available at: www.roukenglenpark.co.uk (Accessed: 20th May 2016).

Sakai, E., Kasuga, T., Sugiyama, T., Asaga, K., and Daimon, M. (2006) Influence of superplasticizers on the hydration of cement and the pore structure of hardened cement. *Cement and Concrete Research*, **36,** 2049-2053.

Sakuraba, Y. (2016) Potential of thermoelectric power generation using anomalous Nernst effect in magnetic materials. *Scripta Materialia*, **111**, 29-32.

Schwindt, P.D.D, Knappe, S., Shah, V., Hollberg, L. and Kitching, J. (2004) Chip-scale atomic magnetometer. *Applied Physics Letters,* **85**, 6409-6411.

Selvåg, J. (2006) NATO JRP Electronic MCM NO Phase 1 Report – Sensor Technology. Norwegian Defence Research Establishment.

Sheinker, A. and Moldwin, M.B. (2016) Magnetic anomaly detection (MAD) of ferromagnetic pipelines using principle component analysis (PCA). *Measurement Science and Technology,* **27**, 045104.

Smith, K. (1997) Caesium Optically Pumped Magnetometers – Basic Theory of Operation. Technical Report M-TR91, Geometrics.

Spaldin, N.A. (2010) Magnetic Materials Fundamentals and Applications. Cambridge University Press.

Stille, H., Gustafson, G., and Hassler, L. (2012) Application of New Theories and Technology for Grouting of Dams and Foundations on Rock. *Geotechnical and Geological Engineering,* **30**, 603-624.

Szitkar, F., Dyment, J., Le Saout, M., Honsho, C., and Gente, P. (2016) Dyking at EPR 16°N hypermagmatic ridge segment: Insights from near-seafloor magnetics. *Earth and Planetary Science Letters,* **453**, 288-297.

Tan, Ö. and Zaimoglu, A.S. (2004) Taguchi approach for investigation of the setting times on cement-based grouts. *Indian Journal of Engineering & Materials Sciences,* **11,** 63-67.

Tan, Ö, Zaimoglu, A.S., Hinislioglu, S, and Altun, S. (2005) Taguchi approach for the optimisation of the bleeding on cement-based grouts. *Tunnelling and Underground Space Technology,* **20,** 167-173.

Taylor, H.F.W. (1997) *Cement chemistry*, 2nd edition. London, Thomas Telford Publishers.

Telford, W.M., Geldart, L.P. and Sheriff, R.E. (1990) Applied Geophysics. Cambridge University Press.

Tolppanen, P and Syrjänen, P. (2003) Hard Rock Tunnel Grouting Practice in Finland, Sweden and Norway. Finnish Tunnelling Association.

US Army Corps of Engineers (1995) Chemical Grouting. Engineering and Design, Engineers Manual.

Wang, B, Xia, D., Yu, Y., Jia, J., Nie, Y., and Wang, X. (2015) Detecting the sensitivity of magnetic response on different pollution sources – A case study from typical mining cities in northwestern China. *Environmental Pollution,* **207,** 288-298.

Whitfield, J.M. and Henderson, A.E. (2008) The Dounreay ILW Shaft Isolation Project – Advanced Rock Grouting in the Nuclear Environment. Ritchies. Presentation.

Widmann, R. (1996) International Society for Rock Mechanics Commission on Rock Grouting. *International Journal of Rock Mechanics and Mining Sciences & Geomechanics Abstracts*, **33,** 803-847.

Zhang, F., Xie, X., and Huang, H. (2010) Application of ground penetrating radar in grouting evaluation for shield tunnel construction. *Tunnelling and Underground Space Technology*, **25**, 99-107.

Zhang, Q., Al-Nuaimy, W., and Huang, Y. (2007) Interpretation of borehole magnetometer data for the detection and characterisation of unexploded bombs. *Journal of Applied Geophysics,* **61**, 206-216.